# Experimental testing of masonry structures subjected to extreme loads

Ahmad Morsel

# MEMOIRE DE DOCTORAT DE

L'ECOLE CENTRALE DE NANTES

ECOLE DOCTORALE N° 602
*Sciences de l'Ingénierie et des Systèmes*
Spécialité : Génie Mécanique

Par

**Ahmad MORSEL**

# Experimental testing of masonry structures subjected to extreme loads

**Projet de recherche doctoral présenté et soutenu à l'École Centrale de Nantes, le 4 Avril 2024**
**Unité de recherche : UMR 6183, Institut de recherche en Génie Civil et Mécanique (GeM)**

**Rapporteurs avant soutenance** :

| | |
|---|---|
| Michel ARRIGONI | Professeur ENSTA HDR, Ecole Nationale Supérieure de Techniques Avancées Bretagne |
| Yann MALECOT | Professeur des universités, Université Grenoble Alpes |

**Composition du Jury :**

| | | |
|---|---|---|
| Présidente : | Irini DJERAN-MAIGRE | Professeure des universités, Institut National des Sciences Appliquées de Lyon |
| Examinateurs : | Michel ARRIGONI | Professeur ENSTA HDR, Ecole Nationale Supérieure de Techniques Avancées Bretagne |
| | Yann MALECOT | Professeur des universités, Université Grenoble Alpes |
| | Sandra ESCOFFIER | Chargée de recherche, Université Gustave Eiffel, Campus de Nantes |
| | Benjamin RICHARD | Dr, Ingénieur de recherche HDR, IRSN, Fontenay-aux-Roses |

| | | |
|---|---|---|
| Directeur de recherches doctorales : | Ioannis STEFANOU | Professeur des universités, Ecole Centrale de Nantes |
| Co-dir. de recherches doctorales : | Panagiotis KOTRONIS | Professeur des universités, Ecole Centrale de Nantes |
| Co-enc.de recherches doctorales : | Filippo MASI | Senior research fellow, University of Sydney, Australie |

The authors would like to acknowledge the support of the Region Pays de la Loire and Nantes Métropole under the Connect Talent programme (CEEV: Controlling Extreme EVents - BLAST: Blast LoAds on STructures), https://blastructures.eu/.

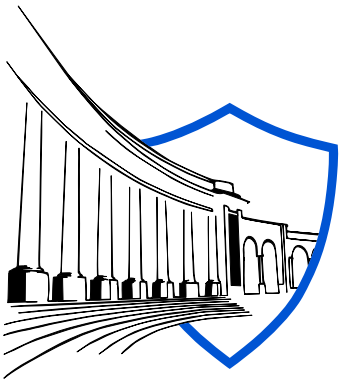



"*Science is not only a discipline of reason but, also, one of romance and passion.*"
Stephen Hawking

# Acknowledgments

Having reached the end of my PhD journey, after around a three years of preparation meticulous amount of work within the GeM laboratory of ECN, this journey has become a part of my life and a story that I will tell to my children later. It is a story that is full of special moments, challenging times, and individuals who surrounded me, supported me, and advised me throughout this adventure. It is a unique experience which has affected me both personally and professionally as a researcher.

First and foremost, I would like to express my sincere gratitude to my Advisors: Ioannis Stefanou, Panagiotis Kotronis, and Filippo Masi, for their guidance, support, availability, and contributions to the success of this PhD. I admire our team spirit that has allowed us to develop this research project from scratch, and I am deeply thankful for all the motivation and knowledge that I have received. I am truly grateful for the honor of working alongside such esteemed professionals, and look forward to continuing our collaborative efforts in the future.

I would also like to thanks to Guillaume Racineux for his contributions related to the explosive source, for all our discussions, and the knowledge I gained from him. Moreover, I would like to thank Emmanuel Marché for his help in installing the cabin, conducting the experiments, and for assisting me in tackling several technical challenges related to the explosive source.

I would also like to express my gratitude to the jury members for evaluating my work and engaging in fruitful and dynamic discussions during the defense. First of all, I would like to thank the two reviewers, who have accepted to examine my PhD work: Michel Arrigoni and Yann Malecot. Thank you for your interest in this work and and for your valuable feedback and comments. Special thanks to Irini Djeran-Maigre for chairing my thesis jury. I appreciate your help and support as supervisors for my internship and research engineer work before starting my thesis and as a jury member. Your help, guidance, and feedback were invaluable. I also appreciate the examination of my thesis by Sandra Escoffier and Benjamin Richard. Thank you for your insightful questions and feedback, and for your contributions as members of previous CSI committees.

My appreciation also goes to Ecole Centrale de Nantes for hosting me, to the GeM laboratory, and its staff, particularly: Patrick, Katia, Sandra, Marine, and Cannelle. Many thanks to CRED and Pierrick Guegan for their assistance and work related to imaging techniques and conducting several experiments using high-speed cameras.

Now it's time to thank my colleagues in the CoQuake group with whom I spent most of my time in the lab: Alex, Saba, Diego, Abdallah, and Georgios.

I would like to thank my colleagues for our shared moments and discussions, including Imane, Salma, Mickaël, Julien, Siderta, Ghita. Special thanks to Rana, Dania, Dana, Bassel, Baraa, Moeen, Mosbah, Ahmad, Paulina, Issa – your presence and support have greatly enriched my doctoral journey.

I finally thank my family for their continuous love, support, and encouragement

throughout my doctoral studies. To my father, Ali, who has been my inspiration and support, and to my mother, Rima, for her blessings and being near to me in my difficult times. To my siblings: Iman, Fatima, Muhammad, Hussien, Hassan, Yasser, and Imad – your presence has made every moment a celebration and joy.

Last, but not least, I would like to express my deepest gratitude to my special person Hayat. Your unwavering love, encouragement, and support have been the guiding light that has illuminated my path throughout this journey.

# Abstract

Masonry structures are characterized by bricks, stones, or concrete blocks, held together with or without mortar. This is also the case for historical and monumental structures, which are often exposed to accidental or deliberate explosions. In this thesis, we aim to investigate the dynamic response and failure mechanisms of masonry structures when subjected to dynamic loading originating from blast events.

The response of stone structures to explosions is insufficient to investigate by relying only on numerical and analytical tools. Therefore, experiments are mandatory to improve the current understanding and validate existing models. To this end, we study the effects of an explosive event on structures using reduced scale experiments under laboratory conditions.

We present herein a novel experimental platform (miniBLAST), to study masonry assets based on scaling laws for the rigid-body response of structures. In particular, exploding wires allow us to recreate loading conditions analogous to those in high explosive materials., with minimum costs and high reproducibility. The proposed setup and methodology can be used to investigate, for the first time, the response of masonry structures under blast loads in a safe laboratory environment.

Our platform enables us to collect data and analyze in detail the fast dynamics of masonry structures under explosions. The experimental setup offers a high degree of control and repeatability, particularly in terms of the detonation of exploding wires, the resultant blast waves and structural response.

Relying on miniBLAST, we analyze the explosive source in detail to understand the explosion mechanism. This study shed light on the influence of electric circuit system on shock wave formation. The calculation of the TNT equivalence factor allows us to up-scale the explosive loads originating from the exploding wire.

Our experiments serve the purpose of validating existing numerical works, and reveal the salient features of masonry structures under blast loads. Basing on Particle Tracking Velocimetry to study in 3D the rigid body motion (i.e. the Parthenon of Athens). The results from this experimental platform are intended to enhance and refine both existing and new computational models for structures subjected to blast loads. Moreover, to draw appropriate protective strategies for masonry buildings, ancient and modern ones.

**Keywords:** Masonry, Blast loads, Fast-dynamics, Reduced-scale experiments, Scaling laws, Exploding wires, TNT equivalence, Particle Tracking Velocimetry (PTV), Parthenon of Athens.

# Résumé

Les structures en maçonnerie se caractérisent par des briques, des pierres ou des blocs de béton, maintenus ensemble avec ou sans mortier. C'est également le cas pour les structures historiques et monumentales, qui sont souvent exposées à des explosions accidentelles ou délibérées. Dans cette thèse, nous visons à étudier la réponse dynamique et les mécanismes de défaillance des structures en maçonnerie lorsqu'elles sont soumises à des charges dynamiques issues d'événements explosifs.

La réponse des structures en pierre aux explosions est insuffisante pour être étudiée en se fiant uniquement aux outils numériques et analytiques. Par conséquent, des expériences sont nécessaires pour améliorer la compréhension actuelle et valider les modèles existants. À cette fin, nous étudions les effets d'un événement explosif sur les structures à l'aide d'expériences à petite échelle sous conditions de laboratoire.

Nous présentons ici une nouvelle plateforme expérimentale (miniBLAST) pour étudier les actifs en maçonnerie basée sur des lois de mise à l'échelle pour la réponse des structures en corps rigide. En particulier, les fils explosifs nous permettent de recréer des conditions de chargement analogues à celles des matériaux explosifs haute performance, avec des coûts minimes et une grande reproductibilité. La configuration et la méthodologie proposées peuvent être utilisées pour étudier, pour la première fois, la réponse des structures en maçonnerie aux charges explosives dans un environnement de laboratoire sûr.

Notre plateforme nous permet de collecter des données et d'analyser en détail la dynamique rapide des structures en maçonnerie sous les explosions. La configuration expérimentale offre un haut degré de contrôle et de reproductibilité, notamment en ce qui concerne la détonation des fils explosifs, les ondes de choc résultantes et la réponse structurelle.

En nous appuyant sur miniBLAST, nous analysons en détail la source explosive pour comprendre le mécanisme de l'explosion. Cette étude éclaire l'influence du système de circuit électrique sur la formation des ondes de choc. Le calcul du facteur d'équivalence au TNT nous permet de mettre à l'échelle les charges explosives issues des fils explosés.

Nos expériences servent à valider les travaux numériques existants et révèlent les caractéristiques saillantes des structures en maçonnerie soumises à des charges explosives. En utilisant la vélocimétrie par suivi de particules pour étudier en 3D le mouvement des corps rigides (par exemple, le Parthénon d'Athènes). Les résultats de cette plateforme expérimentale sont destinés à améliorer et à affiner à la fois les modèles informatiques existants et nouveaux pour les structures soumises à des charges explosives. De plus, pour élaborer des stratégies de protection appropriées pour les bâtiments en maçonnerie, anciens et modernes.

**Mots-clés:** Maçonnerie, Charges explosives, Dynamique rapide, Expériences en échelle reduite, Lois d'échelle, Fils explosés, TNT équivalence, Vélocimétrie par Suivi de Particules (PTV), Parthénon d'Athènes.

# Contents

# Introduction

In this Thesis, we investigate the dynamic response of masonry structures subjected to extreme loads and, in particular, those arising from explosions by designing a novel, reduced-scale laboratory platform enabling highly repeatable and controlled experimental tests.

Masonry structures have being frequently exposed to accidental or deliberate explosions. Among others, we refer to the explosion of the Parthenon of Athens (Greece) in 1687 (Mommsen, 1941), the Kanto explosion (Japan) in September 1923 (Charles, 2014), Port Chicago (United States) in 1944 (Doss, 2011), the chemical plant in Flixborough (England) in 1974 (Health and Safety Executive, 1975), the archaeological site of Palmyra (Syria) in 2015 (Barnard, 2015), and the explosion in Beirut (Lebanon) on August 4, 2020 (Sivaraman and Varadharajan, 2021).

Masonry structures are characterized by blocks arranged in specific patterns and interacting with each others through interfaces (joints). Blocks are generally made of bricks, stones, or concrete, while interfaces can either be dry or with mortar. The analysis of masonry structures attracted and continues to attract significant scientific research, mostly due to the fact that a vast amount of historical buildings and a considerable part of ancient and modern constructions are made of masonry. In the last decades, research was mainly focused on the mechanical behavior of structures under quasi-static and seismic loading via experimental, numerical, and theoretical means (Richard et al., 2016; Djeran-Maigre et al., 2022a; Gabrielsen et al., 1975; Li et al., 2020, 2017; Michaloudis and Gebbeken, 2019; Godio et al., 2018; Djeran-Maigre et al., 2022b; Petry and Beyer, 2014; Yadav et al., 2021; Knox et al., 2018; Banci et al., 2018; Yadav et al., 2023; Tomaževič et al., 2009). However, the increased threats against buildings and infrastructures by means of explosions (accidental and/or deliberate) renders the investigation of the behavior of masonry structures against fast dynamic loads essential for preserving the cultural heritage and preventing human losses.

At present, the knowledge of the dynamic response and failure mechanisms of masonry structures under explosions is insufficient and mostly relies on numerical and analytical tools. In this context, experiments are necessary as they can improve our understanding of the highly nonlinear structural response and its interaction with shock waves, during an explosion. Large-scale experiments are typically carried in specialized testing areas with restricted access (Godio et al., 2021; Pereira et al., 2015; Ahmad et al., 2014; Ngo et al., 2007; Keys and Clubley, 2017; Sielicki and Łodygowski, 2019). A variety of experiments has been conducted to characterize diverse explosive sources and the corresponding blast-induced loading on structures (Wang, 2014; Tyas, 2018; Filice et al., 2022). Additionally, studies on the propagation of shock waves resulting from explosions enabled shedding light on the temporal evolution of the pressure in confined structures and urban settings including tunnels (Trélat et al., 2007; Pennetier et al., 2015; Fouchier et al., 2017; Zyskowski et al.,

2004; Sochet et al., 2019; Gault et al., 2020). It is worth noticing that blast-induced waves and loads are also employed in hydro-forming applications for shaping large metal plates, this is includes measuring the pressure loads exerted on the part by using a designed sensors (Tartière et al., 2021; Arrigoni et al., 2018, i.e. polyvinyliden fluoride, ). Nevertheless, blast experiments of (masonry) structures are extremely limited in number when compared to other loading scenarios and, in particular, seismic loads.

Experimental testing of full scale structures (prototype) exposed to blast loads is non trivial due to the associated cost, which hinders studies of the repeatability of the loading conditions, measuring devices, environmental hazards, and safety risks that must be considered when designing and carrying out experiments (Draganić et al., 2018). Complexity also increases when dealing with masonry structures due to their non-linear behavior and complex failure modes.

An alternative method used to investigate the effects of an explosive event on structures is to resort to reduced-scale experiments in laboratory conditions, Morsel et al. (2022). Reduced scale experiments ensure a high degree of repeatability, moderate cost, and reduced hazards associated with personnel and environmental safety. Under controlled conditions, explosive tests at reduced scale can be handily generated using various explosive sources, solid or chemical explosives (Sochet, 2010; Hargather and Settles, 2007). Such experiments use small charges that typically range from few milligrams for laboratory tests (Hargather, 2005; Kleine et al., 2005; Hargather and Settles, 2007) to few kilograms for a reduced-scale field test (Neuberger et al., 2007).

In parallel, appropriate scaling laws are essential to design reduced-scale experiments, assuring a similarity between the reduced-scale model and the full-scale prototype. The concept of similarity involves identifying the essential conditions to conduct reduced-scale experiments based on full-scale ones and predicting the structural response of the latter from the analysis of the model (Baker et al., 1991). Note that the derivation of scaling laws related to both the blast load and the structural response is essential, yet challenging, owing to the inherent complexity of the physical phenomena involved, including energy release during explosion, structural response, shock wave propagation.

The key point of this Thesis is the design, installation, and validation of a novel experimental setup enabling controlled and safe investigation of the structural response to explosions of masonry and blocky structures. The setup allows us to address the issues and difficulties related full-scale and field experimental test. More precisely, we

(a) Design an experimental platform to study masonry structures at reduced scale in the laboratory.

In so doing, we present a comprehensive guide explicitly detailing the whole design process. This includes all the essential information on handling experimental errors, data acquisition, safety and other critical aspects. Additionally, we provide a safety protocol to ensure the safety of both the experimental setup and the surrounding environment, with a specific emphasis on addressing noise and sound-related concerns.

Relying on the aforementioned innovative setup, we demonstrate the possibility of replicating blast scenarios for structures with complex geometries. Attention is particularly focused on the analogue explosive source designed and employed throughout this work. We rel analyze the electrical system related to the explosive source "exploding wires" and to understand the underlying mechanism. In particular:

(b) We employ the "exploding wire" technology to recreate blast-induced shock waves and loads and investigate the electric circuit equations and parameters enabling the description of the highly nonlinear electro-mechanical phenomena occurring during the explosion.

The numerical equations related to the current and voltage signals are derived. Based on these equation and by means of best-fit interpolations of the experimental measurements, we obtain the effective values of the electric circuit parameters including the capacitance, electrical resistance, and inductance. Our analysis includes a description of the the explosion mechanisms underlying the phases that occurs during the explosion of the exploding wire and how it leads to the generation of shock waves. Moreover, we provide an estimation to the resistance variation, energy dissipation and temperature raised during explosion.
Next, we present an in-depth analysis of the analogue explosive source.

(c) We characterize the explosive source in terms of its equivalent blast parameters and, namely, impulse, overpressure, shock wave speed and shape.

The investigation includes validating and studying incident overpressure based on shock wave pressure distribution and sphericity over distances. We compare our explosive source with other high explosive sources in terms of shock wave radius, as well as deriving the TNT equivalence factor based on the incident peak impulse and overpressure.

Relying on the above mentioned analysis related to the accuracy and repeatability of our pressure signals, the next step is the experimental validation of the scaling laws first proposed by (Masi et al., 2022). More precisely,

(d) We present a first benchmark of the scaling laws in presence of geometric scaling of a prototype to a reduced-scale model and follow to the comparison of their three-dimensional motion by focusing on rocking and overturning mechanisms Masi et al. (2019).

This validation is based on measuring the displacements and velocity of two different blocks by resorting to particle tracking velocimetry. This first validation sets the basis for substantially more complex structures and mechanisms originating from the detonation of explosive sources. To this end, we utilized the same platform to investigate, for the first time, the effects of an explosion inside an existing monumental structure.

(e) We replicate the explosion that occurred in the Parthenon of Athens in 1687 in our laboratory, reduced-scale platform and identify the collapse mechanisms that shaped today's familiar geometry of this emblematic structure.

Relying on the aforementioned scaling laws, we rebuild the Parthenon using 3D printing for modeling the blocks, multi-drum columns, masonry walls, and colonnades. This investigation is a first step towards understanding and studying the dynamical behavior of complex masonry structures and draw appropriate protective strategies, targeting ancient and modern buildings.
This manuscript is organized into three distinct parts:

- Part I provides detailed information concerning the design and installation process of the proposed experimental setup. By presenting the core reasoning behind the design, we present the sequential steps undertaken to build a controlled and reduced-scale

laboratory platform for investigating the response of structures to blast loads (cf. Chapter 1). Next, we present an in-depth study and analysis of the explosive source (cf. Chapter 2).

- Part II focuses on the study of TNT equivalence, presenting detailed information about how the real explosion is linked to the one produced at reduced scale (cf. Chapter 3). Furthermore, the incident overpressure distribution of the shock wave is investigated by measuring pressure at various angles. Scaling laws are then experimentally validated by investigating the rocking and overturning responses of prototypes and models (cf. Chapter 4).

- Part III, based on the aforementioned studies and investigations, sheds light on the response and collapse of a real masonry structure, the Parthenon of Athens, which, designed at a reduced scale. is tested in our novel experimental setup (cf. Chapter 5).

# Part I

# Experimental platform: design, installation, and explosive source analysis

# Chapter 1

# Designing and installing the experimental platform

*In this chapter, we provide a detailed presentation of the design and install of reduced-scale experiments for studying the dynamic response of structure under blast events in the laboratory. Experiment installation requires organizing and configuring the equipment, instruments, and components within a controlled environment. The methodology followed in the installation process is of vital importance as it ensures the precision and consistency of our system, ensuring safe, controlled, and repeatable investigation of the response of masonry structures to blast waves. We provide an in-depth description of the practical implementation and installation of the devices and tools.*

## 1.1 Introduction

The investigation of the response and potential damage to structures subjected to blast loading is of paramount importance for their protection. In this chapter, we present a novel reduced-scale, experimental platform (miniBLAST) that we designed from scratch for this purpose. Safety is one of the most important factors that we take into consideration throughout the design process. Our design framework is based on scaling laws presented by Masi et al. (2022). Within this chapter we precisely define the design processes and various basic requirements for implementing experiments at reduced scale in the laboratory.

We start by defining basis concepts necessary for understanding the subsequent developments and, in particular, explosive sources and blast parameters. Section 1.2 recalls various explosive sources, presenting the reasoning behind our choice in selecting exploding wires as analogue sources. Next, we present the conceptual reasoning adopted for the design of the platform in Section 1.3, where we also review the scaling laws that form the analytical foundation guiding the present experimental design.

To fully address any safety concern, we opt to conduct experiments within a galvanized steel container cabin. The tests are performed over an optical table which, capable of withstanding the loads resulting from reduced-scale explosions, ensures correct alignment. In order to reduce any source of reflection for the shock waves originating from the exploding wires, we opt for the installation of acoustic foam within the container cabin. This allows us to reduce the amplitude of the sound levels associated with the explosion and guarantee increased safety of the personnel and reduced environmental hazard.

Next, we outline, in Section 1.7, the metrology and system of measurements, comprising

sensors and devices for the measurement of blast-induced pressure, acceleration, current and voltage. Moreover, we present the optical cameras used to measure structures displacement in both 2D and 3D. Then, we present the three-dimensional (3D) printing process for the fabrication of reduced-scale structures and models tested within this work (cf. Section 1.8). Finally, Section 1.9 details the installation procedure followed in assembling the proposed experimental platform.

## 1.2 Explosions and blast loading

Explosions are associated with rapid and sudden releases of energy that produce large amounts of expanding gases. The effect of an explosion on structures varies mainly depending on the explosive charge, the nature of the explosive source, and the distance between the explosive source and the structure.

Figure 1.1 presents the main steps involved in the formation of blast waves for the case of high-explosives[1]. During an explosion, a blast wave is formed due to the rapid increase in the pressure, density, and temperature which originates from the deposition of a large amount of energy in a localized volume (detonation). The blast wave is a combination of a leading shock front and a subsequent expansion zone, propagating outward from the explosive source at supersonic velocities. Within the shock wave, the thermodynamic properties of the gas undergo large and rapid changes. Across the expansion region these properties return to their initial values, albeit gradually and often in an oscillatory manner. The blast wave's propagation speed and amplitude decrease as the distance from the explosive source increase (for more details, we refer to Sochet, 2010; Ngo et al., 2007; Mendonça et al., 2020; Frost, 2018).
The explosive source can be of different types and materials such as, trinitrotoluene (TNT), pentaerythritol tetranitrate (PETN), and dynamite. We define hereinafter the main the quantities describing the loads induced by the detonation of such explosives. Here, we use the term overpressure to denote a differential pressure, relative to ambient one, $P_o$. Following Dewey (2016), we briefly recall the subsequent definitions (see also Figure 1.2):

- The incident overpressure $P_s$ is the pressure associated with the free air pressure[2] waves that have not yet reacted with an obstacle. It does not include any component due to the translational movement of the gas. The peak of the incident overpressure is denoted as $P_{so}$. The incident overpressure is usually measured by transducers mounted on a surface parallel to the flow (see Pape et al., 2010; Dewey, 2016; Walter, 2004).

- The dynamic overpressure $q$ is the pressure due to the gas flow behind the front of the shock wave. The dynamic pressure is responsible of aerodynamic forces, such as lift and drag[3]. The peak of the dynamic overpressure is denoted as $q_o$.

- The reflected overpressure $P_r$ is the pressure that originates when the primary shock of a blast wave strikes a plane surface that is face-on to the blast it is reflected normal to

[1]High-explosives are detonating explosive materials, such as trinitrotoluene (TNT) and C4, characterized by extremely rapid decomposition and the development of high pressures. High-explosives distinguish from deflagrating (or low-) explosives, such as black and smokeless powders, which involve fast burning and produce relatively low pressures.

[2]Free air pressure typically refers to the pressure of the surrounding atmosphere, also known as atmospheric pressure.

[3]Lift and drag are forces exerted on an object by a flowing fluid. Lift is the force acting perpendicularly to the flow direction and drag the one acting in the direction parallel to the flow.

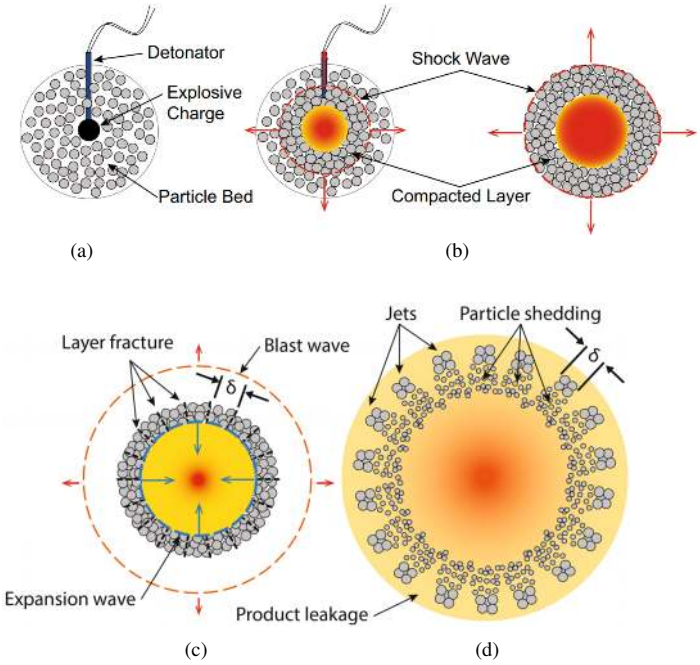


**Figure 1.1:** Schematic animation of the sequence of events triggered by the detonation of a high-explosive charge encased by a layer of particles, as shown in (a). When the shock reaches the interface between the layer and the surrounding air (b), it transmits a blast wave into the air and generates rarefaction waves that travel back into the compacted layer (c). This process causes the layer to expand and fracture, creating fragments roughly the size of the compacted shell thickness ($\delta$). The outward radial movement of these fragments forms particle jets, shedding particles as they move (d). Scheme adapted from Loiseau et al., 2018; Frost, 2018.

the surface, and the gas behind the shock is brought to rest non-isentropically so that the translational kinetic energy is added to the hydrostatic pressure. The resulting pressure on the surface is known as the reflected pressure, with a peak overpressure denoted as $P_{ro}$. The reflected overpressure is usually measured by transducers mounted on a surface perpendicular to the flow (see Walter, 2004), cf. Section 1.7.2.

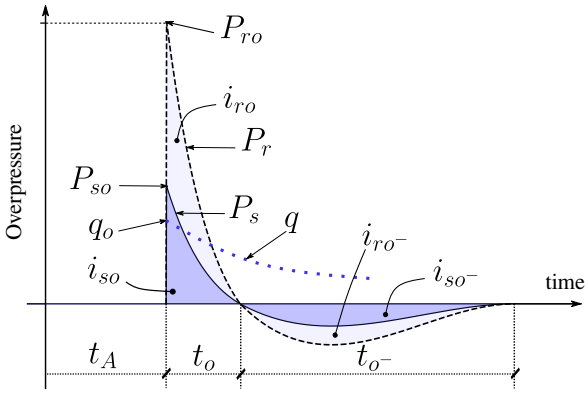


**Figure 1.2:** Time history of the incident $P_s$, dynamic $q$, and reflected $P_r$ overpressure due to an explosion at a fixed distance $D$ from the explosive source, with mass $W$.

Figure 1.2 schematically presents the time history of the incident, the reflected, and the

dynamic overpressure originating from the detonation of an explosive weight, denoted as $W$ (kg), at a distance $D$. The incident and reflected overpressures increase (with a strong discontinuity, shock), to a peak, at the blast wave arrival time, $t_A$. For $t > t_A$, the two overpressures rapidly decrease, with an almost exponential rate, until $t_A + t_o$, the end what we refer to as the positive phase. After $t_A + t_o$, the incident and reflected overpressures take negative values and gradually approach the ambient pressure (negative phase).

During the negative phase (with duration $t_{o^-}$), the decrease (in absolute value) of the pressure is smaller, than the decrease of the peak overpressure of the positive phase, while the duration is often much longer. Besides the primary peaks $P_{ro}$ and $P_{so}$, secondary and tertiary shocks can also develop, resulting from the repeated over-expansion, subsequent implosion, and re-expansion of the detonation products (see Figure 1.1).

With reference to Figure 1.2, the positive phase impulse is computed as,

$$i_{so} = \int_{t_A}^{t_A+t_o} P_s(t)\, dt, \tag{1.1}$$

and the negative phase impulse as,

$$i_{so^-} = \int_{t_A+t_o}^{t_A+t_o+t_{o^-}} P_s(t)\, dt. \tag{1.2}$$

The modeling of blast loads often relies on empirical formulas for estimating the aforementioned parameters and the time history of the positive and negative phases. For the sake of simplicity, here we consider the particular case of a (hemispherical) surface burst[4], as shown in Figure 1.3, as the experiments presented in this manuscript only consider this particular case. The empirical formulas for the blast parameters rely on best-fit interpolations of experimental results (mainly on those of Kingery and Bulmash (1984), see (Masi, 2020, Appendix A), which allow for the determination of the overpressure peak, the time duration, and the impulse, among others, from the knowledge of the TNT equivalent explosive weight $W$, the standoff distance $D$ (distance between the explosive weight and the impinged surface) and the Hopkinson-Cranz scaled distance, $Z = D/\sqrt[3]{W}$. As an example, Figure 1.3 shows the positive phase of the incident overpressure at varying standoff distance. As $D$ increases, the arrival time $t_A$ and positive phase duration $t_o$ increase, while the peak incident overpressure $P_{so}$ decreases.

Additionally, we introduce the following scaled blast parameters: scaled positive (and negative) incident impulse $i_{sow}$ (and $i_{sow^-}$), scaled positive (and negative) time duration $t_{ow}$ (and $t_{ow^-}$), and scaled arrival time $t_{Aw}$. These quantities are defined as their non-scaled counterparts divided by the cubic root of the explosive weight $W$, e.g. $i_{sow} \equiv i_{so}/W^{1/3}$. The cubic root scaling enables to represent the scaled parameters independently of the value of the explosive weight or, equivalently, of the explosive's internal energy (refer also to Chapter 3.

Explosives can be classified according to their physical state into solid, liquid or gas (cf. Meyer et al., 2016; Zapata and García-Ruiz, 2021; Needham, 2010; Cooper and Kurowski, 1997). Solid explosives are typically classified as high explosive sources, while other types are categorized as low explosives. A high explosive source (such as TNT) generates gas

[4]Surface burst is an explosion occurring almost at ground surface, the blast waves immediately interact locally with the ground and they next propagate hemispherically outwards and impinge onto the structure.

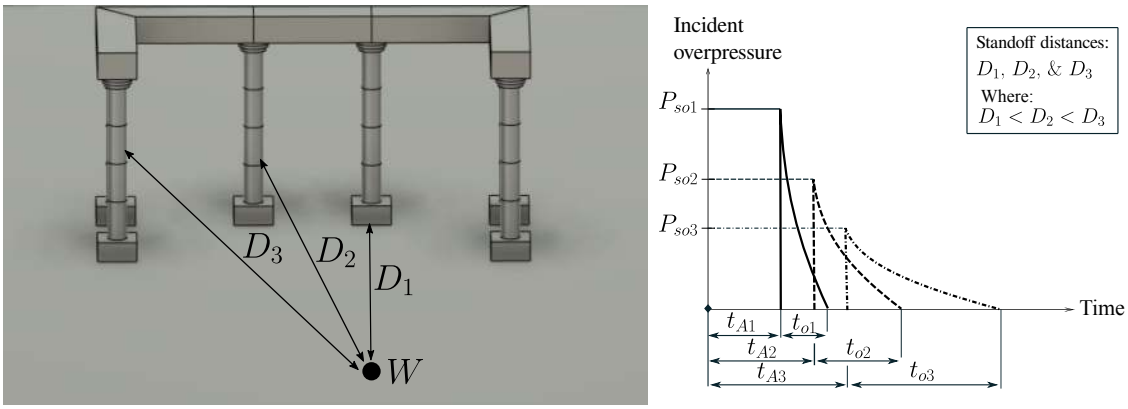


**Figure 1.3:** The influence of standoff distance $D$ on the arrival time $t_A$, the positive phase duration $t_o$ and the peak incident overpressure $P_{so}$.

with extreme rapidity and has a shattering effect[5]. Explosive sources can also be classified on the basis of their sensitivity to ignition as secondary or primary explosives[6] (Ngo et al., 2007). Examples include TNT, C4 and ANFO explosives.

Based on the aforementioned classification, we identified the most effective explosive source or explosive analogue to be used in the experiments presented and developed within this manuscript. In particular, our findings led us to the conclusion that high explosives and gaseous sources are not optimal. This is primarily due to the fact that they either necessitate materials with extremely small or excessively large volumes, rendering them difficult to use in the laboratory. For instance, gaseous materials require substantial volume sizes, often around 1 m, which poses practical challenges to implement reduced-scale experiments with uniform geometric scaling. Additionally, solid, high-explosive materials, including TNT, require extremely small weights, as low as 1 $\mu$g, making their utilisation problematic within the scope of our proposed experimental setup. These issues are further exacerbated by safety concerns and environmental hazard related to the storage of high-explosives.

Alternatively, Hansen (1993–2011); Liverts et al. (2015); Ram and Sadot (2012); Cunrath and Wickert (2015), among others, conducted experimental tests by resorting to exploding wires to generate the loads induced by blast waves. In so doing, they have investigated various scenarios by changing the wire properties, including length, diameter, and material. We found that, for particular choices of these properties the resulting incident and reflected overpressures are adequate for the spectrum of equivalent explosive weights investigated in our experiments – based on the adopted scaling laws (presented in subsection 1.5). This, together with the possibility of storing, without any hazard, the analogue explosive source (exploding wire) is the motivating reason behind our choice.

[5]Shattering effect refers to the ability of high explosives, like TNT, to produce a sudden release of energy. This rapid energy release generates a shock wave that propagates through nearby materials, causing them to fracture, break, or shatter.

[6]Primary explosives are detonated by ignition from a source like a flame, spark, or other means that generate adequate heat. Secondary explosives require a detonator such as exploding wires, dynamite.

## 1.3 Conceptual design of experiments

In the experimental setup proposed and developed in this work, the explosive source is thus represented by exploding wires. When a sufficiently large electric charge is discharged through a thin conductive wire, its temperature increases considerably. This rapid temperature increase causes the wire to undergo a phase transition, generating a shock wave that travels through the air and impinges the structure. The system is composed of a capacitor, a switch and a wire, with length $l_W$, and diameter $d_W$ (see Figure 1.4). By changing the properties of the wire, such as its length, diameter, and the material, it becomes possible to create various blast scenarios.

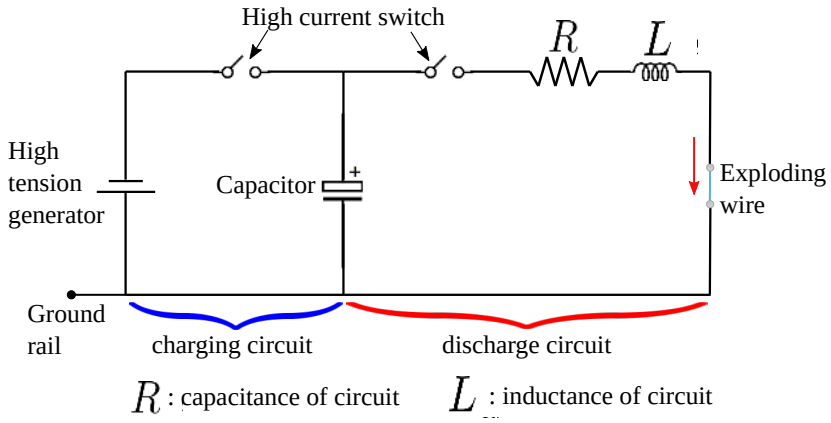


**Figure 1.4:** Schematic diagram of the exploding wire system.

The Exploding Wire Phenomenon (EWP) has gathered substantial attention from researchers across multiple disciplines, including plasma physics, material synthesis, and electronics. For a comprehensive review of the state of the art, we refer to Morsel et al. (2024); Liverts et al. (2015); Liu et al. (2019); Ram and Sadot (2012); Han et al. (2020); Bennett (1958); Mellor et al. (2020); Chace and Moore (1968); McGrath (1966); Gilburd et al. (2012); Hansen (1993–2011); Doney et al. (2010).
The origins of the exploding wire technology and experiments can be traced back to the late 18th century. Nairne (1774) conducted seminal work related to the EWP. In particular, the authors connected relatively lengthy, slender pieces of silver and copper to a Leyden jar[7], which was subsequently discharged. The outcome of the discharge caused the wire to spread all around, resulting in minor injury to the experimenters. Later, a method of depositing a very thin gold film by means of EWP was reported by Faraday (1857) in the early 19th century, providing initial insights into the phenomenon (Chace and Moore, 1968). These studies laid the foundation for the subsequent research by uncovering the fundamental concept of wire disintegration due to high currents.

Exploding wires exhibit distinct characteristics that reflect the underlying physical and electrical mechanisms. As high currents flow through the wire, the Joule heating effect causes a rapid rise in temperature, which results in a subsequent vaporization of the material. Next, a rapid expansion of the high temperature gas generates a shock wave that propagates through the surrounding medium. The disintegration process is complex

[7]Leyden jar is the first device used to store an electric charge. It consists of a glass jar coated with metal foil from inside and outside.

and influenced by various factors such as the wire material, geometry, current magnitude, and ambient conditions. For more details we refer to Chapter 2.

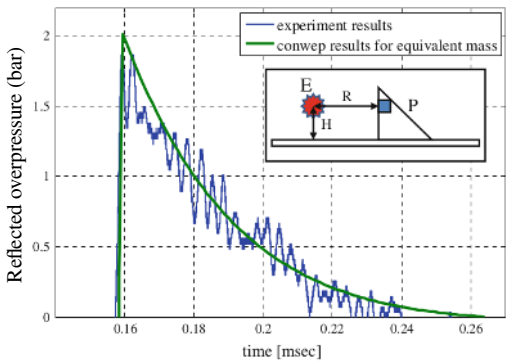


**(a)** Reflected overpressure time history adopted from Ram and Sadot (2012)

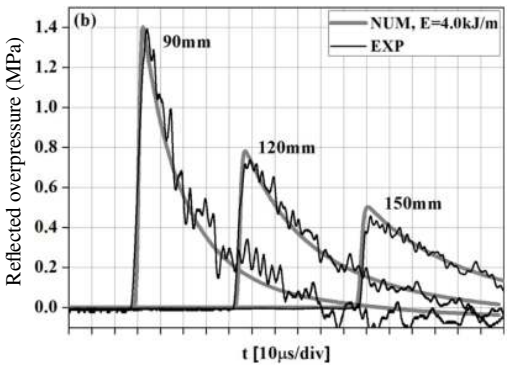


**(b)** Reflected overpressure time history adapted from Liverts et al. (2015)

**Figure 1.5:** Examples of reflected overpressure as function of time measured in case where the wire has (a) a length of 70 mm, a diameter of 0.9 mm, standoff distance ($D$) = 118.5 mm, and a voltage of 4.8 kV, (b) a length of 70 mm, a diameter of 0.9 mm, standoff distance ($D$) = 90, 120 and 150 mm, and a voltage of 4.0 kV.

## 1.4 State of art

Our objective is to study the fast dynamic response and failure mechanisms of structures subjected to blast scenarios experimentally. However, conducting experiments at full scale is expensive, non-repeatable, laborious, and focusing on studying part of the structure, (Godio et al., 2021; Pereira et al., 2015; Ahmad et al., 2014; Ngo et al., 2007; Keys and Clubley, 2017; Sielicki and Łodygowski, 2019). Additionally, it required special testing areas with restricted access and associated safety hazards. Sielicki and Łodygowski (2019) studied the behaviour of masonry wall under blast loading (see Figure 1.6,a). It includes an overview of some crucial aspects dealing with the numerical modeling of brick wall failure under such loading.

Moreover, Keys and Clubley (2017) investigated the out-of-plane response of unreinforced masonry walls subjected to blasts (TNT is used as explosive source). In order to be able to predict the spatial debris distribution produced by masonry panels (see Figure 1.6,b).

Instead, doing experiments at reduced scale ensure a high degree of control and repeatability, moderate cost, and reduced hazards. Experiments in the literature at reduced scale are focusing on measuring shock wave propagation inside a confined structures not in testing structural response, (Trelat et al., 2007; Pennetier et al., 2015). Zyskowski et al. (2004) studied the reflection of pressure of an accidental explosion of a gaseous mixture cloud (hydrogen–air) in an unvented structure (closed box see Figure 1.7) and deals with the detonation phenomenon. The experiments is designed based on Hopkinson scaling law in order to estimate pressure in large-scale geometry. Moreover, an experimental small-scale study investigated the blast wave in a single-story building, Sochet et al. (2019). The blast waves were generated by the detonation of a gaseous charge. The

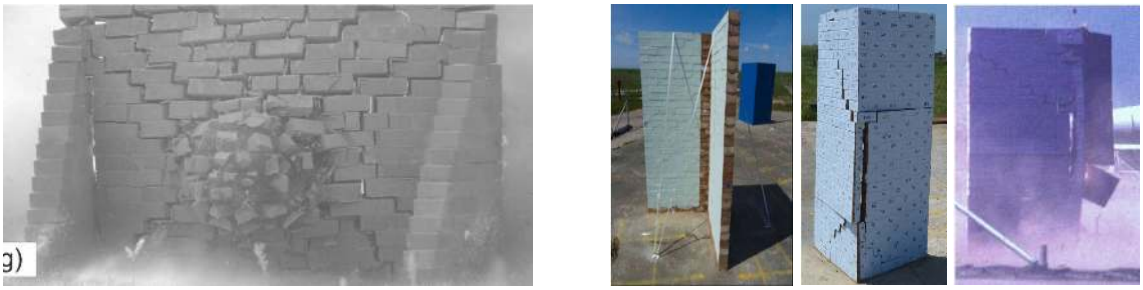

(a) (b)

**Figure 1.6:** Collapse response for wall exposed to TNT blast loads (a), adapted from Sielicki and Łodygowski (2019), and edge wall (b), adapted from Keys and Clubley (2017).

building was divided into two rooms (see Figure 1.8). Another experiments performed by Gault et al. (2020) investigated the influence of explosion center in a confined room and how this variation affects the shock wave propagation and the reflection due to the confined environment. The shock waves were generated by the detonation of a gas charge (stoichiometric hemispherical charge of propane–oxygen mixture). The charge was placed in a small-scale model and designed based on Hopkinson's scaling law (see Figure 1.9).

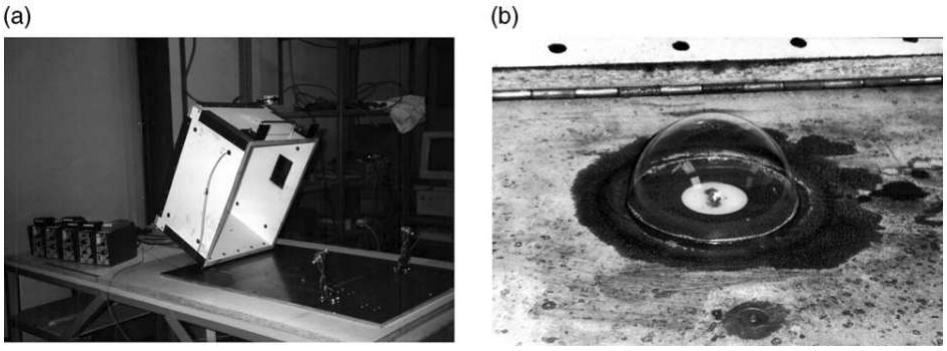


**Figure 1.7:** The experimental setup (a) and soap bubble confining the explosive mixture (b). Adapted from Tomaževič et al. (2009).

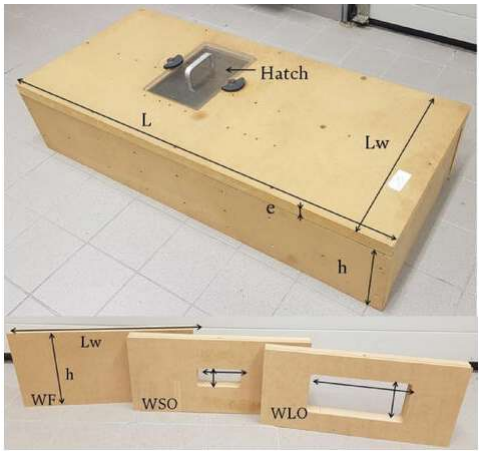


**Figure 1.8:** Single-story building, adapted from Sochet et al. (2019).

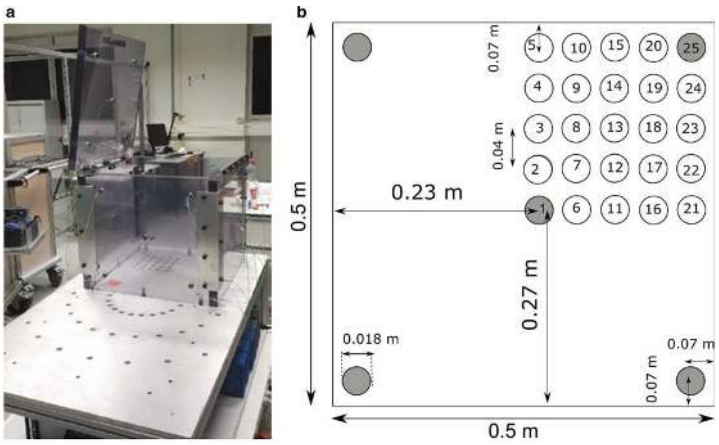


**Figure 1.9:** Small-scale model (a), and mapping of the sensors and the charge-triggering matrix on the floor (b). Adapted from Gault et al. (2020).

## 1.5 Scaling laws for reduced-scale testing

Understanding how masonry structures respond to explosive forces requires a combination of numerical, analytical, and experimental approaches. However, conducting full-scale blast experiments is challenging due to the nature of the loading. To address this problem, scaling laws were proposed by Masi et al. (2022) for the dynamic response and failure modes of masonry and blocky structures under blast loads. Validation was achieved through numerical simulations considering various mechanisms like rocking, uplifting, and sliding (Masi et al., 2022, 2019). Building upon these findings, our goal is to validate and/or falsify the numerical findings by means of experiments.

### Methodology

The derivation of the scaling laws was based on dimensional analysis and the Π theorem. Dimensional analysis is a useful tool in providing an appropriate relationship between different physical quantities (density, energy, etc.) in terms of fundamental dimensions (length, mass, etc.) (Baker et al., 1991). The Π theorem states that if there is a relationship between physical quantities and a certain number of dimensions, then there is an equivalent law that can be expressed as a relationship between certain dimensionless quantities (Logan, 2013).

In the following, we consider a masonry structure, of arbitrary shape, composed of masonry units (blocks), interacting through interfaces (joints) with an angle of friction $\mu$. The scaling laws proposed by Masi et al. (2022) are derived based on the following assumptions:

1. Rigid-body response. The structure is subjected to a blast load and undergoes a rigid-body motion (it is therefore assumed that deformations are negligible with respect to the rigid-body response). This hypothesis is realistic for masonry structures under low confinement, e.g. for columns and retaining walls or during rocking-like collapse of interior partitions.

2. Blast loads. The load resulting from an explosion is characterized in terms of its maximum specific thrust ($\mathcal{P}$) and maximum specific impulse ($\mathcal{I}$). For relatively small targets, where it is reasonable to assume that the blast wave acts uniformly and

simultaneously on all impacted surfaces, the maximum specific thrust and impulse are computed as the peak overpressure and impulse of an equivalent blast load, applied to the structure's centroid. Accordingly, the pressure load is considered to be applied exclusively on the front surface $S$ of the target.
For the mathematical tractability of the problem, the blast loads are additionally considered as impulsive. This assumption lies on the fact that the characteristic time of the load is much smaller (at least, two orders of magnitude) than the time response of the structure.

3. Friction and gravity. The model and the prototype share the same gravitational field and friction coefficient.

Following the aforementioned assumption, Masi et al. (2022) considered two scaling factors: (1) the geometric scale factor, namely $\lambda = \frac{\tilde{l}}{l}$, and (2) the density scale factor $\gamma = \frac{\tilde{\rho}}{\rho}$ (density of the structure), where the superscript tilde in $\tilde{l}, \tilde{\rho}$ denotes the quantities of the model (reduced scale structure) – characteristic length and density, respectively – while $l$ and $\rho$ denote the analogous quantities in the prototype (full scale structure), see Figure 1.10.

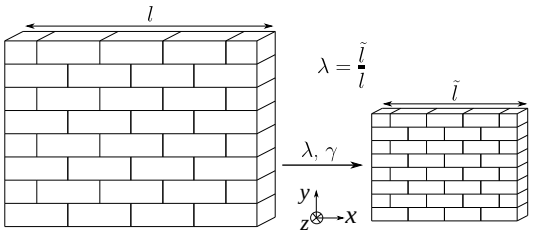


**Figure 1.10:** Geometric and mass scaling of a masonry structure: prototype (left) and model (right), with geometric scaling $\lambda$ and density scaling $\gamma$ factors.

Table 1.1 summarizes the scaling factors proposed by Masi et al. (2022) and Figure 1.11 represents two typical cases, where the scaling laws can be applied.

**Table 1.1:** Scaling factors

| Variable | Scaling factor | Variable | Scaling factor |
|---|---|---|---|
| Length, $l$ | $\lambda$ | Linear displacement, $x$ | $\lambda$ |
| Time, $t$ | $\lambda^{1/2}$ | Linear velocity, $\dot{x}$ | $\lambda^{1/2}$ |
| Material density, $\rho$ | $\gamma$ | Linear acceleration, $\ddot{x}$ | 1 |
| Mass, $m$ | $\gamma\lambda^3$ | Angle, $\theta$ | 1 |
| Blast impulse, $i_{ro}$ | $\gamma\lambda^{3/2}$ | Angular velocity, $\dot{\theta}$ | $\lambda^{-1/2}$ |
| Blast pressure, $P_{ro}$ | $\gamma\lambda$ | Angular acceleration, $\ddot{\theta}$ | $\lambda^{-1}$ |
| Friction angle, $\varphi$ | 1 | Mass moment of inertia, $J$ | $\gamma\lambda^5$ |

Figure 1.12 displays the dependency of the scaling factors for the peak of the reflected overpressure $\lambda_{P_{ro}}$ (a), the scaled distance $\lambda_Z$ (b), and the reflected impulse $\lambda_{i_{ro}}$ (c), as function of the geometric scaling factor $\lambda$ and the density scaling factor $\gamma$. It is worth noticing that when both $\lambda$ and $\gamma$ are smaller than the unit, the scaled distance in the model is smaller than that in the prototype. Similarly, the overpressure peak and impulse

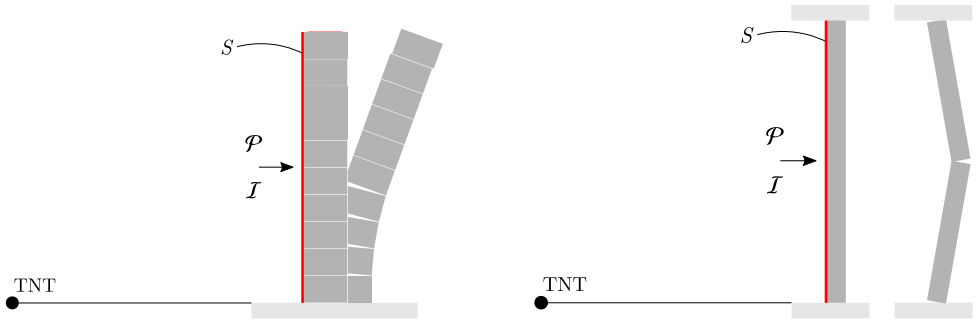


**Figure 1.11:** A multidrum column (a) and a one-way spanning wall (b) under blast loading (adapted from Masi et al. (2022)).

are also reduced, which demonstrates the effectiveness of the proposed scaling approach to reduce the blast load and, therefore, to enable tests in the laboratory.

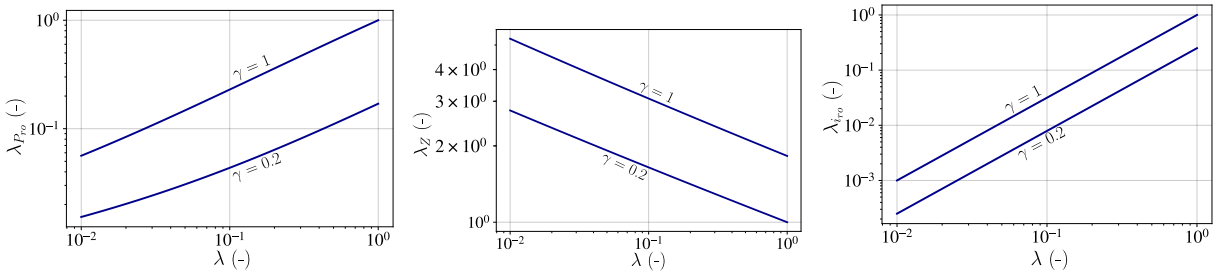


**Figure 1.12:** Scaling factors for the peak of the reflected overpressure peak $\lambda_{P_{ro}}$ (a), scaled distance $\lambda_Z$ (b), and impulse $\lambda_{i_{ro}}$ (c), function of the geometric scaling factor $\lambda$ and the density scaling factor $\gamma$.

### Comparison with an analytical model

Masi et al. (2022) showcased the ability of the proposed scaling laws by resorting to benchmarks including analytical/numerical models of single block and multi-block structures undergoing combination of rocking, sliding, uplifting, and impacts. For the sake of conciseness, herein we briefly recall the analyses and findings related to the analytical model. The latter focuses on pure rocking mechanisms and is based on the following assumptions (cf. Masi et al., 2019):

1. The target structure is a slender, rigid rectangular block with uniformly distributed mass, $m$. The dimensions of the block are $2b \times 2h \times 2w$ (width×height ×depth). The radial distance from the rocking pivot point $O$ to the block's center of gravity is represented by $r = h/\cos(\alpha)$ (slenderness length), with $\alpha$ the slenderness angle (see Figure 1.13).

2. The contact with the horizontal plane is assumed to occur at a single point, referred to as point $O$, without any contact moment being taken into account. This contact is considered to be unilateral.

3. The pressure generated by the explosion is applied to the sole front surface $S$ (referred to as the incident/front surface, as shown in Figure 1.13). It is assumed that the blast wave impinges surface $S$ simultaneously and uniformly. This resulting load is considered to always act horizontally, targeting the block's center of mass. This assumption is made because the duration of the loading pulse is exceedingly short (less than 1 ms).

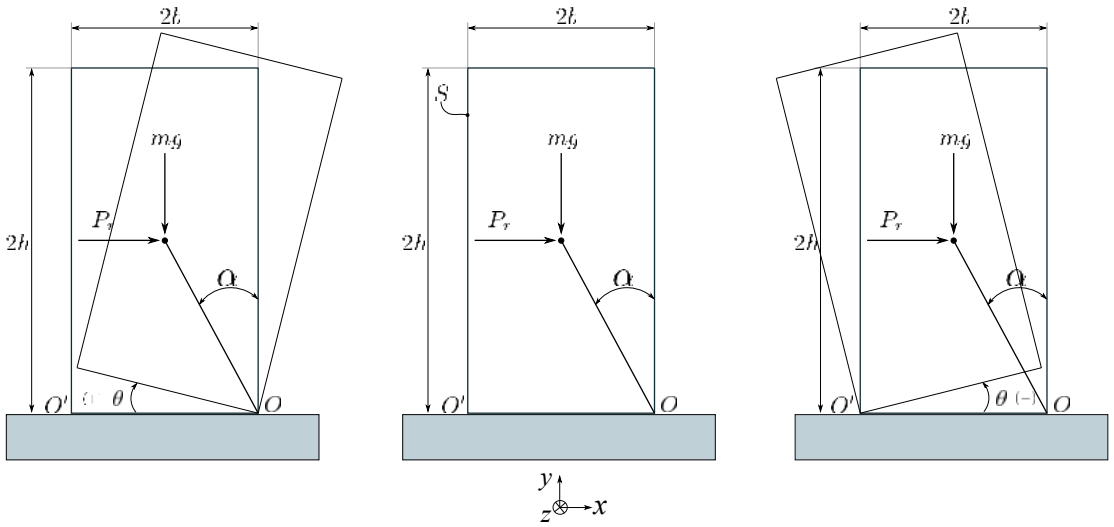


**Figure 1.13:** Configuration of the rocking problem for the analytical model: a rectangular column, rigid block resting on a horizontal plane with uniformly distributed mass, subjected to uniform pressure load due to an explosion.

Depending on the characteristics of the excitation and the friction angle, the rigid block predominantly exhibit sliding, rocking, or both. The conditions for the initiation of pure rocking and sliding can be determined from the rotational and translational equilibrium, respectively. More precisely, rocking initiates when the moment due to blast actions exceeds the restoring moment due to gravity. The initiation condition reads

$$\frac{S}{mg} P_{ro} \geq \tan \alpha \tag{1.3}$$

where $P_{ro}$ is the reflected overpressure peak acting on block's front surface $S$, and $g$ is the gravitational acceleration. Sliding initiates when

$$\frac{S}{mg} P_{ro} \geq \tan \varphi \tag{1.4}$$

where $\varphi$ is the angle of friction. Notice that for slender blocks, i.e. $\alpha \leq 20°$ , which are of interest here, and for angles of friction $\varphi \approx 30°$ (typical value for interfaces involving geomaterials), rocking is critical.

The positive and negative phases of the explosion are considered using the empirical relationship provided by (see Masi, 2020, Appendix A). It is also assumed that the explosive source is in close proximity to the ground, indicating a surface burst. The equations of motion for a rocking response mechanism are given in Masi et al. (2019):

$$\mathcal{I}\ddot{\theta} + mgr \sin\left(\alpha \mathrm{sgn}(\theta) - \theta\right) = SrP_r(t) \cos\left(\alpha \mathrm{sgn}(\theta) - \theta\right), \tag{1.5}$$

where $\mathcal{I} = \frac{4}{3}mr^2$ is the moment of inertia with respect to the pivot point and $\theta = \theta(\mathrm{t})$ is the inclination angle, $m$ is the mass, $g$ is the gravitational acceleration, and $\mathrm{sgn}(\cdot)$ denotes the signum function. We define also the frequency parameter $q_f = \sqrt{3g/4r}$ ($\mathrm{s}^{-1}$) (see Masi et al., 2019).

In Figure 1.14, we present the normalized rocking angle, $\phi = \theta/\alpha$, and normalized rocking velocity, $\dot{\phi} = \dot{\theta}/(\alpha q_f)$, solutions of Eq. (1.5) as function of the dimensionless time $\tau$ (where $\tau = tq$). The plots depict the response to a 10 kg TNT explosive charge at varying standoff distances, considering a block with parameters $\alpha = 15°$ , $h = 1$ m, $\rho = 2000$ kg/m$^3$.

The analytical model enables to calculate the minimum standoff distance required to prevent toppling (see Figure 1.14) and provides valuable insights into the primary factors that influence the rocking response of a block under explosive loads. For example, the negative phase of the blast wave, acting as a restoring moment, considerably reduces the amplitude of the rocking angle, see Figure 1.14 (b).

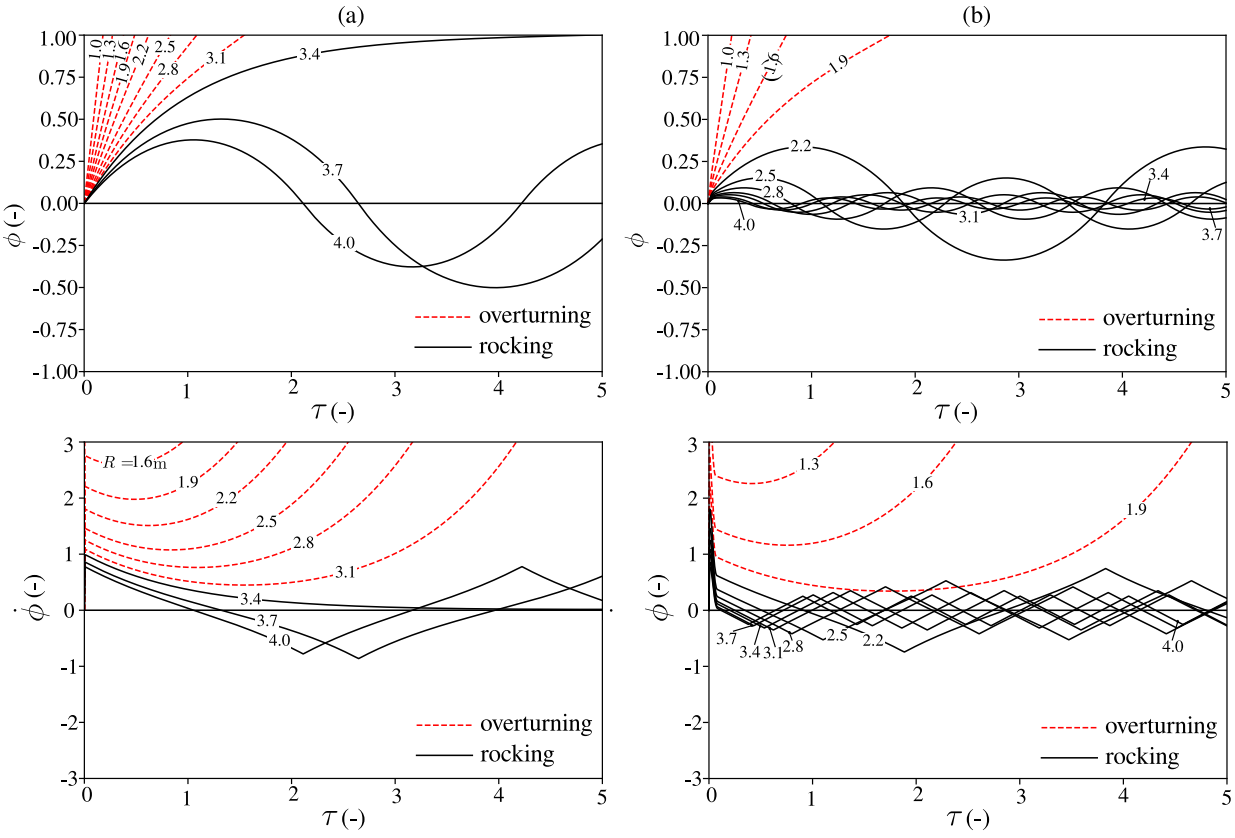


**Figure 1.14:** Normalized inclination angle, $\phi$, and angular velocity, $\dot{\phi}$, of the rocking block considering (a) only the positive phase of the blast wave, and (b) accounting for both positive and negative blast phases. The plots refer to a TNT explosive weight $W = 10$ kg and a rigid target with $\alpha = 15°$ , $h = 1$ m, $\rho = 2000$ kg/m$^3$, for stand-off distances $\in [1, 4]$ m. Red dashed curves indicate overturning.

To validate the scaling laws, the responses of the prototype and the model are compared using numerical integration of the nonlinear Eq. (1.5). For the sake of clarity, we present one of the scenarios considered in (Masi et al., 2022). More precisely, we assume a prototype block with the following characteristics: density $\rho = 2000$ kg/m$^3$, height

$2h = 10$ m, slenderness angle $\alpha = 15°$. The block is subjected to the load arising from the detonation of an explosive weight $W$ at a standoff distance $D = 2$ m. For the model, the following geometric and density scaling factors are considered: $\lambda = 1/200$ and $\gamma = 1$. Three TNT equivalent quantities are examined: (a) $W_a = 50$ kg, (b) $W_b = 100$ kg, and (c) $W_c = 79.8$ kg. It can be seen in Figure 1.15 that the prototype and the up-scaled model have the same behavior. For $W_{pa} = 50$ kg, the prototype block rocks without overturning; for $W_{pb} = 100$ kg the prototype overturns while for the intermediate case $W_{pc} = 79.8$ kg it represent the critical explosive quantity of both systems.

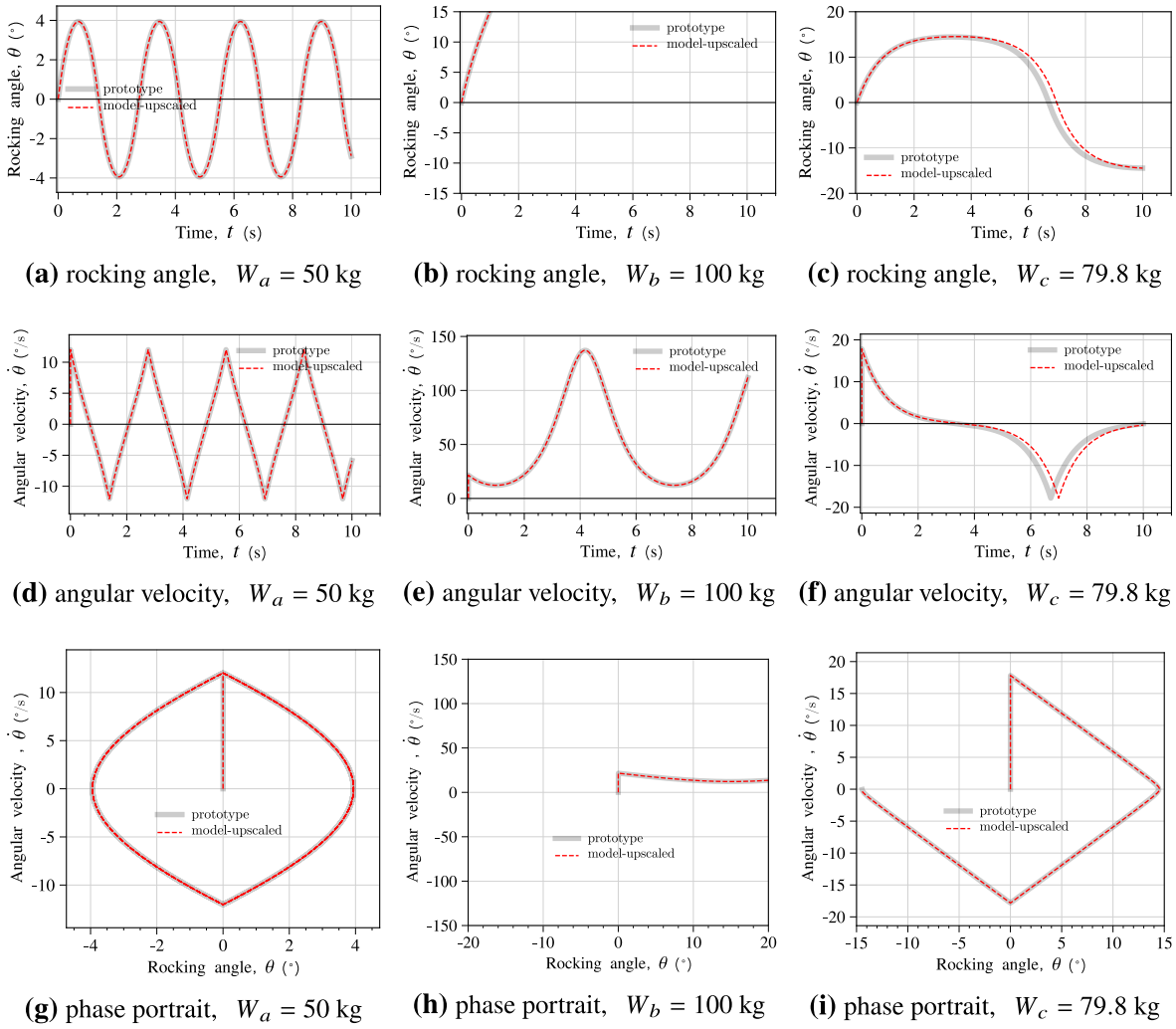


**(a)** rocking angle, $W_a = 50$ kg **(b)** rocking angle, $W_b = 100$ kg **(c)** rocking angle, $W_c = 79.8$ kg

**(d)** angular velocity, $W_a = 50$ kg **(e)** angular velocity, $W_b = 100$ kg **(f)** angular velocity, $W_c = 79.8$ kg

**(g)** phase portrait, $W_a = 50$ kg **(h)** phase portrait, $W_b = 100$ kg **(i)** phase portrait, $W_c = 79.8$ kg

**Figure 1.15:** Comparison between the prototype and the model responses ($\lambda = 1/200$) for three TNT equivalent quantities, $W = 50kg$ (left column), $W = 100kg$ (central column), and $W = 79.8kg$ (right column). The response of the model is upscaled, i.e., all quantities are multiplied by the inverse of the scaling factor (adapted from Masi et al. (2022))

### 1.5.1 Experiments scenarios

The range of pressures and geometric scaling that we considered in the design of our experimental platform include the aforementioned three scenarios, and more in general consider $\lambda \in [1/200 - 1/50]$ for $\gamma \in [0.5 - 1]$. Accordingly, we present the peak incident

overpressure as a function of explosive quantity ($W$) in Figure 1.16. This pressure is computed for two values of $\gamma$ (0.5 and 1) and for $\lambda \in [1/50, 1/100, 1/150, 1/200]$ at a distance ($D$) of 10 m. Notably, an increase in explosive quantity ($W$) results in a rise in pressure. Similarly, higher values of $\lambda$ and $\gamma$ correspond to increased pressure. It is worth noticing that utilizing exploding wires as an explosive source we are able to create the presented pressure ranges (refer to Figure 1.5).

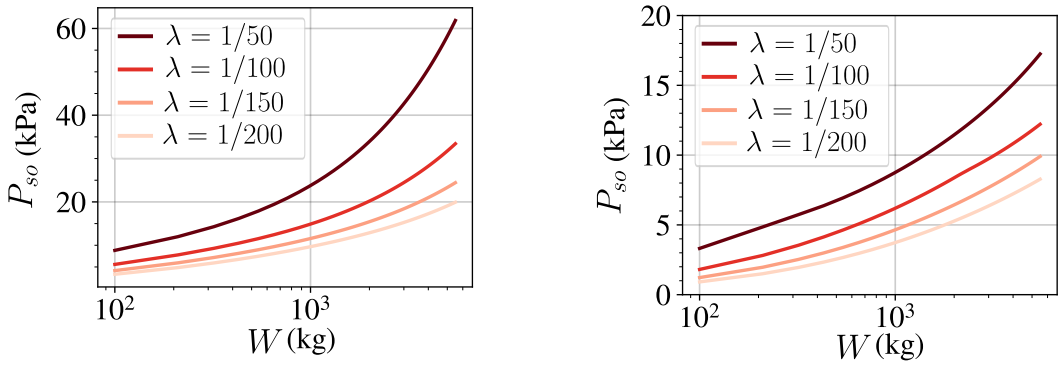


**(a)** $\gamma = 1.0$ **(b)** $\gamma = 0.5$

**Figure 1.16:** Peak incident overpressure ($P_{so}$) as function of explosive quantity ($W$) for $\gamma = 1.0$ (a), and $\gamma = 0.5$ (b), for $D = 10$ m and $\lambda \in [1/50, 1/100, 1/150, 1/200]$.

## 1.6 Components of the experimental platform

The novel experimental platform was designed for the Research Laboratory of Civil Engineering and Mechanics (GeM) at Centrale de Nantes (ECN) and it is presented hereinafter, Morsel et al. (2023). The adopted safety protocol assures compliance with the national and international standards (Héroux et al., 2015; French Government, 2006; AFNOR, Juin, 2000; for Occupational Safety and , NIOSH; TREATY, April, 2003), see also Appendix A.
In this section, we introduce the various components comprising our platform and the reasoning behind their design/selection.

### 1.6.1 Sound safety

In this section, our objective is to present the safety of our experiments for involved personnel and for the equipment, considering the scenarios detailed above in Section 1.5.1. Our critical safety concern is safety of hearing. The sound level $L_s$ (in dB) can be calculated using Eq. (A.2):

$$L_s = 20 \log_{10} \left( \frac{P_{ro}}{P_o} \right), \tag{1.6}$$

where $P_o$ the fixed reference pressure, considered equal to $2\text{x}10^{-5}$ (Pa).

Figure 1.17 presents the variation of the sound level $L_s$ (in dB) as function of $\lambda$, computed for the scenarios detailed in Section 1.5.1. The calculations determine the sound level at a distance of 15 meters, representing the distance between the personnel and the explosive source. It is worth noting that for optimal safety, we consider the reflected overpressure, which offers a more conservative approach compared to the incident

overpressure.
The black line represents the maximum audible sound level of 135 dB, according to French standards (French Government, 2006). Meanwhile, the green line signifies the 8-hour exposure sound level of 80 dB, according to French standards (French Government, 2006).

We observe that the experiments are unsafe for hearing since the sound level exceeds the acceptable hearing threshold of 135 dB. So, to conduct safety experiments in the laboratory, we propose two measures to ensure physical and acoustic isolation. In order to guarantee personnel and equipment safety, the experiments are perfomed inside a container cabin (detailed in Section 1.6.2). In addition, acoustic foam is installed inside the container cabin to absorb and dampen the sound emitted from the explosion (explained in details in Section 1.6.6).

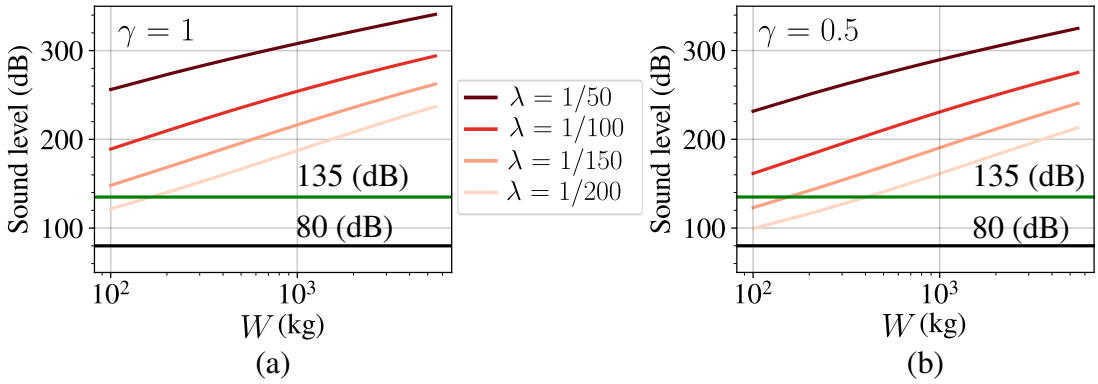


**Figure 1.17:** Sound pressure level (in dB) as function of explosive quantity ($W$) for $\gamma = 1.0$ (a), and $\gamma = 0.5$ (b) at distance 15 m from the explosive source.

### 1.6.2 Container cabin

As discussed above and to ensure the safety of both individuals and the equipment, we opt to conduct the experiments inside a container cabin (see Figure 1.18). The latter provides a controlled and secure environment.

To determine the cabin dimensions, we take into account two factors: (1) the available space in the lab and (2) the minimum dimensions necessary for accommodating the table and data acquisition system (further details are outlined in the subsequent sections). As a result, a galvanized steel cabin is selected, (Savitanks, 2023), with length 4 m, width 2.3 m, and height 2.2 m. The cabin is additionally reinforced in various locations to minimize low frequency vibrations by using rivets and rubber plates (details are provided in Section 1.9.1).

### 1.6.3 Ventilation system

To design an appropriate ventilation system for our needs, we require a system that can rapidly remove dust particles produced during the explosion of the wires, fully replacing the cabin's air within a specific time-frame. Our ventilation system design commences with calculating the volume of air to be extracted, approximately 20 $m^3$ in 2 minutes. For this purpose we opt for a LM315EC fan and duct connections to expel the air outside the lab, using a filter for environmental compliance (refer to Figure 1.19).


**Figure 1.18:** A galvanized steel container cabin of length 4 m, width 2.3 m, and height 2.2 m (panel sheet thickness = 1.5 mm), Savitanks (2023).

In prioritizing safety, we incorporate an additional phase that combines ventilation and air extraction to ensure cleansing of the cabin air (for 2 min). This phase necessitates another LM315EC fan and a filter to regulate incoming air and safeguard the fan's operation (see Figure 1.19). The duct's size (160 mm) has been recommended and designed by the company Asair (2023), which made the installation.

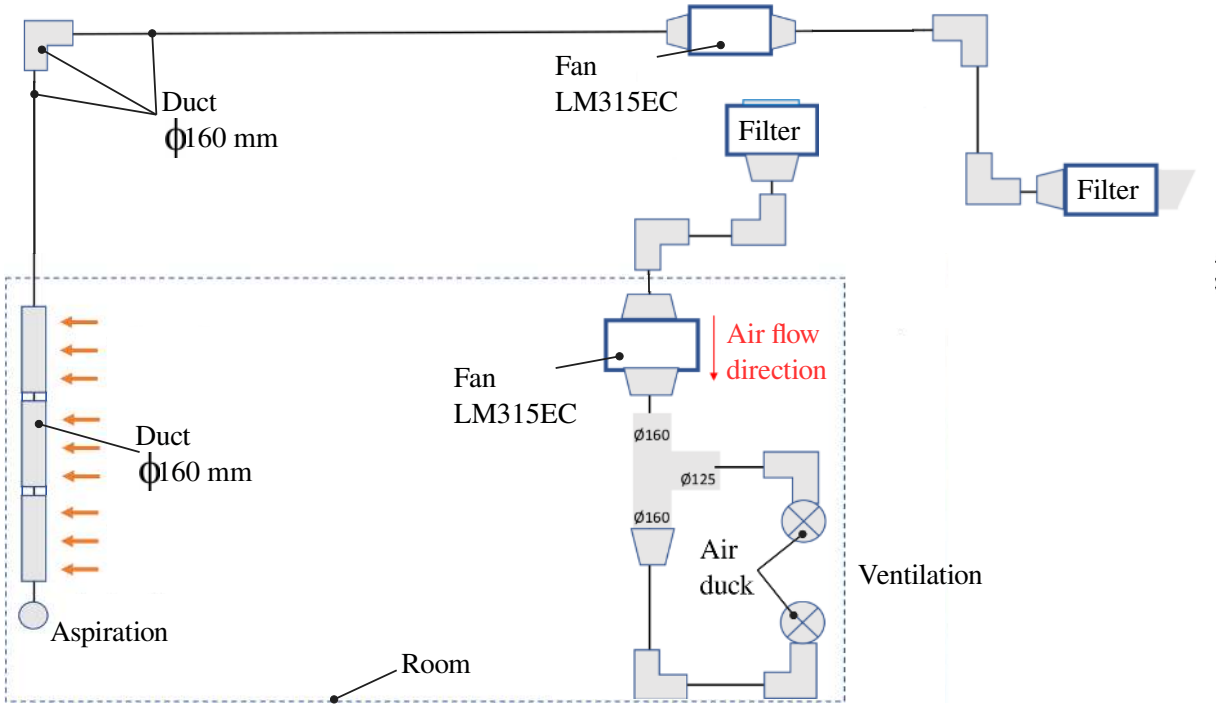


**Figure 1.19:** Design plan of the ventilation system.

### 1.6.4 Non-magnetic optical table

The experiments and the tested models (reduced-scale structures) are placed on a table that is (1) well aligned with accuracy ± 0.3 mm, and (2) stiff enough to endure the load coming from the explosion without undergoing notable deflection (see Figure 1.20). Moreover, the table is non-magnetic, in order to avoid potential interference to the piezoelectric sensors (more details are provided in Section 1.7.2).

After a comprehensive evaluation of the available tables, the Newport (mKs) non-magnetic optical table has been chosen (Newport, 2023). The table is composed of six pneumatic supports (S-2000 support) that are able to withstand the load coming from the explosion. Deflection is found negligible, approximately 1.50 ($\mu$m), for a concentrated load of 150 kg at its center. The load corresponds to 46 kPa applied to a 20 cm diameter area at the center of the table. This value represents the average load that could be exerted on the optical table top (based on the scenarios presented in Section 1.5.1). Additionally, ambient noise that might affect structural response is not a concern in our experiments, given our focus on rapid dynamic phenomena occurring in milliseconds. Although we have not employed an isolation system yet, this will can be easily taken into account. For further details about the optical table specifications, we refer to Appendix B.


**(a)** S-2000 support **(b)** Table panel

**Figure 1.20:** Newport optical table support (a) and table panel 1200 x 1800 mm, 472.4 mm thick (b).

### 1.6.5 Design of the exploding wire system

As part of the design process, the setup of the exploding wire system is a crucial step. As outlined in Section 1.3, the exploding wire system primarily comprises the following main components: a capacitor, a switch, and a wire. The capacitor is connected to electrodes via a cable. To accommodate this setup, a 16 mm thick cable extending from the capacitor is necessary. The cable starts at the capacitor and traverses the container cabin, with the cable head positioned at the midpoint of the optical table (see Figure 1.21). At this cable head, we install two electrodes (a cathode and an anode). To avoid drilling a hole through the optical table, we design two plates (White GPO3 Polyester glass mat), bottom plate of thickness equal to 1.5 cm and top plate of thickness 3.5 cm, which are positioned above the table (see Figure 1.21). The cable can then pass through these plates, without any need to modify the optical table. In this way, we ensure that the cable is isolated from the table's surface, providing a safe and isolated path. Furthermore, this method facilitates the passage of the cable inside the plates, ensuring that only the electrodes are visible on

the table's surface. This solution is also motivated by the need of creating hemispherical explosions (more details are provided in Chapter 4).

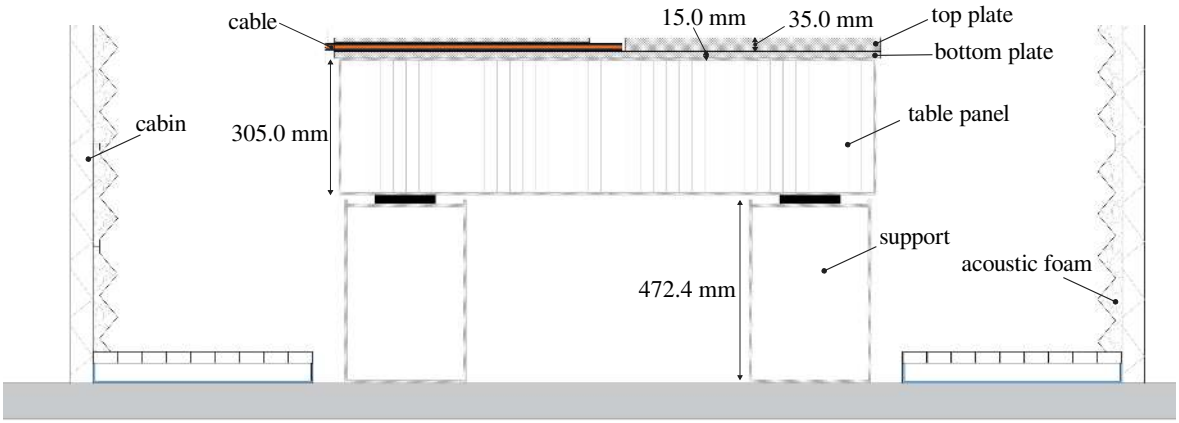


**Figure 1.21:** Design of an exploding wire system comprising two plates with a cable passing through them.

### 1.6.6 Acoustic foam

Due to its availability and low cost, acoustic foam is an attractive choice since the 1980s of design techniques and methodologies to dampen and mitigate sounds and pressure Borsov et al. (1980); Domergue et al. (2009); Hartman et al. (2006); Del Prete et al. (2013). The acoustic foam "Mousse melaminr pyramides griss SE40M1" we installed has a pyramid shape, Figure 1.22, and is fire resistant, detailed specifications are provided in Table 1.2.

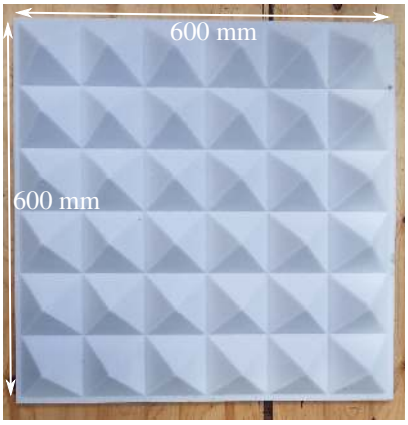


**Figure 1.22:** Acoustic pyramid foam.

Six critical cases were taken into consideration in selecting the shape of the acoustic foam, but also its positing and thickness (see Figure 1.23). In all cases, the shock wave is reflected away from the structure.

The sound reduction values for various frequencies is presented in Table 1.2 for 3 cm foam thickness. In order to check the sound reduction (damping) in our experiments the frequency $f_r$ is calculated as $f_r = 1/t_o$, with $t_o$ the positive time duration of the shock

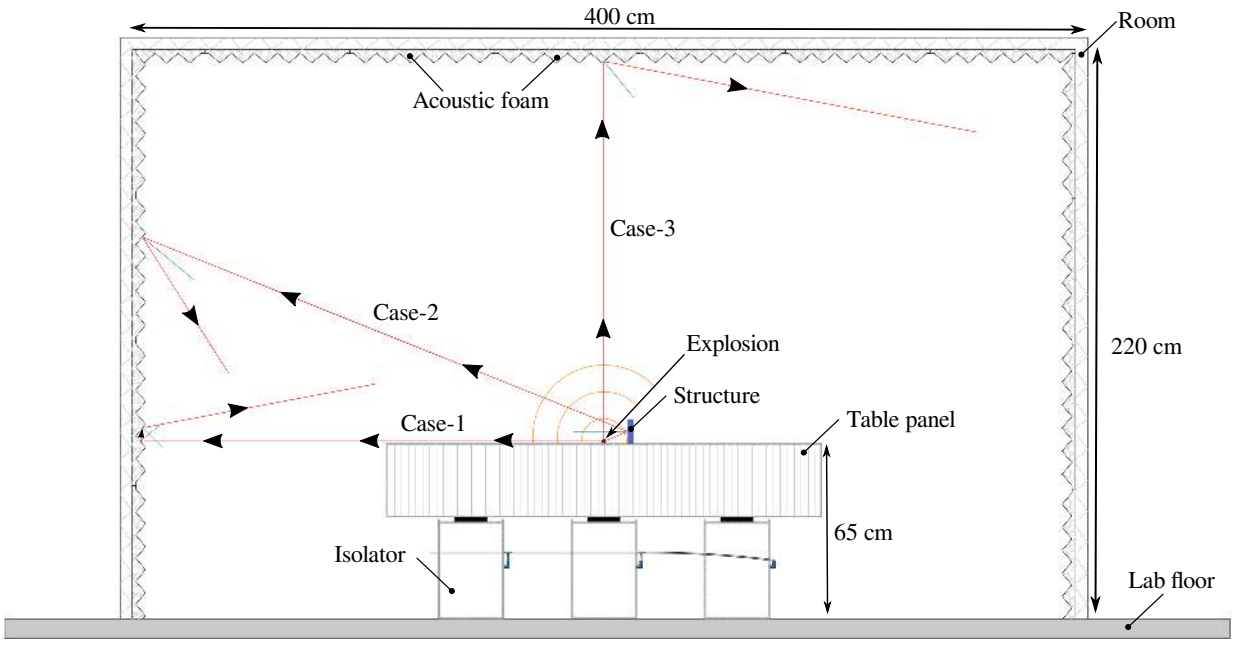


**(a)** Longitudinal cross-section

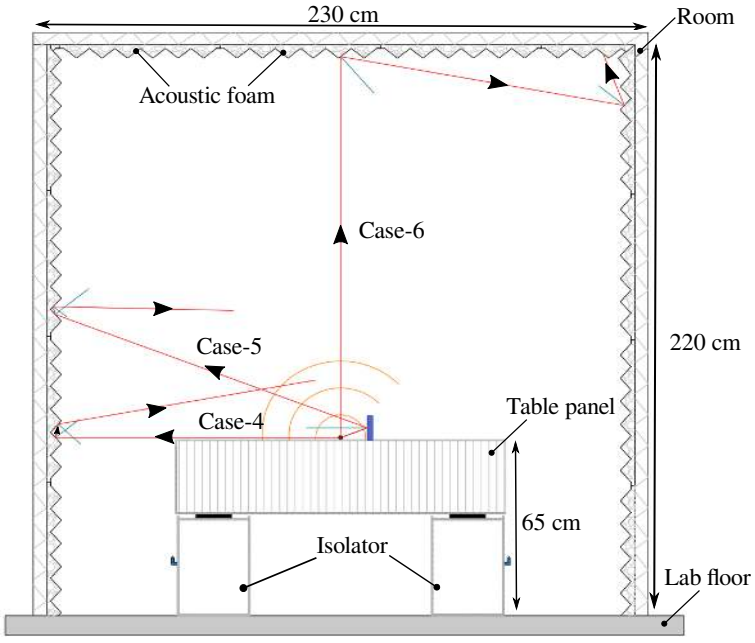


**(b)** Transverse cross-section

**Figure 1.23:** Cross-sections of the room showing the acoustic foam installation and shock wave reflection, longitudinal (a) and transverse (b).

**Table 1.2:** Acoustic pyramid foam's specifications per panel, (Solutions Elastomeres, 2023)

| | |
|---|---|
| Matter | gray melamine foam (clear) |
| Dimensions (mm) | 600 x 600 |
| Total thickness (mm) | 55 |
| Pyramids dimension (mm) | 95 x 95 x 40 |
| Sound reduction | |
| Frequency: $(100 \div 400$ Hz) | 17.21 dB |
| Frequency: $(400 \div 2000$ Hz) | 37.53 dB |
| Frequency: $(2000 \div 10,000$ Hz) | 49.01 dB |
| Density (Kg/m3) | $8 \div 11$ |
| Compressive stress 10% | $4 \div 20$ (KPa) |
| Tensile strength (kPa) | $120 \div 180$ |
| Elongation at break % | $16 \div 29$ |

Note: sound reduction is measured on a 31 mm thick flat plate (1 mm thick metal plate plus 30 mm foam)

wave. Figure 1.24 displays the variation of the shock wave frequency (in kHz) as a function of the standoff distance $D$, for the scenarios presented in Section 1.5.1. Here, the frequency is calculated based on the distance between the explosive source and the foam and it is derived from the six scenarios illustrated in Figure 1.23, ranging from 1 m to 1.7 m.

As a result, in our experiments, the frequency ranges between 1.254 kHz and 28.888 kHz (refer to Figure 1.24). The anticipated sound reduction after installing the acoustic foam is between 37.53 and 49.01 dB. Additionally, in our experiments, we used thicker foam, measuring 5 cm in thickness, to enhance damping.

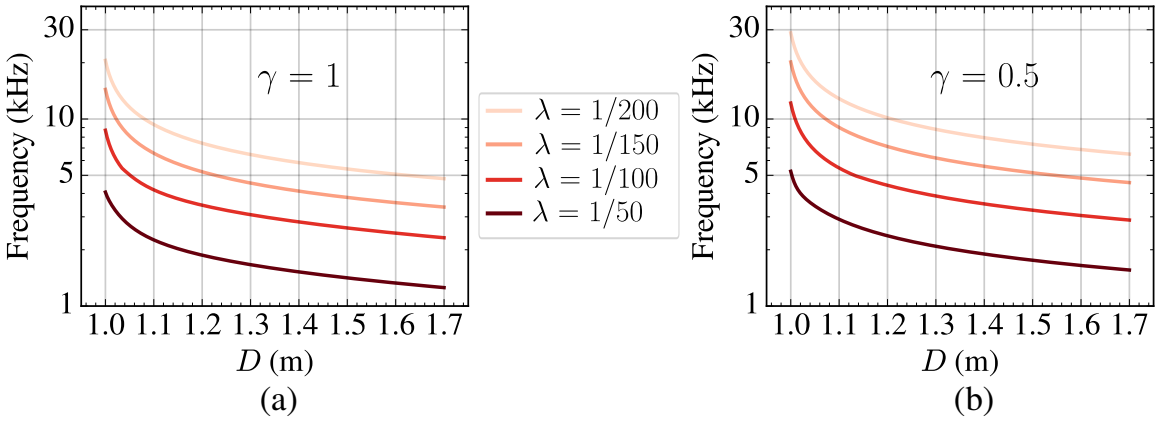


**Figure 1.24:** Shock wave frequency ($f_r$) as a function of the standoff distance ($D$), for $\gamma$ = 1.0 (a), and $\gamma$ = 0.5 (b), $\lambda \in [1/50, 1/100, 1/150, 1/200]$. The total mass of explosives is 500 kg.

## 1.7 System of measurements

Herein, we outline the devices and system of measurements employed in the designed experimental platform. In parallel, all sources of uncertainties associated with each component are discussed. Further details can be found in Appendix C.

### 1.7.1 Data acquisition devices

A data acquisition system[8] is an essential component of the system of measurements as it is responsible for capturing and digitizing analog signals from various sensors. It provides a bridge between the physical world and digital data, allowing signals to be processed and analyzed by computers. The measurements from our sensors are recorded using two different data acquisition devices, (1) the Oscilloscope Nicolet Sigma 30 (ONS) and (2) the Data Acquisition System (DAS) TraNET FE 404.

#### Oscilloscope

Oscilloscopes enable real-time visualization and analysis of electrical waveforms. They allow for the precise examination of the characteristics of the signal and are hence essential for troubleshooting electronic circuits and systems. The oscilloscope we select disposes of a trigger functionality. This is used to synchronize events and recording data at the same time. Additionally, the oscilloscope has a sufficiently high frequency capability to accurately capture signals at 100 MS/s. This frequency range is optimal for the signals of interest in these experiments: for instance, this allow us to measure current and voltage signals lasting 10 µs.

The ONS is utilized for collecting data from the transducers and voltage probes (see Section 1.7.2). It is also equipped with four channels, with a storage capacity of up to 1 GB. For the oscilloscope uncertainties, we account for a DC offset[9] of ± 0.25% relative to the measured signal (for instance, for a peak current of 45 kA, the error will be within ± 0.1125 kA). The oscilloscope provides amplitude resolution of 12 bits, ensuring precise measurement capabilities.


**Figure 1.25:** The oscilloscope Nicolet Sigma 30 (ONS).

[8] A data acquisition system is a combination of hardware and software components used to acquire, store, and process data from sensors. It typically consists of analog-to-digital converters, signal conditioning circuitry, data acquisition boards, and a computer to store and analyze the data.

[9] The DC offset denotes the presence of a constant voltage (or current), different from zero, in the output signal.

#### TraNET FE 404

In our experiments, we need another data acquisition system that must operate at sufficiently high speed measurements to capture the shock wave and structure acceleration. In the most critical scenario, the shock wave exhibits a positive time duration of $t_o = 0.01$ ms. To ensure the recording of the shock wave's peak, $P_{so}$, it is important to sample at least 200 data points within this time frame ($t_o$). Consequently, the data acquisition system should feature a sampling speed of 20 MS/s. Additionally, the acquisition system must be capable of providing functional voltage to the sensors. Taking these two criteria into account, the DAS TraNET FE 404 is selected.

The DAS TraNET FE 404 has 8 channels with a maximum sample rate of 20 MS/s and an amplitude resolution of 16 bits up to 5 MHz and 14 bits up to 20 MHz. It has a range error[10] of ± 0.03 % (typical) to 0.1 % (maximum) (from the measured value), a DC offset of ± 0.03 % (typical) to ± 0.1 % (maximum), and an input noise of ± 3.57 mV. Its specifications are summarized in Appendix C, Table C.1.


**Figure 1.26:** The data acquisition system (DAS) TraNET FE 404.

### 1.7.2 Sensors

In order to study the rigid-body response of structures submitted to blast loads, we must measure the impinging pressure on the structure, its acceleration, as well as the current and voltage discharged within the electrical system (a detailed study and explanation of the electrical system is provided in Chapter 2). Our experimental platform incorporates a variety of sensors, including pressure transducers, current transducers and voltage probes. Each sensor has its range of uncertainties and specifications.

Integrated Electronics Piezoelectric (IEPE) transducers are selected as they eliminate the uncertainties related to cable length and the triboelectric effect[11]. A detailed explanation of the origins of uncertainties and our strategies for addressing them is provided in Appendix C.

#### Pressure transducers

In order to characterize accurately the pressure load and the time signature of a blast-induced pressure, pressure transducers are required. These transducers should be positioned

[10]Range error refers to the difference between the expected range of values and the actual values obtained.

[11]Triboelectric effect is a phenomenon that results in the generation of electric charge through the contact and separation of materials, caused by the exchange of electrons, (Pan and Zhang, 2019).

in two ways: parallel to the shock wave's propagation to measure the reflected overpressure and perpendicular to the shock wave to measure the incident overpressure.
It is worth noticing that we have included thermal insulation aluminum foil in all our sensors to isolate the transducers from thermal transients. For more details, we refer to Appendix D.

**Reflected overpressure** The 603CBA family transducer has been selected for measuring the reflected overpressure. These transducers can measure a wide range of pressures spanning from 14 bar to 100 bar, they have an operating temperature range of up to 120°C, a high natural frequency resulting in very fast rise time[12] (<0.4 $\mu$s), they are compact in size (see Figure 1.27), and voltage as the output signal (Kistler, 2023). To study various blast scenarios, pressure transducers with different pressure ranges are selected hereinafter:

- The 603CBA0014 Kistler transducer has a pressure range up to 20.0 bar with sensitivity[13] 414.9 mV/bar. The DC offset is less than ± 32 $\mu$bar within the operating temperature range (from −55°C to 120°C), and the linearity error is ± 0.05% from the full-scale output (20 bar) which gives an error of ± 0.01 bar. Axial acceleration sensitivity[14] is ± 0.00014 bar/g and radial acceleration sensitivity ± 0.00001 bar/g. As the pressure transducer is inside a fixed support, g can be considered much smaller than 1g and thus the axial and radial acceleration can be taken equal to ± 0.00014 bar and ± 0.00001 bar respectively. The total cumulative error due to the above is ± 0.010182 bar, which is quite satisfactory for our needs.

- The 603CBA0035 Kistler transducer has a pressure range up to 45.51 bar with sensitivity 136.9 mV/bar. The DC offset is less than ± 79 $\mu$bar within the operating temperature range (from −55°C to 120°C), and the linearity error is ± 0.11% from the full scale output (45.51 bar) which gives an error of ± 0.050061 bar. Axial and radial acceleration sensitivities are the same as for the 603CBA0014 Kistler transducer (± 0.00014 bar and ± 0.00001 bar respectively). The total cumulative error is ± 0.05029 bar, which is again quite satisfactory for our needs.

- The 603CBA0070 Kistler transducer has a pressure range up to 84.4 bar with sensitivity 68.96 mV/bar. The DC offset is less than ± 160 $\mu$bar within the operating temperature range (from −55°C to 120°C), and the linearity error is ± 0.18% from the full-scale output (84.4 bar) which gives an error of ± 0.15192 bar. Axial and radial acceleration sensitivities are the same as for the 603CBA0014 Kistler transducer (± 0.00014 bar and ± 0.00001 bar respectively). The total cumulative error is ± 0.15223 bar, which is quite satisfactory for our needs.

**Incident overpressure** The Kistler 6233A0050 pencil probe is used to measure incident overpressure as it has low rise time (less than 1 $\mu$s), a critical feature for capturing rapid pressure changes, typically associated with shock waves. It also exhibits a high sensitivity

[12]The rise time denotes the duration for the signal to increase from 10% to 90% of the full-scale output

[13]Sensitivity is the ratio of the change in the output (usually low voltage) of the device to the change in the physical quantity (e.g. current, voltage, pressure etc.) being measured.

[14]Acceleration sensitivity is the sensitivity of a pressure transducer to acceleration, usually measured in mV/g. It is the amount of output voltage generated by the transducer when subjected to a certain level of acceleration

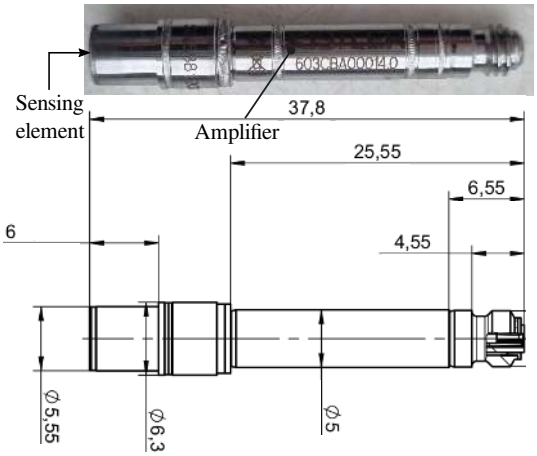


**Figure 1.27:** The 603CBA Kistler pressure transducer (dimensions in mm), Kistler (2023).

of 1400 mV/bar, a wide pressure measurement range, up to 2 bar, and a broad operating temperature range, spanning from $-55°C$ to $125°C$. Its acceleration sensitivity is $\pm$ 2 mbar/g, equivalent to $\pm$ 0.002 bar for $g = 1$. The linearity error is within $\pm 0.58\%$ of the full-scale output (2 bar) which gives an error of $\pm 0.0116$ bar. The total cumulative error of the pencil probe is $\pm$ 0.0136 bar, which is quite satisfactory for our needs.

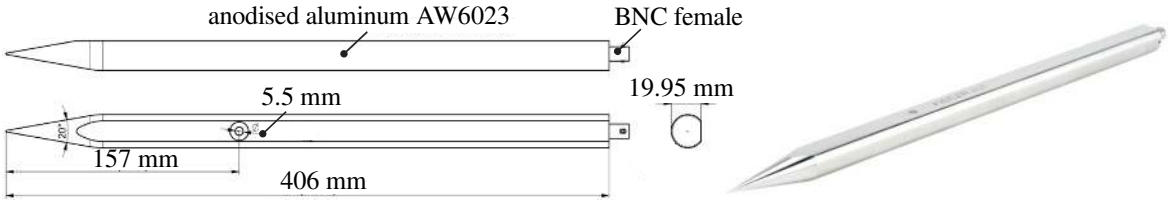


**Figure 1.28:** Dimensions of pencil probe type 6233A0050, Kistler (2023).

### Accelerometers

Kistler 8763B1K0A uni-axial accelerometers are selected for several compelling reasons. First, they offer an extensive range of acceleration measurements. Second, they exhibit a low level of uncertainty, enhancing the accuracy of the measurements. Third, these sensors are compact and lightweight, facilitating easy mounting on the structure without significantly affecting the structural response, as illustrated in Figure 1.29 (Kistler, 2023). We have selected two different ranges of accelerometers based on the our scenarios: (1) the 8715B1K0S00 transducer which has a wide acceleration range up to 1000 g and a sensitivity 5.1 mV/g, and (2) the 8715A5000M5 transducer with an acceleration range up to 5000 g and a sensitivity 1.023 mV/g.
The estimated uncertainty for both accelerometers is about 0.9% of the measured value. Their specifications are summarized in Table C.4.

### Current sensor

Current sensors play an important role in real-time monitoring of electrical currents in circuits and systems. Current measurements are important in this setting for analyzing

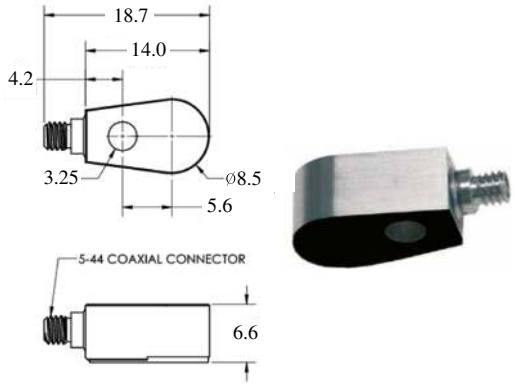


**Figure 1.29:** The Kistler 8763B1K0A uniaxial accelerometer.

the detonation of exploding wires. The criteria that guided our choice of the current sensor are (1) a non-invasive measurement capability (not direct electrical contact with the current-carrying conductor) and (2) the frequency range.

The Rogowski current waveform transducer model CWT03-Ltd has been used which has a measurements range from 300 mA to 300 kA and a negligible rise time. The sensor converts high currents into voltage with a sensitivity of 10 mV/kA. The DC offset remains below ± 2 mV (± 0.2 kA) within an operating temperature range from -20°C to 100°C. Its linearity error is within ± 0.05% of the full-scale output (300 kA), resulting in an error of ± 0.15 kA. The positional accuracy[15] is ± 0.5% of the measured value. Therefore, for a peak I ≈ 50 kA (as in the experiments presented the following chapters), the total cumulative error is ± 0.6 kA, which is quite satisfactory for our needs.

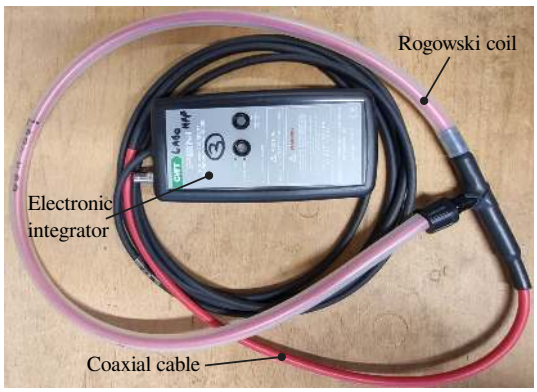


**Figure 1.30:** The Rogowski current waveform transducer model CWT03-Ltd.

### Voltage probe

Voltage measurements are necessary to study the electrical circuits parameters and to determine the evolution of the resistance of the explosive wire (see Chapter 2). For our experiments, the voltage probe should be able to accurately measure voltage up to 20 kV.

The Tektronix P6015A High Voltage Probe (HPV) is used as it offers a wide range of input voltage capabilities, ranging from 1.5 kV to 20 kV for direct current (DC) and alternating current (AC) measurements. The voltage sensor features a rapid rise time of

[15]The positional accuracy is the deviation from the expected output due to changes in the position of the coil of the transducer.

4.67 ns and provides a 1000X attenuation, with a sensitivity of 1 V/1 kV. The linearity error is within $\pm 0.5\%$ (0.1 kV), a temperature error $\pm 0.006\%/°C$ (where a temperature rise of 60°C at 20 kV leads to an error equal to 3.6 V), and a DC offset equal to $\pm 0.018\%/kV$ (at 20 kV the DC offset is 3.6 V). The total cumulative error at 20 kV is about $\pm$ 0.1072 kV, which corresponds to an error $\pm 0.536\,\%$, which is acceptable of the need of our study.


**Figure 1.31:** The High voltage probe Tektronix P6015A.

### 1.7.3 Optical cameras

The response of masonry structures to explosions can be hardly experimentally investigated using only sensors and accelerometers. Image techniques are very helpful to measure displacements in 2D and 3D.

One of the main objectives of our experimental campaign is to quantify the rigid-body motion of the tested structures. The numerical studies performed by Masi et al. (2019, 2022) showed that the considered structure's (multi drum column, block) time response is approximately 0.7 seconds. Therefore, the required optimal frames per second (fps) is around 200 frames per second (fps). We do not intend to measure the shock wave using high-speed imaging, which would necessitate a frame rate of approximately 50000 fps. Based on a desired window size of approximately 40 $\times$40 cm$^2$, a resolution of about 0.64 megapixels is therefore sufficient for our applications.

Given the above characteristics we decided to use three GoPro cameras which are more affordable and have sufficient resolution and frame rate (see Table 1.3) for the needs of these investigations. Appropriate correction for distortion were made. For more details we refer to Chapter 4.


**Figure 1.32:** GoPro HERO11 camera.

**Table 1.3:** GoPro HERO11 specifications.

| | |
|---|---|
| **general** | |
| Color depth: | 10-bit |
| Lens focal range | 12 mm |
| Max aperture | F2.8 |
| Max mechanical shutter speed | 1/2000s |
| Max speed (fps) | 240 |
| **sensor** | |
| Sensor type | CMOS |
| Sensor size | 1/1.9 |
| Sensor dimensions | 6.40 x 5.60 mm |
| Sensor area | 35.84mm$^2$ |
| Sensor resolution | 27.13 megapixels |
| Max image resolution | 5312 x 2988 |
| Max native ISO | 6,400 |
| Min native ISO | 100 |
| **video features** | |
| Max video resolution | 5.3K60 / 4K120 / 2.7k240 |
| Video formats | H.264, H.265 |

## 1.8 3D printing

Three-dimensional (3D) printing is a technology to create 3D models and mechanical parts. 3D printing is performed by layering materials based on a digital model. It offers numerous advantages, including rapid prototyping, customization, reduced waste, and the ability to create complex geometries (as in our case) that are hard to achieve using traditional manufacturing methods.
Two 3D printing technologies are used in this work to print the tested structures:

1. Fused Deposition Modeling (FDM). The Ultimaker S5 3D printer allows to print large volumes (max 330 x 240 x 300 mm$^3$), allowing for the creation of large-scale models and structures. The Ultimaker S5 delivers high-quality, consistent results with precision down to 1 mm. Moreover, the high printing speed, up to 300 m/s, saves time in printing structures.

2. Stereolithography (SLA). The 3D SLA 3L printer can print large structures as it has a large build volume of 335 $\times$200 $\times$300 mm$^3$. It can print in high-resolution with a precision of 25$\mu$m.

## 1.9 Installation of the experimental platform

The key point of this section is to detail the steps ensuring an appropriate installation of the experimental platform, composed of the several components already presented in previous sections. In so doing, it enables one to rebuild the same experimental setup designed and used throughout this work.

The installation procedure structures around six main steps. First, we assemble and mount the optical table, carefully correcting any horizontal misalignment and ensuring a planar surface, where the structures will be tested. Then, we install the container cabin

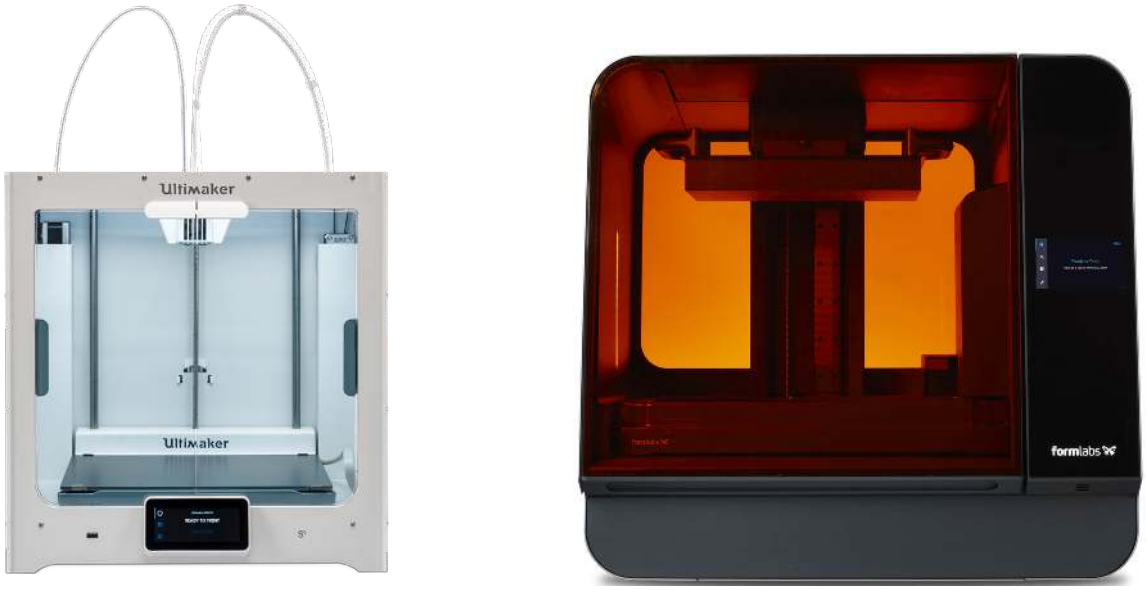


**(a)** S5 ultimaker **(b)** Form 3L

**Figure 1.33:** 3D printers: Ultimaker S5 (fused deposition modeling) (a), SLA (stereolithography) (b).

and proceed to reinforcing its structure to mitigate low-frequency vibrations. This step is essential for reducing eventual noise caused by the impinging of shock waves onto the cabin's interior panels. Next, we equip the cabin with a ventilation system. The latter prevents the accumulation and the leak of aluminum dust produced by the denotation of exploding wires. The subsequent step involves the mounting of the exploding wire system, composed of cable, electrodes and two plates. Finally, we install panels of acoustic foam over the cabin's interior walls (side, roof, and corners) and the interior pipes of the ventilation system. The panels, acoustically isolated, reduce at minimum the reflection of shock waves, and thus enables to study the response of structures (models, cf. Section 1.5) to shock waves with reduced disturbances from the surrounding.
At the end, to verify that the sound levels arising during the detonation of exploding wires fall within the laboratory's range and standard limits (cf. French Government, 2006), we conduct preliminary tests and record the corresponding sound levels outside of the cabin and at a distance of 1 m. These preliminary tests also allow to assess the performance of the container's reinforcement, of the acoustic foam, as well as to verify the correct installation of the exploding wire system.

### 1.9.1 Installation of the optical table

The optical table is installed within the allocated space in the laboratory as depicted by Figure 1.34. The table is composed of (*i*) six pneumatic, rigid supports to ensure appropriate leveling in case of uneven floors and vibration isolation and (*ii*) a honeycomb stiff panel 120 cm wide, 180 cm long, and 30.5 cm high, with a overall weight of 500 kg (cf. subsection 1.6.2). The mounting procedure involves the following steps: (1) positioning of the table supports (S-2000) and mounting of (2) the table panel, as detailed hereinafter. For more details, we refer to the user manual (Newport, 2023).

### Positioning of the supports

Figure 1.34 displays the positioning of the six supports for the optical table. The supports, with diameter equal to 25.40 cm and height equal to 47.24 cm, are regularly spaced with a distance equal to 70 cm with respect to their centroid, along the $x$-direction, and equal to 65 cm, along the $y$-direction.

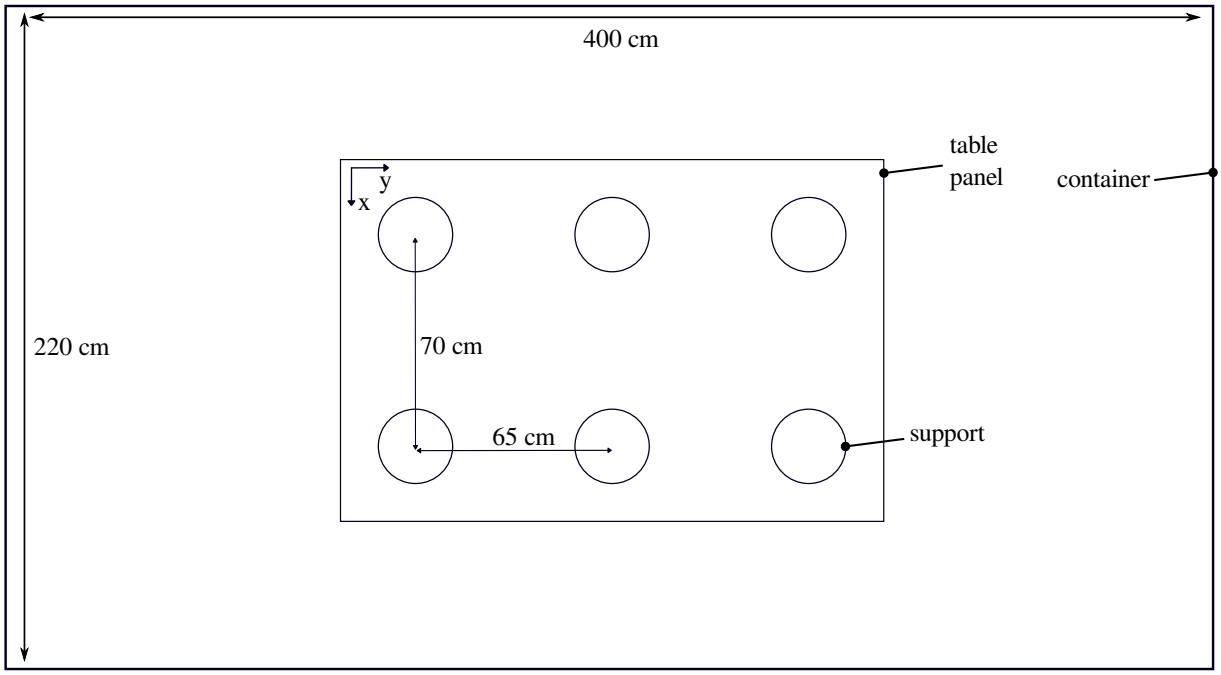


**Figure 1.34:** Plan with the dimensions of the container cabin and the optical table, showing the position of the table supports.

### Installation of the table panel

With the supports positioned as in Figure 1.34, we raise the table panel and position it above the six supports by loosely securing the connecting clamps using bolts (see Figure 1.35). The table panel is secured to the support by fastening the support plate with bolts and clamps (three per support) underneath the table panel (refer to Figure 1.35). At this point, we proceed to the leveling of the supports to correct for the misalignment caused by the uneven floor of the laboratory. In so doing, we first position a level (inclinometer) at the center of the table. Then, we manually adjust each one of the supporting plates at the top of the pedestals by adjusting the hexagonal nut and recursively assure that the table is leveled. Once this step is completed, we tighten all clamp bolts to secure the table to the pedestals and ensure a perfect horizontal alignment along both the width and length axes.

The table supports comprise a system of stabilizers to isolate the table from eventual floor vibrations. However, in our setting, stabilizers are not activated and supports are left rigid (see Figure 1.36). Indeed, the characteristic time of the explosion (of the order of a few milliseconds) is much shorter than the stabilization system's time response, which in turn would result in spurious isolation with a pronounced time lag.

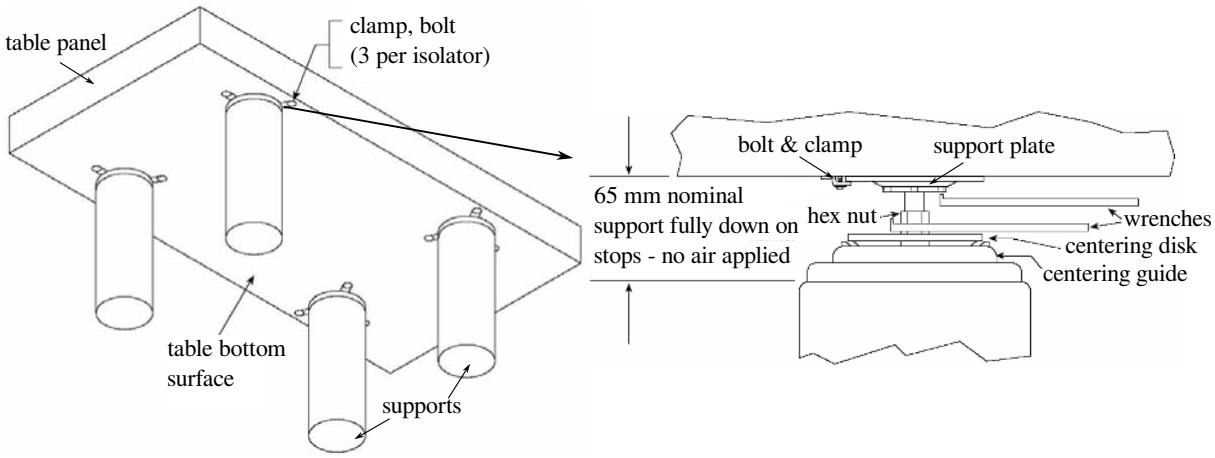


**Figure 1.35:** Optical table bottom showing clamps and bolts position with respect to the top of the pedestals.

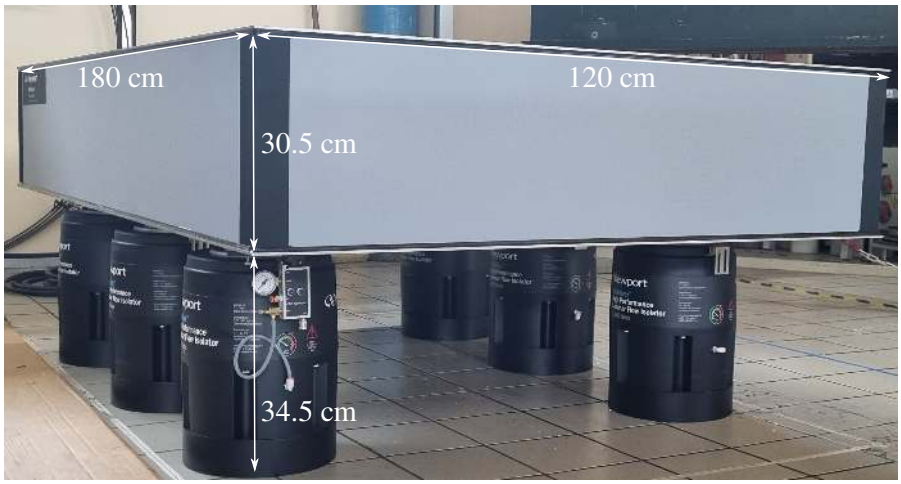


**Figure 1.36:** Installation of optical table.

### Mounting of the container cabin

After having installed the optical table, we proceed with the mounting of the container cabin. As discussed earlier (cf. Section 1.6.2), the cabin allows to isolate the experimental platform from the rest of the laboratory equipment, thus it provides a safe setting for the laboratory personnel (containing the shock waves) and a closed and controlled environment to ensure high repeatability of the experiments.

The container cabin, depicted in Figure 1.37a, is made of galvanized steel, is mounted in situ (see Figure 1.37b), around the assembled optical table. In particular, we start by positioning the bottom rails. Then, we insert the four corner posts and the vertical panels inside the rails, as shown in Figure 1.37a. Next, the roof panel is positioned over the structure using the corresponding rails. The roof, with its own weight, secures the entire structure of the container. Finally, we position the door and a series of vertical rebars at the connections between the different vertical panels, using bolts.

The resulting container has to be reinforced to reduce at maximum its low frequency vibrations caused by the presence of small gaps between the rails, the vertical panels, and the rebars. To this end, we introduce fasteners, i.e., approximately 600 rivets, to provide additional fixation of the vertical panels. Furthermore, to reduce the aforementioned gaps, we also insert rubber sheets with a thickness of 0.5 cm between the rails and the panels.

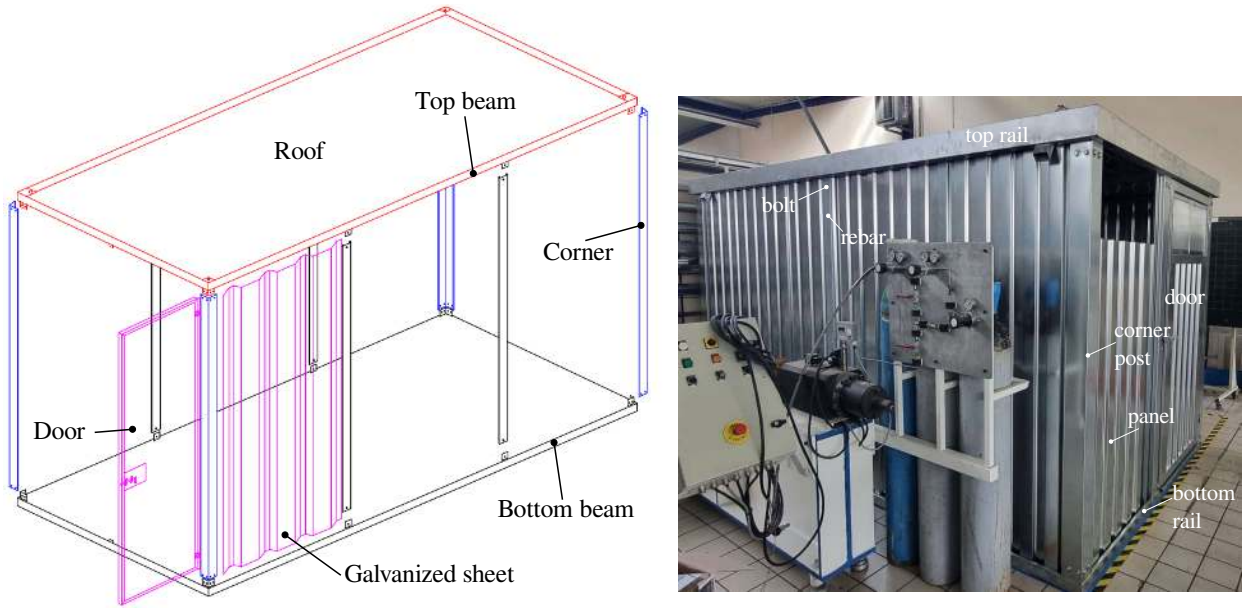


**(a)** Sketch of the container cabin

**(b)** Container cabin installed

**Figure 1.37:** Sketch of the container cabin (a), and container installed (b) composed of a door, roof with rails, bottom rails, vertical panels, and corner posts.

## 1.9.2 Installation of the ventilation system

After having installed the container cabin, we proceed with the installation of the ventilation system. As discussed earlier (cf. Section 1.6.3), the ventilation system allows the removal of aluminum dust generated during the explosion from the cabin and ensuring a continuous supply of fresh air in to the cabin. Thus it provides a safe setting for the laboratory personnel.

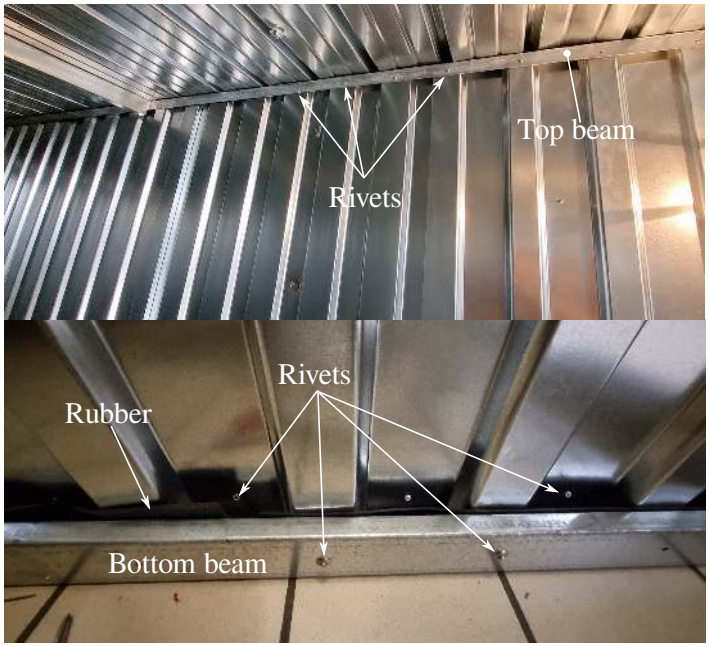


**Figure 1.38:** Reinforcement of the container cabin using rivets and rubber sheets to fill gaps between the rails and the vertical panels.

The installation of the ventilation system is delegated to the enterprise Asair (www.asair.fr) due to the inherent complexity of the system and to ensure the safety of the personnel. The installation starts by positioning two fans (model: LM315EC), one for ventilation and another for air extraction. Subsequently, two filters are securely positioned, one on the cabin and another outside of the laboratory. A series of ducts, both inside and outside the cabin, are then installed and connected to the filters and the fans. Thorough testing and ongoing adjustments are conducted to ensure the efficiency and functioning of the ventilation system. To this end, maintenance,involving cleaning/replacement of filters, is periodically required.

The control of the ventilation system takes place from outside the cabin, as illustrated in Figure 1.39b. Additionally, we install an electrical system (e.g. cables for light and electrical outlet), along with electrical connections for ventilation system (see Figure 1.39a). It is worth noting that the ventilation system consists of two working processes: first, air is extracted from the cabin (for a duration of approximately two minutes) to remove most of the accumulated dust, then simultaneous air extraction and ventilation (or a duration of approximately two minutes) ensure the removal of all dust and cleaning of the cabin.

### 1.9.3 Installation of the exploding wires system

As part of the installation process, the setup of the exploding wire system is a crucial step. As outlined in Section 1.6.5, the exploding wire system primarily comprises two main components: a generator and a capacitor. The capacitor is connected to electrodes via a coaxial cable. To accommodate this setup, a thick 1.6 cm cable extending from the capacitor is necessary. The cable starts at the capacitor and traverses the container cabin, with the cable head positioned at the midpoint of the optical table (see Figure 1.40). At this cable head, the installation of the two electrodes cathodes and anodes is required (see Figure 1.40). To this end, we install two plates, bottom plate of thickness equal to 1.5 cm


**(a)** Electrical connections **(b)** Ventilation system control

**Figure 1.39:** Ventilation system installed including electrical panel (a) and ventilation system control (b).

and top plate of thickness 3.5 cm, positioned above the table (see Figure 1.40). The cable can then pass through these plates. In this way we ensures that the cable is electrically isolated from the table. Furthermore, this method facilitates the installation of the wire inside the plates, ensuring that only the electrodes are visible on the table's surface. This also aligns with the aim of generating quasi-hemispherical explosions (for more details, we refer to Chapter 4).

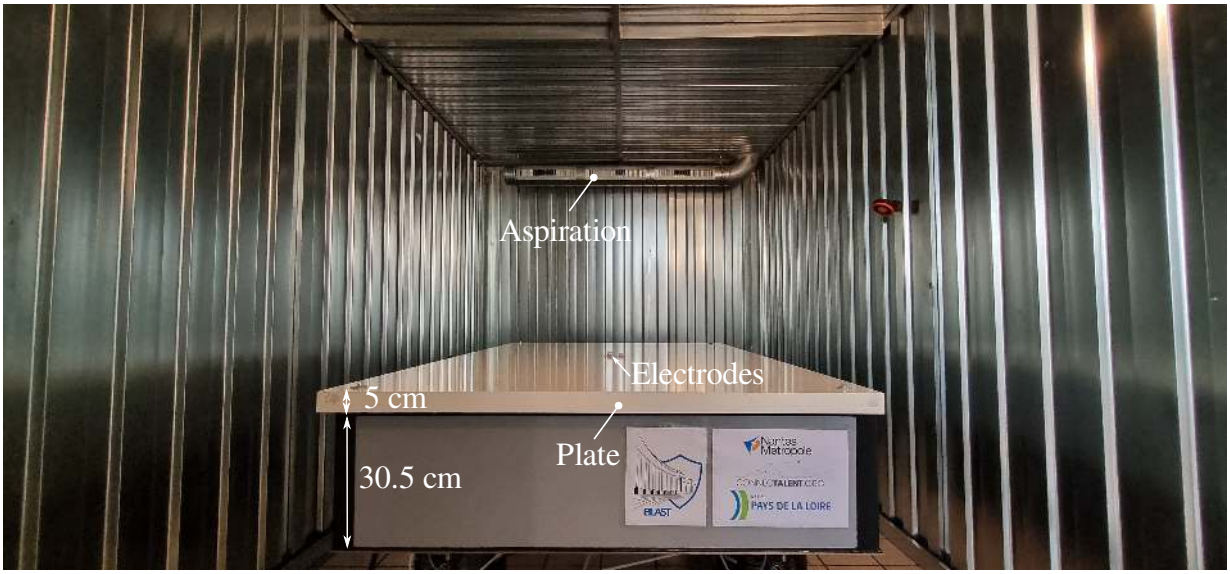


**Figure 1.40:** Installation of the exploding wire system including cable and electrodes.

### 1.9.4 Installation of the acoustic foam

As detailed in subsection 1.6.6, the acoustic foam is used to prevent any reflections coming from the walls and enhancing experiments safety. The installation process of the acoustic

foam is critical and demands close attention. In particular, we start by cleaning the walls and the roof, followed by marking the positions of each foam panel with the help of a tape. We then proceed to the installation by putting adhesive (Bostik MSP 108 RENOFIX) on the panel regions where the foam is positioned and hold for a few seconds to ensure the bonding of the adhesive.

To ensure accurate acoustic isolation, certain areas of the cabin requires cutting of the foam panels in smaller pieces.

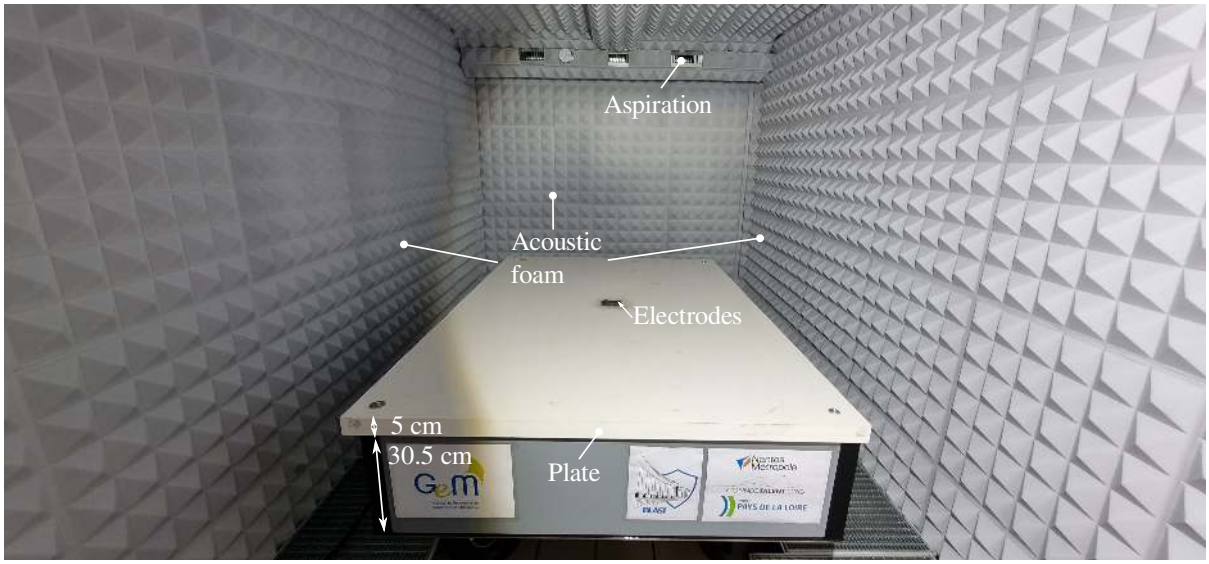


**Figure 1.41:** Acoustic foam installation including walls, roof and edges.

Throughout our explosion tests, ensuring that the resultant sound levels adhered to established standards was paramount. To achieve this, real-time measurements were conducted using a sound meter. This approach enabled us to quantitatively evaluate the sound produced during the experiments. The collected sound meter data was then compared against the french standard, French Government (2006), which specify a maximum permissible sound level limit of 80 dB for 8 hours, with a maximum sound level of 135 dB. Notably, our findings revealed that the sound levels produced by our experiments consistently fell well within the permissible range, with a maximum peak value of 115.1 dB recorded at a distance of 1 m from the cabin. It is worth noting that numerous experiments were conducted under varying scenarios to assess sound levels, and we present here a representative critical case.

### 1.9.5 Completion of the container cabin

This section focuses on the installation of the remaining components, notably the ground plate designed to capture any flying particles resulting from an explosion. Additionally, we install an electric bar to take any residual charges on the electrodes after explosion (refer to Figure 1.43). This thorough installation process ensures that every detail is carefully addressed to establish a controlled and secure environment for the execution of our experiments. The next step will involve analyzing the exploding wires system, which will be discussed in detail in Chapter 2.

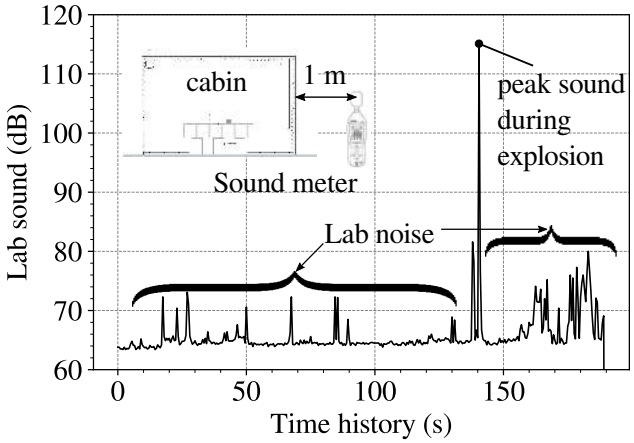


**Figure 1.42:** Verification of sound level during experiment.

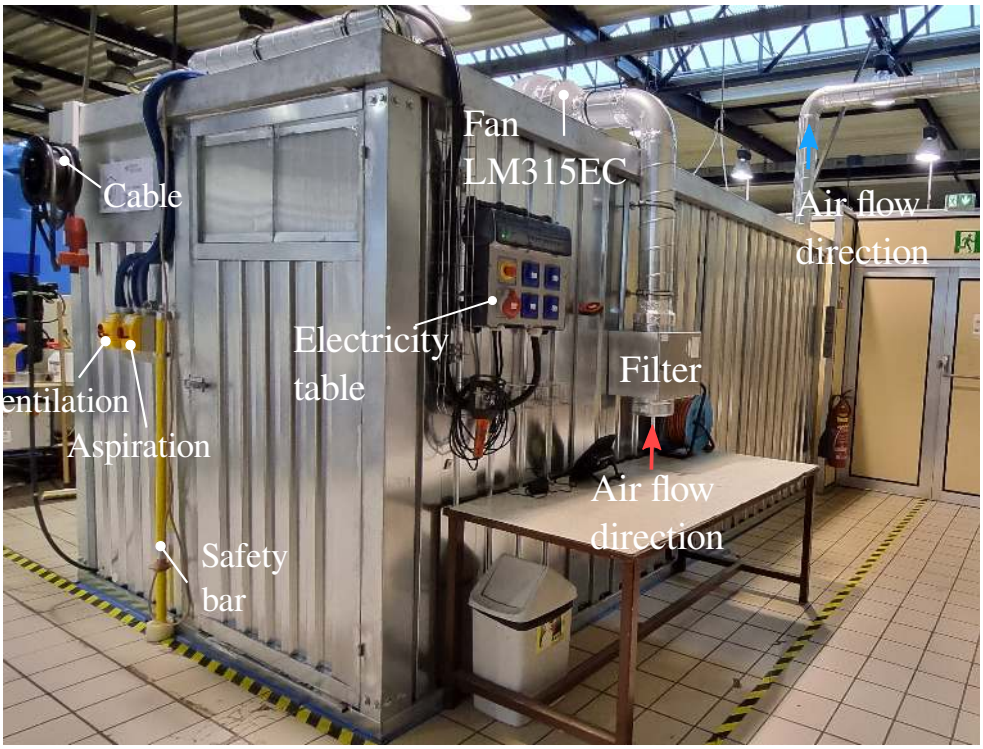


**Figure 1.43:** Cabin installation is finished and ready to conduct experiments.

## 1.10 Concluding remarks

Here we presented the design methodology of the experimental platform including container cabin, optical table, acoustic foam, data acquisitions and sensors, 3D printing and optical cameras (refer to Figure 1.44).

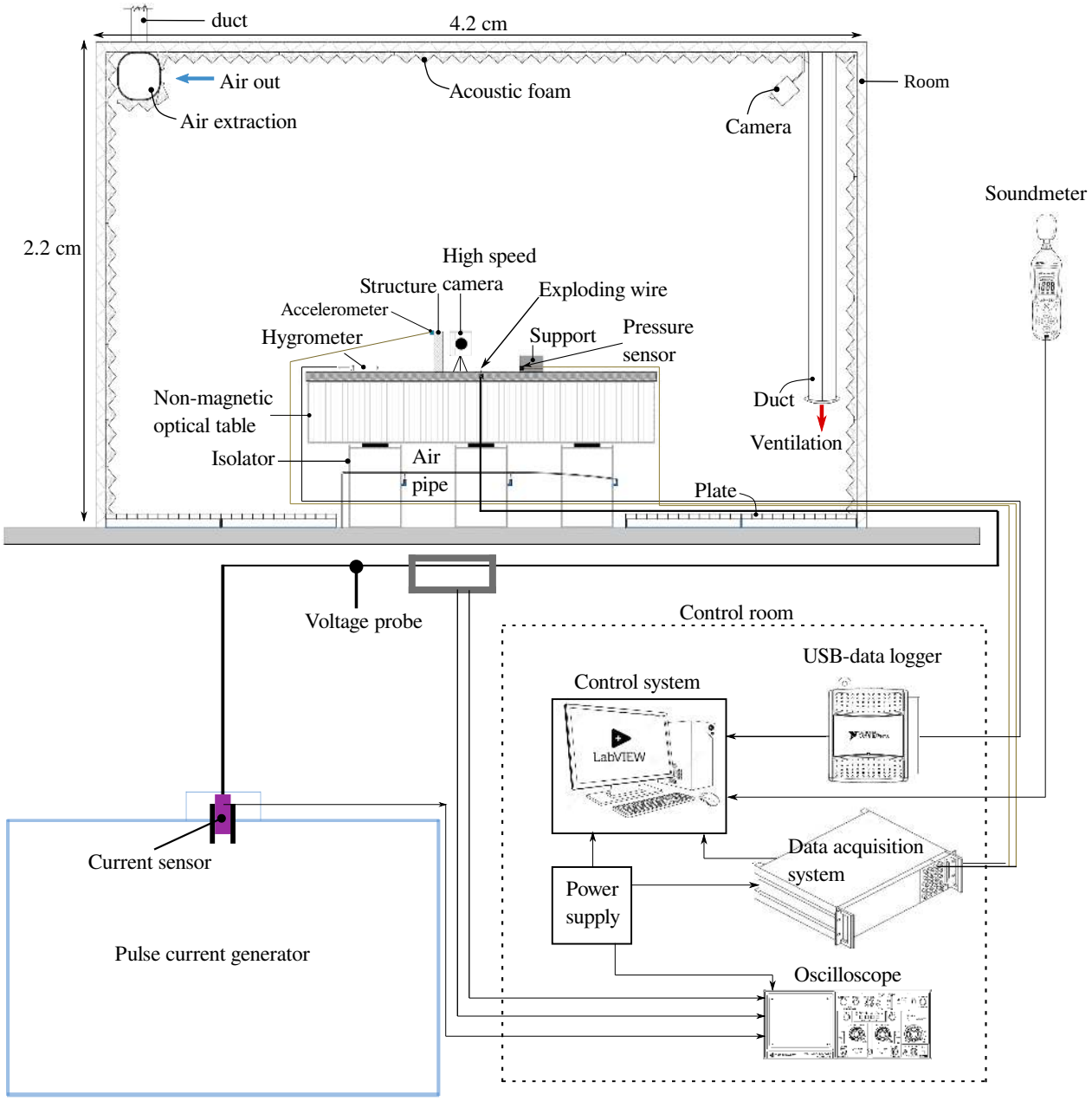


**Figure 1.44:** Experimental setup of a reduced scale experiments assembled and located at the Ecole Centrale de Nantes.

# Chapter 2

# Blast source: Exploding wires

*In Chapter 1, we focused on the design and installation of the experimental setup to study masonry structures at reduced scale. We introduced essential parameters and explanations related to the exploding wire system, which will serve as the explosive source on a reduced scale. In this Chapter, we present the electric parameters and the model derivation of the exploding wire circuit. Furthermore, we explore the intricate mechanisms underlying the phenomenon of the exploding wire and how it leads to the generation of shock wave. Then, we perform calculations to determine the inductance and resistance of the aluminum wire, quantify the temperature rise during explosion, and assess the energy deposition within the system. All the previous derivations are of utmost importance as they form the foundational knowledge for understanding the explosive load and therefore the resulting structural response.*

## 2.1 Introduction

The primary focus of this chapter is to provide a detailed explanation of the exploding wires system. We start with the presentation of the electrical system and the current and voltage equations as well as the determination of the electrical resistance, the inductance and the capacitance of the pulse current discharge circuit. The wire's phase transition is explained and the resistance developed during current discharge is calculated. Moreover, we estimate the temperature raised during the discharge, as well as an estimation for the dissipated energy through the wire.

## 2.2 Pulse Current Generator

Experiments were carried out with a Pulse Current Generator (PCG) assembled and located at Ecole Centrale de Nantes (Figure 2.1). The PCG consists of two circuits, as shown schematically in Figure 2.2: (1) a charging circuit made up of an electric source, a high current switch, and twelve capacitors, and (2) a discharge circuit comprising six Ignitron switches (Ignitron NL7703 mercury switches) and a coaxial cable that connects the capacitor with the electrodes. For every two capacitors, one NL7703 Ignitron switch is used to control the discharge of the charge. By varying the number of the connected capacitors, the characteristics of the PCG can be changed in terms of its resistance, capacitance and inductance.

The twelve capacitors are connected in parallel and have an equivalent nominal value

**Figure 2.1:** Pulse Current Generator (PCG) at Ecole Centrale de Nantes.

of capacitance, $C$, equal to 408 µF. It is worth noticing that this value of capacitance is the nominal value, where we are going in Section 2.4 to find the effective capacitance. The resistance of the discharge circuit, $R$, that connects the PCG and the electrodes results from the internal resistance of the PCG and the resistance of the coaxial cable. In a similar way, the total inductance of the discharge circuit, $L$, is due to the internal inductance of the PCG and that of the coaxial cable home made (see Section 2.4).

The maximum voltage that can be applied to the capacitors is 15 kV. The NL7703 Ignitron switches can handle a maximum voltage equal to 20 kV, with peak currents of 100 kA. The minimum and maximum energy that can be stored inside the capacitor are 5 J and 46 kJ, respectively. The characteristics of the discharge circuit of the PCG are detailed hereafter. To achieve this, a series of discharge experiments are conducted, and voltage and current transients are measured. The high current switch and the Ignitron switches are never closed.

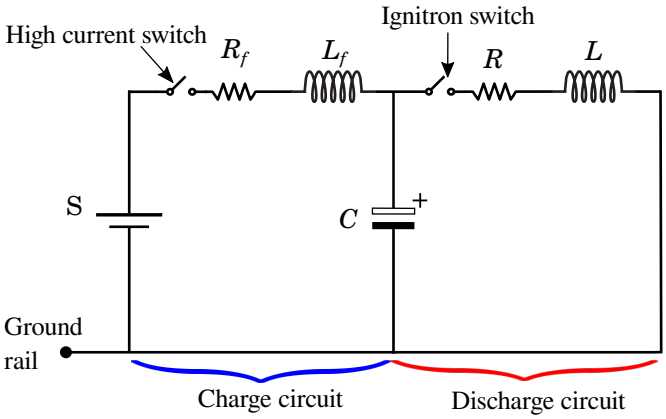


**Figure 2.2:** Schematic representation of the PCG charge and discharge circuits.

## 2.3 RLC characterization

### 2.3.1 Preliminaries

The discharge experiments can be modeled by the RLC circuit, shown in Figure 2.3. According to Kirchhoff's voltage law (Tung and Kwan, 2001),

$$u_L + u_R + u_C = 0, \tag{2.1}$$

where $u_R$, $u_C$ and $u_L$ are the potential difference (voltage) of the resistor ($R$), the capacitor ($C$), and the inductor ($L$), respectively.

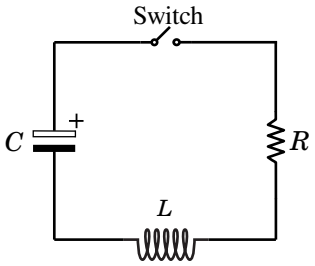


**Figure 2.3:** RLC discharge circuit.

#### Resistor

Electrical resistance is the property of materials to impede the flow of the electric charge. The circuit element used to model this behaviour is called resistor and is denoted by $R$. In our discharge experiments the electrical resistance is linked to (1) the elements of the capacitor and (2) the wiring that connects the capacitor with the experimental device for the explosion tests.

According to the Ohm's law (Tung and Kwan, 2001), the potential difference across a resistor is proportional to the current passing through the resistor

$$u_R(t) = Ri(t), \tag{2.2}$$

where $i(t)$ is the current (measured in Ampère, A) and $R$ the electrical resistance (in Ohm, $\Omega$), which is considered constant in the following. According to Tung and Kwan (2001), the resistance of a resistor can be expressed in function of the resistor's material resistivity, $\rho_s$, as follows

$$\rho_s = \frac{RS}{l}, \tag{2.3}$$

where $S$ is the cross sectional area, assumed constant in time, of the material of the resistor and $l$ its length.
The power dissipated through the resistor is

$$P_R(t) = u_R(t)i(t) = i^2(t)R = \frac{u_R^2(t)}{R}. \tag{2.4}$$

Thus, the energy dissipated through the resistor is

$$E_R(t) = \int_0^t P_R(t)\,dt = R\int_0^t i^2(t)\,dt = \frac{1}{R}\int_0^t u_R^2(t)\,dt. \tag{2.5}$$

### Inductor

The inductor stores energy in a magnetic field when current passes through it. According to Lenz's law (Tung and Kwan, 2001), the potential difference (voltage) of an ideal inductor is

$$u_L(t) = L\frac{di(t)}{dt}, \tag{2.6}$$

where $L$ is the inductance (measured in Henry, H) and considered constant in the following. The power of the inductor is

$$P_L(t) = u_L(t)i(t) = L\frac{di(t)}{dt}i(t) \tag{2.7}$$

Therefore, the energy stored by an (ideal) inductor is given by the expression

$$E_L(t) = \int_0^t P_L(t)\,dt = L\int_0^t \frac{di(t)}{dt}i(t)\,dt = \frac{1}{2}Li^2(t) \tag{2.8}$$

### Capacitor

An ideal capacitor consists of two electrical conductors separated by a dielectric (or insulating) material (Tung and Kwan, 2001). An ideal capacitor stores electric charge $\Delta q(t) = q(t) - q(0)$ according to the following expression

$$\Delta q(t) = Cu_C(t), \tag{2.9}$$

where $u_C(t)$ is the potential difference (voltage) at the ends of the capacitor and $C$ its capacitance (measured in Faraday, F), which is considered constant herein. The current is equal to $i(t) = dq(t)/dt$, and, therefore, Eq. (2.9) becomes

$$u_C(t) = \frac{1}{C}\int_0^t i(t)\,dt. \tag{2.10}$$

The energy stored by a capacitor is given by (Späth and Becker, 2002)

$$E(t) = \int_0^t u_C(t)i(t)\,dt = \int_0^t u_C(t)\frac{dq(t)}{dt}\,dt, \tag{2.11}$$

and using Eq. (2.9) by

$$E(t) = \int_0^t \frac{1}{C}q(t)\frac{dq(t)}{dt}\,dt = \frac{1}{2}\frac{q^2(t)}{C} = \frac{1}{2}Cu_C^2(t). \tag{2.12}$$

## 2.3.2 RLC circuit discharge

Using Eq. (2.2, 2.6, 2.9), Eq. (2.1) becomes

$$L\frac{di(t)}{dt} + Ri(t) + \frac{1}{C}\int_0^t i(t)\,dt = 0. \tag{2.13}$$

The initial conditions in the case of RLC discharge are $u_C(0) = U_0$, $q(0) = CU_0$ and $i(0) = 0$. Moreover, using Eq. (2.13), we obtain $L\frac{di(t)}{dt}|_{t=0} + \frac{q(0)}{C} = 0$, therefore, $\frac{di(t)}{dt}|_{t=0} = -\frac{U_0}{L}$. By differentiating Eq. (2.13) with respect to time and dividing by $L$, we obtain

$$\frac{d^2i(t)}{dt^2} + \frac{R}{L}\frac{di(t)}{dt} + \frac{i(t)}{LC} = 0. \tag{2.14}$$

This differential equation admits solutions of the form

$$i(t) = Ae^{st}, \tag{2.15}$$

where $A$ and $s$ are complex constants.
By substituting Eq. (2.15) into the above differential equation and dividing by $Ae^{st}$ results to the characteristic equation

$$s^2 + \frac{R}{L}s + \frac{1}{LC} = 0, \tag{2.16}$$

which is a quadratic equation in terms of the exponent $s$ and, therefore, its solution is

$$s = -\frac{R}{2L} \pm \sqrt{\left(\frac{R}{2L}\right)^2 - \frac{1}{LC}}. \tag{2.17}$$

Let denote with $\alpha = \frac{R}{2L}$ the damping coefficient and with $\omega_0 = \frac{1}{\sqrt{LC}}$ the resonant frequency of the circuit (Hagood and Von Flotow, 1991). Eq. (2.17) can be re written as

$$s = -\alpha \pm \omega, \tag{2.18}$$

where $\omega = \sqrt{\alpha^2 - \omega_0^2}$, which is equal to the frequency of the system, as it will be shown below.
The following three cases are distinguished depending on the parameters $R$, $L$, $C$ and consequently by $\alpha$ and $\omega$

1. $\alpha > \omega_0$, leads to two real roots. In this case the circuit is said to be *over-damped*.
2. $\alpha < \omega_0$, leads to two complex roots. In this case the circuit is said to be *under-damped*.
3. $\alpha = \omega_0$, which means that the two roots of the equation are equal. In this case the circuit is said to be *critically-damped*.

### Over-damped case

In this case $\alpha > \omega_0$ and the general solution of Eq. (2.15) is

$$i(t) = A_1 e^{-(\alpha-\omega)t} + A_2 e^{-(\alpha+\omega)t}. \tag{2.19}$$

By applying the initial conditions at $t = 0$ we have

$$\begin{cases} i(0) = 0 \\ \dfrac{di(t)}{dt}|_{t=0} = -\dfrac{U_0}{L} \end{cases} \Rightarrow \begin{cases} A_1 + A_2 = 0 \\ A_1(\omega - \alpha) - A_2(\omega + \alpha) = -\dfrac{U_0}{L} \end{cases} \Rightarrow \begin{cases} A_1 = -\dfrac{U_0}{2L\omega} \\ A_2 = \dfrac{U_0}{2L\omega}. \end{cases}$$

The equation of the current thus becomes

$$i(t) = \frac{U_0}{2L\omega} e^{-\alpha t} \left(-e^{\omega t} + e^{-\omega t}\right). \tag{2.20}$$

Integrating Eq. (2.19) with respect to time, we obtain the charge of the capacitor, i.e.,

$$\begin{aligned} q(t) &= \int_0^t i(t)\, dt + q(0) = \frac{U_0}{2L\omega}\left(-\frac{e^{-(\alpha-\omega)t}}{\omega - \alpha} - \frac{e^{-(\alpha+\omega)t}}{\omega + \alpha}\right) + A_3 \\ &= \frac{CU_0}{2\omega} e^{-\alpha t}\Big( (\omega - \alpha)\, e^{-wt} + (\omega + \alpha)\, e^{\omega t}\Big), \end{aligned} \tag{2.21}$$

where $A_3$ is a constant to be determined according to the initial conditions. In particular, at $t = 0$ we have $q(0) = CU_0$, which after some calculations results to $A_3 = 0$. The equation of the capacitor's voltage thus becomes

$$u_C(t) = \frac{U_0}{2\omega} e^{-\alpha t} \Big( (\omega - \alpha)\, e^{-\omega t} + (\alpha + \omega)\, e^{\omega t} \Big). \tag{2.22}$$

**Under-damped case**

In this case $\alpha < \omega_0$ and the general solution of Eq. (2.15) is

$$\begin{aligned} i(t) &= A_1 e^{(-\alpha+\omega j)t} + A_2 e^{(-\alpha-\omega j)t} \\ &= e^{-\alpha t} \left( A_1 e^{\omega j t} + A_2 e^{-\omega j t} \right), \end{aligned} \tag{2.23}$$

with $j = \sqrt{-1}$ and $A_1$ and $A_2$ are constants to be determined from the initial conditions. Equivalently,

$$i(t) = e^{-\alpha t} \Big( A_3 \cos(\omega t) + A_4 \sin(\omega t) \Big), \tag{2.24}$$

where $A_3$ and $A_4$ are again constants to be determined by the initial conditions.
By applying the initial conditions we have

$$\begin{cases} i(0) = 0 \\ \dfrac{di(t)}{dt}|_{t=0} = -\dfrac{U_0}{L} \end{cases} \Rightarrow \begin{cases} A_3 = 0 \\ A_4 = -\frac{U_0}{L\omega}. \end{cases}$$

The equation of the current, thus, becomes

$$i(t) = -\frac{U_0}{L\omega} e^{-\alpha t} \sin(\omega t). \tag{2.25}$$

Integrating Eq. (2.24) with respect to time we obtain

$$\begin{aligned} q(t) &= q(0) + \int_0^t i(t)\, dt \\ &= \frac{CU_0}{\omega} e^{-\alpha t} \big( \alpha \sin(\omega t) + \omega \cos(\omega t) \big) + A_5 \\ &= \frac{CU_0}{\omega} e^{-\alpha t} \big( \alpha \sin(\omega t) + \omega \cos(\omega t) \big), \end{aligned} \tag{2.26}$$

where $A_5$ is a constant to be determined by the initial conditions. In particular, at $t = 0$ we have $q(0) = CU_0$ and, therefore, $A_5 = 0$.
Consequently, the capacitor's voltage is

$$u_C(t) = \frac{U_0}{\omega} e^{-\alpha t} \Big( \alpha \sin(\omega t) + \omega \cos(\omega t) \Big). \tag{2.27}$$

**Critically damped case**

In this case $\alpha = \omega_0$ and the general solution of Eq. (2.15) is

$$i(t) = e^{-\alpha t} (A_1 + A_2 t). \tag{2.28}$$

By applying the initial conditions we have

$$\begin{cases} i(0) = 0 \\ \dfrac{di(t)}{dt}|_{t=0} = -\dfrac{U_0}{L} \end{cases} \Rightarrow \begin{cases} A_1 = 0 \\ A_2 = -\frac{U_0}{L}. \end{cases}$$

The equation of the current becomes

$$i(t) = -\frac{U_0}{L} t e^{-\alpha t}. \tag{2.29}$$

Integrating Eq. (2.19) with respect to time, we obtain the charge of the capacitor

$$\begin{aligned} q(t) &= \int_0^t i(t)\, dt + q(0) \\ &= CU_0(\alpha t + 1)e^{-\alpha t} + A_3, \end{aligned} \tag{2.30}$$

where $A_3$ is a constant to be determined by the initial conditions. In particular, at $t = 0$, we have $q(0) = CU_0$, thus $A_3 = 0$.
Consequently, the capacitor's voltage is

$$u_C(t) = U_0(\alpha t + 1)e^{-\alpha t}. \tag{2.31}$$

## 2.4 RLC characterization: Identification of parameters

In this Section, we identify the overall electrical resistance, inductance, and capacitance of the PCG discharge circuit (Figure 2.1). To this end, we conduct 10 discharge experiments in order to measure the current transients. The latter are then fitted with the equations of the RLC circuit model (detailed in Section 2.3), and the governing parameters are identified by means of a least-squares regression.

Our system comprises an electric circuit illustrated in Figure 2.4, consisting of various components: a capacitor ($C$), a resistance ($R$) formed by the internal resistance of the PCG, the resistance of the two coaxial cables ($R_{\text{AB}}$ and $R_{\text{BC}}$), and an additional resistor $R_a$ (see Figure 2.4). Additionally, there's an inductance ($L$) made up of the internal inductance of the PCG and the inductance of the two coaxial cables ($L_{\text{AB}}$ and $L_{\text{BC}}$). Then, after fitting the current transients we determine the optimized parameters for each circuit. Moreover, two separate sets of experiments ( (each set representing a different circuit) were conducted to determine the electric circuit parameters, where we measure the current in each circuit. It is worth noting that the first coaxial cable has a length 2.7 m and diameter 10 mm, and the second coaxial cable has a length 8 m and diameter 4 mm.
To determine these parameters, we performed the following experiments:

1. For the first circuit (PCG + additional resistor + cable-1 in Figure 2.4), we measured the current transients ($i_1$) (utilizing the CWT03-Ltd Rogowski Current Waveform Transducer) see Figure 2.5a. The experiments are performed for $E_C$ equal to 5000 kJ.

2. For the second circuit (first circuit + cable-2, as presented in Figure 2.4), we measured the circuit's current ($i_2$), see Figure 2.5b. The current were recorded using an oscilloscope Nicolet Sigma 30. More detailed information can be found in Chapter 1, which covers sensor uncertainties and specifications. The experiments are performed for $E_C$ equal to 5000 kJ.

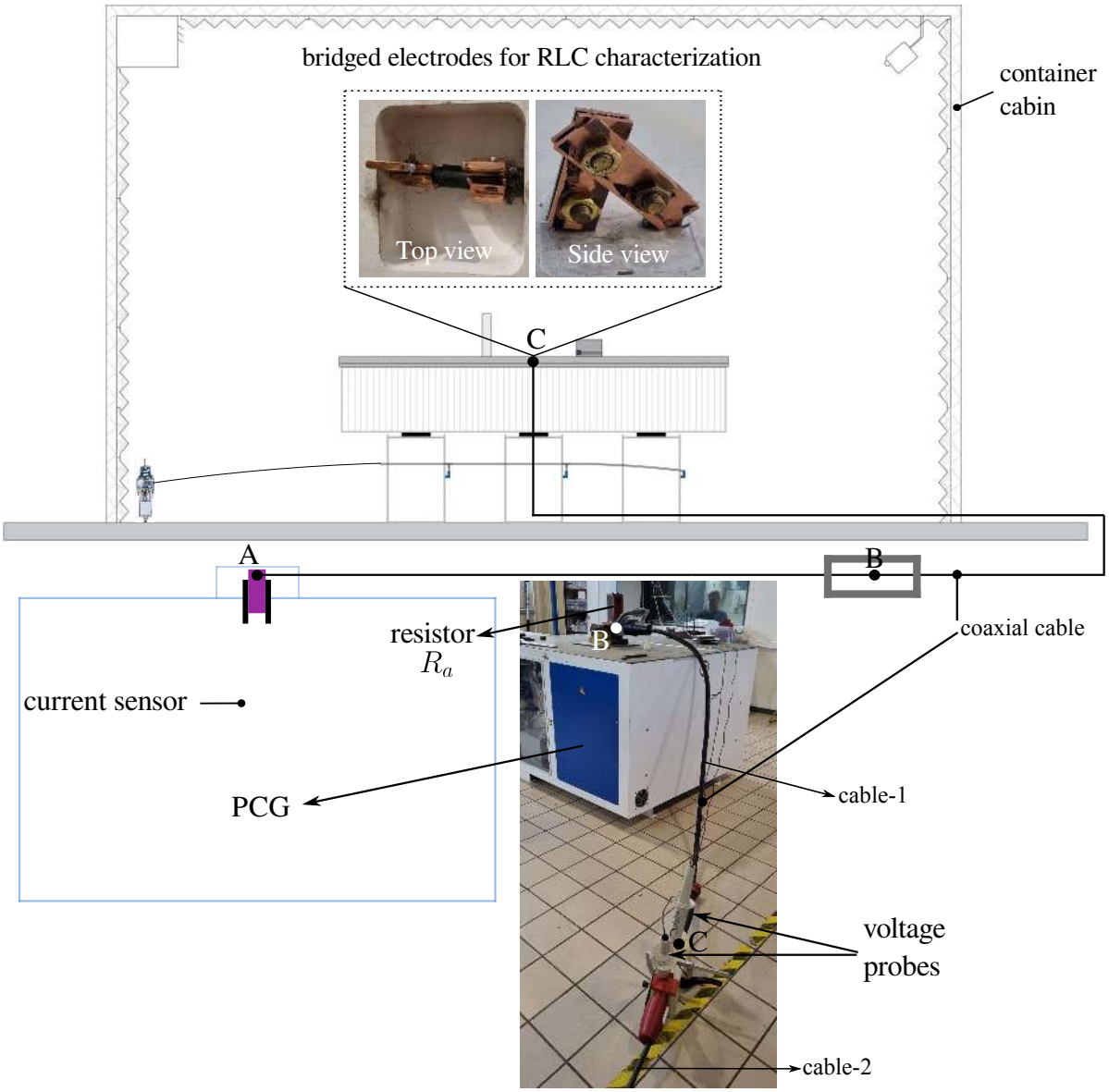


**Figure 2.4:** Experimental configuration of the PCG, cable connections, and current sensor.

Figure 2.5a show the evolution in time of the discharge current for first circuit. To ensure experiment repeatability, five measurements were performed. The consistent repeatability across the five experiments is evident (refer to Figure 2.5a). Furthermore, the current signals are synchronized to start from the same initial point at $t = 0$, where the black line serves as the trigger, as illustrated in Figure 2.5. The trigger signal signifies the moment of discharge initiation. However, as depicted in Figure 2.5, there's always a small delay of time which is around $\Delta t \approx 9$ $\mu$s, which is required for the ignitron switch to close and initiate the discharge.

The measurements include direct current (DC) offset is less than 0.2 kA (corresponding to 20 mV, given by the device's sensitivity 10 mV/kA). The linearity error of $\pm 0.05\%$ of the full-scale output, which in the case of the current sensor is equal to 300 kA. The linearity error is $\pm 0.1$ kA, and the positional accuracy is $\pm 0.5\%$ of the measured current value.

Therefore, the total cumulative error in the signal measured in this sensor is $\pm 0.5\% i_1 + 0.35$ kA.
Moreover, Figure 2.5b show the evolution in time of the discharge current (for circuit two). The repeatability for measurements are clear showing the validity of the acquisition system in terms of capturing signals. The current has a total cumulative error in the signal measured $\pm 0.5\% i_2 + 0.35$ kA.

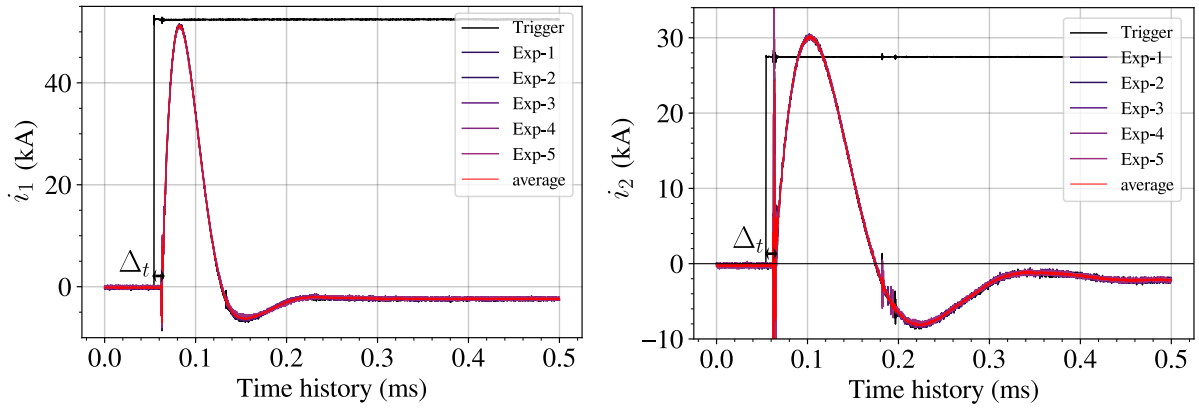


**(a)** Discharge current $i_1$

**(b)** Discharge current $i_2$

**Figure 2.5:** Evolution of the discharge current for circuit one (a), and discharge current for circuit two (b) as function of time.

### 2.4.1 Optimization of the circuit parameters

Based on the experimental results shown in Figure 2.5, we can observe that the underlying RLC circuit model is *under-damped*. Therefore, the equation that describe the current transient is Eq. (2.25). Here, for the sake of simplicity, we will focus on the average of the five experiments (see Figure 2.6), as all experiments are repeatable. Moreover, we cut the noises at the beginning of the signal. For solving the fitting of the circuit equation with the experimental measurements, we use the Python library Scipy (Virtanen et al., 2020), namely the `curve_fit` function, relying on the trust region reflective algorithm due to its robustness.

From first circuit we optimize three parameters $I_1 = \frac{U_1}{L_1 \omega_1}$, $\alpha_1$ and $\omega_1$ and from circuit two we optimize the following parameters: $I_2 = \frac{U_2}{L_2 \omega_2}$, $\alpha_2$ and $\omega_2$ ($\alpha = R/2L$, $\omega = \sqrt{\omega_0^2 - \alpha^2}$, and $\omega_0 = 1/\sqrt{LC}$) (see Table 2.1).

As we have the value of the stored voltage inside the capacitor $U_0 = 4.95$ kV, and from the optimized parameters, we calculate the effective values of the capacitance $C_n$, the initial value of the energy, $E_{Cn}$, the equivalent resistance, $R$ (it is the resistance $R_2$, which is the resistance of cable two and $R_1$), the equivalent inductance, $L$ (it is the inductance $L_2$, which is the inductance of cable two and $L_1$), the resistance, $R_1$ (it is the internal resistance of the generator, additional resistor resistance ($R_a$) and cable one resistance ($R_{\text{AB}}$)), and the inductance, $L_1$ (which is the internal inductance of the generator and the inductance of first cable $L_{\text{AB}}$). The coefficient of determination $R_i^2$ for the current, Eq.

(2.25) is 0.999 for both current transients.

The results from the optimization are summarized in Tables 2.2. Figure 2.6 compares the experimental measurements of the currents transient with the RLC circuit model obtained from the best-fitting. A very good agreement is found with mean values of $R_i^2$ greater than 0.999.

**Table 2.1:** Circuits optimized parameters.

| $I_1$ (kA) | $\alpha_1$ (ΩmH) | $\omega_1$ (rad/s) | $I_2$ (kA) | $\alpha_2$ (ΩmH) | $\omega_2$ (rad/s) |
|---|---|---|---|---|---|
| 143.8076 | 36.7035 | 44.4809 | 65.3047 | 14.1484 | 26.2846 |

**Table 2.2:** RLC parameters calculated based on the optimized parameters.

| $E_{Cn}$ (kJ) | $C_n$ (μF) | $R_1$ (mΩ) | $L_1$ (μH) | $R$ (mΩ) | $L$ (μH) | $R^2_{i_1}$ (-) | $R^2_{i_2}$ (-) |
|---|---|---|---|---|---|---|---|
| 4.767 | 389.165 | 56.805 | 0.773 | 81.601 | 2.883 | 0.999 | 0.999 |

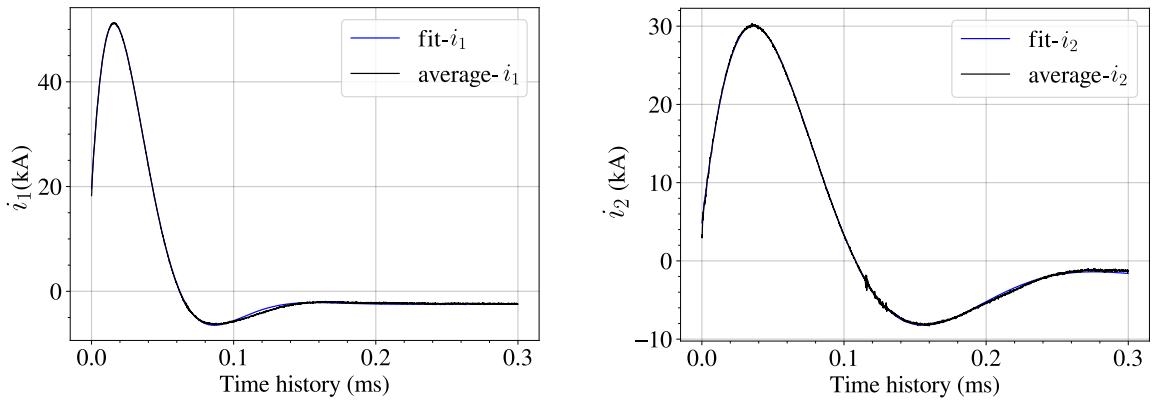


**(a)** $i_1$ **(b)** $i_2$

**Figure 2.6:** Discharge current for circuit one (a) and circuit two (b) obtained from the experiments and compared with the RLC circuit model with best-fitted parameters.

## 2.5 Shock wave generated by exploding aluminum wires

### 2.5.1 Physical processes during wire's explosion and shock wave generation

A typical exploding wire system, as shown in Figure 2.7(a), comprises a discharge circuit that incorporates a capacitor, denoted as $C$, a thin wire (see Figure 2.7(b)) of electrical resistance $R_W$ and inductance $L_W$, a resistor $R$, an inductor $L$, and an ignitron switch.

When a sufficiently large electric charge is discharged through thin wire (for example made of copper, tungsten, gold, aluminum, etc.), its temperature increases considerably and fast. This rapid temperature increase causes the wire to undergo phase transitions, and generate a pressure shock wave (see Section 2.4). This explosive process is accompanied by the emission of a bright flash of light and smoke (see Figure 2.8). More specifically, according to Duerksen (1972), the following phenomena take place in the course of the above process:

S1. During discharge, the developed current heats up the wire, due to ohmic heating, until melting (see Figure 2.7(b)). In other words the wire from solid becomes liquid.

S2. At melt, the current continues to flow through the wire, and the temperature increase further. As a result the wire expands in volume and transits from liquid to gas ("boiling stage"). However, this transition is not uniform across the length of the wire. More specifically, experimental evidence (Liu et al., 2019) shows the formation of onduloids (striations, as depicted in Figure 2.7(c)). At this stage, the apparent electrical resistance of the wire increase significantly, as the air between the onduloids is not a good conductor.

S3. Then, electrical (dielectric) breakdown occurs between the onduloids, and, thus, conductivity increases substantially (Figure 2.7(d)). Naturally, this stage is characterized by the appearance of electric arcs, i.e. of plasma, which marks the final phase transition in the system. The plasma expands rapidly during this stage due to its electrical conductivity.

S4. The previous stages are accompanied by the formation of a pressure shock wave that propagates outwards the wire.

The whole phenomena resembles to the phenomena of natural lightning but in a smaller scale (see Figure 2.8)!

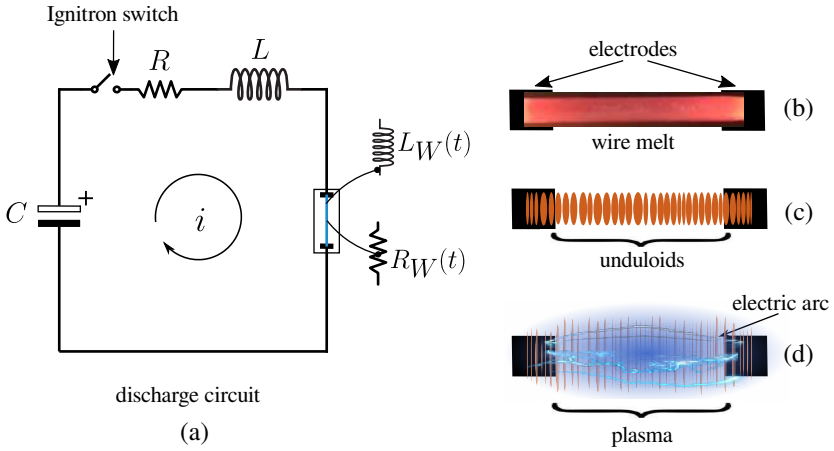


**Figure 2.7:** Exploding wire circuit (a) and stages of the explosion mechanism: (b) wire melt, (c) formation of onduloids, and (d) electrical breakdown and the appearance of electric arcs (plasma).

The above stages are documented in Liu et al. (2019). Specifically, an aluminum wire with a diameter of 100 $\mu$m and a length of 2 cm was placed inside a closed chamber

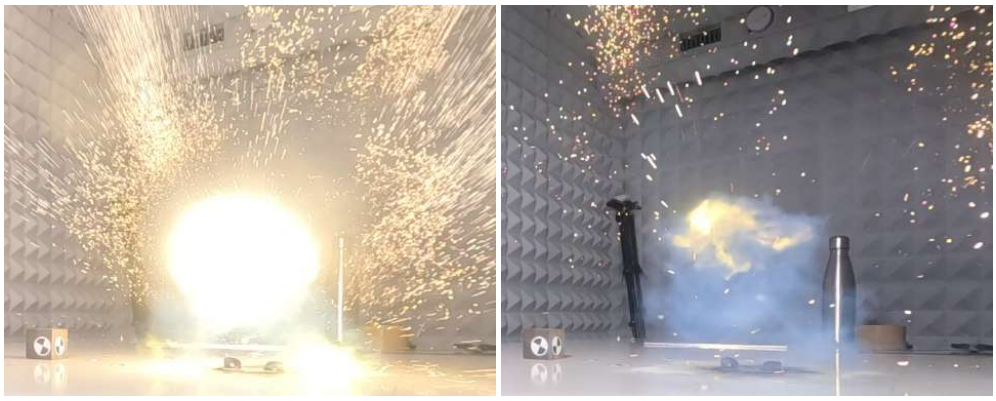


**Figure 2.8:** Explosion of exploding wire with spherical light at time $t = 12.5$ ms (a), and the dust produced at $t = 25$ ms (b), the images are captured by using GoPro11 with 240 fps and resolution 2704 $\times$1520 pixels.

filled with argon gas (argon gas is used to perform a controlled environment in terms of plasma generation), and laser shadowgraphs of the exploding wire were captured using a high-speed camera, as depicted in Figure 2.9.

We observe the formation of onduloids at time 376 ns (Figure 2.9(b), which becomes more pronounced at time $t = 743$ ns (Figure 2.9(c)). A shock wave is then formed around the wire, as evidenced by the sharp line of compressed air in Figure 2.9(d). Next, the onduloids become even more pronounced, the density of the materials across the wire becomes non-uniform as depicted in Figure 2.9(f) to 2.9(i), (see also Chittenden et al. (2000)) and the shock wave travels outwards.

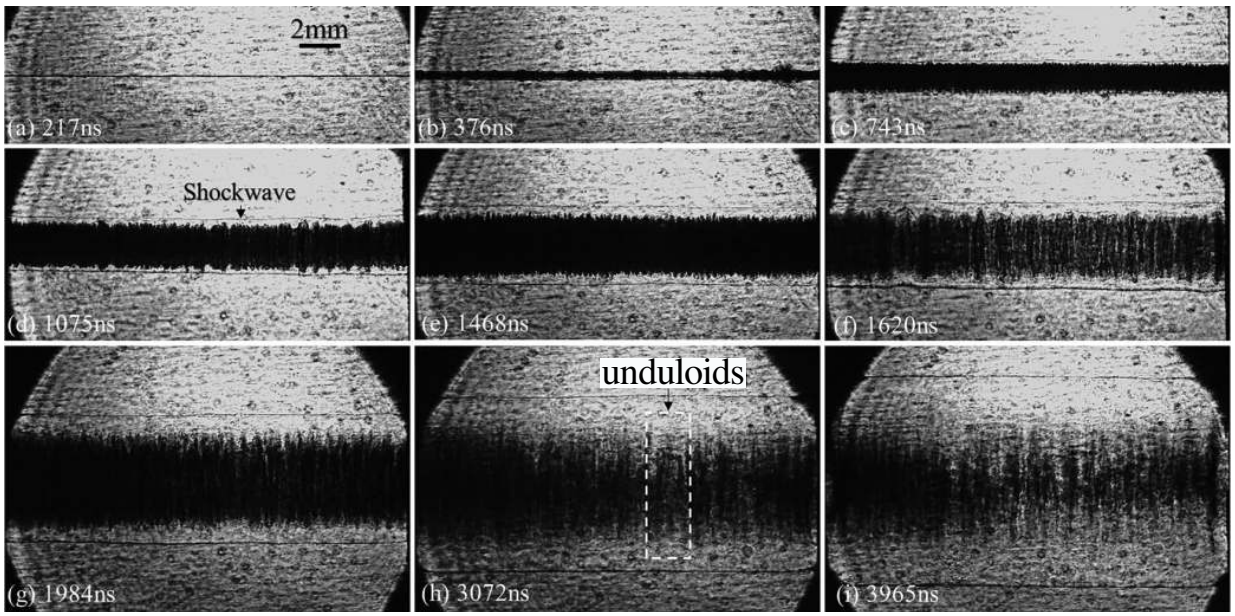


**Figure 2.9:** Laser shadowgraphs of exploding an aluminum wire under 15 kV charging voltage, at different time instances, adapted from Liu et al. (2019).

The diameter of the wire and the current density[1] play a substantial role in influencing the amount of energy dissipated into the wire and the rate at which the plasma expands (Tucker and Neilson, 1959; Liu et al., 2019). According to Zhao et al. (2013), the higher the amount of dissipated energy into the wire until the voltage peak that takes place at the end of stage 2 due to the increase of resistivity, the greater the rate of expansion of the plasma will be. Furthermore, thinner wires result in a more uniform expansion of the plasma along the wire's length, and therefore to higher plasma expansion rates (Chandler et al., 2002).

The plasma dynamics are also affected by the material of the wire. In our experiments, we utilize aluminum wires. Aluminum exhibits a relatively higher resistivity when compared to copper leading to higher energy dissipation. Gaining insights into the evolution of the wire's resistivity over time is important, as it provides a better comprehension of the intensity of the produced shock wave.

### 2.5.2 Estimation of temperature rise

The specific heat at constant strain is defined by the following equation

$$C_V = \frac{dq_W(T)}{dT}, \tag{2.32}$$

where $q_W$ is the heat mass density at a point in the wire, $T$ is the temperature, and $C_V$ is the specific heat per unit mass measured in the state of constant strain. In the following we assume uniform conditions over the entire mass of the wire (more detailed analyses exceed the scope of the Section).

The heat, $Q_w$, required to change the temperature of the whole wire by $\Delta T$ is equal to:

$$\Delta Q_W = \int_{m_W} \int_0^{\Delta T} \frac{dq_W(T)}{dT}\, dT = \int_{m_W} \int_0^{\Delta T} C_V\, dT = C_V m_W \Delta T, \tag{2.33}$$

where $\Delta Q_W = Q_W(T_2) - Q_W(T_1)$, $\Delta T = T_2 - T_1$, and $m_W$ is the mass of the wire.

Based on the first law of thermodynamics, and assuming that a part of the electric energy, $\Delta E_R$, flowing through the wire is transformed to heat that has been generated over the wire due to ohmic heating, the energy dissipated through the wire can be calculated as

$$\Delta Q_W = \chi \Delta E_R, \tag{2.34}$$

where $0 \leq \chi \leq 1$ is the coefficient of performance. For $\chi = 1$, the temperature increase is estimated as follows

$$\Delta T = \frac{\Delta E_R}{m_W C_V}. \tag{2.35}$$

In our case, $C_V$ cannot be considered constant due to the phase transitions that occur in the wire. For the sake of simplicity, we consider two phases solid and liquid, (Desai

[1] Current density refers to the amount of electric current passing through a unit area of the wire's cross-section. It is typically measured in amperes per square meter ($A/m^2$) and represents the concentration of electric current within the wire at a specific point in time during the discharge of current.

et al., 1984; Liu et al., 2019). The values of $C_V$ as a function of temperature are digitized from Liu et al. (2019) (see also Desai et al. (1984)) and are presented in Figure 2.10a. Using Eq. (2.35) and referring to Figure 2.10b, we calculate the energy dissipated in the liquid and solid phases under normal laboratory conditions ($T = 24°$) for a wire with a diameter of 0.6 mm, length 3.6 cm, and density 2.71 g/cm$^3$.

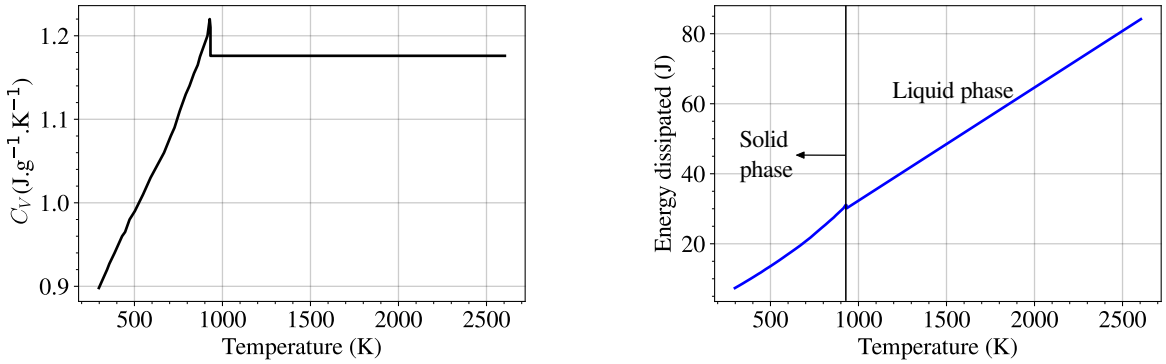


**(a)** Heat capacity **(b)** Energy dissipated

**Figure 2.10:** Specific heat per unit mass with respect to temperature (digitized from Liu et al. (2019)) (a) and energy dissipated (b) as function of temperature of an aluminum wire (wire length equal to 3.6 cm, diameter equal to 0.6 cm).

The thermal properties of aluminum wire are summarized in Table 2.3.

**Table 2.3:** Thermal properties of aluminum wire.

| **Parameters** | **Value** | **Reference** |
|---|---|---|
| Melting temperature $T_{melt}$ | 933 K | Yang et al. (2015) |
| Boiling temperature $T_{boil}$ | 2467 K | Leitner et al. (2017) |
| Heat capacity of liquid $C_{V-\text{liquid}}$ | 1.18 J g$^{-1}$ K $^{-1}$ | Yang et al. (2015) |
| Heat capacity at $T = 24°$ | 0.9 J g$^{-1}$ | Yang et al. (2015) |

### 2.5.3 Identification of the wire's characteristics

In this Section, we identify the inductance $L_W$ and we estimate the evolution of the electrical resistance $R_W$ of the wire during the discharge (Figure 2.7(a)). The inductance of the aluminum wire is approximated using the simplified formula by Robert et al. (2010),

$$L_W = \frac{\mu_0 l_W}{2\pi}\left[ln\left(\frac{2l_W}{r}\right) - \frac{3}{4}\right] \tag{2.36}$$

where, $\mu_0$ is the permeability of free space (referred to as the air permeability), equal to $4\pi \times 10^{-7}$ H/m, $l_W$ is the wire length, and $r$ is the wire radius.

In our experiments we used very thin aluminum wire's with $l_W = 3.6$ cm and $d = 0.6$ mm. Using Eq. (2.36), the wire's inductance ($L_W$) is estimated equal to $3.406 \times 10^{-2}\mu$H, which is two order of magnitude lower than the inductance of the discharge circuit ($L = 2.883\,\mu$H,

see Section 2.4). Therefore, we will neglect it as $L_W \ll L$.

To identify the wire's resistance $R_W$, we conducted three experiments in which we measure the current and voltage transients at the wire's extremities (see Figure 2.11). It is worth noting that all three experiments demonstrated excellent repeatability. In the following, we will use only the data from one of the three experiments (Ex-1). Both signals (current and voltage) are synchronized and the green line in Figure 2.11 shows the synchronization of the trigger signal. The trigger signal signifies the moment of discharge initiation. However, as depicted in Figure 2.11, there's always a small delay of time which is around $\Delta t \approx 9$ $\mu$s, which is required for the ignitron switch to close and initiate the discharge.

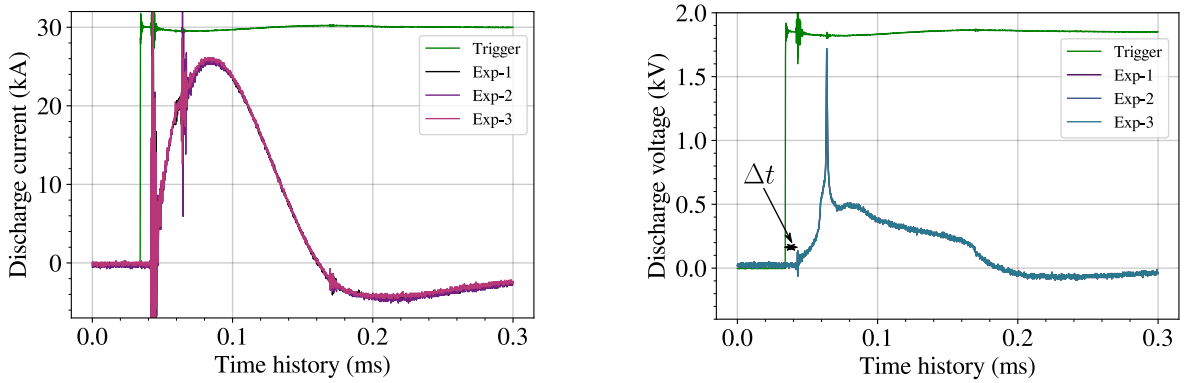


**(a)** Measurements of discharge current

**(b)** Measurements of discharge voltage

**Figure 2.11:** Evolution of the discharge current (a) and voltage (b) measured at wire's extremities.

In Figure 2.12a we plot together the current and the voltage as function of time. We identify point 1, marking the initiation of the discharge (see Figure 2.12a). Between point 1 and point 2, melting takes place, as explained in Section 2.5.1 (refer to Figure 2.7(b)). Point 2, is associated with the voltage peak and it is followed by electrical breakdown and the formation of plasma, as previously detailed (see Figure 2.7(c)). The electrical breakdown is followed by an increase in the current flow, reaching current peak at point 3. The creation of the shock wave accompanies the above two stages, i.e. points 2, 3.

In Figure 2.12b, we present the current, $i$, as function of the voltage, $u_W$. The slope of the $i.u_W$ plot represents the conductance ($G$) of the wire, while the resistance is the inverse of the slope ($R_W = 1/G$).

We observe that the phenomena taking place during stage 2 are very fast to capture with the sampling rate of our measuring devices, which is already quite high (10 MS/s). The noise is also significant. Therefore, we interpolate both signals (current and voltage) to smooth out irregularities and noise. We perform this interpolation using the Python library Scipy (Virtanen et al., 2020), specifically utilizing the `UnivariateSpline` function, which employs a one-dimensional cubic spline interpolation algorithm. The interpolated current and voltage are presented in Figure 2.13, and the smoothed $i.u_W$ plot is shown in Figure 2.14b.

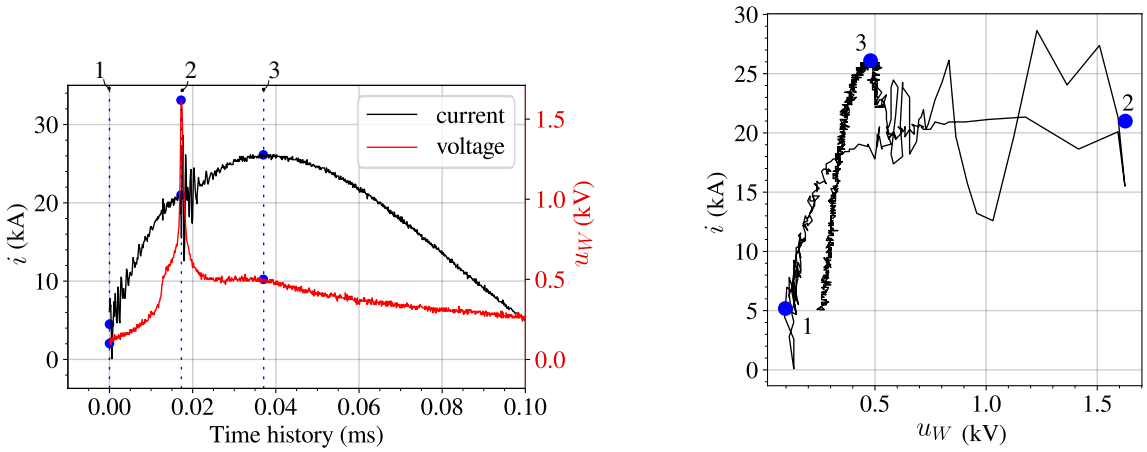


**(a)** Discharge current/voltage **(b)** $i$–$u_W$

**Figure 2.12:** Evolution of the discharge current/voltage (a) and $i.u_W$ plot (b).

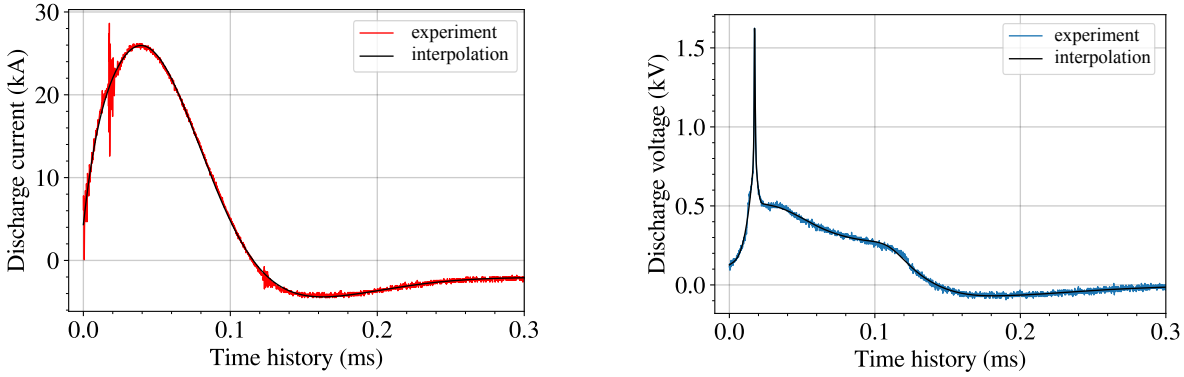


**(a)** Current **(b)** Voltage

**Figure 2.13:** Evolution of experimental and interpolated current (a) and voltage (b).

As previously discussed in Section 2.5.1, at the beginning of the discharge, conductivity progressively increases until it approaches the boiling stage, stage S2. At point 1 $G_1a = 63.636$ A/V ($R_{W1a} = 0.016\ \Omega$). Subsequently, conductivity decreases and resistance increases reaching $G_{1b} = 12.8$ A/V ($R_{W1b} = 0.078\ \Omega$) and then $G_{1c} = 0.668$ A/V ($R_{W1e} = 1.497\ \Omega$). It is worth pointing out the progressive decrease of the conductivity at stage S2, point 2. In particular, Figures 2.16b, 2.17 illustrate that between points 1 and 2, the wire enters its melting stage, followed by boiling stage and the formation of onduloids at voltage peak.

After point 2 there is a substantial increase in conductivity (decrease in resistance) occurring between points 2 and 3 as expected due to the electrical breakdown and plasma expansion (stage S3). This change is reflected in the conductivity values: $G_{2a}$ = -1.240 A/V ($R_{W2a}$ = -0.806 Ω), $G_{2b}$ = -23.333 A/V ($R_{W2b}$ = -0.0428 Ω), and $G_{2c} = -80.000$ A/V ($R_{W2c}$ = -0.012 Ω). This stage is characterized by a notable increase in the current flow (refer to Figure 2.12a).

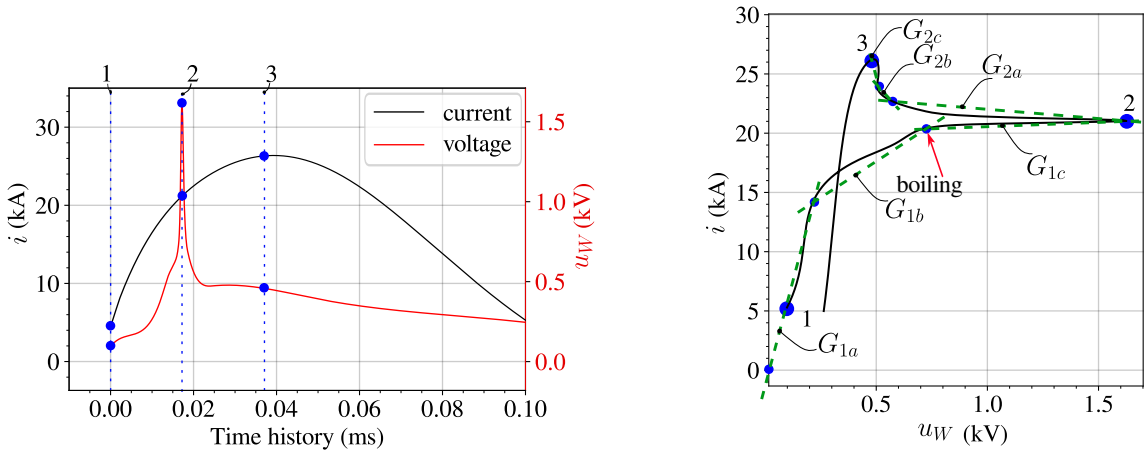


**(a)** Discharge current/voltage

**(b)** $i$–$u_W$

**Figure 2.14:** Evolution of the discharge current/voltage (a) and $i.u_W$ plot (b) between the wire's extremities.

The resistance of the wire is calculated as

$$R_W(t) = \frac{du_W(t)}{di(t)}. \tag{2.37}$$

The above derivative is calculated using the interpolated data of Figure 2.12a, utilizing the `DerivativeCentralSpline` function. This method approximates the derivative of $u_W(t)$ with respect to $i(t)$ using the central finite difference scheme, which considers the values of both functions $u_W(t)$ and $i(t)$ at neighboring points to estimate the rate of change between these functions.

Based on studies by Liu et al. (2019); Desai et al. (1984); Richardson et al. (2014), the resistivity of aluminum wire at $T = 20°C$ is determined to be $2.82 \times 10^{-8}\Omega$. Assuming a uniform resistivity along and across the aluminum wire (for thin wire), the initial resistance is equal to $0.0036\Omega$. This value was confirmed using an ohmmeter (M210) to measure the wire's resistance, yielding $R_W = 0.0036\Omega$. It's important to note that the resistance measured at point 1, denoted as $R_{W1}$, equals to $0.0025\Omega$, which is close to the value we

measured using the ohmmeter. This difference is attributed to the fact that we didn't start the derivation of the current and voltage at point zero (due to the noises at the beginning of the signals).

Figure 2.15 presents the calculated resistance over time. As expected, an increase in resistance occurs from point 1 to point 2, reaching its peak at point 2 ($R_{W2} = 1.726, \Omega$). Subsequently, from point 2 to point 3, there is a decrease in the resistance, until zero at point 3 electrical breakdown (see Figure 2.15).

The negative resistance observed here is a result of the highly non-linear phenomena that occur between points 2 and 3. In such cases, the relationship between voltage and current can become non-ohmic. In other words, as the current increases, the voltage decreases, leading to a negative (apparent) resistance (see Figure 2.12a). Furthermore, it is worth pointing out that the system is open, allowing the energy from the magnetic field and the plasma zone around the wire to influence the system, resulting in apparent negative resistance, $R_W$.

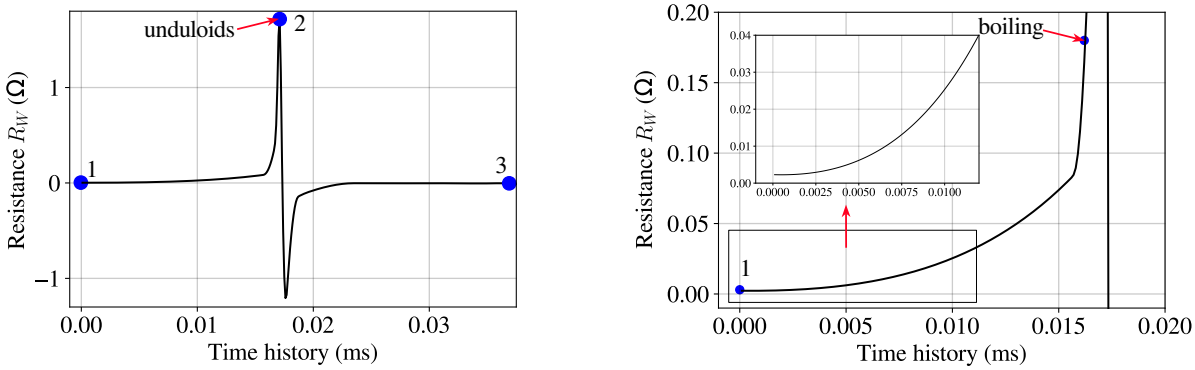


**Figure 2.15:** Evolution of the aluminum wire resistance as function of time (ms).

The power and energy dissipation in the aluminum wire are computed using Eq. (2.4) and Eq. (2.5), respectively. Figure 2.16 illustrates the evolution of the power and energy dissipated as functions of time. According to the calculation of the dissipated energy we expect that at $t = 0.0162$ ms we have the boiling stage, as demonstrated in Figure 2.16b, and at time $t \approx 0.005$ ms we estimate the melting of the wire (we can also see this in Figure 2.17).

Our experiments show the connection between the dissipated energy and the raised temperature during explosion. Indeed, Figure 2.17 presents the estimated temperature variation over time. Notably, aluminum has a melting temperature of approximately 660 °C (equivalent to 933.45 K), while its boiling temperature is 2470 °C (or 2743.15 K). At point 3, the temperature can reach as high as 12000 K. It's important to note that this is a rough estimation of the temperature developed during explosion due to the specific heat capacity ($C_V$) variation and underlying complex phenomena that take place. However, the estimated temperature can provide an idea of how temperature is evolving in the wire.

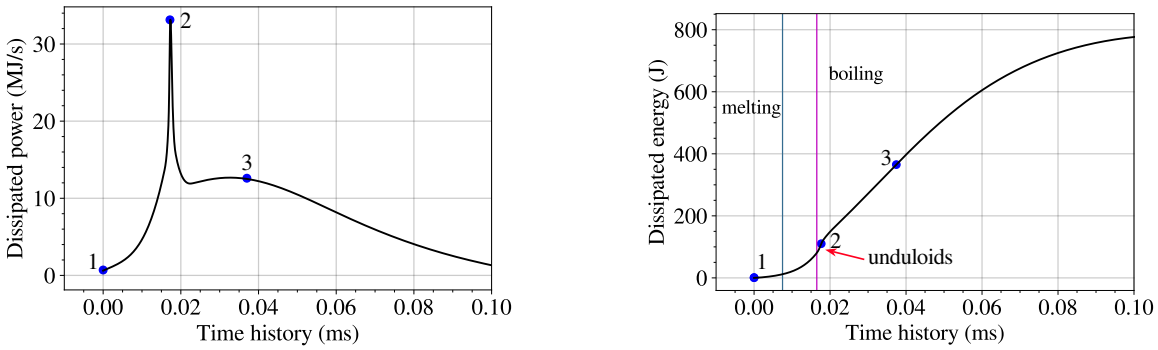


**(a)** Power dissipated (MJ/s)

**(b)** Energy dissipated (J)

**Figure 2.16:** Evolution of dissipated power (a) and dissipated energy (b) as function of time.

## 2.6 Concluding remarks

In this chapter, we analyzed the electric circuit system and the phenomena associated with the formation of shock waves. The equations of current and voltage of an RLC circuit are recalled. Then, the electrical parameters are identified through fitting the current measurements with the current equation. We detailed the four stages preceding blast wave formation: current discharge and wire melting, onduloid formation, electrical breakdown and appearance of electric arcs, and pressure shock wave formation. The wire inductance $L_W$ was identified to be negligible compared to the discharge circuit's inductance ($L = 2.883$ $\mu$H). The electrical resistance $R_W$ of the wire reached a maximum value of 1.726 $\Omega$ at stage S2, with energy dissipation in the aluminum wire estimated at around 800 J and a temperature rise during discharge estimated to reach 12000 K.

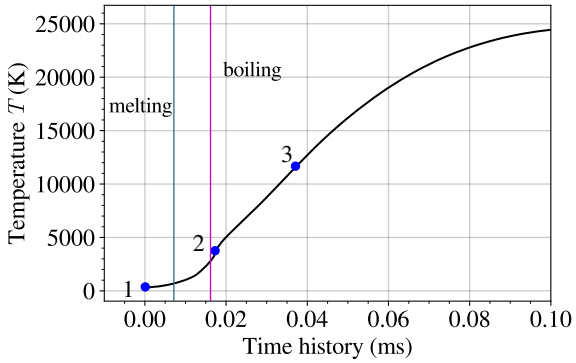


**Figure 2.17:** Estimated variation of temperature in the aluminum wire as function of time.

# Part II

# Analysis of the blast loads and validation of the scaling laws

# Chapter 3

# Analysis of the exploding wire explosive source

*Chapter 2 presented an in-depth exploration of the electric parameters, model derivation, and underlying mechanisms governing the mechanism of the exploding wire. This foundational knowledge is crucial for understanding the explosion load and subsequent structural responses. In the current chapter, we characterize the blast loading stemming from the detonation of exploding wires as well as the resulting blast parameters and, namely, the overpressure peak, impulse, arrival time, and time duration of both the positive and negative phases. Next, we focus on identifying the equivalence of the explosive source with standard high explosives, namely TNT. A comparison is made between exploding wire and other high explosive sources (C4, TNT, etc.) and finally we analyze the shape of the shock wave to gain insights into how pressure varies at different angles and distances.*

## 3.1 Introduction

The characterization of the parameters describing the blast loading, including overpressure, impulse, and time evolution that result from the detonation of an explosive is crucial for studying the dynamic response of a structure. For this, empirical or semi-empirical models (Kingery and Bulmash, 1984) are often used, mostly considering TNT as the reference explosive source.

Different explosive sources can however lead to different blast parameters even for the same explosive mass (Grisaro et al., 2021). In such scenarios, an equivalent TNT mass ($m_{\mathrm{TNT}}$) is established such that it delivers identical blast load parameters at the same distance $D$ with the considered mass of the explosive (for an extensive review, we refer to Xiao et al., 2019). The TNT is historically used as a reference due to its well-established explosive properties and consistent behavior. Furthermore, many experimental data are available concerning blast waves arising from the detonation of TNT. In our experiments, we resort to using exploding wires as explosive sources, thus it is interesting to characterize the equivalency that exist between the resulting loads with those arising from the detonation of an equivalent TNT explosive weight. In so doing, we start by defining the TNT Equivalence Factor (EF), namely

$$EF = \frac{E_{\mathrm{TNT}}}{E_{\mathrm{EW}}}, \tag{3.1}$$

where $E_{\mathrm{TNT}}$ and $E_{\mathrm{EW}}$ are, respectively, the internal energy associated with the detonation

of a mass $m_{\text{TNT}}$ of TNT and the one associated with the detonation of the exploding wire.

Determining the TNT equivalent factor is not trivial, since it depends on a variety of parameters including the nature of the explosive (Formby and Wharton, 1996; Dewey, 2005; Kleine et al., 2003), the selected equivalency parameter (peak overpressure, energy, impulse, etc.) (Grisaro et al., 2021; Shin et al., 2015), the standoff distance (Esparza and Edward, 1986; Xiao et al., 2020; Chiquito et al., 2019), the burst type (free air or surface burst), the measurements (field or laboratory tests), the confinement (casing effect, internal blast events), and the charge shape (spherical, hemispherical, cylindrical, cubic, etc.) (Departments of the Army, the Navy, and the Air Force, 1990).

In addition, the time histories of blast loads generated by different explosives are in general different. Even if the peak pressures may coincide, the shock wave time history, impulse, or the arrival and duration of secondary shocks can considerably differ. Each of these blast parameters can be used to determine a TNT equivalence, leading to different TNT equivalent factors (Xiao et al., 2019). It is therefore important to specify which parameter is used to identify the TNT equivalent factor and how it varies with standoff distance (Sochet, 2010; Sochet and Maillot, 2018).

Herein, we first present the experimental setup employed to measure the incident overpressure due to exploding wires' detonation. Experimental repeatability, sampling rate, and uncertainties are then discussed. Then, we present the overpressure measurements at different standoff distances $D$ and due to several stored energies $E_C$. Based on these results, we compute and show the incident impulse, the overpressure peak, and other blast load parameters, including the speed of the primary shock waves, as function of both $D$ and $E_C$. Particular attention is also devoted in characterizing the shape of the incident blast wave, which is confirmed to be hemispherical (see also Chapter 1).

The dependency of the incident impulse and pressure on the explosive type and shape is then studied. A comparison is made between exploding wire and other high explosive sources. Finally, the TNT equivalent factor based on the knowledge of the incident peak overpressure and the incident impulse is provided. These results enable to shed light on the equivalency of our exploding wire source with commonly adopted solid explosives and, in particular, TNT.

## 3.2 Experimental configuration

We are interested in measuring the incident blast wave arising from the detonation of an exploding wire. To this end, we use a 6233A0050 pencil probe (pressure) sensor, which is positioned on the optical table at a distance $D$ (standoff distance) from the exploding wire and its eventual motion is prevented with the use of tape. The configuration presented in Figure 3.1 enables the generation of various blast waves based on the desired scenarios. Details about the sensor and the data acquisition system TraNET FE 404 are given in Chapter 1.

Notice that, in all scenarios presented hereinafter, an aluminum foil is used to shield the sensor from thermal transients, which would result in non negligible spurious negative incident pressures (for more details, we refer to Appendix D).

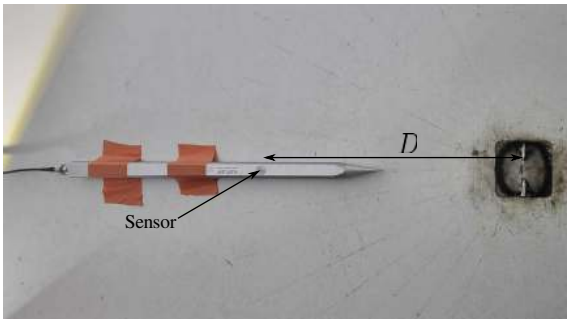


**Figure 3.1:** Experimental setup of the pencil probe sensor 6233A0050 placed on the optical table, at distance $D$ from the explosive source.

## 3.3 Experimental results

Following the aforementioned setup, we conduct a total of 90 experiments to adequately capture the time history of the blast loading at varying of both the standoff distance and the (capacitor) stored energy. The pencil probe presented above enables us to record with high accuracy the time evolution of the incident overpressure ($P_s$).

### 3.3.1 Analysis of the signal

The first step is to verify that the recorded signal accurately represents the intended shock wave phenomena. Figure 3.2 presents the time evolution of the incident overpressure $P_s$ for three identical tests in order to demonstrate the repeatability of our experimental setup and platform. In this case, the pressure measurements are conducted using a wire of diameter equal to 0.6 mm and length equal to 3.6 cm. The pencil probe is at a standoff distance $D$ equal to 30 cm and the energy stored in the capacitor is 5 kJ.
It is worth recalling, as previously mentioned in Chapter 1, that the measurement uncertainties in the pencil probe are: (a) acceleration sensitivity ± 200 Pa/g, equivalent to ± 0.2 Pa for $g = 1$, and (b) linearity error $\pm 0.58\%$ of the full-scale output (200 kPa) corresponding to an error of $\pm 1.160$ kPa. The total cumulative error of the pencil probe is thus $\pm 1.36$ kPa.
Throughout the experiments, we record overpressure signals at a sampling frequency equal to 5 MHz – that is, 5000 points are recorded at every 1 ms. Figure 3.2b compare the sampling frequency with the temporal variation of the overpressure signal. Note that the selected acquisition speed enables a high-resolution characterization of the overpressure time evolution as it is visible from the many recorded values during the arrival of the shock wave. This demonstrates that our setup allows for a robust evaluation of the overpressure peak and of the arrival time.

Whilst the shock wave impinges the pencil probe at 0.6 ms, notice the presence of a non-zero signal measurement well ahead of the arrival time. This takes place at time $t_1$ (refer to Figure 3.2a). In order to verify that such a signal corresponds to eventual vibrations of the optical table at the moment of the detonation of the exploding wire[1], we repeated the same experimental test but changing the location of the pencil probe. More precisely, the latter was fixed above the table, thus avoiding any propagation of

[1]Indeed, the sound speed through the optical table is much larger than that of the surrounding air, assumed at ambient temperature. This implies that sound propagates much faster through the table and it thus might induce oscillation in the pressure measurements well before the arrival time ($t_A = 0.6$ ms).

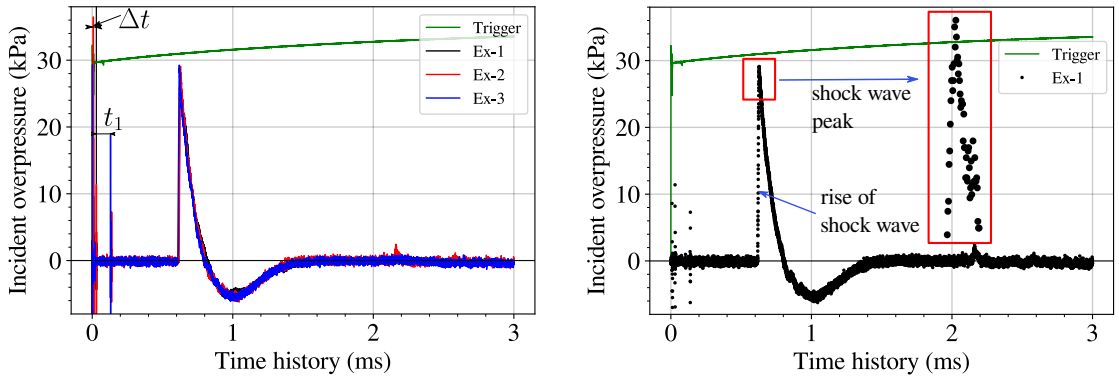


**(a)** $P_s$ repeatability **(b)** $P_s$ points

**Figure 3.2:** Time evolution of the incident overpressure $P_s$ for three identical experiments (a) and sampling frequency for one of the three experiments (b). The signal corresponds to a standoff distance of 30 cm and an energy of 5 kJ.

vibrations through the pressure transducer (see Figure 3.3). The time evolution of the incident overpressure for this second scenario is presented in Figure 3.4. We can observe the existence of a signal similar to the first scenario, cf. Figure 3.2. Also notice that the overpressure peaks in Figure 3.2a and 3.4 are different. As a result, the analysis does not confirm the cause of the early non-zero signal as provoked by eventual induced vibrations of the optical table.

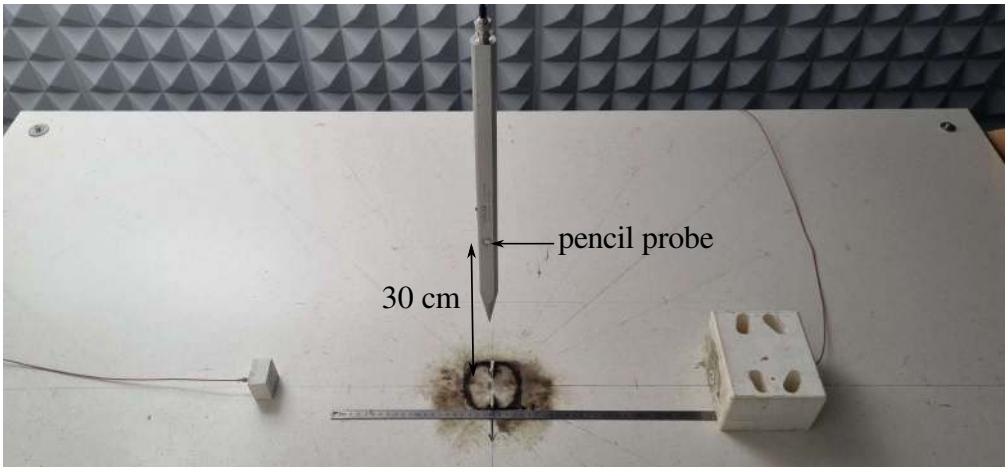


**Figure 3.3:** Experimental setup of the pencil probe 6233A0050 placed above the optical table at distance $D$ 30 cm.

However, by further inspecting the temporal evolution of the pressure signal with that of the electric current, we can infer the origin of the presence of the initial spike in the overpressure time history. Figure 3.5 shows both the current and the overpressure, with a zoom over the region where the apparently spurious signal is located. It can be observed that the peaks on the pressure measurements coincide with the oscillations of the current measurements, indicating that they are most probably linked by electromagnetic noise. The same conclusion can be drawn for the signal measurements observed between 0 and 0.2 ms (Figure 3.2a). In the following, both these early signal measurements are neglected as they are considered to originate from electromagnetic noise/oscillations and do not

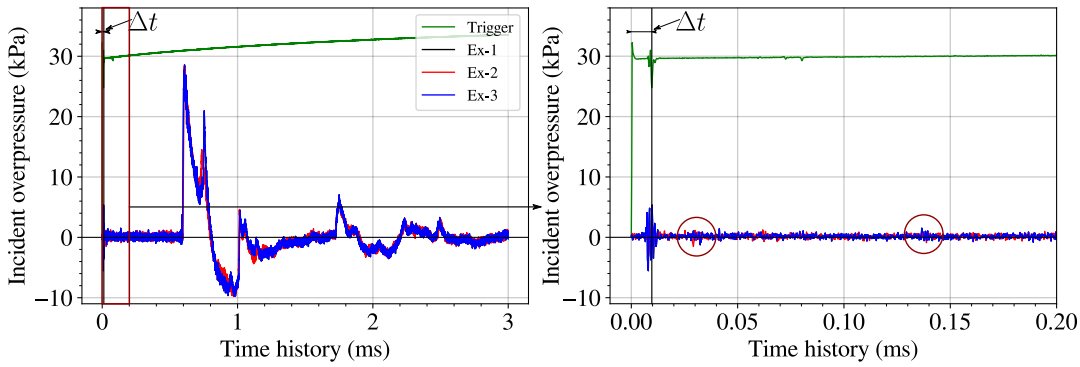


**Figure 3.4:** Evolution of the incident overpressure $P_s$ as function of time, at $D$ 30 cm, for wire diameter 0.6 mm, a wire length 3.6 cm, and an energy level of 5 kJ.

affect the following analysis. Furthermore, a fragment flying at supersonic speed passing above the sensor could also result in such sharp peaks. Faster camera imaging could help answer this question.

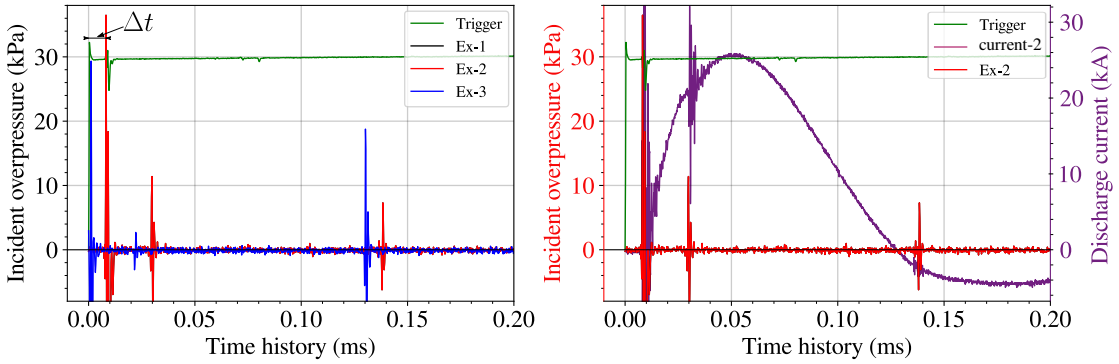


**(a)** $P_s$ at $D = 30$ cm

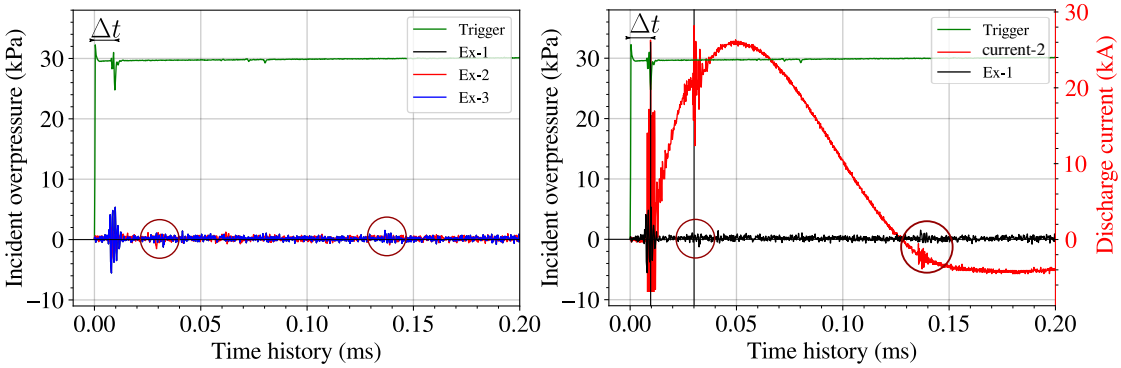


**(b)** $P_s$ at $D = 30$ cm

**Figure 3.5:** Zoom of the evolution of the incident overpressure $P_s$ for $t \in [0.0, 0.2]$ ms, for the probe pencil sensor fixed on the table (a) and above the table (b) and an energy level of 5 kJ.

### 3.3.2 Time evolution of the incident overpressure

Throughout all experiments, we use a wire diameter of 0.6 mm and length of 3.6 cm. The standoff distance is made varying between 20 and 70 cm, while the energy levels

span between 0.5 and 10 kJ. In parallel, to ensure the repeatability and robustness of the experiments and signal acquisition, we repeat the same, identical test three times (three distinct measurements). Figure 3.6 displays the time history of the incident pressure for several standoff distances, at varying of the energy level. All measurements are synchronized and start from a common reference point ($t = 0$ ms), which corresponds to the current discharge (cf. Chapter 2). From the results, we can notice that the larger is the stored energy, the higher is the amplitude of the incident pressure. Conversely, the larger the standoff distance $D$ is, the smaller is the value of the overpressure.

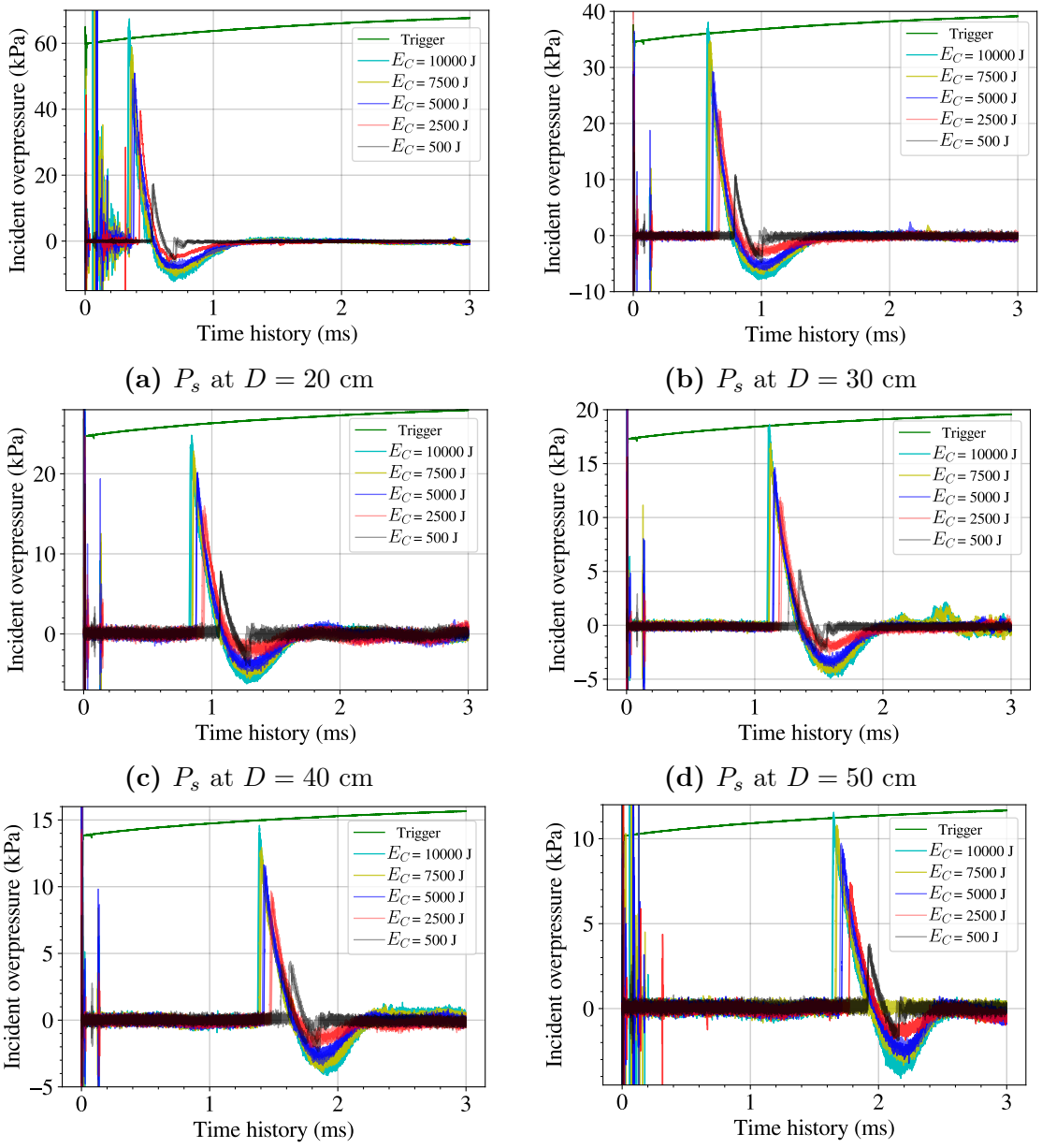


**(a)** $P_s$ at $D = 20$ cm **(b)** $P_s$ at $D = 30$ cm

**(c)** $P_s$ at $D = 40$ cm **(d)** $P_s$ at $D = 50$ cm

**(e)** $P_s$ at $D = 60$ cm **(f)** $P_s$ at $D = 70$ cm

**Figure 3.6:** Evolution of the incident overpressure $P_s$ at $D = 20$ cm (a), $D = 30$ cm (b), $D = 40$ cm (c), $D = 50$ cm (d), $D = 60$ cm (e) and $D = 70$ cm (f) as function of time for different energy levels.

## 3.4 Characterization of the explosive source

Herein, we characterize the explosive source by means of the associate impulse, overpressure peak, shock wave speed, and shape.

### 3.4.1 Blast parameters: overpressure, impulse, arrival time, and time duration

The time evolution of the incident impulse is presented in Figure 3.7. The impulse is computed by integrating in time the recorded incident overpressure based on Eq. (1.1), cf. Chapter 1).

Figure 3.8 presents the peaks of the incident overpressure (positive, $P_{so}$, and negative, $P_{so^-}$), the peaks of the incident impulse (positive, $i_{so}$, and negative, $i_{so^-}$), the arrival time ($t_A$), the positive phase duration ($t_o$), and the negative phase duration ($t_{o^-}$) for different energies $E_C$ and standoff distances $D$. As mentioned in Section 2.4, there's always a small delay time between the trigger and the current discharge. This delay is around $\Delta t \approx 9$ $\mu$s, and here we subtracted this $\Delta t$ from the arrival time, as this accounts for the estimated travel time of the shock wave occurring simultaneously with the current discharge.

We observe that as the energy $E_C$ increases, both $P_{so}$ and $i_{so}$ increase, while the time-related parameters ($t_A$, $t_o$, and $t_{o^-}$) decrease. Furthermore, as the standoff distance $D$ decreases, $P_{so}$ and $i_{so}$ decrease, while $t_o$, $P_{so^-}$, and $t_A$ increase. These trends demonstrate the influence of the energy and the standoff distance on the blast parameters.

Figure 3.9 presents the blast parameters as function of the scaled distance $Z_e$, which we define according to the cubic-root scaling introduced by Hopkinson (1915); Cranz (1925) in terms of the internal energy of the explosive source ($E$), namely

$$Z_e \equiv \frac{D}{E^{1/3}}. \tag{3.2}$$

It is worth noticing that the above definition assumes that the stored energy $E_C$ is entirely converted into the resulting internal energy of the blast ($E = E_C$). Despite the verification of the latter assumption is outside the scope of this work, the definition (3.2) enables a direct computation of the blast parameters and, as discussed hereinafter, of the TNT equivalency.

From Figure 3.9, we can observe that the blast parameters of the explosion resulting from the detonation of the exploding wire follows almost perfectly the cubic-root scaling proposed by Hopkinson (1915); Cranz (1925). In addition, the presentation of the parameters in terms of the scaled distance $Z_e$ enables a direct comparison of the source here employed with other explosives (cf. Section 3.5).

As $Z_e$ increases, both $P_{so}$ and $i_{so}$ decrease. This is an evidence that higher energy releases lead to higher values of pressure and impulse. However, the time-related parameters ($t_A$, $t_o$, $t_{Aw}$, and $t_{ow}$) increase as $Z_e$ increases.

Figure 3.10 presents the arrival time $t_A$ function for different standoff distances $D$ as measured during our experiments and compares it compared with measurements obtained for different explosive sources (Kleine et al., 2003; Winter, 2021; Hargather, 2013). Notice that the exploding wire setup yields similar values with those related to the detonation of 1 g of pentaerythritol tetranitrate (PETN).

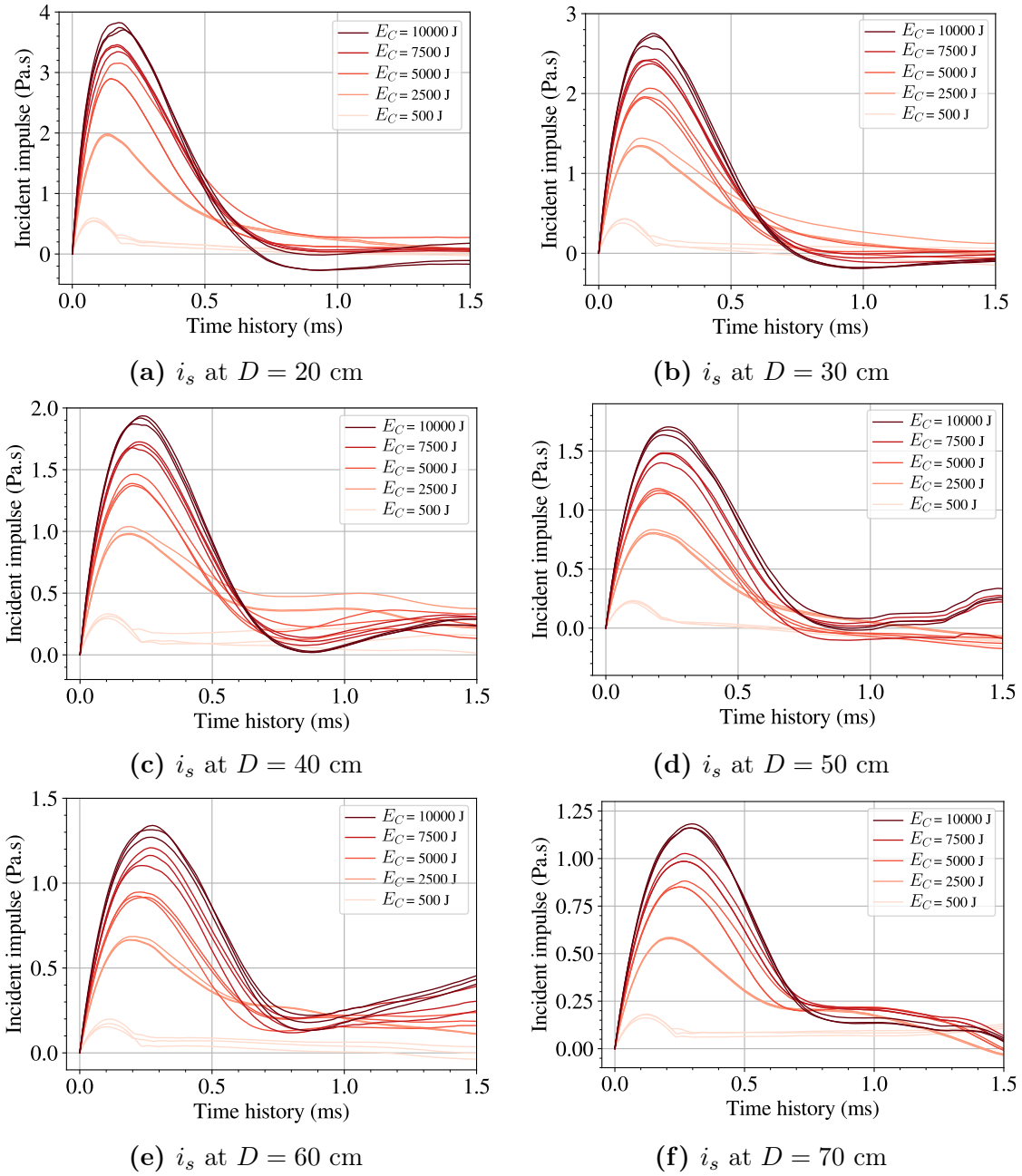


**(a)** $i_s$ at $D = 20$ cm **(b)** $i_s$ at $D = 30$ cm

**(c)** $i_s$ at $D = 40$ cm **(d)** $i_s$ at $D = 50$ cm

**(e)** $i_s$ at $D = 60$ cm **(f)** $i_s$ at $D = 70$ cm

**Figure 3.7:** Evolution of the incident impulse at $D = 20$ cm (a), $D = 30$ cm (b), $D = 40$ cm (c), $D = 50$ cm (d), $D = 60$ cm (e) and $D = 70$ cm (f) as function of time for different energy levels.

### 3.4.2 Shock wave speed

The shock wave speed $U_s$ at the shock front is computed as

$$U_s = D/t_A. \tag{3.3}$$

The variation of $U_s$ with respect to the standoff distance and stored energy levels is presented in Figure 3.11: the shock wave speed varies between a maximum of 817 m/s and a minimum of 370 m/s (supersonic regime – assuming the surrounding air is at constant and ambient temperature). The shock wave speed is found to decrease at increasing standoff distances – this is in agreement with all other high explosives. Moreover, the

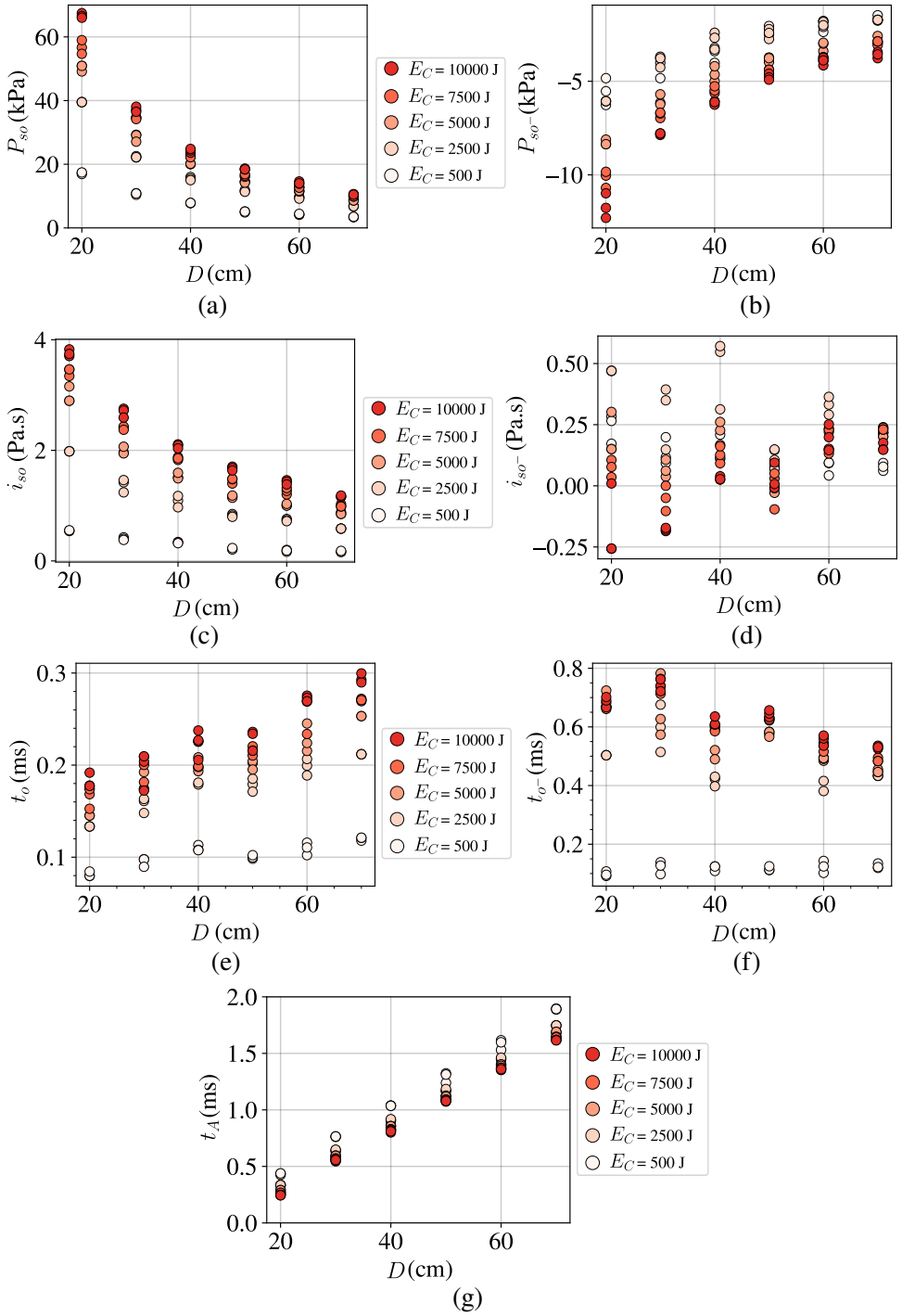


**Figure 3.8:** Evolution of $P_{so}$ (a), $P_{so^-}$ (b), $i_{so}$ (c), $i_{so^-}$ (d), $t_o$ (e), $t_{o^-}$ (f), and $t_A$ (g), for different energies $E_C$ and standoff distances $D$.

lower the energy, the slower the blast wave, and vice versa.

### 3.4.3 Shape of the shock wave

The discussion about the shape of the shock wave has been of interest from long time, back to the research conducted in Bennett (1958). In their study, the researchers used a mirror and high speed camera to record the light flash emanating from the exploding wire and con-

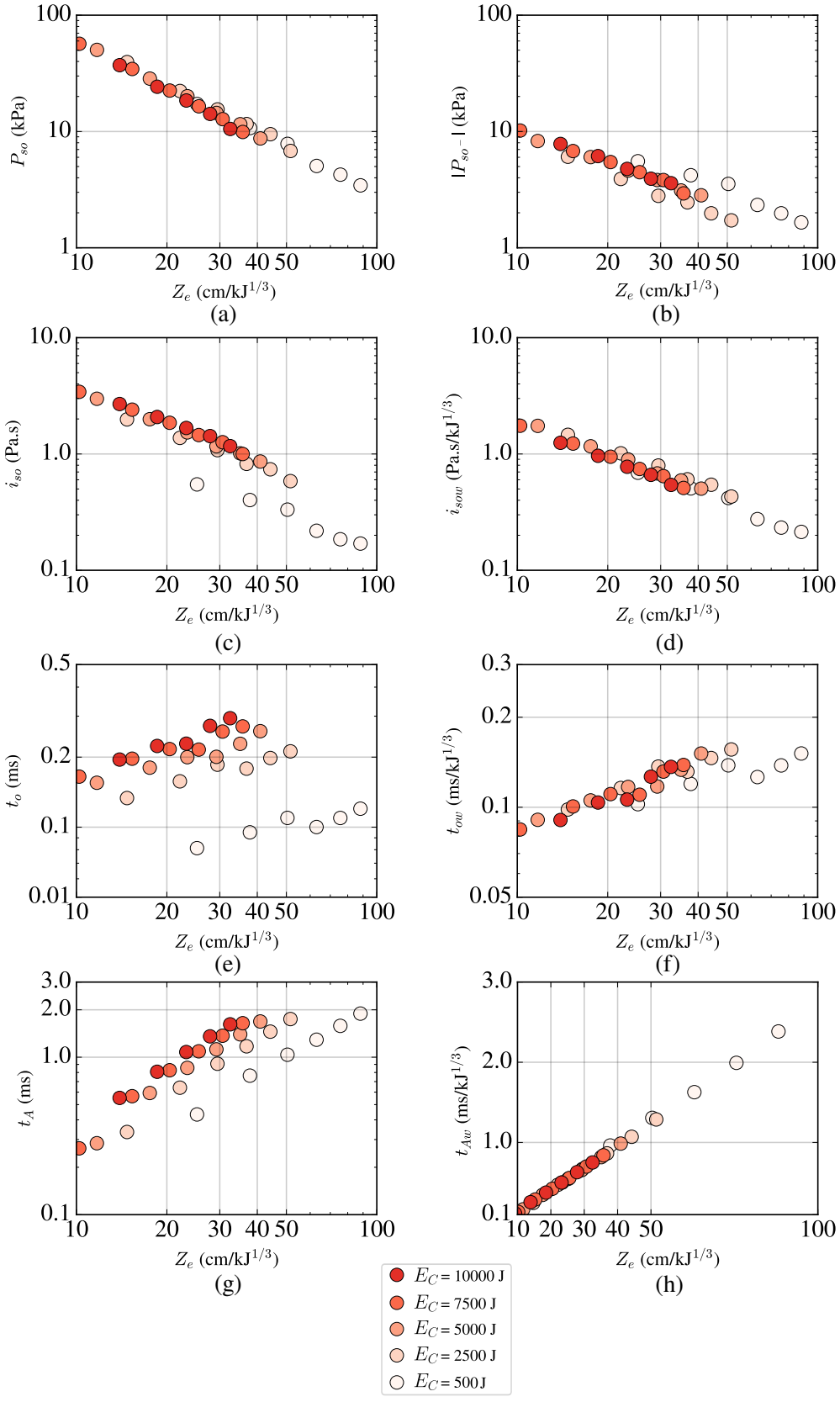


**Figure 3.9:** Evolution $P_{so}$ (a), $P_{so^-}$ (b), $i_{so}$ (c), $i_{sow}$ (d), $t_o$ (e), $t_{ow}$ (f), $t_A$ (g), and $t_{Aw}$ (h), for a wire diameter 0.6 mm, at varying of the scaled distance $Z_e$.

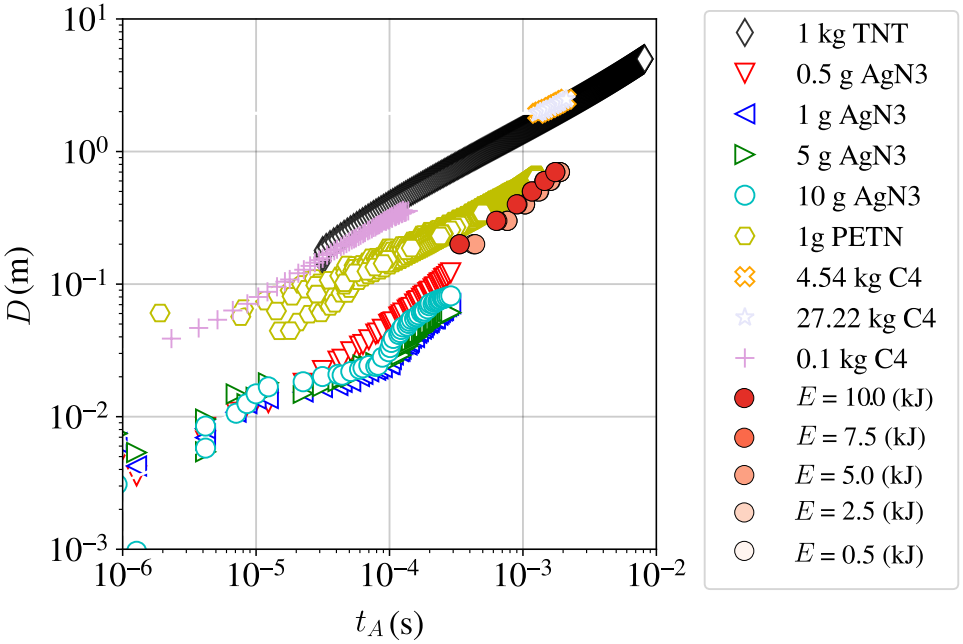


**Figure 3.10:** Comparison between different type of high explosive materials and our exploding wire experiments in terms of the standoff distance and the arrival time. The data related to AgN3 are digitized from Kleine et al. (2003), PETN is digitized from Winter (2021), C4 from Hargather (2013) and the TNT is calculated based on empirical formulas of Kingery and Bulmash (1984).

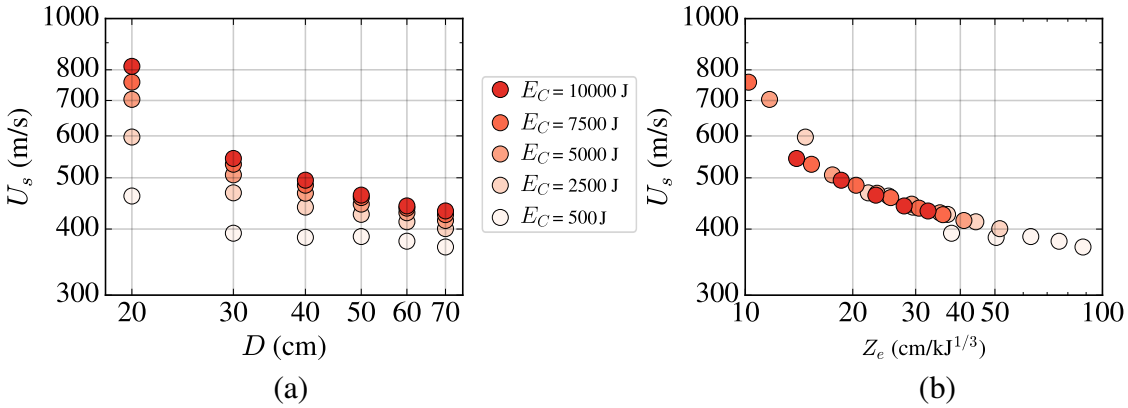


**Figure 3.11:** Shock wave speed $U_s$ as function of $E_C$ for different standoff distances $D$ (a), and scaled distance $Z_e$ (b).

cluded that the shock wave exhibited a cylindrical shape. In a more recent study presented by Mellor et al. (2020), the authors detailed the evolution of the shock wave shape using the Schlieren technique, capturing the transition from an ellipsoidal to a spherical expanding shock wave. They also noticed that the shock wave shape varies with the shock wave speed.

To identify the shock wave shape in our experiments, we measure the incident overpressure at two standoff distances (30 cm and 50 cm), varying the relative inclination between the pencil probe and the exploding wire, with a total of six different measurement angles ($\pm 0, 30, 60, 90°$) (see Figure 3.12. To increase the spatial resolution of the measurements, we use two pencil probes are used at a time. As discussed above, we always perform three

identical experiments for checking the repeatability of the measurements and the shock wave formation, see Figure 3.3, for $D = 30$ cm and $E_C = 5.0$ kJ.

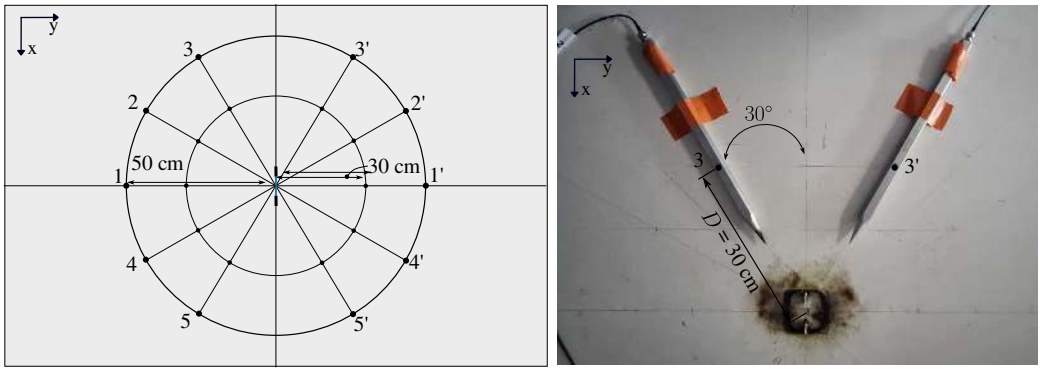


**Figure 3.12:** The installation plan for the pencil probes to identify the shock wave shape. Measuring the incident overpressure at two standoff distances (30 cm and 50 cm) and various angles (0, 30, and 60 degrees).

We conduct a total of ten experiments considering an energy level equal to 5 kJ. The time evolution of the incident overpressure is presented in Figures 3.13 and 3.14, for $D = 30$ and $D = 50$ cm, respectively. The peak incident overpressure values $P_{so}$ are presented in Table 3.1.

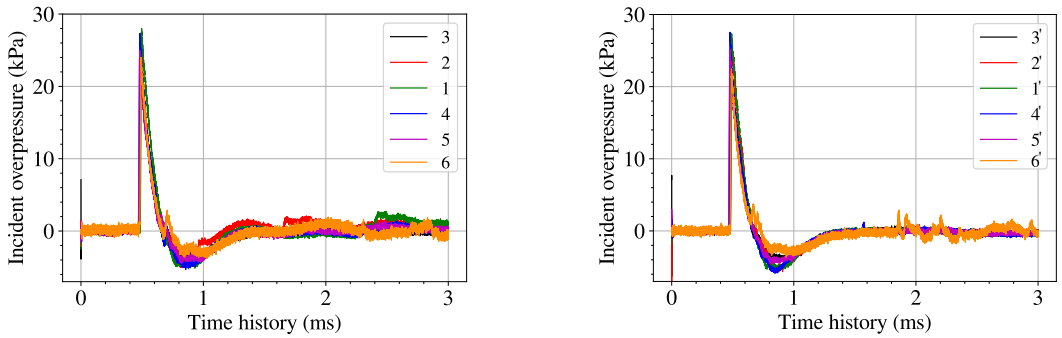


**(a)** $P_s$ at $D = 30$ cm (left) **(b)** $P_s$ at $D = 30$ cm (right)

**Figure 3.13:** Evolution of the incident overpressure $P_s$, from the pencil probe positioned at the left (a) and at the right (b).

Based on these measurements, we show in Figure 3.15, the spatial distribution of the incident overpressure peak ($P_{so}$) which can be interpreted as a good approximation of the shock wave's shape. More precisely, we can observe that for $D = 30$ cm the shock wave is almost elliptical, with the minor axis oriented as the exploding wire. This is thought to be caused by boundary effects taking place at the two edges of the wire and exacerbated by the presence of the two electrodes. Instead, for $D = 50$ cm, the shock wave is almost perfectly circular (hemispherical). This transition at increasing of the standoff distance is similar to what found by Mellor et al. (2020).

## 3.5 TNT equivalence factor

Based on the above analysis and identification of the blast parameters characterizing the explosion associated with the exploding wire, we present the calculation of the TNT

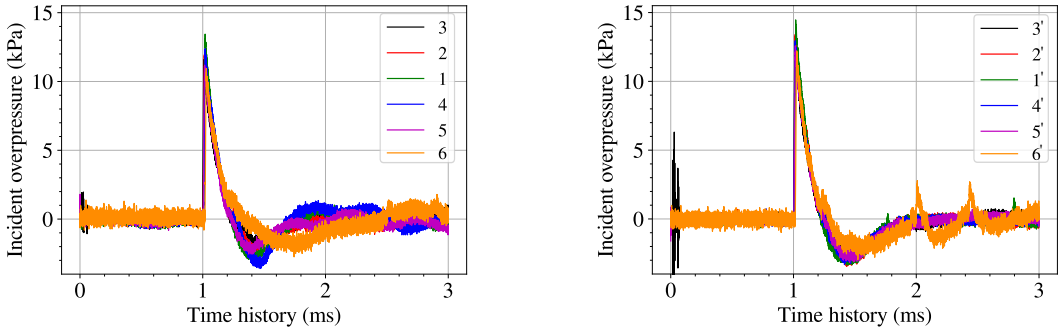


**(a)** $P_s$ at $D = 50$ cm (left) **(b)** $P_s$ at $D = 50$ cm (right)

**Figure 3.14:** Evolution of the incident overpressure $P_s$, from the pencil probe positioned at the left (a) and at the right (b).

**Table 3.1:** Incident overpressure measurements at different angles.

| | $D = 30$ cm | $D = 50$ cm |
|---|---|---|
| Location (#) | $P_{so}$ (kPa) | $P_{so}$ (kPa) |
| 1 | 27.99 | 14.64 |
| 1′ | 27.34 | 14.47 |
| 2 | 27.37 | 13.04 |
| 2′ | 26.68 | 13.40 |
| 3 | 24.51 | 12.63 |
| 3′ | 25.25 | 12.58 |
| 4 | 27.32 | 13.48 |
| 4′ | 27.54 | 12.95 |
| 5 | 25.00 | 12.19 |
| 5′ | 25.16 | 12.58 |
| 6 | 24.55 | 12.05 |
| 6′ | 23.28 | 12.45 |

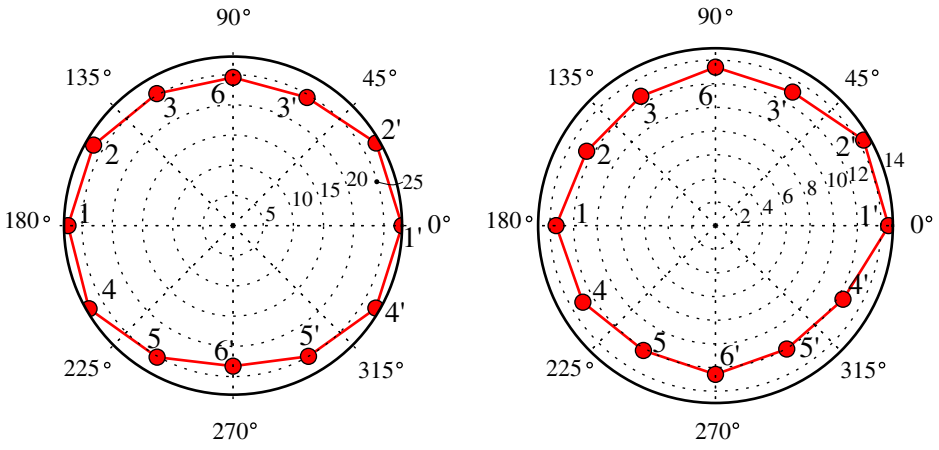


(a) 30 cm (b) 50 cm

**Figure 3.15:** Shock wave shape (elliptical) at distance 30 cm (a) and 50 cm (b).

equivalence factor $EF$ based on the peak incident overpressure and the peak scaled impulse. First, we calculate the equivalency factor $EF$ based one the equivalence of the incident overpressure between the exploding wire and TNT as following (Xiao et al., 2020):

$$EF_{p_{so}} = \left( \frac{Z_{e\mathrm{EW}}}{Z_{e\mathrm{TNT}}} \right)^3_{p_{so}^{\mathrm{EW}} = P_{so}^{\mathrm{TNT}}} \tag{3.4}$$

where the scaled distance of the exploding wire is $Z_{e\mathrm{EW}}$, calculated as presented in Eq. (3.2), and $Z_{e\mathrm{TNT}}$ is the scaled distance for the TNT. For computing $Z_e$ for TNT we assume that all internal energy of the TNT is released in the explosion and thus $E_{\mathrm{TNT}} = e_{\mathrm{TNT}} m_{\mathrm{TNT}}$, where $e_{\mathrm{TNT}} = 4.184 MJ/kg$ is the specific (per unit mass) internal energy of TNT.

Similarly, we also adopt the definition of the TNT equivalency factor based on the scaled incident impulse (Esparza, 1986) – that is,

$$EF_{i_{sow}} = \left( \frac{Z_{e\mathrm{EW}}}{Z_{e\mathrm{TNT}}} \right)^3_{i_{sow}^{\mathrm{EW}} = i_{sow}^{\mathrm{TNT}}}. \tag{3.5}$$

Both $P_{so}$ and $i_{isow}$ are presented in Figure 3.16, as functions of the scaled distance $Z_e$. The plot shows the experimental data (represented by dots) and the pressure and impulse calculated based on the empirical best-fit interpolations related to a hemispherical TNT explosion (Kingery and Bulmash, 1984; Masi, 2020). Notice how both the experimental values and the best-fit interpolations (for TNT) have almost the same tendency at varying of the scaled distance – this suggests, once more, that the cubic-root scaling is also valid for the exploding wire and not only for high explosives.

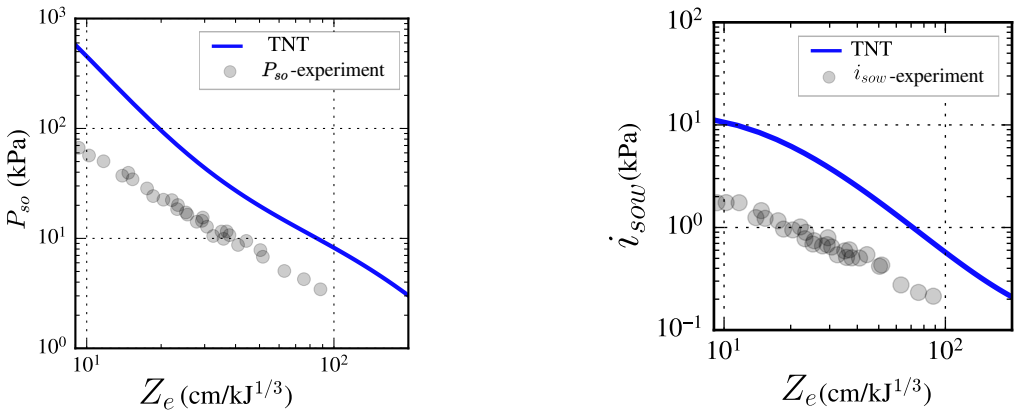


**(a)** Incident overpressure **(b)** Incident scaled impulse

**Figure 3.16:** Variation of the incident overpressure $P_{so}$ (a) and the scaled incident impulse $i_{sow}$ (b) as functions of $Z_e$.

We present the TNT equivalence factors against $Z_e$ for the peak incident overpressure and scaled impulse in Figure 3.17. We observe a large contrast in the values of the equivalence factor for small scaled distance between the definition using the peak overpressure (where $EF_{p_{so}} = 0.08$) and that one using the scaled impulse (where $EF_{i_{sow}} = 0.01$). However, at larger scaled distances, the two definitions tend to converge to the same value, namely 0.1. We recall that, assuming the same hypothetical standoff distance between the exploding wire and the TNT source, an $EF = 0.1$ means that $E_{\mathrm{TNT}} = 0.1 E_{\mathrm{EW}}$ or, equivalently, $E_{\mathrm{EW}} = 10 E_{\mathrm{TNT}}$.

Figure 3.17 additionally shows a best-fit interpolation of the two definitions of the equivalence factor. This is obtained by performed a LASSO polynomial regression (with maximum polynomial degree equal to 12 (for more details, we refer to Masi, 2024). Accordingly the following equations are found

$$EF_{p_{so}} \equiv \left( \frac{Z_{e\mathrm{EW}}}{Z_{e\mathrm{TNT}}} \right)^3_{p_{so}^{\mathrm{EW}}=P_{so}^{\mathrm{TNT}}} = 0.04 - 0.007 Z_e^2, \tag{3.6}$$

$$EF_{i_{sow}} \equiv \left( \frac{Z_{e\mathrm{EW}}}{Z_{e\mathrm{TNT}}} \right)^3_{i_{sow}^{\mathrm{EW}}=i_{sow}^{\mathrm{TNT}}} = 0.13185922 - 0.04206613 Z_e^3. \tag{3.7}$$

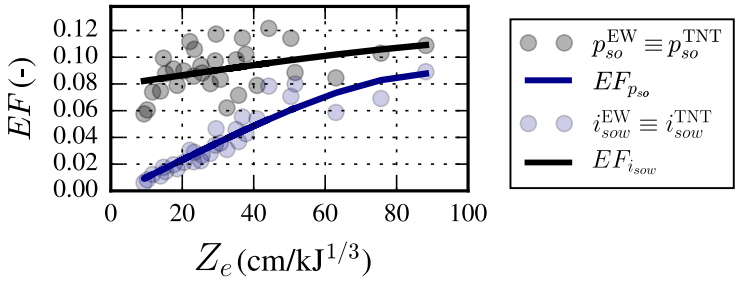


**Figure 3.17:** The TNT equivalence factors for peak incident overpressure and reduced impulse ($EF_{p_{so}}$ and $EF_{i_{sow}}$) as functions of $Z_e$.

Based on the aforementioned interpolation, we can finally compute the equivalent TNT mass, $m_{\mathrm{TNT}}^{\mathrm{eq}}$, whose detonation yields the same value of the peak of the incident overpressure and of the peak of the scaled impulse at a fixed standoff distance. The mass is computed using Eqs. (3.4, 3.5) and reads

$$m_{\mathrm{TNT}}^{\mathrm{eq}} = EF \frac{E_C}{e_{\mathrm{TNT}}}, \tag{3.8}$$

where we recall that we consider $E_C = E_{\mathrm{EW}}$. Figure 3.18 presents $m_{\mathrm{TNT}}^{\mathrm{eq}}$ as a function of the energy levels for each standoff distance $D$. It is clear that as we increase $E_C$, $m_{\mathrm{TNT}}^{\mathrm{eq}}$ also increases. However, when we increase $D$, the equivalent mass increases (see Figure 3.18).

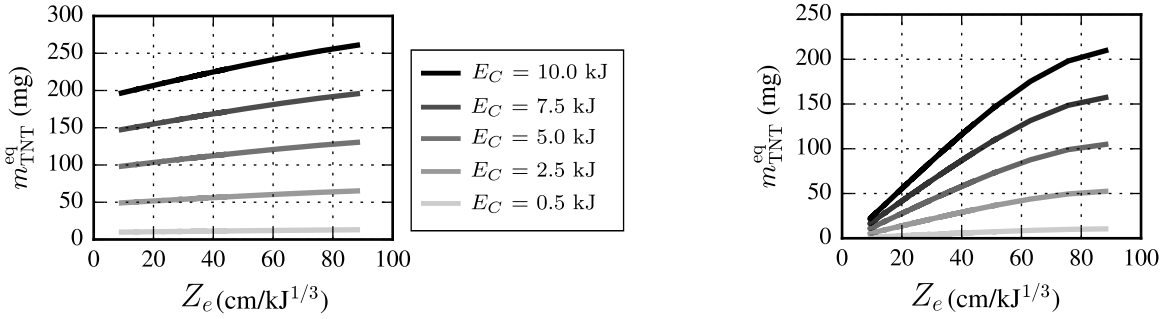


**(a)** Incident overpressure

**(b)** Incident scaled impulse

**Figure 3.18:** Equivalent TNT mass corresponding to the energy levels considered and further assuming similarity of the peak of the incident overpressure $P_{so}$ (a) or of the scaled incident impulse $i_{sow}$ (b). at varying of the scaled distance $Z_e$.

# Chapter 4

# Rigid-body response of blocky structures and validation of the scaling laws

*Chapter 3, presented an experimental characterization of the explosion generated by the exploding wire for different stored energy ($E_C$) and standoff distance ($D$). The incident overpressure and impulse levels characterizing the explosive source. are measured and used to derive the TNT equivalence factor. as a function of time. The chapter ends with an analysis of the shock wave isotropy and an estimation of the equivalence factor between TNT charge and explosive wire charge. In this Chapter we investigates the validity of the scaling laws for the rigid-body response of blocky structures subjected to blast loading. In so doing, we present the methodology used to measure the three-dimensional (3D) motion of printed rigid blocks, by resorting to Particle Tracking Velocimetry (PTV). Next, we introduce a modification of the scaling laws first proposed in (Masi et al., 2022, cf. Chapter 1) in order to account for the difference between the impulsive loading arising from TNT explosive charges and that originating from the exploding wire employed throughout this work. Finally, we compare the results of a small-scale prototype with an even smaller-scale model. Despite some differences in the dynamic response, mainly due to the restitution coefficient of the impacts happening during rocking, the model and the prototype responses provide a first validation of the scaling laws in terms of the resulting impulsive load.*

## 4.1 Introduction

To assess the validity of the scaling laws proposed in (Masi et al., 2022), we start by presenting the prototype and model, consisting of a rigid prismatic block, as well as the loading and scaling scenarios considered. To this end, we provide a modified version of the aforementioned scaling laws by requiring the similarity of the impulsive loading acting on the model and the prototype in terms of the energy level $E_C$ stored in the capacitor (cf. Chapter 3). Then, we describe the Particle Tracking Velocimetry (PTV) software employed to measure the 3D motion of both prototype and model. Attention is also focused on the image system calibration and techniques in order to assure accurate and precise measurements of the block motion. Finally, we analyze the results in terms of the displacement and the velocity. The model response is compared with that of the prototype by means of the employed scaling laws. The results show agreement in terms of the resulting blast impulse, despite some differences existing in the way energy is dissipated through impacts in the model and the prototype.

## 4.2 Problem statement

### 4.2.1 Materials and boundary conditions

Throughout this Chapter, we consider both prototype and model as a prismatic block, shown in Figure 4.2. The dimensions of the block are $2b \times 2h \times 2w$ (width $\times$height $\times$depth). We consider slender blocks – that is, with a slenderness angle $\alpha = \tan^{-1}(h/b) < 20°$. In this scenario, rocking and overturning are the predominant response mechanisms, compared to sliding and uplifting when the angle of friction $\varphi$ between the block and the plane is much smaller than $\alpha$ (cf. Masi et al., 2019). The rocking motion takes place around the rocking pivot point $O$ which is located at a distance $r = h/\cos(\alpha)$ from the center of gravity. Herein, we select a slenderness angle $\alpha$ equal to 5.655°. The prototype and model blocks are built using additive manufacturing using the S5 ultimaker printer (see Chapter 1), see Figure 4.2.

Table 4.1 presents the geometrical and mass properties of both the prototype and model, as well as the measured angle of friction between the block and the optical table. More precisely, we consider a unit scaling of the mass (density): $\gamma = \tilde{\rho}/\rho = 1$, with $\tilde{\rho}$ the mass density of the model and $\rho$ the mass density of the prototype. A geometrical scaling factor $\lambda = \tilde{l}/l = 0.5$ is considered. It is worth noticing that this scaling factor is only considered for the two-dimensional geometry of the block ($h$ and $b$) and the standoff distance $D$. The dimension $w$ is kept the same in the model and the prototype as we ensure a two-dimensional rocking (and overturning) motion and, thus, the depth of the block does not influence the rigid-body response (cf. Masi et al., 2019). In addition, this choice enables us to avoid the influence of reflection and diffraction that may take place at the edges of the model (phenomenon referred to as clearing effect Rigby et al., 2013).

**Table 4.1:** Prototype and model blocks characteristics: geometry, mass, and angle of friction – $\mu$, mean value, and $\sigma$, standard deviation (based on five different measurements).

| | $2b$ (mm) | $2h$ (mm) | $2w$ (mm) | $\rho$ (kg/m$^3$) | $\mu(\varphi)$ (°) | $\sigma(\varphi)$ (°) |
|---|---|---|---|---|---|---|
| Prototype | 10 | 100 | 100 | 411 | 19.92 | 0.121 |
| Model | 5 | 50 | 100 | 411 | 20.10 | 0.129 |

Both prototype and model are constrained to rock in a two-dimensional setting. This is ensured by installing four bars, fixed around the block edges in order to prevent the block from sliding and assuring the rocking and overturning around a pivot point (O), cf. Figure 4.3. More specifically, we extract a triangle of width 1 cm from each edge of the block, with the same blocks thickness and a slope of 30 degrees (see Figure 4.1). This feature will help us to prevent the blocks from sliding without affecting their response.

### 4.2.2 Revisiting the scaling laws

The scaling laws proposed in (Masi et al., 2022) ensures similarity of the rigid-body response of the model and of the prototype, as well as of the effective impulsive loading stemming from the detonation of an explosive charge. The scaling laws consider a TNT explosive charge and propose to identify the reduced-scale (model) equivalent TNT mass

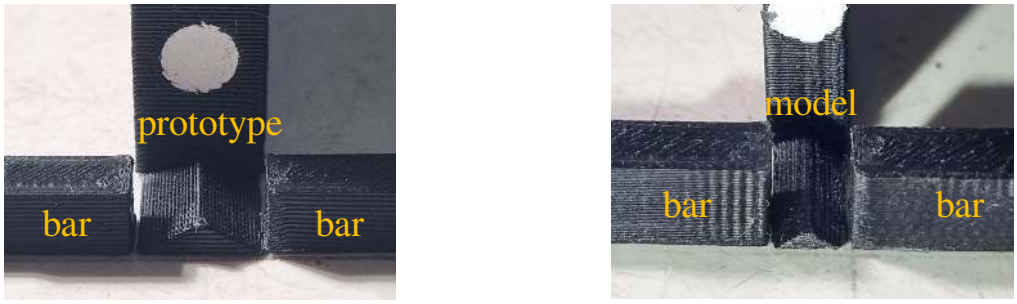


(a) (b)

**Figure 4.1:** Prototype and model bar connections with the block.

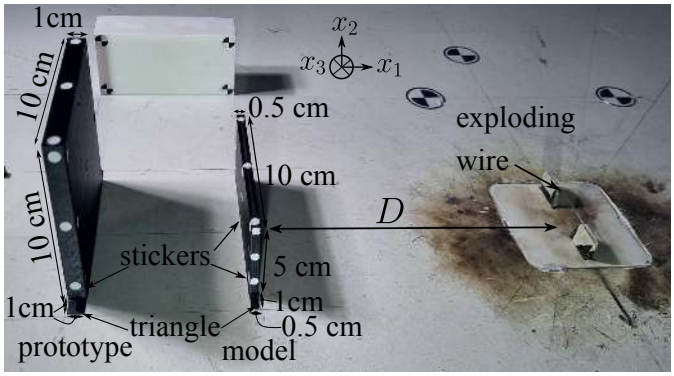


**Figure 4.2:** Prototype and model dimensions.

such that the scaling factor of the impulsive loading satisfies (with $i_{ro}$ the reflected impulse)

$$\lambda_{i_{ro}} = \frac{\tilde{i}_{ro}}{i_{ro}} = \gamma\sqrt{\lambda^3}. \tag{4.1}$$

In the scenario herein considered $\gamma = 1$ and Eq. (4.1) simplifies to $\lambda_{i_{ro}} = \lambda^{3/2}$.

However, the characterization of the blast parameters presented in Chapter 3 consists of identifying the evolution of the incident blast parameters with respect to the standoff distance and the energy level. That is, only measurements of the incident impulse, $i_{so}$, are available. In order to compute the corresponding reflected impulse $i_{ro}$, one could assume a perfectly normal shock wave and, relying on Rankine-Hugoniot relationships for normal shocks (cf. Masi, 2020), an expression for the reflected impulse could be found as function of the peak of the incident overpressure and the positive phase time duration. However, in so doing, assumptions related to the temporal evolution of the overpressure time history must be made. To avoid such idealizations, we opt herein to reformulate the scaling laws in terms of the incident impulse, $i_{so}$, which is a direct measure (with no assumptions and independent of the multiple reflections and diffractions that would take place when measuring the reflected blast parameters).

In so doing, we reformulate the scaling laws according to

$$\lambda_{i_{so}} = \frac{\tilde{i}_{so}}{i_{so}} = \lambda^{3/2}. \tag{4.2}$$

Next, we express the incident impulse $i_{so}$ as a function of the energy level $E_C$ and the standoff distance, i.e., $i_{so} = i_{so}(E_C, D)$. Thus the similarity of the reduced-scale model

with the full-scale prototype is given by the solution of the following nonlinear algebraic equation

$$\text{find } \tilde{E}_C \text{ such that } \quad \frac{\tilde{i}_{so}\left(\tilde{E}_C, \tilde{D}\right)}{i_{so}\left(E_C, D\right)} - \lambda^{3/2} = 0, \tag{4.3}$$

given $E_C$, $D$, $\lambda$, where $\tilde{D} = \lambda D$. In order to find the reduced-scale energy level $\tilde{E}_C$, we must solve the nonlinear equation (4.3) numerically. This is done by relying on linear interpolations of the positive incident impulse $i_{so}(E_C, D)$ from the measured values presented in Chapter 3.

For the sake of completeness, herein we consider two scenarios. The former consists of a pure rocking response of the prototype, while the latter refers to overturning. By solving the rocking equation of motion (1.5) for the prototype, we find that the first scenario is obtained by setting $E_C = 10$ kJ, at $D = 60$ cm, while the latter is achieved by keeping the same energy level, but reducing the standoff distance to $D = 40$ cm. Table 4.2 resumes the two scenarios considered for the prototype and shows the reduced-scale standoff distance and energy level obtained for the model by solving Eq. (4.3).

**Table 4.2:** Prototype and model experiments scenarios.

| | Scenario | $E_C$ (kJ) | $D$ (cm) |
|---|---|---|---|
| Prototype | Rocking | 10 | 60 |
| | Overturning | 10 | 40 |
| Model | Rocking | 0.674 | 30 |
| | Overturning | 0.721 | 20 |

## 4.3 3D particle tracking velocimetry

In order to investigate the validity of the scaling laws, the 3D motions of both the prototype and the model must be measured. To this end, we rely on particle tracking velocimetry (PTV). More precisely, we employ an optical system constituted by three high resolution 2704 ×1520 pixels cameras (GoPro11) mounted over the optical table. The resulting resolution is 0.112 mm/pixel and a sampling frequency of 240 Hz is selected. The field of view of the three cameras cover the blocks and the surrounding environment with a field of approximately 303 ×170 mm. The three cameras – camera-1 (C1), camera-2 (C2), and camera-3 (C3) – are placed in a way to avoid producing any reflections to the blocks (refer to Figure 4.3). The lighting system consists of two LED spotlights to ensure uniform lighting of the block (see Figure 4.3). The TEMA software is used for the 3D motion reconstruction, Image Systems (2004).

To measure the time evolution of the displacements of the blocks, we place circular stickers (with diameter equal to 5.0 mm) uniformly distributed over the block's surfaces. These stickers are hence tracked to measure the displacements and reconstruct the rigid-body response, along the three-dimensional space (denoted by the triplet $x_1 - x_2 - x_3$). The three cameras are controlled via a remote control (using bluetooth). Particle Tracking Velocimetry (PTV) is subdivided in two parts: (1) stereo calibration and data recording and (2) post-processing.

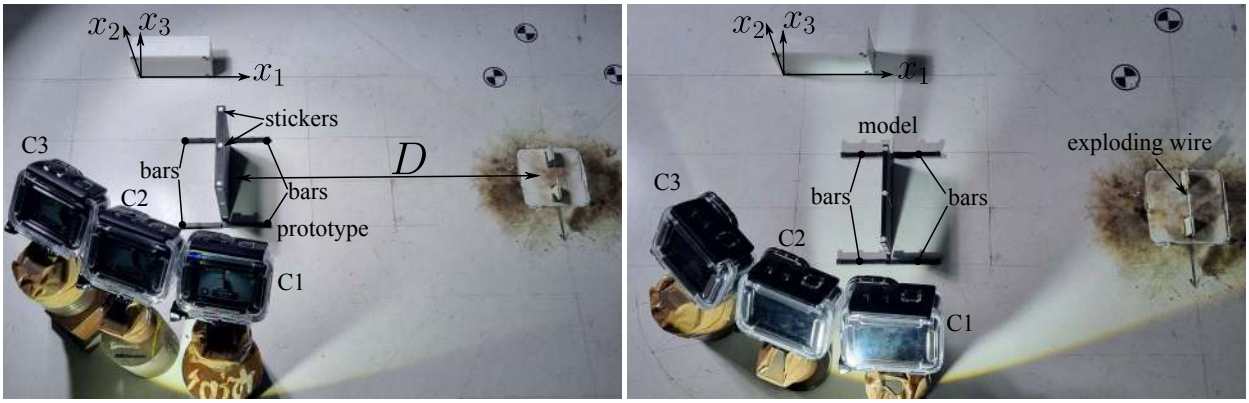


**Figure 4.3:** Installation of blocks and cameras for the prototype (a), and the model (b).

### 4.3.1 Stereo calibration and data recording

Two sets of videos are recorded: 1) for the cameras calibration and 2) for the block response.

The first set of videos are related to the cameras calibration (stereo calibration) in order to determine parameters for lenses correction and the transformation between each camera field of view to enable 3D measurements (within the plane imaged by each camera and in depth)[1]. Stereo calibration is a critical step in order to assure the accurate 3D reconstruction and depth perception of the field later by using TEMA software. This process involves moving a panel board in-front of the three cameras employed in the experimental setup. The board is positioned at different angles and depths to cover the windows of each camera and to calculate, later, the distortion parameters (as detailed in next Section 4.3.2). To this end, Figure 4.5 displays the panel and four points that must be imaged by three cameras to enable calibration. For appropriate calibration, the panel board is in this setup positioned at different angles ($20 \div 50°$), which enables capturing the intrinsic distortion of the cameras.

After stereo calibration, we proceed by performing the experiments and recording, with each camera, the field of view which images the block and its rigid-body response, see Figure 4.3. The recorded videos are then imported in the TEMA software for performing the post-processing steps detailed hereinafter to extract the complete three-dimensional motion of each of the stickers positioned over the block.

### 4.3.2 Post-processing

We detail hereafter the post-processing steps required to perform the PTV analysis and extract the three-dimensional motion of the block. Post-processing includes the following steps:

1. Synchronization. It is important to note that recorded videos are not perfectly synchronized. The videos for the cameras calibration are synchronized by tracking the motion of the same point in the panel board and then applying a shift in a way all the three cameras videos have the same movement at the same time frame (see

[1]Stereo vision involves using two or more cameras to capture images of the field from different viewpoints to re-construct the 3D field later.

Figure 4.4). The videos for the block response are also synchronized by using the explosion as trigger event. During explosion there is a bright flush of light that leads to cameras saturation. This saturation appears as white frames in the recorded videos. We therefore shift the three cameras videos to start from the same white frame, related to the same time step.

2. STEREO CALIBRATION. The synchronized videos for the cameras calibration are used to perform stereo calibration, which is done for each two videos that share the common window. In our case we calibrate cameras C1 and C2 together and then C2 and C3. We first define the square size in the panel board (which is of size 12.25 mm), and we track four centered points in each frame (see Figure 4.5). Having 4 frames with different positions and angles is sufficient for the calibration. For the case where the two videos are not synchronized the software stops the calibration and sends an alert message (which works as a first check for a good synchronization). At the end of the calibration the software divides the window of each camera into 16 colored regions with the green indicating a good calibration and the red a bad one (where measurements cannot be trusted). In our experiments we took care that the position of the block is inside the green region, see Figure 4.6. Two files are then extracted providing the appropriate lens parameters for each camera.

3. BLOCK RESPONSE. The 3D rigid response of the block is then measured. This is done through importing the three synchronized videos with the associated files containing the lens parameters for each camera. In this stage we define the points we want to track i.e. P1-P6, for the camera C1, then we define the same for C2. During this process we can re-check the calibration by visualizing that the software projects a line related to the common points between C1/C2 (see Figure 4.7).

TEMA software has different tracking algorithms. In our experiments, we used the "gravity" function to track the center of the stickers area. For the white (saturated) frames, where the points are not visible, we used the "sleep" function that orders the software to stop tracking and produces a gap in the output data. TEMA can interpolate (liner or cubic polynomial interpolation) the missing data provided there are measurements both before and after the gap.

## 4.4 Results

The TEMA software is used to monitor the time evolution of the 3D displacements of the block's points P1-P6 (cf. Figure 4.7). The movement of point P3 is presented hereafter, located at the top of the block. We present the results both in terms of displacements (measured) and velocities (computed using a finite difference scheme) along the three directions $x_1$, $x_2$ and $x_3$. For each experimental scenario presented in Table 4.2, three experimental tests are performed in order to investigate the repeatability of the obtained measurements and of the rigid-body response. We first present and analyze the responses of the prototype and model independently, then we compare the results to check the validity of the scaling laws.

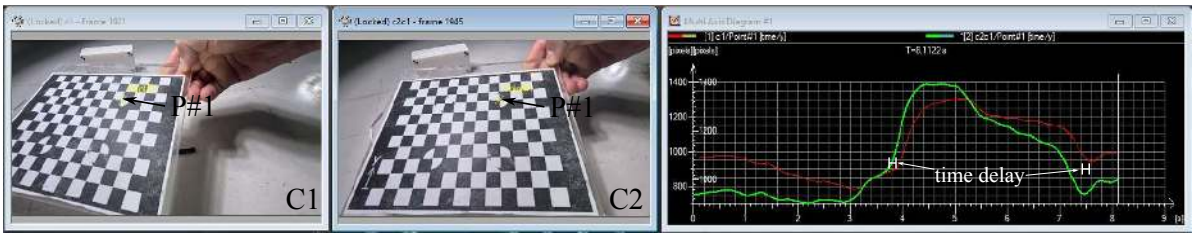


(a)

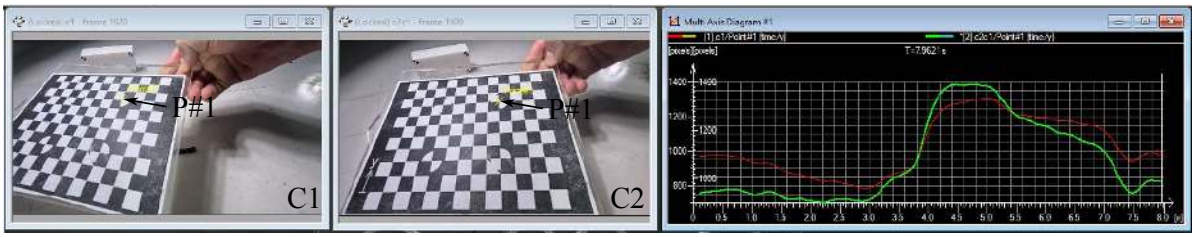


(b)

**Figure 4.4:** Synchronization of cameras C1 and C2 by tracking the position of point P1.

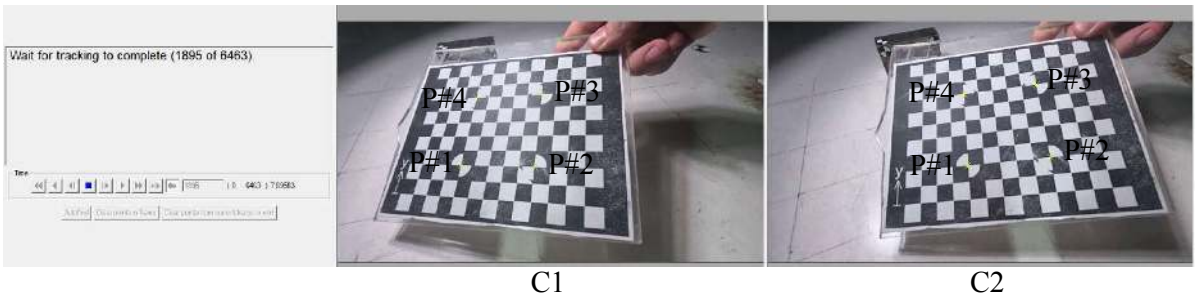


**Figure 4.5:** Stereo calibration of cameras C1 and C2.

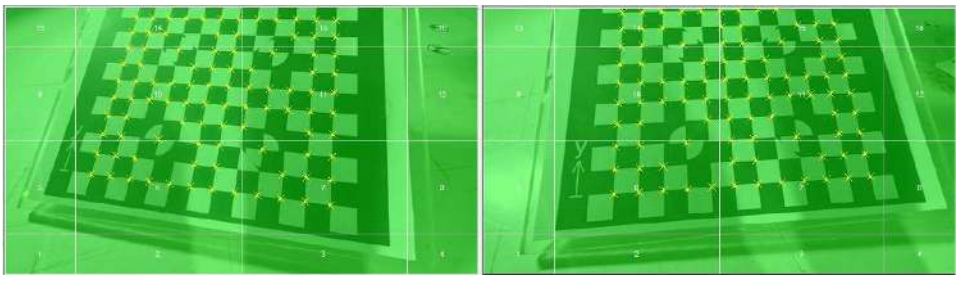


**Figure 4.6:** Stereo calibration validation (green region).

### 4.4.1 Rocking and overturning of the prototype

**Rocking** The prototype is positioned at a standoff distance $D = 60$ cm and subjected to the blast loads arising from the exploding wire with an energy level $E_C = 10$ kJ. To investigate the accuracy of the 3D measurements we present in Figure 4.8 the distance between points P1 and P3 and P4 and P6. The distance P1-P3 is found equal to $79.87 \pm 0.112$ mm (Figure 4.8 (a)), with an amplitude of variation being of the same order of magnitude than the pixel size. Notice that the nominal value of the distance is 80 mm. The slight difference between the latter and the measured mean value (equal to 0.13 mm) is within the spatial resolution of the 3D measurements, thus verifying the accuracy of the PTV

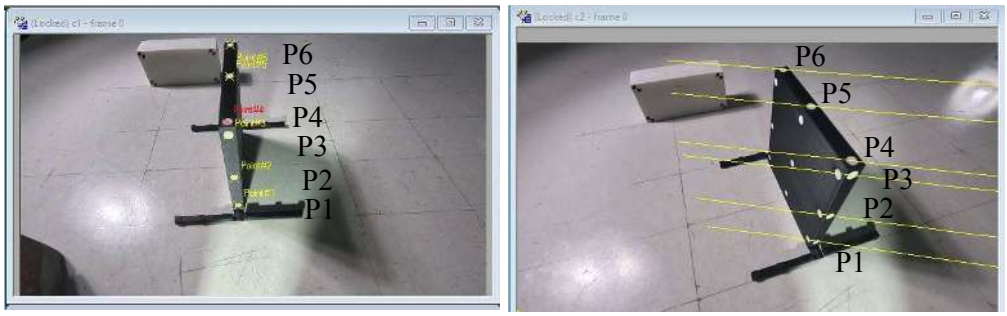


**Figure 4.7:** Tracking P1-P6: projection lines indicate the position of the points in camera C2 based on the points fixed in camera C1.

analysis. The distance P4-P6 is found equal to $87.8 \pm 0.112$ mm (Figure 4.8 (b)), while the nominal value is 88 mm, validating again the 3D PTV.

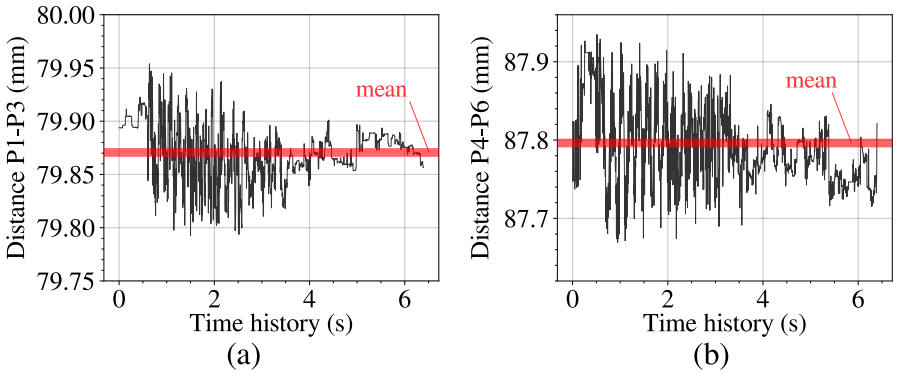


**Figure 4.8:** Time history of the measured distance between points P1 and P3 (a) and P4 and P6 (b), see Figure 4.7.

Figure 4.9 displays the measured 3D displacements (along $x_1$, $x_2$, and $x_3$) as function of time and the corresponding velocities. We can first observe that the results of the three experimental tests are similar, with only some minor differences arising for $t > 2.5$ s, see Figure 4.9(a,d). This result illustrates the high repeatability (1) of the impulsive loading (see also Chapter 3) and (2) of the rocking motion. It is also worth noticing that the displacement $u_3$ (and, equivalently, the velocity $v_3$) is of the order of the spatial resolution of the cameras, indicating thus that the predominant response of the block is a motion towards the $x_1$ axis. The result demonstrates therefore that the designed boundary conditions are effective in constraining the rigid-body rocking motion within the plane $x_1 - x_2$.

**Overturning** For the second scenario (overturning), the prototype is positioned at a standoff distance $D = 40$ cm and the energy level is kept the same ($E_C = 10$ kJ). Figure 4.10 presents the time history of the 3D displacements and velocities of point P3. Once again, we can observe a high repeatability of both the impulsive loading and the rigid-body response, particularly for the motion along $x_1$ and $x_2$. Furthemore, the impacts following overturning (at around $t = 0.9$ s) display a repeatable behavior.

The final displacement along the axis $x_1$ is equal to 85 mm. This value coincides

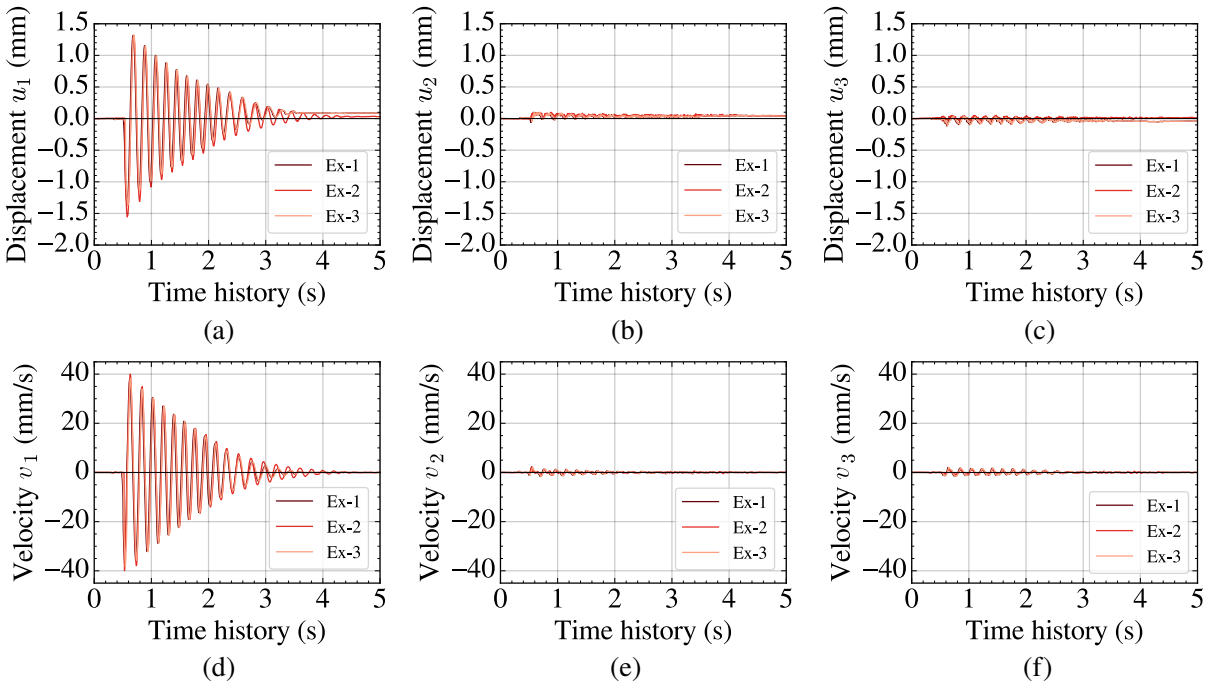


**Figure 4.9:** Time history of the displacements (a-c) and velocities (d-f) for the rocking scenario ($D = 60$ cm, $E_C = 10$ kJ) of the prototype. The results refer to point P3 (see Figure 4.7).

with the nominal distance between point P3 and the base of the block, demonstrating that the PTV analysis enables accurate measurements. Furthermore, displacements along the $x_3$ axis are found negligible (of the order of 2 mm), thus demonstrating that the designed boundary conditions ensure a two-dimensional motion within the $x_1 - x_2$ plane. Finally, the time evolution of the velocities illustrates again the high repeatability of the experimental tests. Indeed, the velocities ($v_1$ and $v_2$) of the three tests present the same peaks and time variation, demonstrating that even the complex dynamics of the impacts of the block with the optical table are well captured and are repeatable.

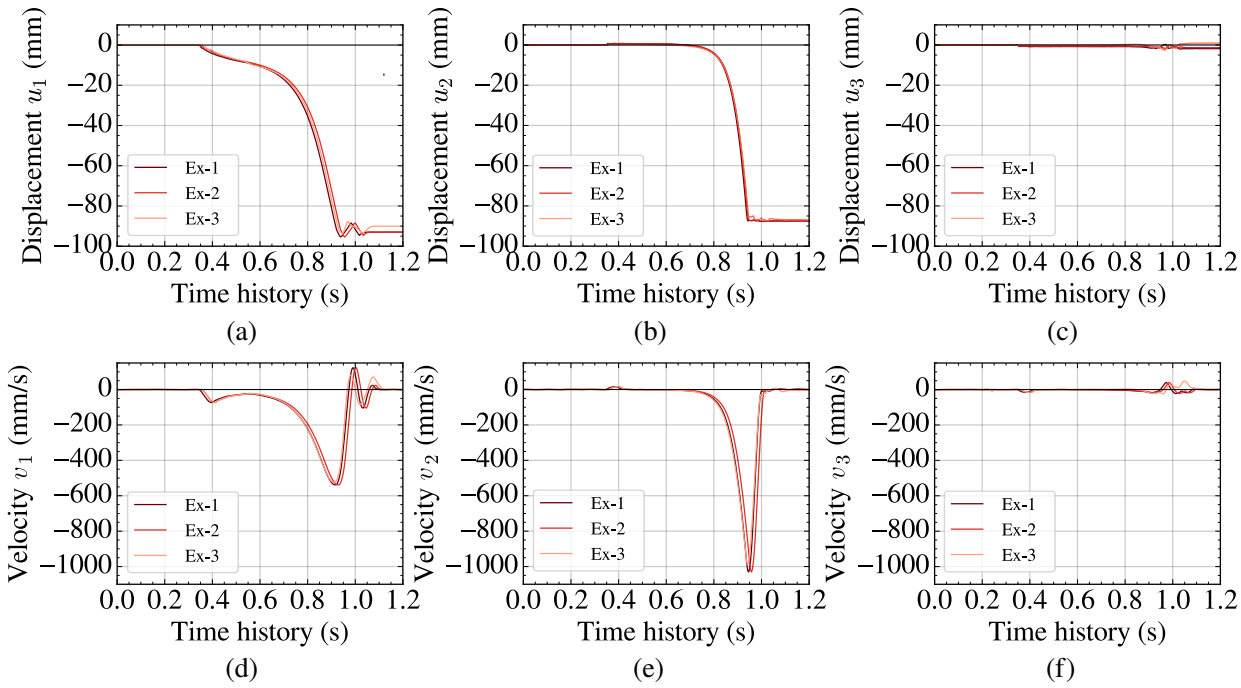


**Figure 4.10:** Time history of the displacements (a-c) and velocities (d-f) for the overturning scenario ($D = 40$ cm, $E_C = 10$ kJ) of the prototype. The results refer to point P3 (see Figure 4.7).

### 4.4.2 Rocking and overturning of the model

**Rocking** The model is located at a standoff distance $\tilde{D} = 30$ cm and the reduced-scale energy level is $\tilde{E}_C = 0.674$ kJ. Figure 4.11 presents the time evolution of the displacements $u_1$, $u_2$, $u_3$ and the velocities $v_1$, $v_2$, $v_3$, for the same point P3. Results show an overall good degree of repeatability during the first rocking phase $t < 0.7$ s. However, a difference in the rate at which energy is dissipated during rocking can be observed at later stages. This is additionally exacerbated by the difference in the first peak of the displacement (and velocity), which then propagates and gives different time evolutions.
This difference may stems from two different causes. First, the considered boundary conditions that probably affect the dynamics of the rocking system. This may be due to the presence of multiple impacts with friction at the contact of the lateral bars (cf. Figure 4.3) and the block which would be at the origin of rich non-smooth dynamics. Second, the energy level stored in the capacitor is extremely small compared to the energy related to the prototype (0.674 kJ versus 10 kJ). Such a small energy may involve different nonlinear phenomena in the generation of plasma and, thus, of the subsequent shock wave, suggesting a weaker repeatability of the blast loads generated at small energies.

**Overturning** The model is located at a standoff distance $\tilde{D} = 20$ cm and the reduced-scale energy level is $\tilde{E}_C = 0.721$ kJ. Figure 4.12 presents the displacements and the velocities of point P3 as function of time. Contrary to the rocking scenario, we observe high repeatability of the rigid-body response of the model along the three different directions. This result suggests that the cause for the relatively weak repeatability in the rocking scenario is due to the presence of the boundary conditions that are of particular importance during rocking (with multiple impacts) rather than overturning.

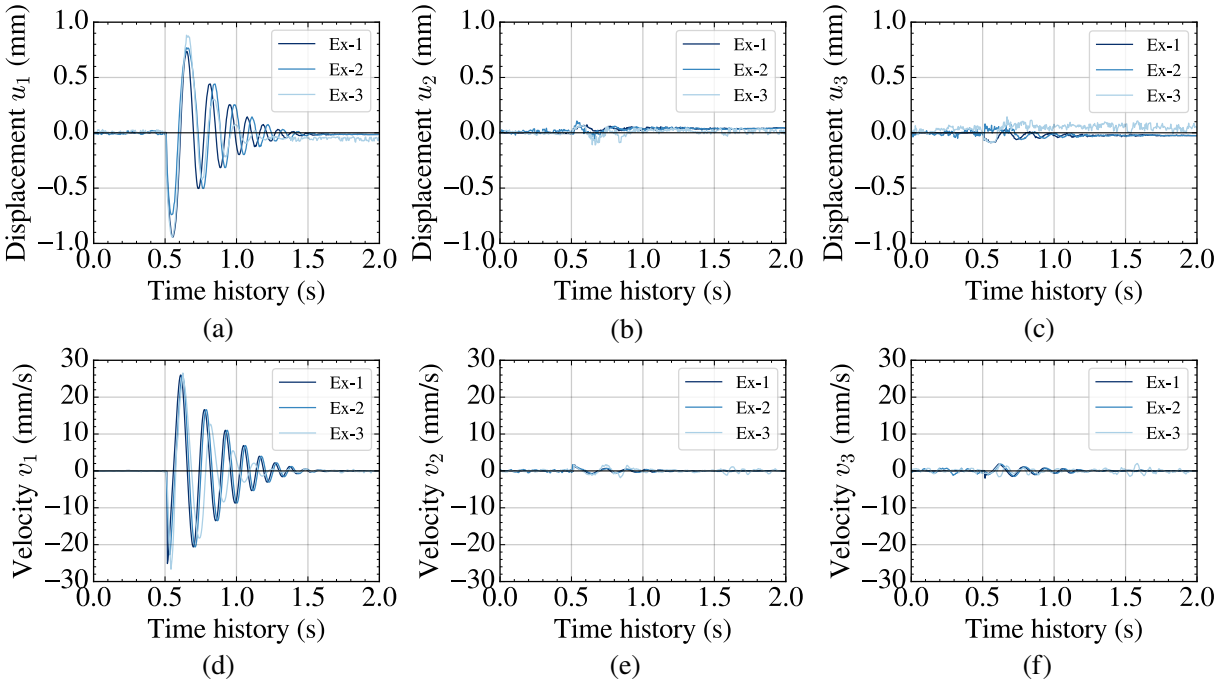


**Figure 4.11:** Time history of the displacements (a-c) and velocities (d-f) for the rocking scenario ($D = 30$ cm, $E_C = 0.733$ kJ) of the model. The results refer to point P3 (see Figure 4.7).

In the overturning scenario, we can additionally observe a final displacement equal to 47.5 mm along $x_2$ which coincides with the nominal distance between the initial position of point P3 and the optical table on which the block is resting. Finally, notice that the displacement along $x_3$ is of the order of 1.5 mm, which is negligible, suggesting that the motion lies within the plane $x_1 - x_2$.

### 4.4.3 Comparison of the motions of the prototype and the model

We compare hereafter the rigid-body displacements and velocities of the prototype and the model along the axis $x_1$, where most of the motion takes place. To avoid the propagation of uncertainties due to the finite spatial resolution of the corresponding PTV analysis, we opt for down-scaling the prototype response. In particular, the displacements of the prototype are multiplied by the geometric scaling factor $\lambda$, the velocities and the time scale by a scaling factor equal to $\sqrt{\lambda}$, cf. Table 1.1.

**Rocking** We proceed by comparing the results for the rocking scenario (refer to Table 4.2). Figure 4.13 presents the time history of the displacement $u_1$ and velocity $v_1$ of the down-scaled prototype and the model. The plot shows the mean value (obtained by averaging the results obtained from three identical tests) and the 95% confidence interval, denoted by the shaded region.

The responses of the down-scaled prototype and the model are found to be overall similar during the first and second peaks ($t < 0.6$ s), while they differ for higher times. Despite this difference, we should notice that the peak velocities of both the down-scaled prototype and the model are similar. This is a direct consequence of the fact that the blast loading impulse resulting from the scaling laws is similar between the down-scaled

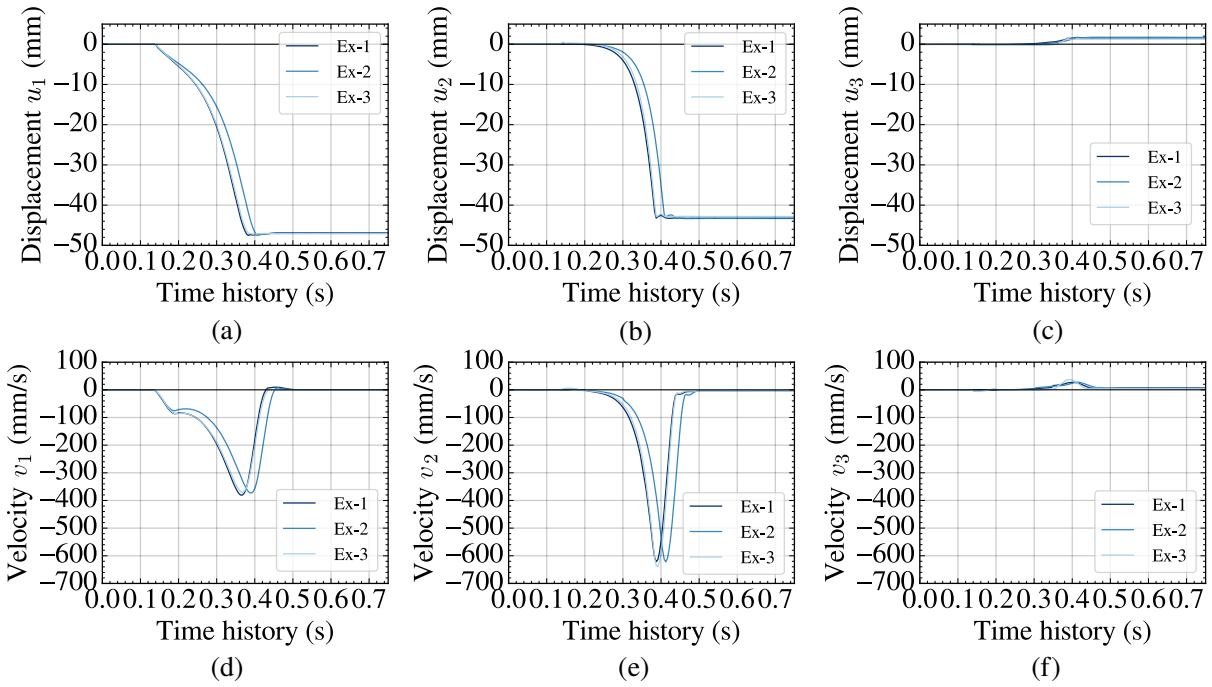


**Figure 4.12:** Time history of the displacements (a-c) and velocities (d-f) for the overturning scenario ($D = 20$ cm, $E_C = 0.722$ kJ) of the model. The results refer to point P3 (see Figure 4.7).

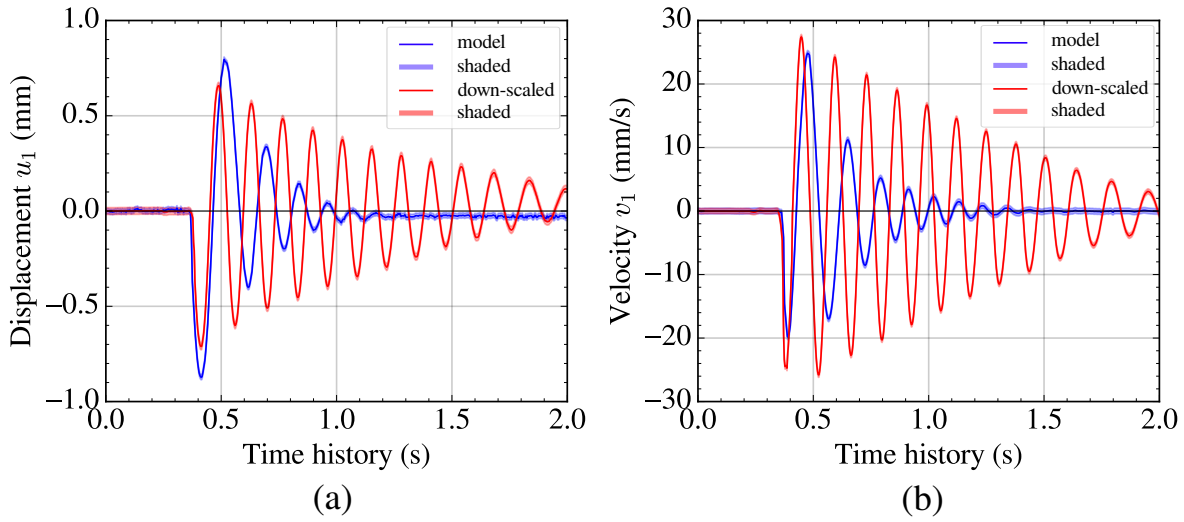


**Figure 4.13:** Rocking scenario: down-scaled prototype and model displacements $u_1$ (a), and velocities $v_1$ (b).

prototype and the model. It also demonstrates that the scaling laws proposed in (Masi et al., 2022) and revisited in Section 4.2 are valid.

It is worth noticing that the differences in the time evolution ($t > 0.6$ s) of the displacements and velocities may due to the boundary conditions as they can induce multiple impacts with friction that would cause a different behavior in the dissipation of energy as the rocking motion advances. To elucidate this point, the restitution coefficient (characterizing the energy dissipation during rocking at each impact) is evaluated hereafter.

More precisely, the dissipation coefficient definition follows the seminal work of Housner (1963), namely

$$e = \left( \frac{\dot{\theta}^{+}}{\dot{\theta}^{-}} \right)^{2} \tag{4.4}$$

where $\dot{\theta}$ is the angular velocity of the rocking block while superscripts $+$ and $-$ denote the value of the angular velocity after and before the impact of the block with the base, respectively.

If the impact is assumed to be inelastic[2] (no bouncing) the rocking motion, after impact, continues smoothly about the pivot point and the moment of momentum is conserved. Under these considerations, Housner (1963) found that the restitution coefficient is only function of the geometry of the rocking block and given by the following expression

$$\eta_{\mathrm{H}} = 1 - \frac{3}{4}\left(1 - \cos(2\alpha)\right). \tag{4.5}$$

In order to compare the aforementioned expression with the experimental results, we assume hereafter that the block motion consists only of rocking, as discussed in subsections 4.4.1 and 4.4.2. Moreover, by solving the equation of motion, the period of free vibration of the first oscillation presented as (Housner, 1963)

$$T = \frac{8}{\sqrt{\frac{3g}{r}}} ln \left[ \frac{1}{1-\theta_0/\alpha} + \sqrt{\left( \frac{1}{1-\theta_0/\alpha} \right)^{2} - 1} \right]. \tag{4.6}$$

We can observe that the restitution coefficient and rocking period depend on the geometry of the block, specifically the slenderness length $r$ and angle $\alpha$. We introduce the following factors that affect $r$ and $\alpha$:

1. The imperfections in block edges arise from printing precision (0.3 mm). Due to this effect, we anticipate variations in the pivotal point, resulting in different slenderness angles and lengths. This effect is observed across the width of the block (see Figure 4.14,a).

2. Friction with the bar results in dissipation at each contact time, as presented in Figure 4.14,b.

3. Small sliding that can occur also affects the dissipation of energy, as shown in Figure 4.14,c.

The issues outlined are responsible for resulting in varying restitution coefficients and oscillation periods, consequently leading to different dissipation of energy between the model and prototype. This discrepancy can be observed by plotting the theoretical results with the experimental results.

By solving the rocking equation (Eq. (1.5)) with the restitution coefficient presented in Eq. (4.5), we can compute the oscillation of the blocks. It's worth noting that for the calculation of the impulsive loading, we relied on the calculated TNT equivalent mass presented in Section 3.5 and empirical formulas to determine the load. Figure 4.15,

[2]Inelastic (no bouncing) means that when the shock wave impinge the block, the block does not goes back or rebound after the impact. Instead, the block undergoes motion smoothly in the direction of the shock wave.

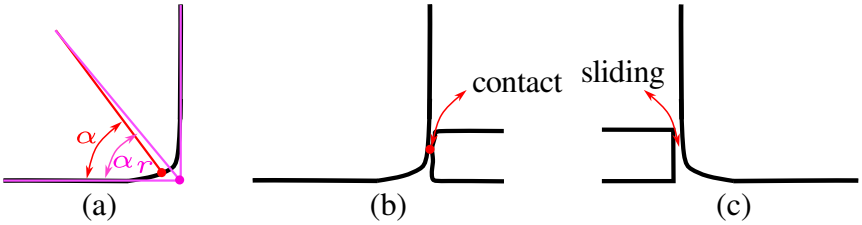


**Figure 4.14:** The impact of the connection between the block and the bar: (a) on $r$ and $\alpha$, (b) on friction, and (c) on sliding.

shows the evolution of the amplitude $u_1$ computed from the rocking equation and for the reduced-scale prototype and the model experimental data as function of time. We can observe that both the model and the down-scaled blocks have different restitution coefficients and oscillation periods compared to the theoretical results. These discrepancies are more pronounced in the model, indicating greater dissipated energy experienced during the impact. These differences are attributed to the effect of the base between the model and the prototype, as well as the boundary conditions discussed previously.

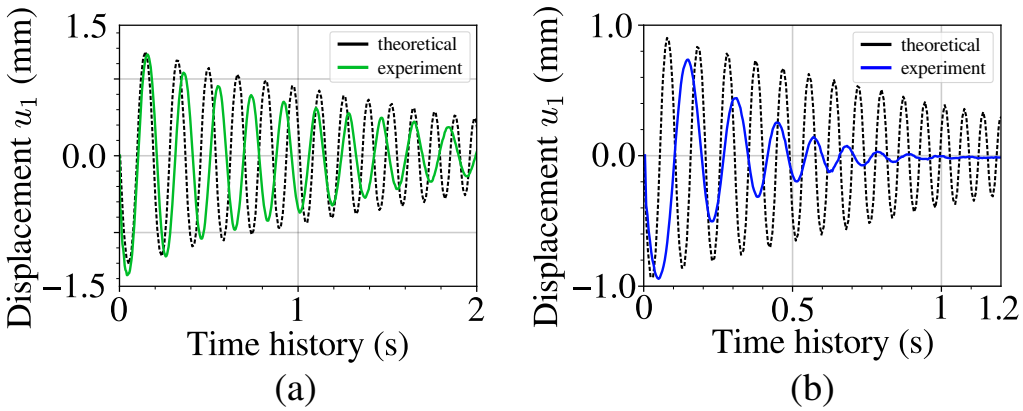


**Figure 4.15:** The rocking oscillation considering analytical expression and as measured from the experimental tests for the reduced-scale prototype (a) and the model (b) function of time.

**Overturning** Figure 4.16 displays the displacement $u_1$ and the velocity $v_1$ of point P3 for the down-scaled prototype and the model. One can notice that the down-scaled prototype and the model yield the same overall response – that is, both overturn. In addition, the multiple peaks in the velocity signal are of the same amplitude, suggesting once again that the scaling of the incident impulse enables to study reduced-scale structures in the experimental platform conceived and designed within this work. The differences in the time evolution are attributed, as previously discussed, on the different influence of the boundary conditions in the prototype and the model. To evaluate the influence of the boundary conditions however, new experimental tests are needed.

## 4.5 Concluding remarks

In this chapter we aimed to validate and/or falsify the scaling laws through rocking and overturning response of rigid blocks. In Figures 4.13 and 4.16, we compared the results of

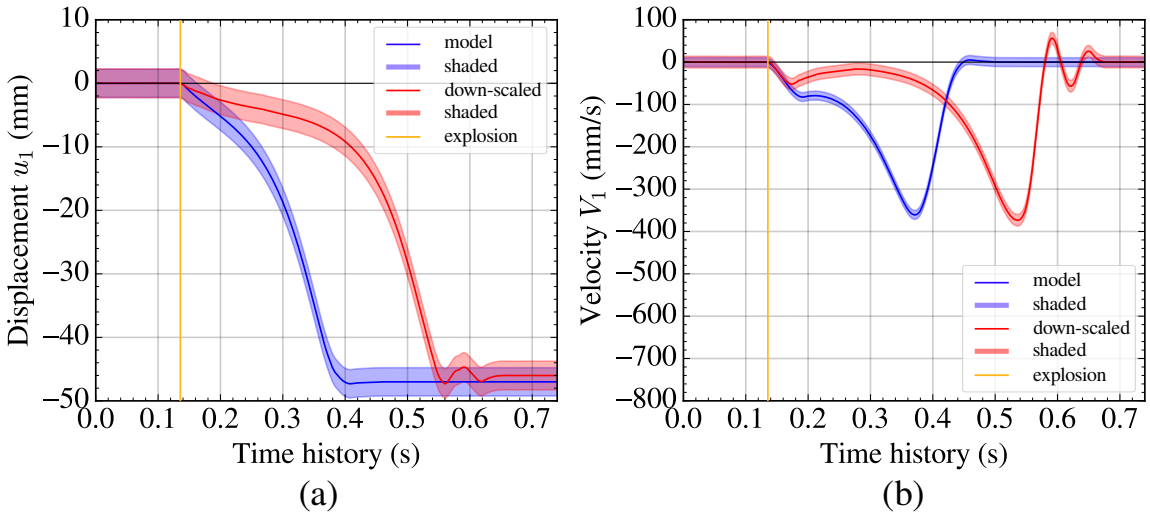


**Figure 4.16:** Overturning scenario: down-scaled prototype and model displacements $u_1$ (a), and velocities $v_1$ (b).

the model and down-scaled structures. It is observed from these figures that the amplitude of the first oscillation is fairly well reproduced by the model, whether for the rocking or overturning mode validate the appropriate scaling of the impulsive loading. However, different oscillation period and damping are observed for later oscillation. This discrepancy is attributed to a friction effect at the boundary conditions (contact between blocks and bars).

# Part III

# Towards reduced-scale testing of complex masonry structures

# Chapter 5

# The Parthenon of Athens

*Chapter 4 focuses on the validation of the scaling laws proposed by Masi (2020) and presented in Chapter 1, allowing the use of reduced-scale models to study the response of unjointed masonry structures subjected to explosions. The validation consists of testing a rigid "prototype" structure of rectangular shape with a height of 10 cm with only one degree of freedom and comparing its response with that of a "model" structure built at half scale. In this Chapter we use the scaling laws verified in Chapter 4 to design the Parthenon of Athens at reduced scale that subjected to explosion in 1687. and to demonstrate, as a proof of concept, the platform's capability to study different types of structures. The tests illustrate the capability of our novel experimental platform to study the dynamical response of masonry structures and world heritage monuments at reduced scale in the laboratory.*

## 5.1 Introduction

We first present the design of the Parthenon's columns, beams and walls in accordance with Tournikiotis (1994); Korres et al. (1999); Zambas (1994). The experimental scenario and the installation of the Parthenon's model on the experimental platform follow, together with details about the position of the cameras, the lights etc. Then, we present some preliminary experimental results showing the destruction happened to the Parthenon after the designed explosion. The chapter end with preliminary results we get from the PTV analysis of showing the trajectory of a defined point.

## 5.2 Architectural design and 3D printing

Parthenon is an iconic temple located atop the Acropolis hill in Athens, Greece, and stands as a testament to ancient Greek architecture and engineering prowess. Constructed in the 5th century between 447 and 438 BC, the Parthenon was dedicated to the goddess Athena and served as both a religious sanctuary and a symbol of Athenian democracy, Tournikiotis (1994). The Parthenon's structure is made of Pentelic marble of density around 2700 kg/m$^3$, a high-quality white marble quarried from Mount Pentelicus near Athens.

In 1687, Venetian forces engaged in battle with the Ottomans at the Acropolis fortification. A bomb detonated, causing the stored gunpowder within the Parthenon to explode. The temple was subsequently divided into two parts, and aside from the cella[1]

[1]Parthenon cella refers to the inner chamber or the central enclosed space within the Parthenon.

walls, Figure 5.2, 14 columns on the north and south sides collapsed as a result of the explosion (see Figure 5.1).

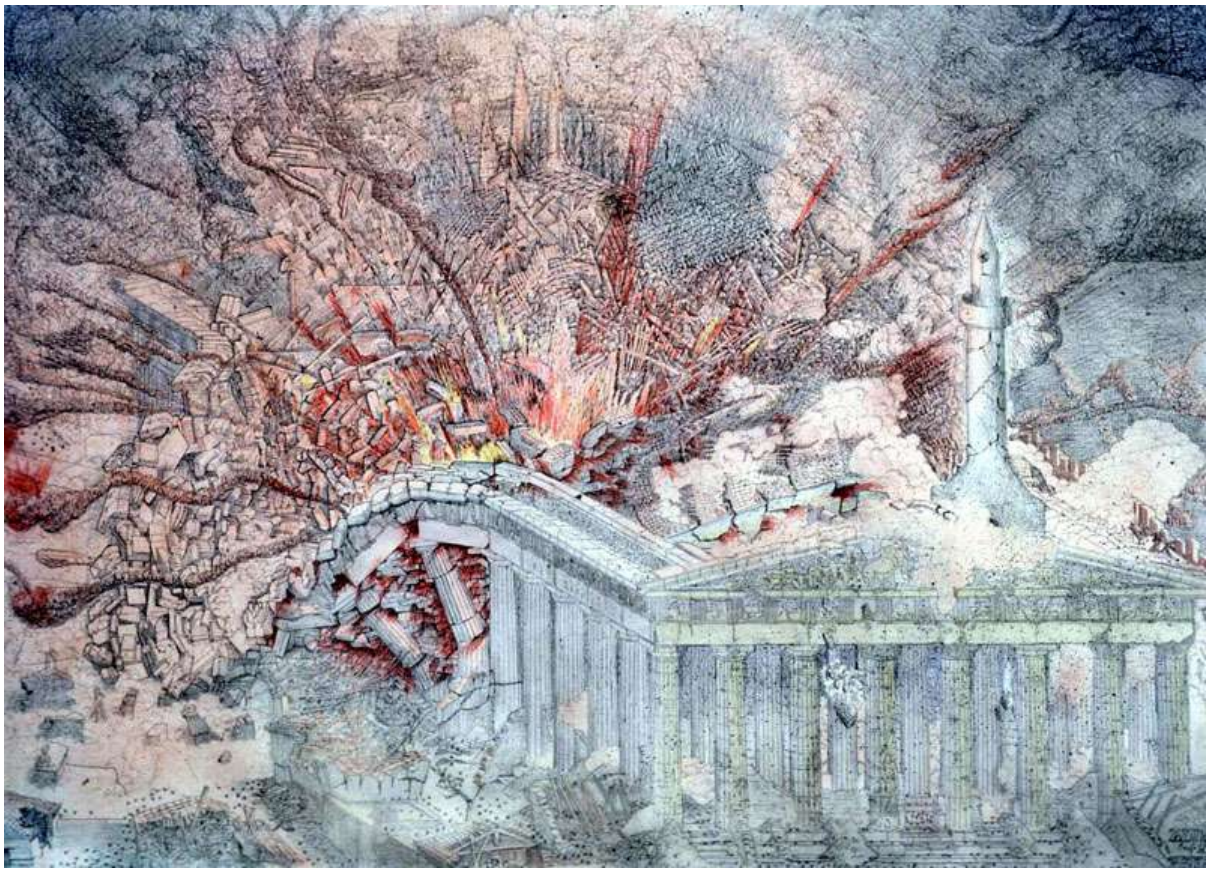

**Figure 5.1:** Parthenon explosion (1687), Tournikiotis (1994)

### 5.2.1 Plan

The Parthenon's design incorporates a Doric order with a hexastyle double-prostyle cella, characterized by its sturdy and harmonious proportions. The temple is built on a rectangular base measuring 69.5 m by 30.9 m, Figure 5.2. The crepidoma has general dimensions of 72.31 $\times$ 33.68 m, and consists of three steps of a total height of 1.59 m. Parthenon features eight columns across the shorter ends (known as the front and back) and seventeen columns along the longer sides (known as the flanks). A detailed 3D presentation of the Parthenon is provided in Figure 5.3.

### 5.2.2 Optical illusions

Parthenon is famous for its optical illusions, see Fig 5.4. Indeed, all Parthenon parts are inclined by a certain angle; there are virtually no straight lines or right angles. In elevation, Parthenon's lines are systematically curved, and the columns, walls and all the other upright features deviate from the perpendicular. The BA (edge column, see Figure 5.4) column is the most inclined by a slope of (almost) 2.6%. At reduced scale this value becomes 0.1%, which is considered hereafter negligible. In other words, columns' inclinations are not considered in the design of the model.

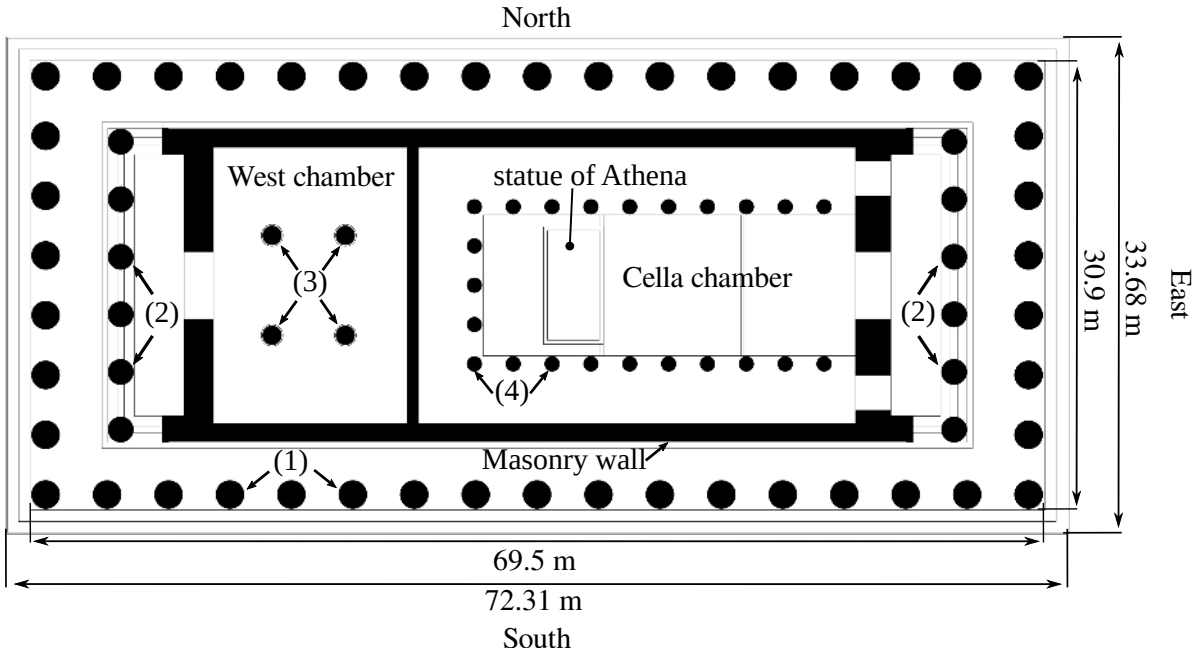


**Figure 5.2:** Parthenon horizontal plan, Tournikiotis (1994)

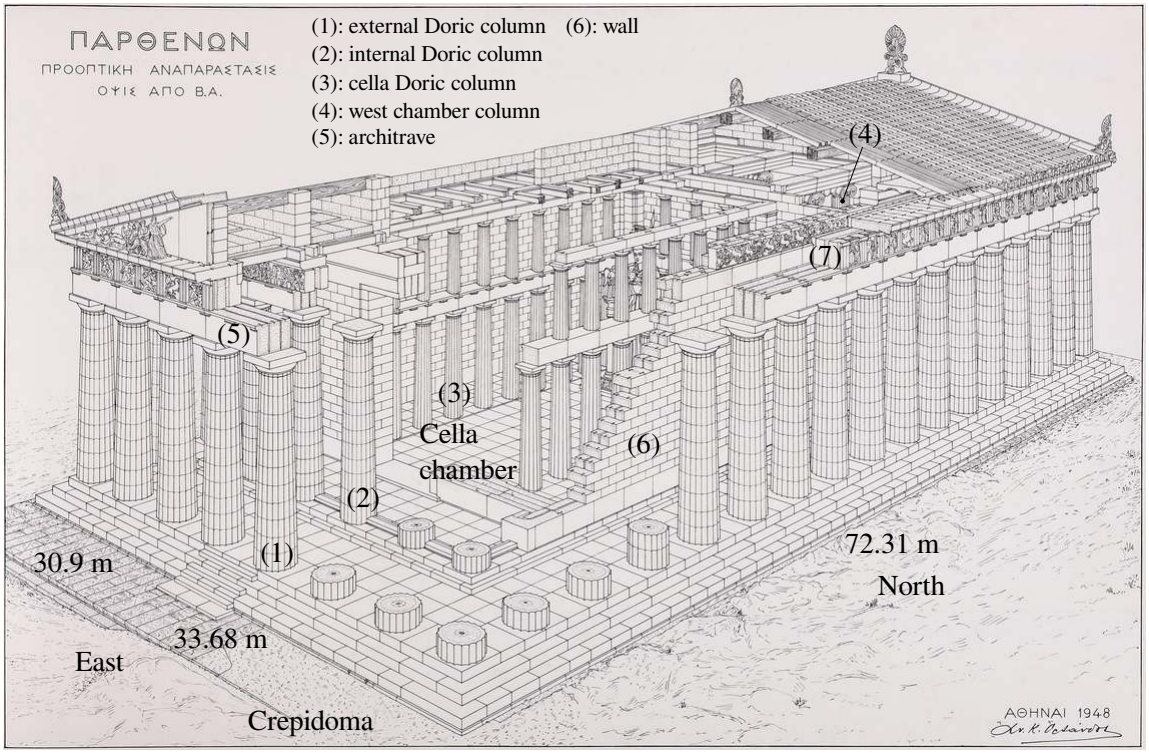


**Figure 5.3:** A detailed 3D representation of the Parthenon, Korres et al. (1999)

The ground has a refinements (inclination) about 25 mm in the middle (in the position of column 9 in Figure 5.4) a full scale, where at reduced scale this refinements become 0.357 mm, and so, we neglect the refinements related to the ground also.

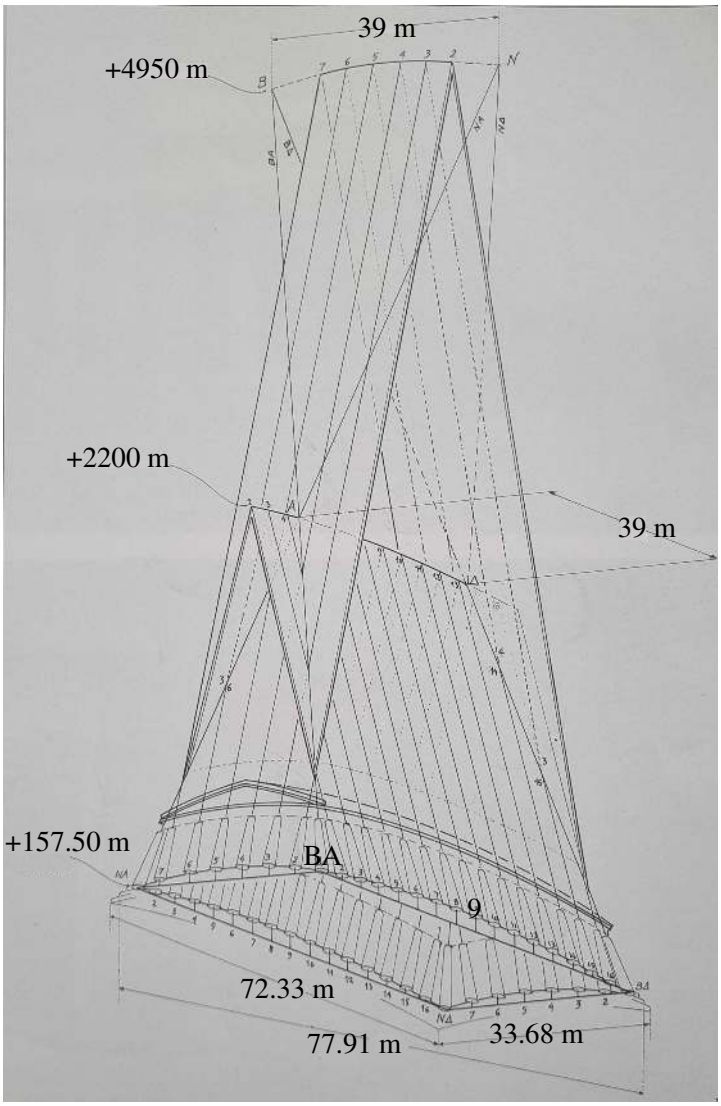


**Figure 5.4:** Parthenon optical illusions details of the columns and base, Tournikiotis (1994).

### 5.2.3 Columns

The forty-six external columns have a diameter of 1.91 m and a height of 10.43 m (labeled as (1) in Figure 5.2). Each column consists of ten drums weighing between five and ten tons, and a capital with a breadth of 2.045 m (average of 2. to 2.09 m) and a weight of eight to nine tons. The column shafts are fluted with 20 shallow vertical grooves. In Doric columns, entasis involves a slight reduction in diameter as the column rises from the base towards the top. The value of the entasis is adopted from Korres et al. (1999). Figure 5.5 shows a vertical section of the Doric column.

Twelve internal columns (labeled as (2) in Figure 5.2), have a diameter of 1.72 m and a height of 9.65 m. Each consists of eleven drums, and a capital with a breadth of 1.75 m. The column shafts are fluted with 20 shallow vertical grooves. The internal Doric column details are given in Figure 5.6.

Four columns in the west chamber "opisthodomos" (labeled as (3) in Figure 5.2), have


**(a)** Front side.

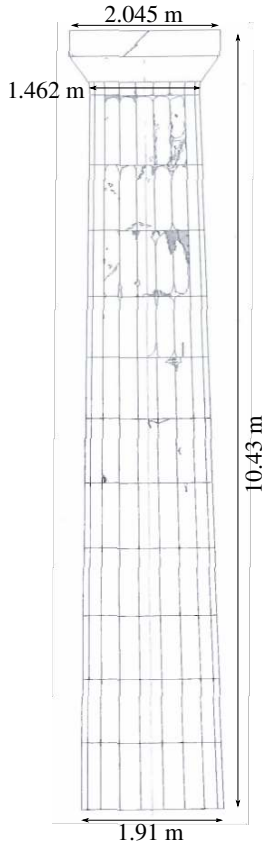


**(b)** Doric column architectural details.

**Figure 5.5:** Doric columns view on the front side of the Parthenon (a) and architectural details (b), (Korres et al., 1999).

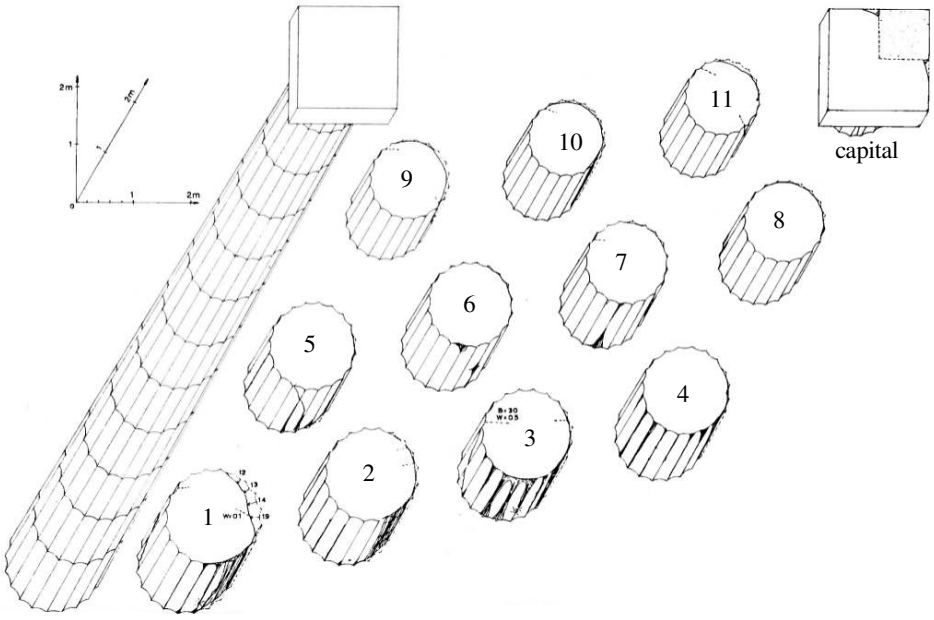


**Figure 5.6:** Parthenon internal Doric column details, Tournikiotis (1994).

a diameter of 1.32 m and a height of 12.5 m. Each consists of eleven drums, and a capital with a breadth of 1.35 m. The column shafts are fluted with 20 shallow vertical grooves.

Details of the west chamber columns are provided in Figure 5.7. The columns follow thee Ionic order or a very early form of the Corinthian order, (Tournikiotis, 1994).

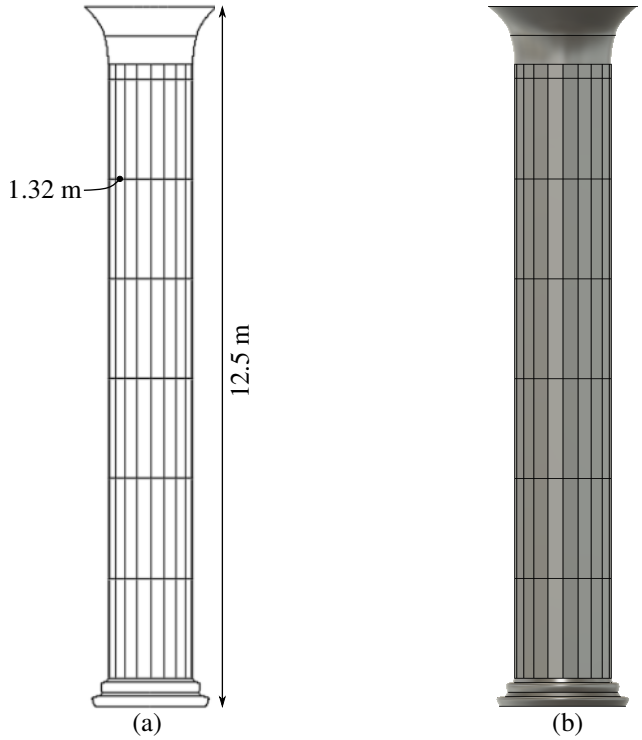


**Figure 5.7:** Parthenon west chamber column cross section (a), and 3D view (b), Tournikiotis (1994)

The columns of the cella are Doric, they have 16 flutes and they form a two story colonnade (that is, one colonnade on top of another), see Figure 5.8. The total height of the two story colonnade is 12.7 m with 23 columns on each level. The shafts of the upper columns are monolithic. The diameter of each column is 1.12 m. The first level has 9 flutes with capital on the top, and then an architrave of thickness 1.15 m, width 1.13 m connected between the center of the consecutive columns (refer to Figure 5.8). This followed by another 5 flutes with capital on top.

### 5.2.4 Architrave

The architrave (see Figure 5.3), is one block high (1.35 m) and three blocks thick (1.80 m). It consists of 138 (= 3 x 46) blocks measuring 4.30 m in length for the regular intervals and up to 4.70 m for the corners (refer to Figure 5.9).

### 5.2.5 Masonry wall

Parthenon walls are of 9.652 height and are composed of 17 rows of blocks; two layer of blocks at each row with bigger blocks at the first row (of height 1.700 m) and then of 0.497 m height, Tournikiotis (1994).

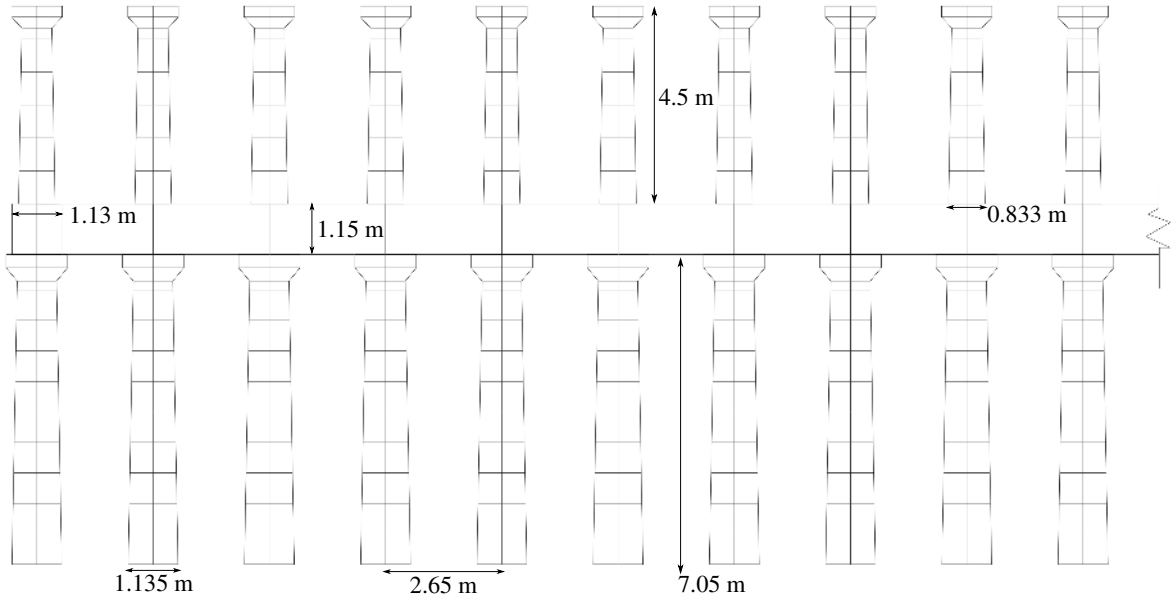


**Figure 5.8:** Parthenon cella chamber north section, Tournikiotis (1994).

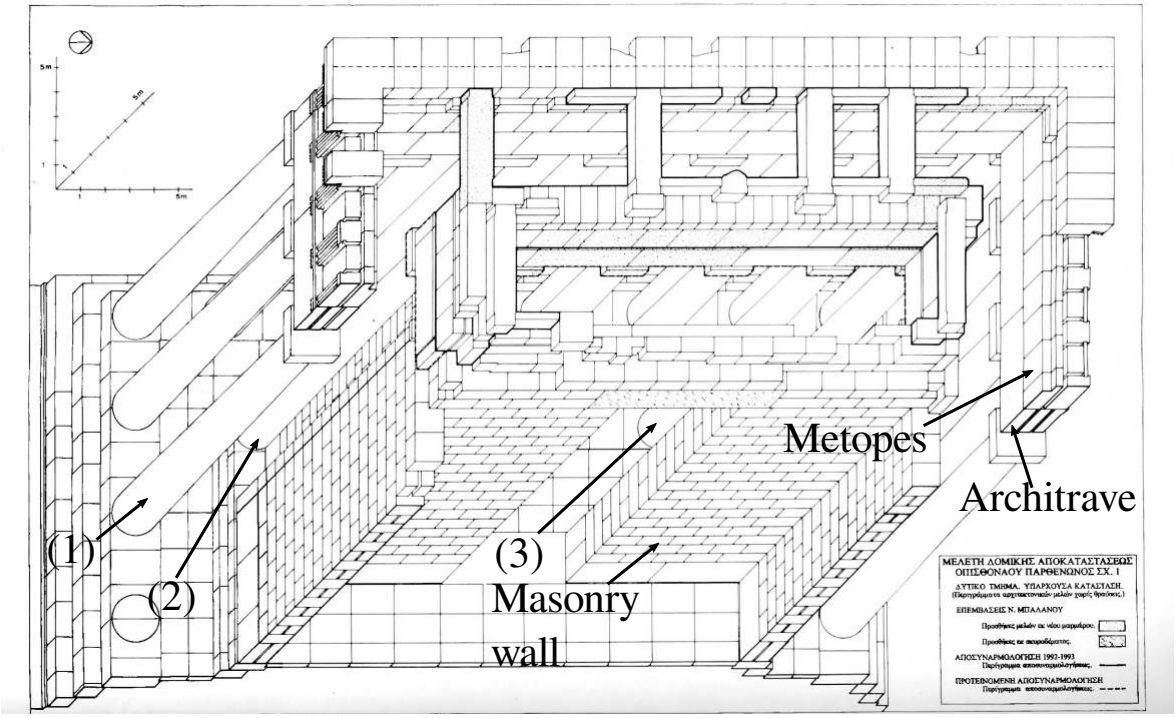


**Figure 5.9:** Parthenon vertical section, Tournikiotis (1994)

## 5.3 3D printing and installation

The adopted reduced scale is $\lambda = 1/70$ and $\gamma = 0.667$ and the model has been printed using the stereolithography 3D SLA 3L printer (see Chapter 1) and Rigid 10K resin. The density of the printed parts is 1800 kg/m$^3$. The following parts have been considered for the design of the model: 1) Base, 2) External columns, 3) Internal columns, 4) Cella column, 5) West chamber column, 6) Architrave, and 7) Masonry walls.

A meticulous attention was given to treat each block in order to achieve the same

friction angle as the prototype (around 35°, in accordance with the friction angle of marble stones). Using an inclinometer with a precision of ±0.1 mm, measurements of the friction angle between the blocks of the external Doric column are summarized in Table 5.1 (10 measurements were performed to reduce uncertainties).

**Table 5.1:** External Doric column friction angle.

| M# | B1-2 | B2-3 | B3-4 | B4-5 | B5-6 | B6-7 | B7-8 | B8-9 | B9-10 | B10-11 | B11-top | $\mu(\varphi)$ | $\sigma(\varphi)$ |
|---|---|---|---|---|---|---|---|---|---|---|---|---|---|
| 1 | 32.8 | 41.2 | 34.9 | 34 | 34.5 | 36 | 40 | 41.1 | 34.4 | 41 | 34.5 | 36.76 | 3.030 |
| 2 | 32.7 | 39 | 36 | 35 | 36 | 35.7 | 40.5 | 39.1 | 35.3 | 40 | 35.3 | 36.78 | 2.256 |
| 3 | 33 | 40.2 | 35 | 35.2 | 35.9 | 35.5 | 41.2 | 38.2 | 34.5 | 40.5 | 36 | 36.84 | 2.504 |
| 4 | 33.5 | 39.5 | 34.2 | 35.5 | 35.2 | 35 | 40.8 | 40.1 | 35.1 | 40.9 | 34.9 | 36.79 | 2.624 |
| 5 | 32.5 | 41 | 35.5 | 34.8 | 36.2 | 34.6 | 41.5 | 38.7 | 35.5 | 40.2 | 35.5 | 36.91 | 2.701 |
| 6 | 33 | 38.9 | 35.3 | 34.5 | 34.9 | 36.5 | 40.1 | 39.2 | 34.9 | 40.7 | 34.8 | 36.62 | 2.401 |
| 7 | 33.1 | 41.5 | 36.2 | 36.5 | 35 | 35.1 | 40.4 | 39 | 34.2 | 40 | 35 | 36.91 | 2.586 |
| 8 | 32.9 | 40.5 | 35 | 35.9 | 34.7 | 35.2 | 41.6 | 39.3 | 35.1 | 39.5 | 34.9 | 36.78 | 2.630 |
| 9 | 33.5 | 40.8 | 34.5 | 34.7 | 36.5 | 34 | 40.5 | 38.2 | 36 | 40.9 | 35 | 36.78 | 2.596 |
| 10 | 33.2 | 41 | 34 | 34.6 | 34 | 34.5 | 41 | 39.2 | 35.7 | 40.2 | 35.7 | 36.65 | 2.792 |
| $\mu(\varphi)$ | 33.02 | 40.36 | 35.06 | 35.07 | 35.29 | 35.21 | 40.76 | 39.21 | 35.07 | 40.39 | 35.16 | 36.78 | 2.547 |
| $\sigma(\varphi)$ | 0.292 | 0.841 | 0.650 | 0.663 | 0.742 | 0.675 | 0.503 | 0.782 | 0.528 | 0.444 | 0.414 | 0.086 | 0.191 |

Where B1-2 is the contact surface between top of drum-1 and bottom of drum-2, B2-3 is the contact surface between top of drum-2 and bottom of drum-3, etc. and B11-top is the contact surface between top of drum-11 and bottom of the capital of the Doric column, $\mu(\varphi)$ is the mean of the friction angles, and $\sigma(\varphi)$ is the standard of deviation.

The following order of construction has been followed: 1) base, 2) walls (block by block), 3) external columns, 4) internal columns and 5) architrave (see Figures 5.10, 5.11, 5.12, 5.13). The Parthenon blocks are installed above each other without the use of mortar (no mortar has been also used in the prototype; this technique, known as dry stone construction, showcases the exceptional craftsmanship of ancient Greek architects and masons). The number of blocks of the Parthenon model are provided in Table 5.2.

**Table 5.2:** Parthenon model: number of blocks.

| Type | Nb. per element | Nb. of elements | Total number |
|---|---|---|---|
| **Columns** | | | |
| External Doric column | 12 | 46 | 552 |
| Internal Doric column | 12 | 12 | 144 |
| West chamber column | 9 | 4 | 36 |
| Cella column | 16 | 23 | 368 |
| **Beams** | | | |
| Architrave | 3 | 46 | 138 |
| Cella beams | 1 | 22 | 22 |
| **Walls** | | | |
| External walls | | 2924 | |
| Internal walls | | 510 | |
| **Total** | | 4694 | |

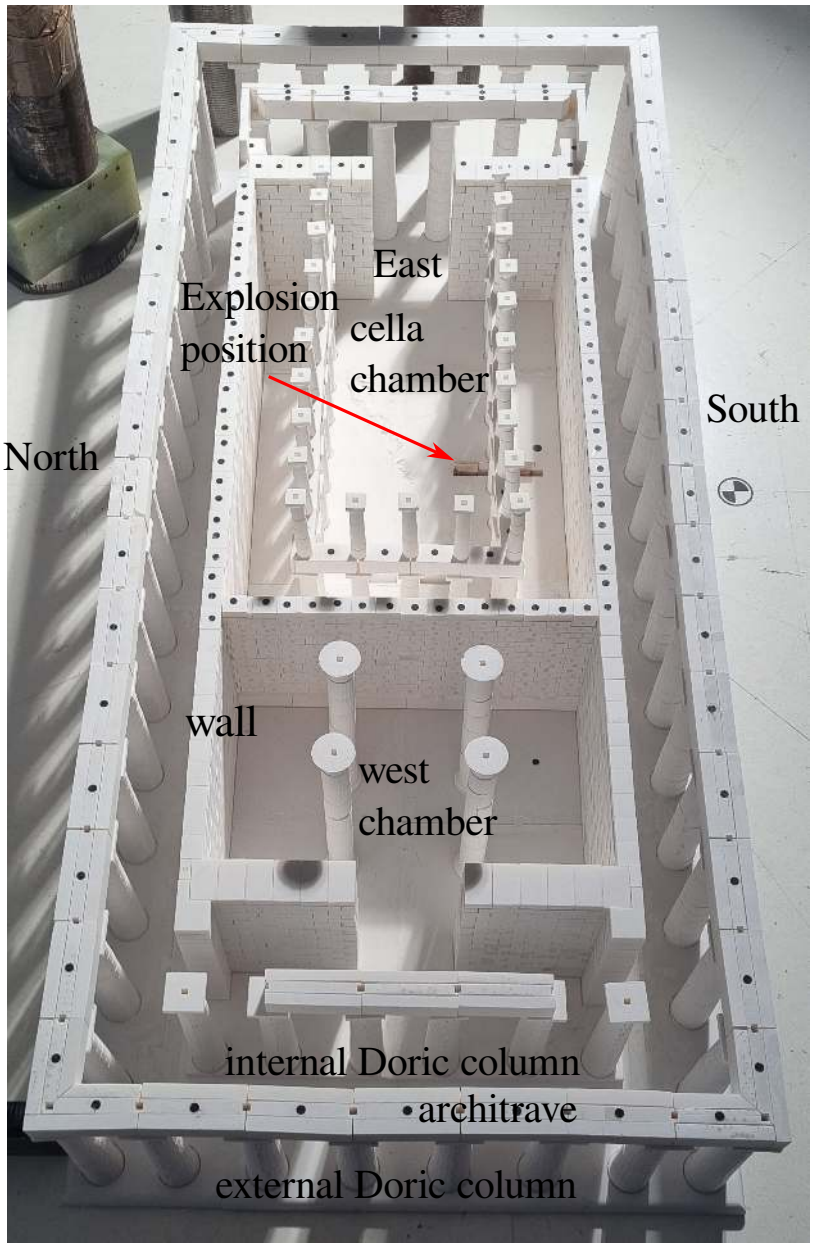


**Figure 5.10:** Parthenon model: top view.

**Figure 5.11:** Parthenon model: south view.

**Figure 5.12:** Parthenon model: west view.

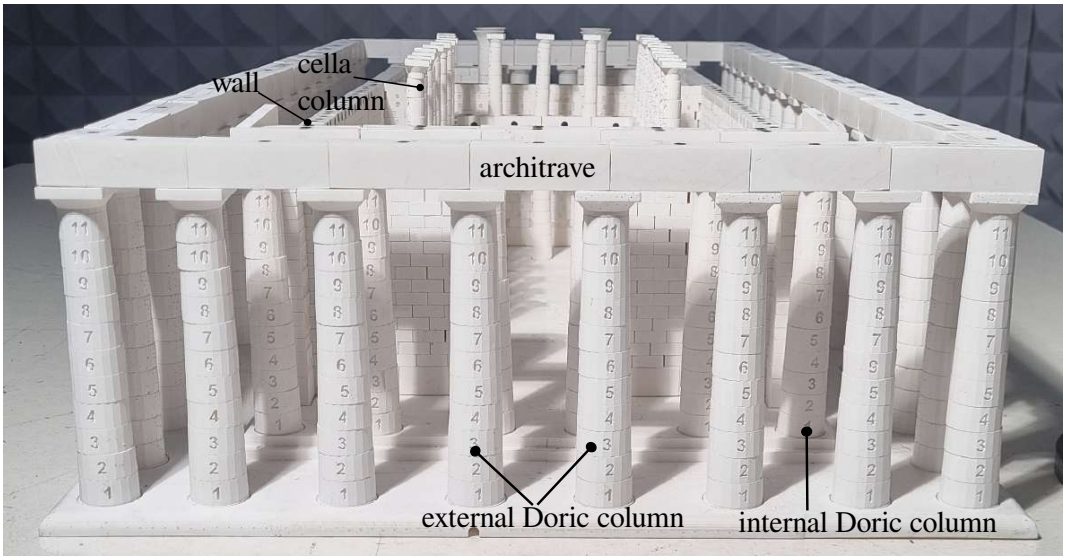


**Figure 5.13:** Parthenon model: east view.

## 5.4 Test

One experiment has been performed with the following conditions: wire length 3.6 cm, wire diameter 0.6 mm, and $E_C = 13$ kJ. The explosion position has been decided based on the real explosion 1687 event, see Figure 5.10. Three GoPro11 cameras were used to film the event and to do PTV measurements, Figure 5.14.

The Parthenon model after the explosion is shown in Figure 5.15. It is worth noticing that the explosion lead to the destruction of the walls in the cella area and to the cella columns. The time evolution of the event shows that destruction starts around 8.33 ms and completes at 1.04 s (Figure 5.16).
Furthermore, we can clearly see a symmetrical collapse of the wall at 20 ms, indicating a spherical shock wave, Figure 5.17. Additionally, we should notice that the explosion in real happened as confined explosion[2] where the effect of the explosion will be much

[2]A confined explosion refers to an explosion that happened within a closed space, such as a building, tunnel, or other structure.

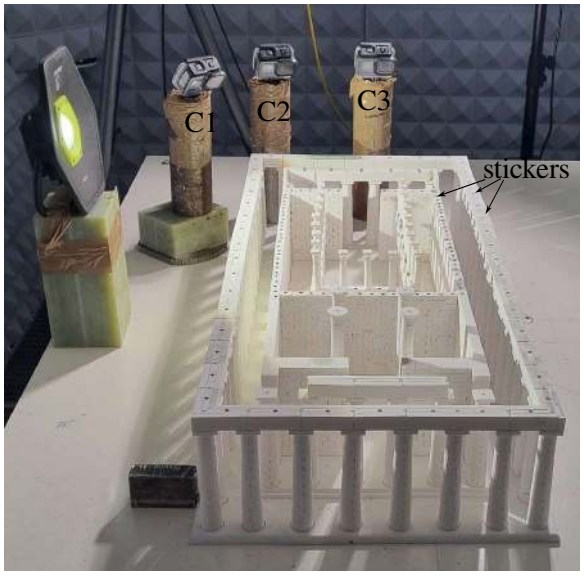


**Figure 5.14:** Parthenon model: the position of the three GoPro11 cameras (C1, C2 and C3).

**Figure 5.15:** Parthenon model after the explosion.

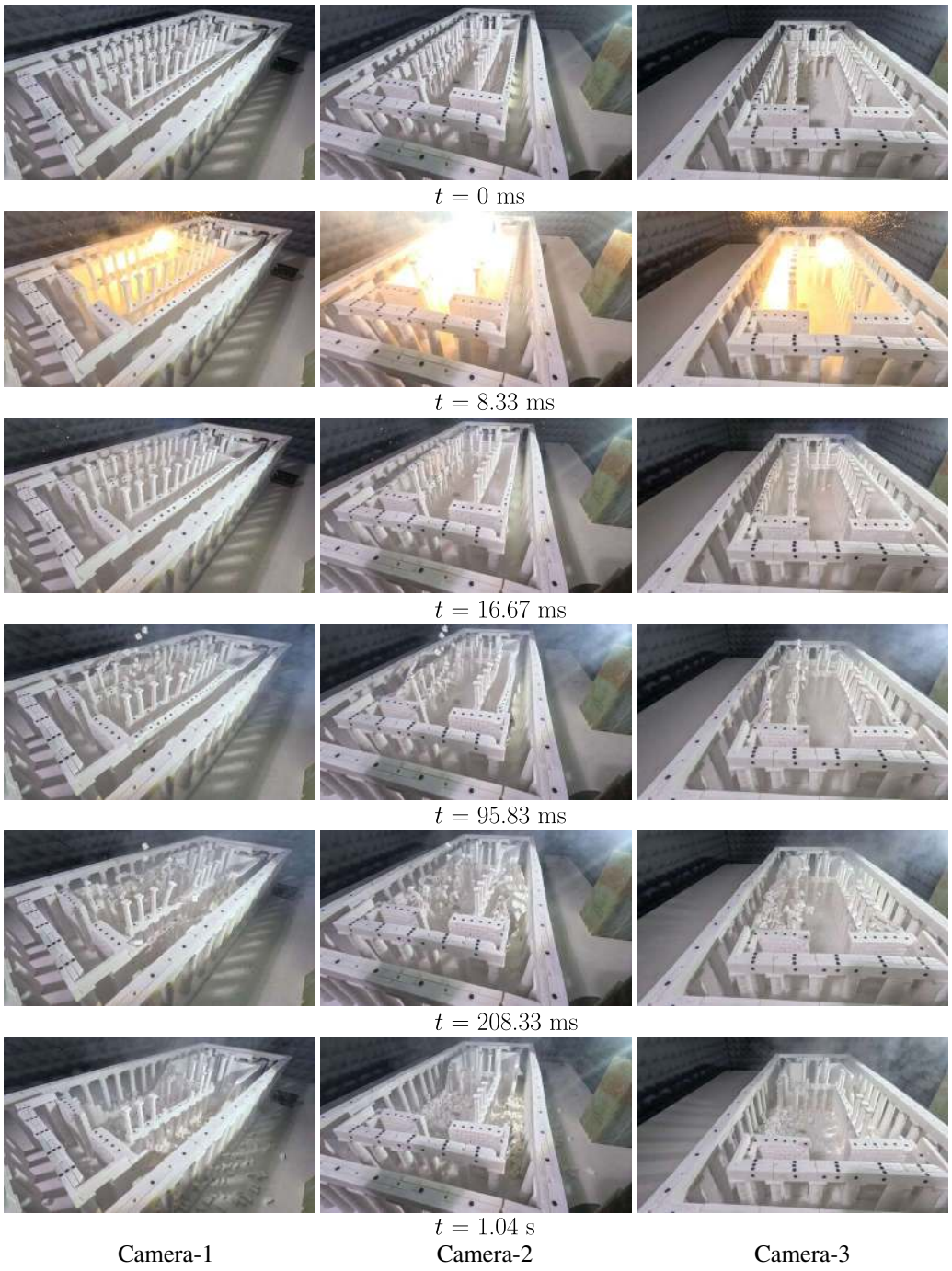


**Figure 5.16:** Parthenon model: time evolution of the destruction event (captured by GoPro cameras at speed 240 fps and resolution 2704 × 1520 pixels).

bigger than in our case as we don't have the roof. Adding to that the partial failure of the roof that will be responsible to even more destruction to the Parthenon. Though, during the explosion a big destruction happened to the walls and cella columns, as well as displacement related to the external columns.

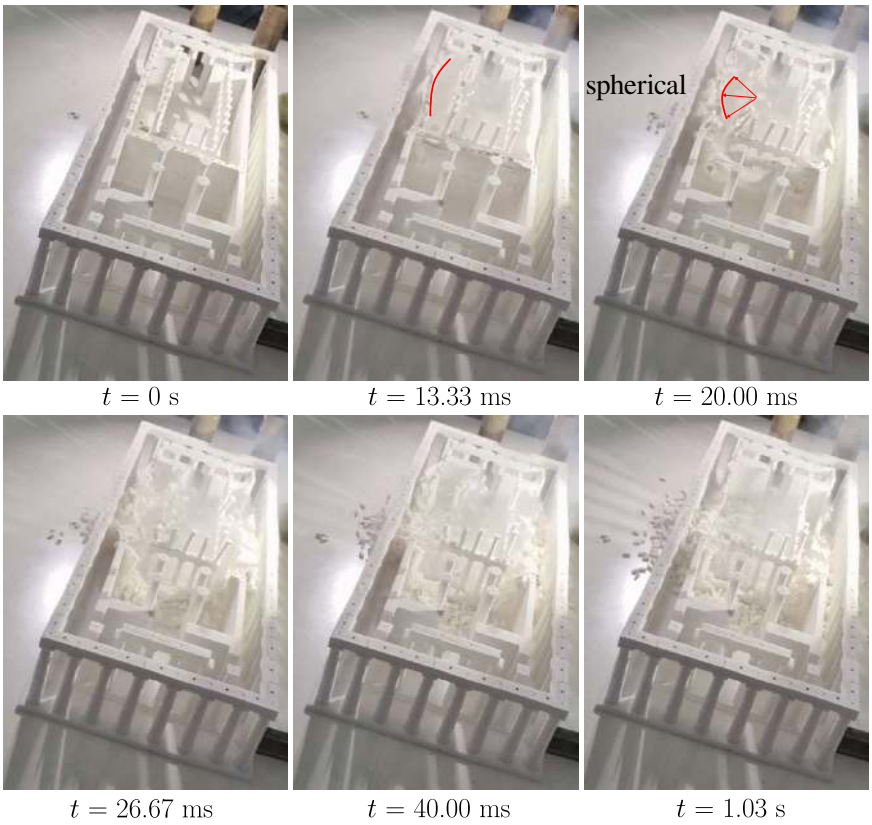


**Figure 5.17:** Parthenon model: time evolution of the destruction event (captured by a mobile phone at speed 30 fps and resolution 474 × 624 pixels), indicating a spherical shock wave at t=20 ms.

## 5.5 Measuring trajectory through PTV analysis

In this part we show the tracking of point P1 placed on the capital of cella column as it present a clear trajectory (see Figure 5.18). It is worth noticing that we are able to track all the visible sticker presented in Figure 5.14. As explained in Chapter 4 three cameras used in our experiments and they are positioned as shown in Figure 5.14. Moreover, same protocol presented in Chapter 4, is followed to perform the calibration and post-processing of the data. Figure 5.18, we show the tracking of point P1 for different time frames. The capital is shafted due to shock wave about $u_2 = 37.7$ mm ($u_1 = 40$ mm and $u_3 = 14.1$ mm) above the initial position then it goes down to reach $u_2 = -110$ mm ($u_1 = -2.6$ mm and $u_3 = 4.6$ mm). Moreover, the capital reach a velocity $v_2 = 628.4$ mm/s ($v_1 = 388.5$ mm/s and $v_3 = 178.5$ mm/s) while goes up, and $v_2 = -1204.2$ mm/s ($v_1 = -2243.1$ mm/s and $v_3 = 22.4$ mm/s) when fall down.

## 5.6 Comparison between the reduced-scale and full-scale response

We have the model collapse shown in Figure 5.19(a) and the prototype collapse shown in Figure 5.19(b). The current version of the Parthenon has been restored to simulate the situation after the explosion, which makes the comparison meaningful, (Korres et al., 1999). Differences marked in red in Figure 5.19 indicate a total collapse in the real explosion

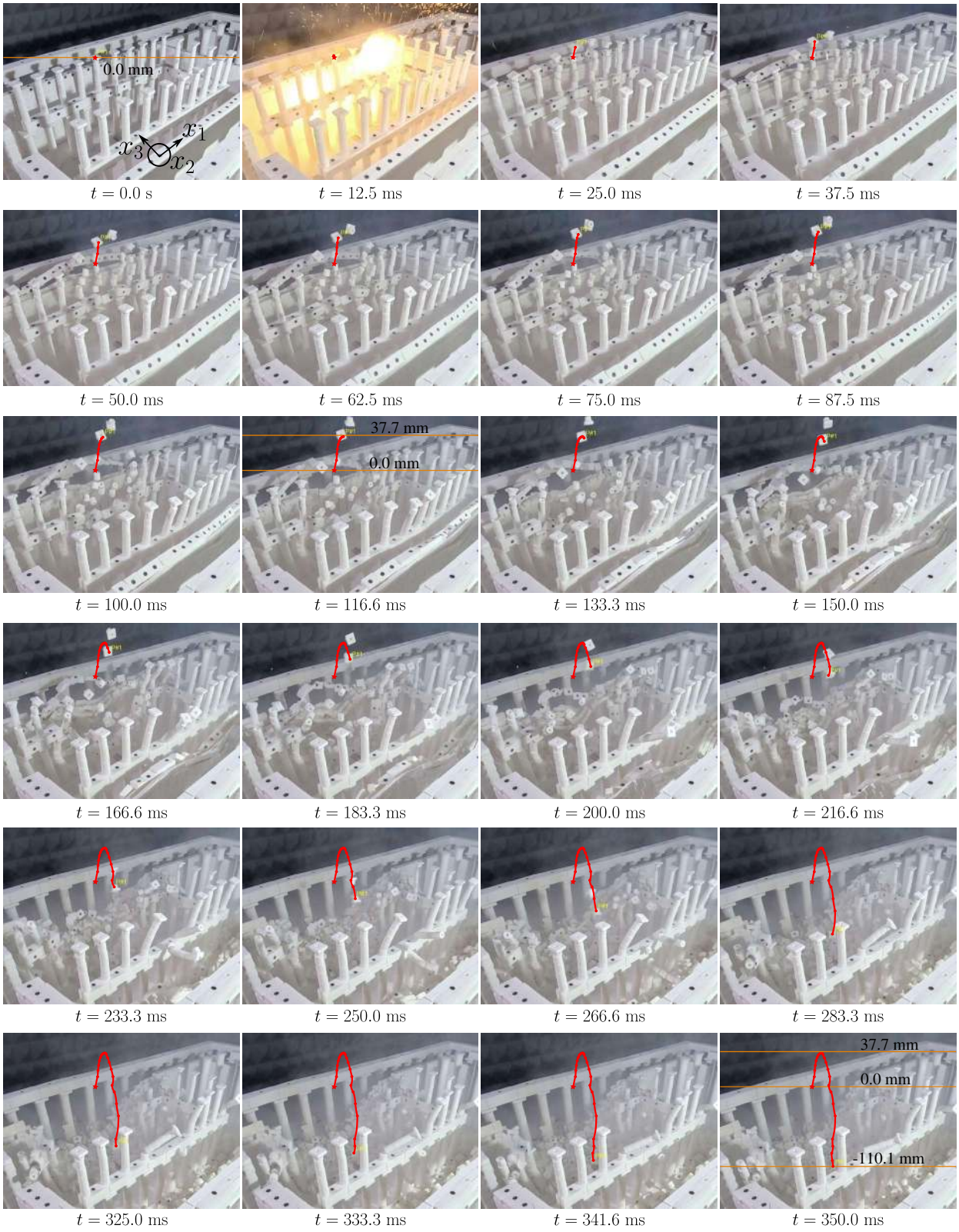


**Figure 5.18:** Three GoPro11 (C1, C2 and C3) positioned on the top of the Parthenon with the stickers to do PTV.

but not in the reduced-scale explosion. However, a qualitative agreements (collapse or non-collapse) are marked in blue, while the green ellipse highlights areas where we observe

the same failure position in both the model and prototype. A good qualitative agreements are observed with some discrepancies between the model and prototype. This can be attributed to the fact that the explosion in the real case is confined (due to the presence of the roof). The failure from the roof is responsible for larger collapses in the Parthenon due to partial failure.

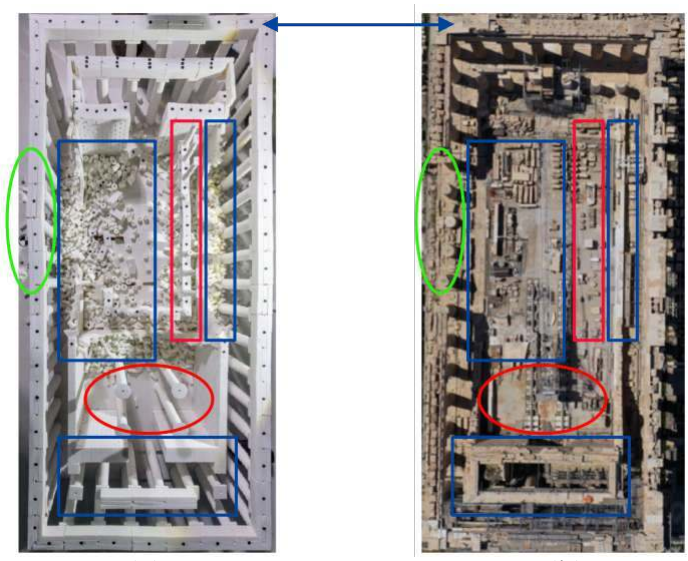


**Figure 5.19:** Comparison between the collapse of the Parthenon of Athens in the model (a) and the prototype (b).

## 5.7 Concluding remarks

In this chapter we presented as a proof of concept the modeling of the explosion of the Parthenon in Athens that occurred in 1687. It is entirely reconstructed (excluding the roof) from its real architecture, using a 1/70 scale model fabricated by using SLA 3D-printed. It is then subjected to an explosion created inside the structure. The displacement and velocity of the capital of Cella columns are calculated based on PTV analysis. It is worth noting that we are able to track the displacement of any stickers visible in the presented frame (see Figure 5.16). This chapter thus demonstrates the capability of the platform (miniBLAST) to study complex structures of considerable size. It also provides an idea of potential future uses to study different structures type or for model validations.

# Conclusions and future work

## 5.8 Concluding remarks

The main objectives of this Thesis were:

1. Design and install a novel experimental platform to study the dynamical response of masonry structures subjected to blast loads at reduced scale in the laboratory.

2. Analyze the explosive source by means of inherent explosion mechanism, the subsequent blast-induced shock wave, the TNT equivalence, and spatial distribution of the pressure.

3. Experimentally validate the scaling laws focusing on rocking and overturning response mechanisms.

4. Study the Parthenon of Athens at reduced scale in the laboratory, as an example of a complex structure subjected to an internal blast.

The manuscript is comprised of five Chapters, whose main developments and findings are summarized below.

**Chapter 1** The first Chapter focuses on the design and installation of the experimental setup to study masonry structures at reduced scale. To this end, we designed a novel experimental setup that facilitates the safe investigation of structural responses to explosions in a controlled laboratory environment. The experimental safety is investigated by measuring the maximum sound level reached during the experiments. This is found to be 110 dB which is below the allowable limit according to French regulations (130 dB). The proposed setup allows us to recreate blast scenarios in a safe and controlled manner.

**Chapter 2** In this Chapter, we analyzed the electric circuit system as well as the phenomena and mechanisms related to the explosive source governing the formation of the shock waves. We derived the current and voltage equations, where the measurements of the signals shows that we are in the *under-damped case*. We identified the overall effective values of the electrical resistance, inductance, and capacitance of the pulse current generator discharge circuit by means of a least-squares regression. The effective value of the capacitance is found to be close to the nominal value with $C = 389.165$ $\mu$F. This is followed by explaining in details the fourth stages prior to the formation of blast wave: (S1) current discharge and wire's melt, (S2) formation of onduloids, (S3) electrical breakdown and appearance of electric arcs, and (S4) formation of pressure shock waves. Finally, we identified the inductance $L_W$, which is two order of magnitude lower than the inductance of the discharge circuit ($L = 2.883$ $\mu$H) and thus can be neglected for the problem at hand. Moreover, we estimated the evolution of the electrical resistance $R_W$ of the wire during

the discharge, where a maximum value of $R_W = 1.726\ \Omega$ reached at stage S3. Additionally, energy dissipated in the aluminum wire is computed and found to be around 800 J, as well as, an estimation of the temperature raise during the discharge which estimated to reach 12000 K.

**Chapter 3** After a brief explanation related to the explosive source circuit and the identification of the circuit parameters and wire characteristics, this Chapter presented an analysis of the shock wave pressure based on incident overpressure measurements. First we corroborated the correct installation of the explosive source and the corresponding blast loading, as well as the robustness and repeatability of the latter. Incident overpressures were captured for different standoff distances $D$ from the analogue explosive charge and different energy levels $E_C$ stored in the capacitor. There, we showed that the incident pressure increases as $E_C$ increases, while it decreases with the increase of $D$. Moreover, the shock wave speed is calculated which is varies between a maximum of 817 m/s and a minimum of 370 m/s and it is found to decrease at increasing standoff distances -– this is in agreement with all other high explosives (i.e. PETN). Additionally, we studied the shock wave pressure distribution, which can be interpreted as a good approximation of the shock wave's shape. The latter was found to be of elliptical shape at relatively small standoff distances and almost (hemi-)spherical at larger distances. Finally, we calculated the TNT equivalence factor in terms of overpressure peak, $P_{so}$, and scaled positive impulse, $i_{sow}$. We observed a significant contrast in the equivalence factor values for small-scale distances between $P_{so}$ and $i_{sow}$, while at larger scaled distances, the two definitions tend to converge to the same value which is around 0.1. Finally, we calculated the equivalent TNT mass, $m^{\text{eq}}_{\text{TNT}}$, corresponding to the explosive analogue utilized in this work. We found that $m^{\text{eq}}_{\text{TNT}} \in [10, 280]$ mg, for the energy levels and standoff tested.

**Chapter 4** In this Chapter we presented the accuracy of the particle tracking velocimetry analysis for measuring the rigid-body motion of rocking/overturning blocks with a relative accuracy equal to $\pm 0.112$ mm. A high repeatability was found in the results of the model and prototype which enabled a first order validation of the scaling laws proposed in (Masi et al., 2022). Moreover, in rocking case we found that the linear displacement and velocity are found to be overall similar during the first and second peaks for the model and the prototype, while they differ for the subsequent rocking impacts. In the overturning scenario, we noticed that both the model and the prototype yield the same overall response. This similar response is due to the fact that the blast loading (impulse) resulting from the scaling laws is indeed similar between the model and the prototype and the difference in time evolution is related to boundary conditions.

**Chapter 5** This chapter presented the construction, the design details, and the experimental (reduced-scaled) explosion of an intricate masonry structure: the Parthenon of Athens. The Parthenon model was printed at scale 1/70 including the external and internal Doric columns, the cella columns, the west chamber columns, the architraves, and the masonry walls. The explosion of the model enabled to observe the predominant collapse mechanisms that happened in the Parthenon during its explosion in 1687. These preliminary results showed the capability of the platform we designed – miniBLAST – to perform different explosion scenarios but also to study complex structures at reduced scale.

## 5.9 Key contributions

For the sake of clarity, we detail, in the form of a list, the principal and secondary findings and developments of our study:

- A novel experimental platform (miniBLAST) to study the dynamical response of reduced-scale masonry structures subjected to blasts was designed and installed. We provided a detailed description including the methodology adopted and reasoning behind the design and installation of the platform as well as the validation of the experimental safety (see Chapter 1). This lies on a safety protocol that can be used in other applications where the sound safety is required (see Appendix A).

- A detailed presentation of the data acquisition devices, sensors, and cameras can be found in Section 1.7). Additionally, we developed and designed LabVIEW software that we used to record and collect data from our sensors (see Section C.1). Furthermore, we conducted an uncertainty analysis detailing all errors associated with the sensors and devices in Section C.2.

- The detailed analysis of the exploding wire system includes a numerical derivation of electrical circuit equation, the characterization of the circuit parameters, and a detailed explanation of the explosion mechanism. This study shed light on the influence of electric circuit system on shock wave formation.

- Moreover, we resolved issues related to thermal transient noises that happened in piezoelectric pressure transducers, which significantly affected our results and led to large negative pressure in our signal. These thermal transients occurred due to high temperature raise (estimated around 12000 K) during our experiments (see Appendix D).

- A high repeatable shock wave is obtained (see Section 3.3). This contributes to achieve repeatable effects on structures (see Section 4.4).

- The energy stored ($E_C$) and standoff distances ($D$) were found to influence the incident overpressure. An increase in $E_C$ results in higher incident pressure, while an increase in $D$ leads to a decrease in incident overpressure, and vice versa.

- Moreover, shock wave speed was found to be supersonic, confirming our assumption about impulsive load. Our findings are in accordance to other high explosive sources (i.e. PETN).

- Shock wave shape by means of pressure distribution was investigated, showing an elliptical shape at close distances (around 30 cm) that transitions into a spherical or hemispherical shape at greater distances (around 50 cm), see Section 3.4.3.

- We calculated the TNT equivalence factor based on both the incident peak overpressure and the incident peak reduced impulse (see Section 3.5), which was found to be approximately 0.1 at larger distances.

- We introduced the PTV system, covering system calibration, verification, and distortion correction (see Section 4.3). The achieved accuracy, approximately $\pm 0.112$ mm, was sufficient for the scenarios and applications considered in this work. The measurements was conducted using GoPro11 cameras. Our application demonstrates the feasibility

of using such cameras for measurements in fast dynamic experiments, provided all necessary requirements are verified.

- We investigated the rocking and overturning responses of blocks at varying scales. Our findings validates that we accurately scaled the incident impulse based on scaling laws, facilitating the study of reduced-scale structures on the experimental platform developed within this work.

- Based on scaling laws, we replicated the Parthenon of Athens in reduced scale, 3D printed and tested under blast loads in the laboratory. This experiment demonstrates the capability of our platform for safely performing experimental tests on masonry structures in the laboratory (see Chapter 5). Moreover, we are able to track particles and parts by measuring the 3D rigid body motion using Particle Tracking Velocimetry (PTV).

## 5.10 Perspectives

In this Thesis, we focused on designing and installing a novel experimental platform that allow us to investigate the response of masonry and blocky structures to explosions in a reduced-scale environment. This work sets the foundations for substantially broader investigations and provides new tools to study the effects of blast on structures and their mitigation. The main perspectives are detailed below.

- In the conducted experiments, we focused on specific scenarios related to the explosive source, considering fixed length, diameter, and height of the exploding wire. To explore substantially more kinds of explosions via the proposed platform, the study of other scenarios is necessary. To this end, one future direction is given by the investigation of the impact of (*i*) the wire position (height), (*ii*) its length, and (*iii*) its diameter. This will allow us to see the variation of pressure distribution and shock wave shape.

- We validated the scaling laws for a specific value of $\lambda$ (see Chapter 4). The obtained results revealed a possible strong influence of the boundary conditions employed to constraint free-standing blocks to rock and overturn in a two-dimensional plane. Further experiments will be undertaken to understand the effect of these boundary conditions. In parallel, testing the response of prototypes and models for different values of $\lambda$ and $\gamma$ will help us to better investigate the (limits of) validity of the scaling laws.

- The experiment we conducted for a reduced-scale model of the Parthenon consists of an ideal benchmark of the capabilities offered by the proposed experimental platform. In upcoming experiments, we will consider the presence of those structural components neglected in the aforementioned test (e.g., the roof) and will adapt the electrical circuit to generate even larger (reduced-scale) explosions by increasing the energy levels stored within the capacitor.

# Bibliography


F. AFNOR. European standard nf en 12973. *AFNOR*, Juin, 2000.

S. Ahmad, A. Elahi, H. Pervaiz, A. Rahman, and S. Barbhuiya. Experimental study of masonry wall exposed to blast loading. *Materiales de Construcción*, 64(313):e007–e007, 2014.

M. Arrigoni, F. Bauer, S. Kerampran, J. Le Clanche, and M. Monloubou. Development of a pvdf pressure gauge for blast loading measurement. *Human Factors and Mechanical Engineering for Defense and Safety*, 2(1):2, 04 2018. ISSN 2367-2544. doi: 10.1007/s41314-018-0012-2. URL https://doi.org/10.1007/s41314-018-0012-2.

Asair. Ventilation system. www.asair.fr, 2023.

W. E. Baker, P. S. Westine, and F. T. Dodge. *Similarity methods in engineering dynamics: Theory and practice of scale modeling*. Elsevier Science Limited, 1991.

F. Banci, E. Hervé-Secourgeon, B. Richard, F. Voldoire, and I. Zentner. New advances in the seismic analysis of nuclear structures and equipment from the sinaps project. In *Proceedings of the SINAPS Conference*, May 2018.

A. Barnard. Isis destroys historic arches in palmyra, syria. *New York Times*, 2015.

F. D. Bennett. Cylindrical Shock Waves from Exploding Wires. *The Physics of Fluids*, 1(4):347–352, 07 1958. ISSN 0031-9171. doi: 10.1063/1.1705893. URL https://doi.org/10.1063/1.1705893.

A. Borsov, B. Gelfand, V. Kudinov, B. Palamarchuk, V. Stepanov, E. Timofeev, and S. Khomik. Shock waves in water foams. In A. OPPENHEIM, editor, *Gasdynamics of Explosions and Reactive Systems*, pages 1027–1033. Pergamon, 1980. ISBN 978-0-08-025442-5. doi: https://doi.org/10.1016/B978-0-08-025442-5.50010-X. URL https://www.sciencedirect.com/science/article/pii/B978008025442550010X.

H. C. C. Sound pulse approximations to blast loading (with comments on transient drag). *Technical Report SC-TM-191-55-51, Sandia Corporation, MD, USA.*, 8 1955. URL https://www.osti.gov/biblio/10153565.

W. G. Chace and H. K. Moore, editors. *Exploding Wires*. Springer New York, NY, 1 edition, 1968. ISBN 978-1-4899-7330-6. doi: 10.1007/978-1-4899-7328-3. URL https://doi.org/10.1007/978-1-4899-7328-3. Copyright Springer Science+Business Media New York 1968.

K. Chandler, D. Hammer, D. Sinars, S. Pikuz, and T. Shelkovenko. The relationship between exploding wire expansion rates and wire material properties near the boiling temperature. *IEEE Transactions on Plasma Science*, 30(2):577–587, 2002.

Charles. *The 1923 Great Kantō Earthquake: The History and Legacy of the Earthquake That Destroyed Tokyo*. Charles River Editors, 2014.

M. Chiquito, R. Castedo, L. M. López, A. P. Santos, J. M. Mancilla, and J. I. Yenes. Blast wave characteristics and tnt equivalent of improvised explosive device at small-scaled distances. *Def Sci J*, 69(4):328–335, 2019.

J. P. Chittenden, S. V. Lebedev, J. Ruiz-Camacho, F. N. Beg, S. N. Bland, C. A. Jennings, A. R. Bell, M. G. Haines, S. A. Pikuz, T. A. Shekovenko, and D. A. Hammer. Electron thermal transport in solid targets irradiated by intense picosecond laser pulses. *Physical Review E*, 61(4):4370–4380, 2000. doi: 10.1103/PhysRevE.61.4370.

P. W. Cooper and S. R. Kurowski. *Introduction to the Technology of Explosives*. Wiley, January 1997. ISBN 978-0-471-18635-9. About the Author: Paul W. Cooper is the author of Introduction to the Technology of Explosives, published by Wiley. Stanley R. Kurowski is the author of Introduction to the Technology of Explosives, published by Wiley.

K. Cranz. *Lehrbuch der ballistik*. Julius Springer, 1925.

R. J. Cunrath and M. Wickert. Numerical analysis of the response of thick wires to extreme dynamic electromechanical loads. *IEEE Transactions on Plasma Science*, 44 (1):121–127, 2015.

E. Del Prete, A. Chinnayya, L. Domergue, and et al. Blast wave mitigation by dry aqueous foams. *Shock Waves*, 23:39–53, February 2013. doi: 10.1007/s00193-012-0400-0. URL https://doi.org/10.1007/s00193-012-0400-0.

Departments of the Army, the Navy, and the Air Force. Structures to resist the effects of accidental explosions. Technical report, Chairman, Department of Defense Explosives Safety Board, November 1990. Army TM 5-1300, NAVY NAVFAC P-397, AIR FORCE AFR 88-22.

P. D. Desai, H. James, and C. Y. Ho. Electrical resistivity of aluminum and manganese. *Journal of Physical and Chemical Reference Data*, 13(4):1131–1172, 1984.

J. Dewey. The tnt equivalence of an optimum propane–oxygen mixture. *Journal of Physics D: Applied Physics*, 38:4245, 11 2005. doi: 10.1088/0022-3727/38/23/017.

J. M. Dewey. *Measurement of the Physical Properties of Blast Waves*, pages 53–86. Springer International Publishing, Cham, 2016. ISBN 978-3-319-23745-9. doi: 10.1007/978-3-319-23745-9_2. URL https://doi.org/10.1007/978-3-319-23745-9_2.

I. Djeran-Maigre, A. Morsel, L. Briançon, E. Delfosse, D. Levacher, and A. Razakamanantsoa. Uses of usumacinta river sediments as a sustainable resource for unpaved roads: An experimental study on a full-scale pilot unit. *Transportation Engineering*, 9: 100136, 2022a. ISSN 2666-691X. doi: https://doi.org/10.1016/j.treng.2022.100136. URL https://www.sciencedirect.com/science/article/pii/S2666691X22000343.

I. Djeran-Maigre, A. Morsel, M. Hussain, D. Levacher, A. Razakamanantsoa, and E. Delfosse. Behaviour of masonry lateral loaded walls made with sediment-based bricks from the usumacinta river (mexico). *Cleaner Engineering and Technology*, 11: 100587, 2022b. ISSN 2666-7908. doi: https://doi.org/10.1016/j.clet.2022.100587. URL https://www.sciencedirect.com/science/article/pii/S2666790822001926.

L. Domergue, R. Nicolas, J.-C. Marle, L. Matthey, M. D'aloisio, L. Buche, and C. Hubert. Shock wave attenuation in aqueous foam. *WIT Transactions on The Built Environment*, 108:83–92, 2009.

R. L. Doney, G. B. Vunni, and J. H. Niederhaus. Experiments and simulations of exploding aluminum wires: validation of alegra-mhd. Technical report, Army research lab Aberdeen proving ground MD weapons and materials research, 2010.

E. Doss. Commemorating the port chicago naval magazine disaster of 1944: Remembering the racial injustices of the 'good war' in contemporary america. http://www.asjournal.org/59-2015/commemorating-port-chicago-naval-magazine-disaster-1944/, 2011. Access Date: Insert Date Here.

H. Draganić, D. Varevac, and S. Lukić. An overview of methods for blast load testing and devices for pressure measurement. *Advances in Civil Engineering*, 2018.

K. D. Duerksen. An exploding wire ion source for ion implantation. Master's thesis, Faculty of the Graduate College of the Oklahoma State University, Southwestern State College Weatherford, Oklahoma, 5 1972.

Esparza and Edward. Blast measurements and equivalency for spherical charges at small scaled distances. *International Journal of Impact Engineering*, 4(1):23–40, 1986.

E. D. Esparza. Blast measurements and equivalency for spherical charges at small scaled distances. *International Journal of Impact Engineering*, 4(1):23–40, 1986. ISSN 0734-743X. doi: https://doi.org/10.1016/0734-743X(86)90025-4. URL https://www.sciencedirect.com/science/article/pii/0734743X86900254.

M. Faraday. Division by the leyden deflagration. *Proceedings of the Royal Institution*, 8: 356, 1857.

A. Filice, M. Mynarz, and R. Zinno. Experimental and empirical study for prediction of blast loads. *Applied Sciences*, 12(5), 2022. ISSN 2076-3417. doi: 10.3390/app12052691. URL https://www.mdpi.com/2076-3417/12/5/2691.

N. I. for Occupational Safety and H. (NIOSH). Occupational noise exposure revised criteria 1998. *U.S. Department of Health, Education, and Welfare, Public Health Service, Center for Disease Control, National Institute for Occupational Safety and Health, DHSS NIOSH Publication No. HIM 73-11001.*, 53:1689–1699, 2013.

S. Formby and R. Wharton. Blast characteristics and tnt equivalence values for some commercial explosives detonated at ground level. *Journal of Hazardous materials*, 50 (2-3):183–198, 1996.

C. Fouchier, D. Laboureur, L. Youinou, E. Lapebie, and J. Buchlin. Experimental investigation of blast wave propagation in an urban environment. *Journal of Loss*

*Prevention in the Process Industries*, 49:248–265, 2017. ISSN 0950-4230. doi: https://doi.org/10.1016/j.jlp.2017.06.021. URL https://www.sciencedirect.com/science/article/pii/S0950423017303200.

French Government. Décret n° 2006-892 du 19 juillet 2006 relatif aux prescriptions de sécurité et de santé applicables en cas d'exposition des travailleurs aux risques dus au bruit et modifiant le code du travail (deuxième partie : Décrets en conseil d'etat). *Official Journal*, 2006. URL https://www.legifrance.gouv.fr/jorf/id/JORFTEXT000000425550.

D. Frost. Heterogeneous/particle-laden blast waves. *Shock Waves*, 28:439–449, May 2018. doi: 10.1007/s00193-018-0825-1. URL https://doi.org/10.1007/s00193-018-0825-1.

B. Gabrielsen, C. Wilton, and K. Kaplan. Final report: Response of arching walls and debris from interior walls caused by blast loading. Final Report DAHC20-71-C-0223, Scientific Service, Inc., 830 Charter Street, Redwood City, California 94063, February 1975.

K. Gault, I. Sochet, L. Hakenholz, et al. Influence of the explosion center on shock wave propagation in a confined room. *Shock Waves*, 30:473–481, 2020. doi: 10.1007/s00193-020-00946-z. URL https://doi.org/10.1007/s00193-020-00946-z. https://link.springer.com/article/10.1007/s00193-020-00946-z.

L. Gilburd, S. Efimov, A. F. Gefen, V. T. Gurovich, G. Bazalitski, O. Antonov, and Y. E. Krasik. Modified wire array underwater electrical explosion. *Laser and Particle Beams*, 30(2):215–224, 2012.

M. Godio, I. Stefanou, and K. Sab. Effects of the dilatancy of joints and of the size of the building blocks on the mechanical behavior of masonry structures. *Meccanica*, 53 (7):1629–1643, 2018. ISSN 1572-9648. doi: 10.1007/s11012-017-0688-z. URL https://doi.org/10.1007/s11012-017-0688-z.

M. Godio, N. W. Portal, M. Flansbjer, J. Magnusson, and M. Byggnevi. Experimental and numerical approaches to investigate the out-of-plane response of unreinforced masonry walls subjected to free far-field blasts. *Engineering Structures*, 239:112328, 2021.

H. Y. Grisaro, I. E. Edri, and S. E. Rigby. Tnt equivalency analysis of specific impulse distribution from close-in detonations. *International Journal of Protective Structures*, 12(3):315–330, 2021.

N. W. Hagood and A. Von Flotow. Damping of structural vibrations with piezoelectric materials and passive electrical networks. *Journal of Sound and Vibration*, 146(2): 243–268, 1991.

R. Han, J. Wu, H. Zhou, Y. Zhang, A. Qiu, J. Yan, W. Ding, C. Li, C. Zhang, and J. Ouyang. Experiments on the characteristics of underwater electrical wire explosions for reservoir stimulation. *Matter and Radiation at Extremes*, 5(4):047201, 2020.

S. Hansen. *Exploding Wires: Principles, Apparatus, and Experiments*. Stephen P. Hansen, 1993–2011. Bell Jar, www.belljar.ne. Available at https://www.belljar.net/Exploding_Wires.pdf.

M. Hargather. Determining the tnt equivalence of gram-sized explosive charges using shock-wave shadowgraphy and high-speed video recording. In *APS Division of Fluid Dynamics Meeting Abstracts*, volume 58, pages LM–001, 2005.

M. Hargather. Background-oriented schlieren diagnostics for large-scale explosive testing. *Shock Waves*, 23, 09 2013. doi: 10.1007/s00193-013-0446-7.

M. Hargather and G. Settles. Optical measurement and scaling of blasts from gram-range explosive charges. *Shock Waves*, 17:215–223, December 2007. doi: 10.1007/s00193-007-0108-8. URL https://doi.org/10.1007/s00193-007-0108-8.

W. F. Hartman, M. E. Larsen, and B. A. Boughton. Blast mitigation capabilities of aqueous foam. Technical report, Sandia National Laboratories, 2006.

Health and Safety Executive. *The Flixborough Disaster: Report of the Court of Inquiry*. HMSO, 1975. ISBN 0113610750.

M.-E. Héroux, H. R. Anderson, R. Atkinson, B. Brunekreef, A. Cohen, F. Forastiere, F. Hurley, K. Katsouyanni, D. Krewski, M. Krzyzanowski, et al. Quantifying the health impacts of ambient air pollutants: recommendations of a who/europe project. *International journal of public health*, 60(5):619–627, 2015.

B. Hopkinson. *British Ordnance Board Minutes 13565*. N/A, 1915.

G. W. Housner. The behavior of inverted pendulum structures during earthquakes. *Bulletin of the Seismological Society of America*, 53(2):403–417, 1963.

Image Systems. TEMA Software. https://imagesystems.se/, 2004.

V. Karlos and G. Solomos. Calculation of blast loads for application to structural components. administrative arrangement no jrc 32253-2011 with dg-home activity a5 - blast simulation technology development. *Unknown*, LB-NA-26456-EN-N, 2013. ISSN 1831-9424. doi: 10.2788/61866.

R. A. Keys and S. K. Clubley. Establishing a predictive method for blast induced masonry debris distribution using experimental and numerical methods. *Engineering Failure Analysis*, 82:82–91, 2017. ISSN 1350-6307. doi: https://doi.org/10.1016/j.engfailanal.2017.07.017. URL https://www.sciencedirect.com/science/article/pii/S1350630716309992.

C. N. Kingery and G. Bulmash. Technical report arbrl-tr-02555: Air blast parameters from tnt spherical air burst and hemispherical burst. Technical Report ARBRL-TR-02555, U.S. Army Ballistic Research Laboratory, 1984.

Kistler. Test & measurement. www.kistler.com, 2023.

H. Kleine, J. Dewey, K. Ohashi, T. Mizukaki, and K. Takayama. Studies of the tnt equivalence of silver azide charges. *Shock Waves*, 13(2):123–138, 2003.

H. Kleine, E. Timofeev, and K. Takayama. Laboratory-scale blast wave phenomena–optical diagnostics and applications. *Shock Waves*, 14(5-6):343–357, 2005.

C. Knox, D. Dizhur, and J. Ingham. Experimental study on scale effects in clay brick masonry prisms and wall panels investigating compression and shear related properties. *Construction and Building Materials*, 163:706–713, 2018.

M. Korres, G. A. Panetsos, and T. Seki, editors. *The Parthenon Architecture and Conservation*. Hellenic Foundation for Culture Committee for the Conservation of the Acropolis Monuments, Athens, 1999.

M. Leitner, T. Leitner, A. Schmon, et al. Thermophysical properties of liquid aluminum. *Metallurgical and Materials Transactions A*, 48:3036–3045, 2017. doi: https://doi.org/10.1007/s11661-017-4053-6.

Z. Li, L. Chen, Q. Fang, H. Hao, Y. Zhang, H. Xiang, W. Chen, S. Yang, and Q. Bao. Experimental and numerical study of unreinforced clay brick masonry walls subjected to vented gas explosions. *International Journal of Impact Engineering*, 104:107–126, 2017.

Z. Li, S. Escoffier, and P. Kotronis. Study on the stiffness degradation and damping of pile foundations under dynamic loadings. *Engineering Structures*, 203:109850, 01 2020. doi: 10.1016/j.engstruct.2019.109850.

H. Liu, J. Zhao, Z. Wu, L. Zhang, and Q. Zhang. Experimental investigations on energy deposition and morphology of exploding aluminum wires in argon gas. *Journal of Applied Physics*, 125(10):103301, 2019.

M. Liverts, O. Ram, O. Sadot, N. Apazidis, and G. Ben-Dor. Mitigation of exploding-wire-generated blast-waves by aqueous foam. *Physics of Fluids*, 27(7):076103, 2015.

D. Logan. *Applied Mathematics*. Wiley, 4th edition, 2013. URL https://www.perlego.com/book/1001329/applied-mathematics-pdf.

J. Loiseau, Q. Pontalier, A. Milne, S. Goroshin, and D. Frost. Terminal velocity of liquids and granular materials dispersed by a high explosive. *Shock Waves*, 28(3):473–487, 2018.

F. Masi. *Fast-dynamic response and failure of masonry structures of non-standard geometry subjected to blast loads*. PhD thesis, École centrale de Nantes, 2020.

F. Masi. *Introduction to Regression Methods*. Wiley, ISTE, 2024. ALERT Doctoral School.

F. Masi, I. Stefanou, P. Vannucci, and V. Maffi-Berthier. Rocking response of inverted pendulum structures under blast loading. *International Journal of Mechanical Sciences*, 157:833–848, 2019.

F. Masi, I. Stefanou, and V. Maffi-Berthier. Scaling laws for the rigid-body response of masonry structures under blast loads. *American Society of Civil Engineers*, 2022.

J. R. McGrath. Exploding wire research, 1774-1963. Memorandum Report 1698, NRL, CO, May 1966. NRL Problem E02-02. Available at https://apps.dtic.mil/sti/tr/pdf/AD0633623.pdf.

W. Mellor, E. Lakhani, J. Valenzuela, B. Lawlor, J. Zanteson, and V. Eliasson. Design of a multiple exploding wire setup to study shock wave dynamics. *Experimental Techniques*, 44:241–248, 2020.

F. Mendonça, G. Urgessa, A. Augusto, and J. A. Rocco. Experimental records from blast tests of ten reinforced concrete slabs. *CivilEng*, 1(2):51–74, 2020.

R. Meyer, J. Köhler, and A. Homburg. *Explosives*. John Wiley & Sons, 2016.

G. Michaloudis and N. Gebbeken. Modeling masonry walls under far-field and contact detonations. *International Journal of Impact Engineering*, 123:84–97, 2019.

T. Mommsen. The venetians in athens and the destruction of the parthenon in 1687. *American Journal of Archaeology*, 45(4):544–556, 1941.

A. Morsel, F. Masi, I. Stefanou, and P. Kotronis. Design of reduced-scale experiments of masonry structures subjected to blast loads. In *Proceedings of the 33rd Workshop ALERT Geomaterials*, Aussois, France, 2022. Poster.

A. Morsel, F. Masi, I. Stefanou, P. Kotronis, G. Racineux, and E. Marché. Reduced-scale testing of masonry structures to explosions. In *Proceedings of the 34th Workshop ALERT Geomaterials*, Aussois, France, 2023. Poster.

A. Morsel, F. Masi, I. Stefanou, P. Kotronis, G. Racineux, and E. Marché. Reduced-scale testing of masonry structures to explosions. In *Proceedings of the 9th International Conference on Structural Engineering and Concrete Technology: ICSECT 2024*, London, United Kingdom, April 14–16 2024. Accepted – in press.

E. Nairne. Vii. electrical experiments by mr. edward nairne, of london, mathematical instrument-maker, made with a machine of his own workmanship, a description of which is prefixed. *Phil. Trans. R. Soc.*, 64:79–89, 1774. doi: 10.1098/rstl.1774.0007. URL http://doi.org/10.1098/rstl.1774.0007.

C. Needham. *Blast Waves*. Springer, 01 2010. ISBN 978-3-642-05287-3. doi: 10.1007/978-3-642-05288-0.

A. Neuberger, S. Peles, and D. Rittel. Scaling the response of circular plates subjected to large and close-range spherical explosions. part i: Air-blast loading. *International Journal of Impact Engineering*, 34(5):859–873, 2007.

Newport. Optical tables and supports system. www.newport.com, 2023.

T. Ngo, P. Mendis, A. Gupta, and Ramsay. Blast loading and blast effects on structures–an overview. *Electronic Journal of Structural Engineering*, 7(S1):76–91, 2007.

S. Pan and Z. Zhang. Fundamental theories and basic principles of triboelectric effect: A review. *Friction*, 7:2–17, 2019.

R. Pape, K. R. Mniszewski, and A. Longinow. Explosion phenomena and effects of explosions on structures. i: Phenomena and effects. *Practice Periodical on Structural Design and Construction*, 15(2):135–140, 2010.

O. Pennetier, M. William-Louis, and A. Langlet. Numerical and reduced-scale experimental investigation of blast wave shape in underground transportation infrastructure. *Process Safety and Environmental Protection*, 94:96–104, 2015. ISSN 0957-5820. doi: https://doi.org/10.1016/j.psep.2015.01.002. URL https://www.sciencedirect.com/science/article/pii/S0957582015000038.

J. M. Pereira, J. Campos, and P. B. Lourenço. Masonry infill walls under blast loading using confined underwater blast wave generators (wbwg). *Engineering Structures*, 92: 69–83, 2015.

S. Petry and K. Beyer. Scaling unreinforced masonry for reduced-scale seismic testing. *Bulletin of Earthquake Engineering*, 12:2557–2581, 2014.

O. Ram and O. Sadot. Implementation of the exploding wire technique to study blast-wave–structure interaction. *Springer-Verlag, Exp Fluids (2012) 53:1335–1345, DOI 10.1007/s00348-012-1339-8*, 2012.

B. Richard, S. Cherubini, F. Voldoire, P.-E. Charbonnel, T. Chaudat, S. Abouri, and N. Bonfils. Smart 2013: Experimental and numerical assessment of the dynamic behavior by shaking table tests of an asymmetrical reinforced concrete structure subjected to high intensity ground motions. *Engineering Structures*, 109:99–116, 02 2016. doi: 10.1016/j.engstruct.2015.11.029.

E. Richardson, T. Skinner, J. Blackwood, M. Hays, M. Bangham, and A. Jackson. An experimental study of unconfined hydrogen/oxygen and hydrogen/air explosions. In *46th JANNAF Combustion Conference, Albuquerque, NM*, pages 8–11, 2014.

S. Rigby, N. Chaudhary, D. Bogosian, T. Payne, and A. Tyas. Large-scale validation of hudson clearing predictions. In *Proceedings of The 17th International Symposium on the Interaction of the Effects of Munitions with Structures (17th ISIEMS)*. ISIEMS, 2017.

S. E. Rigby. *Blast wave clearing effects on finite-sized targets subjected to explosive loads*. PhD thesis, University of Sheffield, 2014.

S. E. Rigby, A. Tyas, T. Bennett, J. A. Warren, and S. Fay. Clearing effects on plates subjected to blast loads. *Proceedings of the Institution of Civil Engineers-Engineering and Computational Mechanics*, 166(3):140–148, 2013.

C. Robert, J. Schirmer, M. Brinkmann, T. Kurz, and C. Teichert. Experiments and simulations of exploding aluminum wires. *International Journal of Energetic Materials and Chemical Propulsion*, 9(3-4):383–396, 2010.

Savitanks. Galvanized container. www.savitanks.com, 2023.

J. Shin, A. S. Whittaker, and D. Cormie. Tnt equivalency for overpressure and impulse for detonations of spherical charges of high explosives. *International Journal of Protective Structures*, 6(3):567–579, 2015.

P. W. Sielicki and T. Łodygowski. Masonry wall behaviour under explosive loading. *Engineering Failure Analysis*, 104:274–291, 2019. ISSN 1350-6307. doi: https://doi.org/10.1016/j.engfailanal.2019.05.030. URL https://www.sciencedirect.com/science/article/pii/S1350630718315838.

S. Sivaraman and S. Varadharajan. Investigative consequence analysis: a case study research of beirut explosion accident. *Journal of Loss prevention in the Process industries*, 69:104387, 2021.

I. Sochet. Blast effects of external explosions. In *Eighth International Symposium on Hazards, Prevention, and Mitigation of Industrial Explosions*, 2010.

I. Sochet and Y. Maillot. Blast wave experiments of gaseous charges. In *Blast Effects*, pages 89–111. Springer, 2018.

I. Sochet, K. Gault, and L. Hakenholz. Propagation of shock waves in two rooms communicating through an opening. In S. Rao, editor, *Direct Numerical Simulations*, chapter 2. IntechOpen, Rijeka, 2019. doi: 10.5772/intechopen.87190. URL https://doi.org/10.5772/intechopen.87190.

Solutions Elastomeres. Mousse mélamine pyramide. www.solutions-elastomeres.com, 2023.

H. Späth and K.-P. Becker. Energy storage by capacitors. *European Transactions on Electrical Power*, 12(3):211–216, 2002.

A. standard. Military standard human engineering design criteria for military systems, equipment and facilities. *AMSC A7245*, 107:1689–1699, 1997.

J. Tartière, M. Arrigoni, A. Nême, H. Groeneveld, and S. Van Der Veen. Pvdf based pressure sensor for the characterisation of the mechanical loading during high explosive hydro forming of metal plates. *Sensors*, 21(13), 2021. ISSN 1424-8220. doi: 10.3390/s21134429. URL https://www.mdpi.com/1424-8220/21/13/4429.

M. Tomaževič, I. Klemenc, and P. Weiss. Seismic upgrading of old masonry buildings by seismic isolation and cfrp laminates: a shaking-table study of reduced scale models. *Bulletin of earthquake engineering*, 7:293–321, 2009.

P. Tournikiotis. *The Parthenon and its Impact in Modern Times*. Melissa Publishing House, 1994. ISBN 960204019X.

N. A. TREATY. Reconsideration of the effects of impulse noise. *RTO organization*, April, 2003.

S. Trelat, I. Sochet, B. Autrusson, K. Cheval, and O. Loiseau. Strong explosion near a parallelepipedic structure. *Journal Shock Waves*, 16(4-5):349–357, 2007. doi: 10.1007/s00193-006-0069-3. URL https://doi.org/10.1007/s00193-006-0069-3. https://hal.archives-ouvertes.fr/hal-00647799.

S. Trélat, I. Sochet, B. Autrusson, O. Loiseau, and K. Cheval. Strong explosion near a parallelepipedic structure. *Shock Waves*, 16(4):349–357, 2007. ISSN 1432-2153. doi: 10.1007/s00193-006-0069-3. URL https://doi.org/10.1007/s00193-006-0069-3.

T. Tucker and F. Neilson. The electrical behavior of fine wires exploded by a coaxial cable discharge system. In Chace and Moore, editors, *Exploding Wires*, volume I, pages 73–82. Plenum Press, New York, 1959.

L. J. Tung and B. W. Kwan. *Circuit analysis*. World Scientific, 2001.

A. Tyas. Experimental measurement of pressure loading from near-field blast events: Techniques, findings and future challenges. *Proceedings*, 2(8), 2018. doi: 10.3390/ICEM18-05364. URL https://doi.org/10.3390/ICEM18-05364.

P. Virtanen, R. Gommers, T. E. Oliphant, M. Haberland, T. Reddy, D. Cournapeau, E. Burovski, P. Peterson, W. Weckesser, J. Bright, et al. Scipy 1.0: fundamental algorithms for scientific computing in python. *Nature methods*, 17(3):261–272, 2020.

P. Walter. Air-blast and the science of dynamic pressure measurements. *Sound & Vibration*, 38(12):10–17, December 2004.

I.-T. Wang. Simulation and experimental validation of the dynamic pressure of shock wave under free-field blast loading. *Journal of Vibroengineering*, 16(7):3547–3556, 2014.

K. Winter. *Irregular reflections of unsteady shock waves*. PhD thesis, New Mexico Tech, 2021.

W. Xiao, M. Andrae, and N. Gebbeken. Air blast tnt equivalence factors of high explosive material petn for bare charges. *Journal of Hazardous Materials*, 377:152–162, 2019.

W. Xiao, M. Andrae, and N. Gebbeken. Air blast tnt equivalence concept for blast-resistant design. *International Journal of Mechanical Sciences*, 185:105871, 2020. ISSN 0020-7403. doi: https://doi.org/10.1016/j.ijmecsci.2020.105871. URL https://www.sciencedirect.com/science/article/pii/S0020740320307931.

S. Yadav, H. Damerji, R. Keco, Y. Sieffert, E. Crété, F. Vieux-Champagne, P. Garnier, and Y. Malecot. Effects of horizontal seismic band on seismic response in masonry structure: Application of dic technique. *Progress in Disaster Science*, 10:100149, 2021. ISSN 2590-0617. doi: https://doi.org/10.1016/j.pdisas.2021.100149. URL https://www.sciencedirect.com/science/article/pii/S2590061721000090.

S. Yadav, Y. Sieffert, F. Vieux-Champagne, Y. Malecot, M. Hajmirbaba, L. Arléo, E. Crété, and P. Garnier. Shake table tests on 1: 2 reduced scale masonry house with the application of horizontal seismic bands. *Engineering Structures*, 283:115897, 2023.

W. Yang, T. Zhang, J. Zhou, W. Shi, J. Liu, and K. Cen. Experimental study on the effect of low melting point metal additives on hydrogen production in the aluminum–water reaction. *Energy*, 88:537–543, 2015.

K. Zambas. Study for the restoration of the parthenon. In *Ministry of Culture Committee for the Preservation of the Acropolis Monuments*, 1994.

F. Zapata and C. García-Ruiz. Chemical classification of explosives. *Critical Reviews in Analytical Chemistry*, 51(7):656–673, 2021.

J. Zhao, Z. Qiaogen, W. Yan, and X. Liu. Plasma characteristics of single aluminum wire electrically exploded in high vacuum. *IEEE Transactions on Plasma Science*, 41(8): 2207–2213, 2013. doi: 10.1109/TPS.2013.2248098.

A. Zyskowski, I. Sochet, G. Mavrot, P. Bailly, and J. Renard. Study of the explosion process in a small scale experiment—structural loading. *Journal of Loss Prevention in the Process Industries*, 17(4):291–299, 2004. ISSN 0950-4230. doi: https://doi.org/10.1016/j.jlp.2004.05.003. URL https://www.sciencedirect.com/science/article/pii/S0950423004000257.

# Part IV

# Appendix

# Appendix A

# Safety recommendations for experimental testing

## A.1 Introduction

Environmental safety is of primary importance and concern in experimental testing. This is exacerbated in scenarios where explosions are involved because of the elevated environmental hazard and risk for the involved personnel. With environmental safety we refer here to the design of safe experiments that do not put the personnel and the equipment at risk in the laboratory. It includes the methodology, policies, and procedures that must be followed to ensure safety. In the particular case of our platform, the primary concern is related to the sound level associated with the detonation of exploding wires and the removal of aluminium dust. The latter issue is fully addressed by the air ventilation system installed within the cabin container. Thus, the only point to be clarified is the safety of the personnel as far it concerns the noise levels associated with our experiments.

## A.2 Safety of scientists against hearing loss

In our experiments, the produced sound is more dangerous as it is considered as impulsive noise. Impulse noises are associated with a sudden increase in sound pressure, which prevents activation of the ear's protective mechanisms referred to as "auditory reflex" and may lead to hearing loss (Karlos and Solomos, 2013). To ensure no excessive noise is produced during experiments, we follow the exposure limits reported in noise legislation (Héroux et al., 2015; French Government, 2006; AFNOR, Juin, 2000; for Occupational Safety and , NIOSH; TREATY, April, 2003)

We focus here on the prevention of noise induced hearing loss and consider the French national law, *Decret* n° 2006-892 (D2006-892) of July 19, 2006 relating to the safety and health requirements applicable in the event of exposure of workers to risks due to noise and amending the labor code (second part: *Decret* in Council of State) (French Government, 2006). The D2006-892 defines the noise pressure limits to which a person can be exposed without partial or total hearing loss. Exposure limit values are set as pre-defined below at an exchange rate of 3 dB, with the exchange rate being the change in the average noise level corresponding to doubling or cutting by half the allowable exposure time $T_{exp}$. There are three limits defined by D2006-892:

1. The average exposure limit values, corresponding to the daily noise exposure level of

87 dB or to a peak sound pressure level equal to 140 dB, using hearing protection (earmuff or ear plugs) devices.

2. The higher exposure values are a daily noise exposure level of 85 dB or a peak sound pressure level of 137 dB. These values can be reached without the need of using hearing protection.

3. The lower exposure values triggering the preventive action provided for a daily noise exposure level of 80 dB or a peak sound pressure level of 135 dB.

It is worth noticing that among other legislations (e.g. standard, 1997; for Occupational Safety and , NIOSH), the D2006-892 one provides the lowest limit for hearing sound, corresponding to the most conservative and safer configuration. Accordingly, the allowable exposure time $T_{exp}$ for hearing the sound for a permanent hearing level as a function of the exposure limit is defined as:

$$T_{exp} = \frac{T_{ref}}{2^{\frac{L_{exp}-L_{ref}}{ER}}}, \tag{A.1}$$

where $T_{exp}$ represents the allowable exposure time for the noise exposure sound level $L_{exp}$, while $L_{ref}$ and $T_{ref}$ correspond to the reference sound level and its allowable exposure time, respectively. The exchange rate, denoted as $ER$, is set at 3 dB, as specified in the works of AFNOR (Juin, 2000); for Occupational Safety and (NIOSH). The sound pressure level is conventionally defined as

$$L_{exp} = 20 \log_{10} \frac{P_{sound}}{P_o}, \tag{A.2}$$

where $P_{sound}$ is the sound pressure, and $P_o$ the fixed reference pressure which is equal to $2\text{x}10^{-5}$ (Pa).

The D2006-892 specifies the lower exposure limit of 80 dB for an 8 hours, while the maximum exposure limit is 135 dB for a maximum duration of 87 ms. Note that this duration is much larger than the characteristic time of the explosions performed within our platform (of the order of few milliseconds). The resulting sound pressure and impulse are represented in Figure A.1 as functions of the allowable exposure duration limits, where the shaded area is the working limit.

To meet the aforementioned exposure limit requirements, we have considered what we refer to as "safe hearing exposure distance", $D_{safe}$, which represents the maximum distance a person should maintain from the explosive source at the moment of detonation to avoid any risk of partial or total hearing loss (noise induced hearing loss). We consider here the reflected overpressure as the $P_{sound}$, which is a safe approach and more conservative – as it accounts for normal shock reflections. Figure A.2 displays the relationship between the safe distance, $\lambda$, and $\gamma$ – the latter representing the geometric and the density scale factors used in reduced-scale experiments (see Masi et al., 2022).

By means of an example, consider $\gamma = 1$ and $\lambda = 1$ (prototype), and an explosive quantity $W_{\text{TNT}} = 1000$ kg: the corresponding safe hearing exposure distance is $D_{safe} = 1225$ m. However, if one consider the reduced-scale scenario, with, for instance, $\lambda = 1/100$, the required safe distance reduces to approximately 6.1 m. This demonstrates the effectiveness of the scaling laws and reduced scale experiments in enhancing safety aspects. It is worth noting that safety requirements become less stringent for low-range explosions. These displayed safe distances are calculated assuming no ear protection is used.

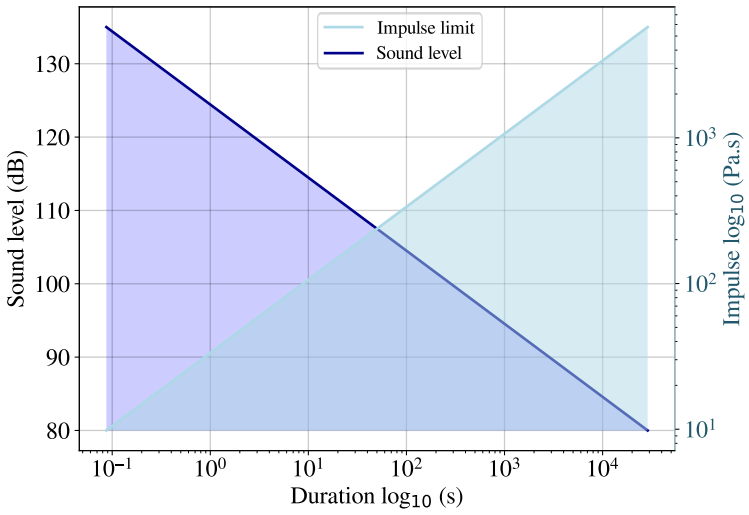


**Figure A.1:** French standard for impulse/sound level as a function of the allowed exposure duration, French Government (2006)

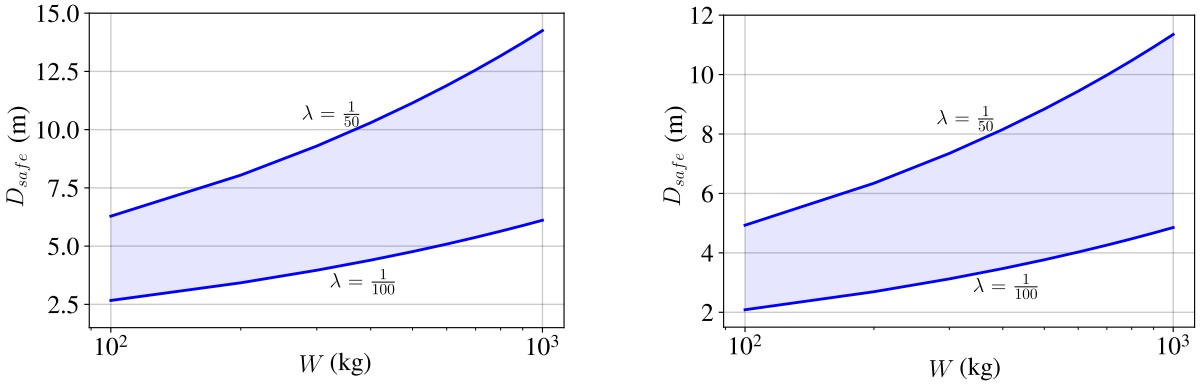


**(a)** For $\gamma = 1$ **(b)** For $\gamma = 0.6$

**Figure A.2:** The required safe distance as function of explosive quantity $W$ for $\gamma = 1$ (a) and for $\gamma = 0.6$ (b).

The safe distance required to prevent hearing loss varies between 2.08 and 14.25 m, depending on different values of $\lambda$ and $\gamma$. To enhance safety and reduce the necessary safe distance, we have therefore chosen to use a container cabin in which we additionally installed acoustic foam for further reducing the sound levels and preventing eventual reflections.

# Appendix B

# Optical table

The optical table is composed of two main parts: (1) the S-2000 non-magnetic support and (2) the optical table panel.

## B.1 S-2000 non-magnetic support

The S-2000 non-magnetic support is selected as it covers all our experiments requirements, including adequate stiffness and the additional possibility of isolating eventual vibrations. The construction, employing high-quality aluminum casting, allows the support to handle high loads with load capacity equal to 907 kg. In our configuration, constiting of six supports, the cumulative load capacity is equal to 5442 kg, thus representing an ideal solution for our experiments as it supports the loads that could applied for the considered scenarios (presented in Section 1.5.1). It is worth noticing that the support could be used as active support (to isolate surrounding noises), but in our applications this option is not active, and the support acts as a rigid one. For the sake of completeness, the specifications of the support are summarized in Table B.1.

**Table B.1:** S-2000 support specifications (Newport, 2023).

| | | | |
|---|---|---|---|
| Support height (mm) | 472.4 | Load capacity per support (kg) | 907 |
| Self centering | Yes | Re-leveling accuracy (mm) | $\pm 0.254$ |
| Height adjustment (mm) | $+27.7/-6.4$ | Weight (kg) | 30.75 |
| Horizontal resonance (Hz) | 1.5 | Horizontal isolation at 10 Hz | 95% |
| Vertical resonance (Hz) | 1 | Vertical isolation at 10 Hz | 98% |
| Maximum air pressure (kPa) | 586 | Horizontal damping | Oil |

The supports also allow for height adjustment to ensure correct table leveling in case of un-level floors Newport (2023), cf. Section 1.9.

## B.2 Optical table panel

The optical table may undergo bending along the two planar directions in case of very localized loads, applied to the center of the panel (see Figure B.1). For this reason, the optical table we employed disposes of two additional support with respect to the standard configuration (with only four supports) and, additionally, the optical table panel has a

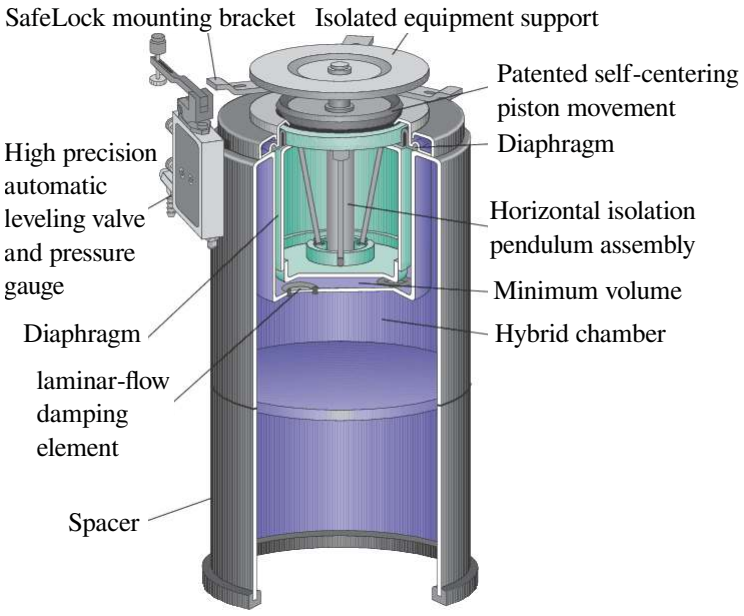


**Figure B.1:** S-2000 support cross section.

thickness of 30.5 cm, which is larger than the standard configuration (see Figure B.2a). In Figure B.2, we show the cross section of the optical table panel. The top and bottom skins as well as the trussed honeycomb core are constructed from non-magnetic 316 series stainless steel. This is beneficial in guaranteeing shielding against eventual magnetic fields, which might affect the signal in piezoelectric sensors (for more details, we refer to subsection C.2). Additional specifications of the optical table are summarized in Table B.2.

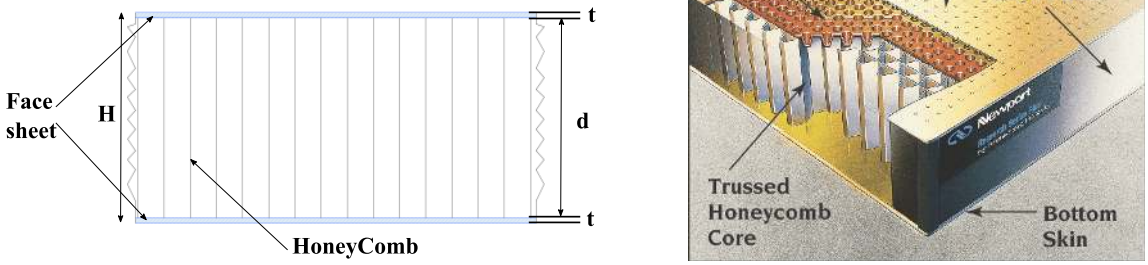


**(a)** Optical table cross section **(b)** Rigid trussed honeycomb core design

**Figure B.2:** Optical table cross section (a) and honeycomb core design (b).

**Table B.2:** Specifications of the optical table

| **Construction** | |
|---|---|
| Broadband damping | Constrained layer core, damped working surface and composite edge finish |
| Working surface | 4.8 mm thick t 316 series non-magnetic stainless steel |
| Surface flatness | $\pm 0.1$ mm over 600 mm$^2$ |
| Bottom skin material | 4.8 mm thick 316 series non-magnetic stainless steel |
| Core construction | Trussed honeycomb, vertically bonded closed cell construction 0.25 mm steel sheet materials, 0.76 mm triple core interface |
| Weight (kg) | 354 |
| Length (mm) | 1800 |
| Width (mm) | 1200 |
| Thickness (mm) | 305 |

# Appendix C

# System of measurements

Herein, we present the details and specifications of the components composing the system of measurements.

## C.1 Data acquisition devices

TraNET data acquisition device is selected to acquire the signal from the several sensors composing the system of measurements. This consists of different modes including (a) continuous data recorder, where a long duration event can be stored to disk and analysed later, (b) controlled recording mode to capture sequential blocks of data, without any loss. The TraNET FE 404 is equipped with eight channels. All the specifications of the TraNET FE 404 are summarized in Table C.1.

**Table C.1:** Specifications of TraNET FE 404 – note that MB refers to Megabyte.

| | |
|---|---|
| Connection | ethernet 1 GBit<br>RJ45 front connector, USB3 port for external HD |
| Operating condition | 0 .. 45 °C |
| Recording modes | Scope, Multi block, Continuous,<br>Event controlled recording, Dual sampling rate |
| Max. sample rate (MHz) | 20 |
| Amplitude resolution | 16 Bit up to 5 MHz, 14 Bit up to 20 MHz |
| Memory per channel (MB) | 16 |

LabVIEW[1] acquisition software is utilized to manage the writing and reading of data recorded on hard disk. Designing the LabVIEW code was challenging and complex because it involved recording a substantial amount of data in a short duration (less than 1 s) while ensuring data integrity. Furthermore, LabVIEW allows us to configure the data acquisition strategy, define recorded channels, set sampling rates, establish trigger conditions, write files, and display real-time measurements (see Figure C.1).

[1]LabVIEW is a system-design platform and development environment for a visual programming language from National Instruments.

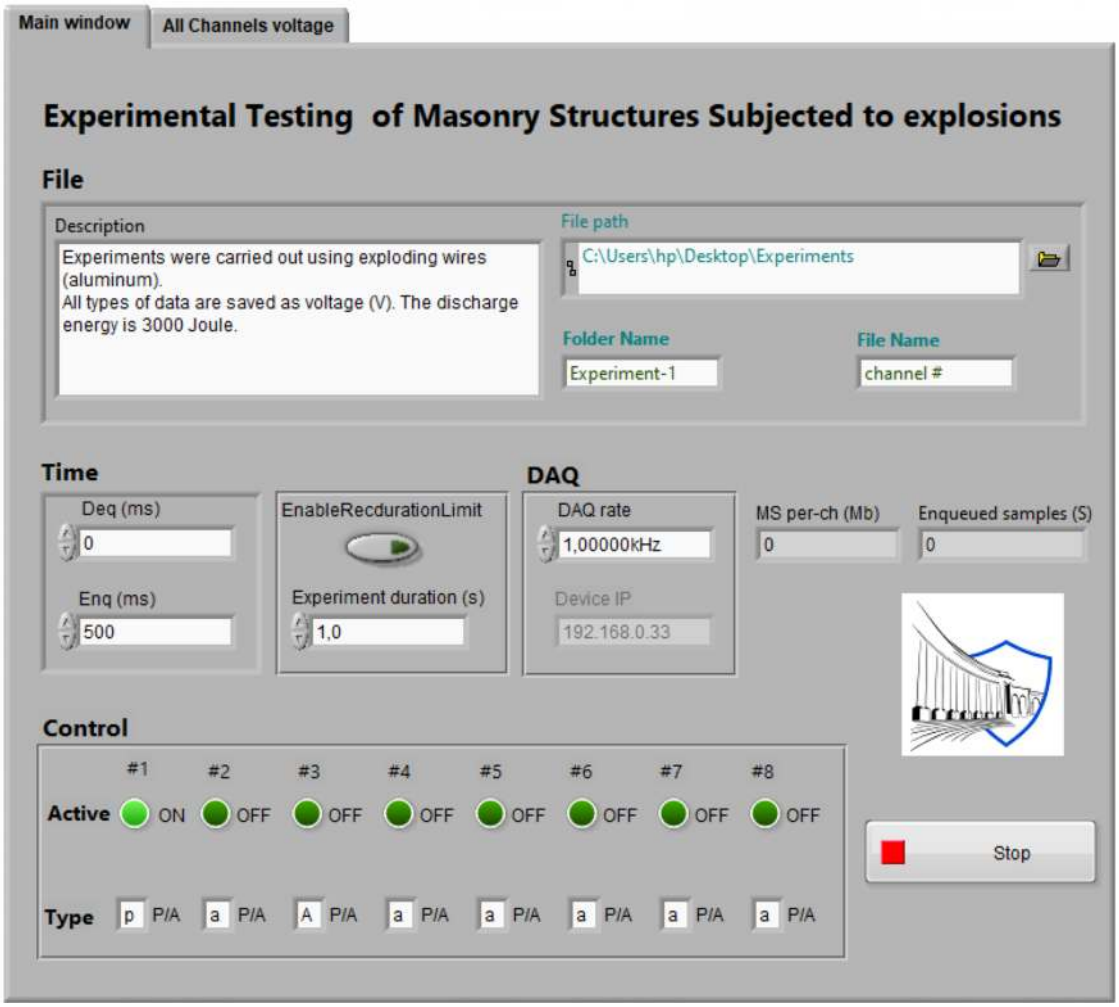


**Figure C.1:** LabVIEW code used to record experimental data.

## C.2 Sensors uncertainties, specifications and installation

**Sensor uncertainties** We present more details about sensors uncertainties (errors), sensors working principles, and how they interact with data acquisition devices to provide accurate measurements.

Measurements uncertainties are inherent in any system and arise from various sources, such as temperature, humidity, vibration, and other environmental factors that can affect the accuracy of the recorded measurements. Uncertainties can also arise from the accuracy of the sensor itself, or from the methodology used to record the measurements.

In this context, each component of the system can introduce its own set of uncertainties. One of the main sensor issues is the influence of cable length on the measured signal. When cables were employed with charge-sensing circuits, noise generated within the cable due to triboelectric effects[2] becomes a problem. However, in our case, we opted for integral-electronics piezoelectric (IEPE) transducers, which enable overcoming the aforementioned triboelectric effects. The IEPE configuration converts the transducer's output from charge to voltage signal. All the sensors presented below have integrated IEPE. Additional source of uncertainties are:

1. Acceleration sensitivity: it is the sensitivity of a pressure transducer to acceleration, usually measured in mV/g. It is the amount of output voltage generated by the transducer when subjected to a certain level of acceleration.

2. Range error: it refers to the difference between the expected range of values and the actual values obtained.

3. Rise time: it denotes the duration for the signal to increase from 10% to 90% of the full-scale output (maximum sensor range).

4. DC offset: it is related to the presence of a constant voltage, different from zero, in the output signal.

5. Linearity error: it is the deviation from a perfectly linear relationship between the input and output of a system. It is typically expressed as a percentage of the full-scale output (maximum sensor range).

6. Positional accuracy: it is the deviation from the expected output due to changes in the position of the coil of the transducer.

7. Thermal transients: it is the deviation from the expected output due to changes in the temperature in the medium due to the explosion.

The previous uncertainties can be subdivided into two categories: (1) dependent errors (rise time, range error, and positional accuracy) and (2) independent errors (acceleration sensitivity, DC offset, and linearity). Dependent error refers to the fact that the error's value is related to the measured signal, while independent refers to the case where the error is independent of the measured value. Moreover, in order to calculate the total errors (uncertainties), there are two possible methods: (1) the cumulative error methods and (2) the root sum squared method.

[2]Triboelectric effect is a phenomenon that results in the generation of electric charge through the contact and separation of materials, caused by the exchange of electrons, (Pan and Zhang, 2019).

The cumulative method is the most conservative one where the overall error is obtained by simple addition of all applicable errors:

$$\text{total error} = \text{rise time} + \text{acceleration sensitivity} + \text{linearity} + \dots \tag{C.1}$$

The root sum squared considers instead the total error according to the following formula:

$$\text{total error} = \sqrt{\text{rise time}^2 + \text{acceleration sensitivity}^2 + \text{linearity}^2 + \dots} \tag{C.2}$$

Given the different variety of possible errors and uncertainties, the root sum squared error is a more appropriate measure of the accuracy provided by the system of measurements.

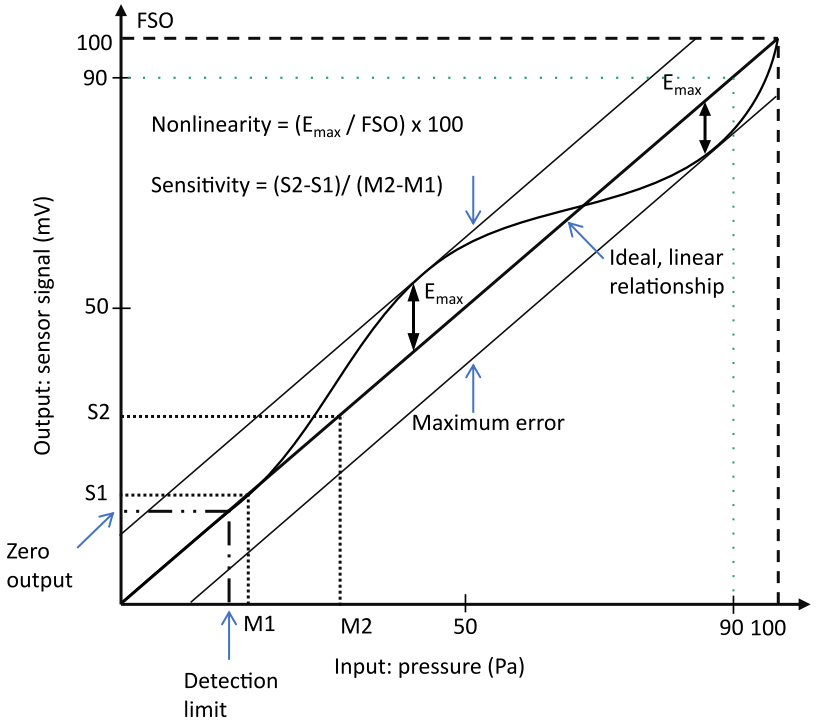


**Figure C.2:** Sensor errors: linearity, sensitivity, and rise time. FSO refers to the full-scale output.

## C.3 Pressure transducers

Here we provide more details and specifications about the pressure transducers. They are distinguished between those that are used to measure the reflected overpressure and those for measuring the incident overpressure.

**Reflected overpressure** The 603CBA family transducer was selected to measure the reflected overpressure for its wide pressure range (between 14 bar to 100 bar), the operating temperature range (up to 200°C), a high natural frequency with very fast rise times ($< 0.4\,\mu_s$), small size and voltage as output signal (Kistler, 2023). All details of the sensor are presented in Table C.2.

**Table C.2:** 603CBA piezoelectric transducer

| **Characteristics** | **603CBA** |
|---|---|
| Output signal | voltage (IEPE) |
| Dimension (mm) | 37.8x5.55 |
| Pressure range (bar) | 14 ÷ 100 |
| Overload (bar) | 1100 |
| Temperature range (°C) | −55 ÷ 120 |
| Rise time (10 ... 90%) ($\mu$s) | $< 0.4$ |
| Natural frequency (kHz) | $> 500$ |
| Temperature coefficient of sensitivity (%/°CC ) | $\approx -0.027$ |
| Acceleration sensitivity (axial) (bar/g) | 0.00014 |
| Acceleration sensitivity (radial) (bar/g) | 0.00001 |
| Supply voltage (by IEPE-Coupler) (VDC) | 22 ÷ 30 |
| Output voltage FSO (V) | ±10 |
| Mass (g) | 4 |

As shown in the geometric configurations (Figure C.3), the sensor is mounted over a support[3] perpendicular to the shock wave in order to measure the reflected overpressure.

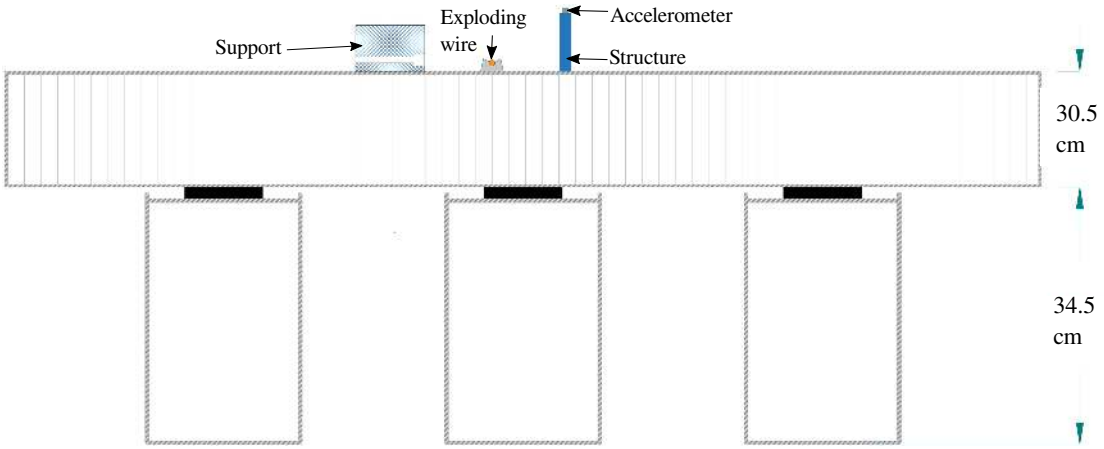


**Figure C.3:** Table cross section: installation of sensors inside support over the table panel.

**Incident overpressure** The incident overpressure is measured using the 6233A0050 pencil probe. This is designed with an integrated amplifier circuit that converts the charge signal from the quartz sensing elements into a voltage output. The device converts the pressure into voltage with sensitivity of 1400 mV/bar. Table C.3 presents the specifications of the pencil probe.

[3]The support have a special design in order to avoid resonance when the shock wave impinged it (frequency analysis). Moreover, dimensions are chosen on the basis of analysis in order to avoid clearing or relief effect coming from the edges, (Rigby, 2014; Rigby et al., 2017; C., 1955).

**Table C.3:** 6233A0050 pencil probe specifications

| **Characteristics** | **6233A0050** |
|---|---|
| Output signal | voltage (IEPE) |
| Dimension (mm) | 406x22.35 |
| Pressure range (bar) | 2 |
| Overload (bar) | 350 |
| Temperature range (°C) | $-55 \div 120$ |
| Rise time ($10 \ldots 90\%$) ($\mu$s) | $< 1$ |
| Natural frequency (kHz) | $\sim 300$ |
| Temperature coefficient of sensitivity (%/°CC ) | $\approx -0.02$ |
| Acceleration sensitivity (mbar/g) | 2 |
| Shock resistance ($< 1$ ms) | 2000 (g) |
| Supply voltage (by IEPE-Coupler) (VDC) | $22 \div 30$ |
| Output voltage FSO (V) | $\pm 10$ |
| Mass (g) | 350 |

## C.4 Accelerometers

We selected 8763B1K0A accelerometers (IEPE uni-axial, see Figure 1.29), from Kistler (2023). Accelerometers with two ranges are selected (1000 g and 5000 g), based on the considered scenarios. The specifications of the accelerometers are summarized in Table C.4.

**Table C.4:** Uni-axial accelerometers characteristics

| **Characteristics** | **8715B** | **8715A** |
|---|---|---|
| Dimension (mm) | 14.7x8.5x6.6 | 10.4x8.5x6.6 |
| Acceleration range (g) | $\pm 1000$ | $\pm 5000$ |
| Frequency range (Hz) | $1 \div 10\,000$ | $1 \div 10\,000$ |
| Sensitivity (mv/g) | $5 \pm 10\%$ | $1 \pm 50\%$ |
| Linearity (%FSO) | 1 | 1 |
| Temperature Range (mm) | -55 ÷ 120 | -55 ÷ 120 |
| Acceleration limit (g) | $\pm 2000$ | $\pm 8000$ |
| Temperature coef. of sensitivity (%/°C) | 0.012 | 0.012 |
| Shock limit (g) | 5000 (1 ms pulse) | 8000 (0.2 ms pulse) |
| Mass (grams) | 1.9 | 2.1 |
| Isolation | ground isolated | ground isolated |

# Appendix D

# Thermal transients

During the explosion of aluminium wires, relatively high temperatures develop around the wire. As a result, thermal transients exist, which result in an apparent noise and discrepancies in the measurements of the output signal of the pressure transducers. Moreover, a transducer equipped with an embedded amplifier produces very recognizable noises when it is subjected to thermal transients. Thermal transients cause the expansion of the pre-load sleeve containing the quartz crystal assembly. The byproduct of this subsequent expansion appears as a negative (i.e., non-return to zero pressure) signal both before and after the blast event (Walter, 2004). The thermal transients could be caused by a bright flash of light generated during the explosion.

The thermal transient responses in our sensors are mitigated by covering the transducer diaphragm's surface with aluminum foil (an electrostatic shielding material). This foil introduces a thermal delay that persists until the blast event ends. We conducted four experiments to illustrate the thermal transient effect on both the incident and reflected overpressures (both short and long durations, for $E_C$ equal to 10.0 kJ and 5.0 kJ). In all cases (reflected and incident measurements), two pressure transducers were used: one with aluminum foil and the other without, with $D$ equal to 30 cm and $d$ equal to 0.6 mm.

Figures D.1 and D.2 display the incident and reflected overpressure as a function of time, respectively. The black curve (with aluminum foil) exhibits a signal that returns to zero and aligns with the ideal shape of the shock wave, as presented in Figure 1.2. Conversely, the signal from the transducer without aluminum foil (red line) displays noise and discrepancies, including a large negative value at the beginning of the signal (before the pressure peak), followed by a noisy signal that fails to return to zero. As previously explained, the aluminum foil introduces a thermal delay that persists until the blast event ends. Afterward, the negative pressure observed could be attributed to thermal transients or reflections coming from the table (see Figures D.1b and D.2b).

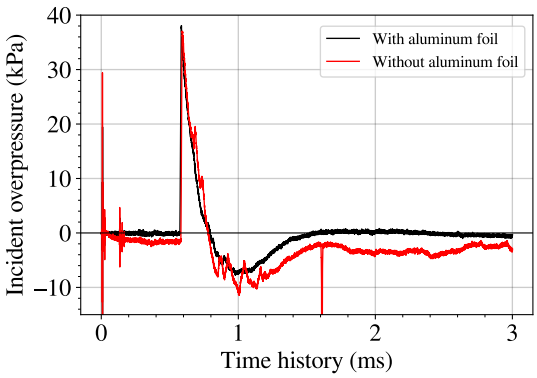


**(a)** Thermal transients in the incident overpressure measurements for short duration.

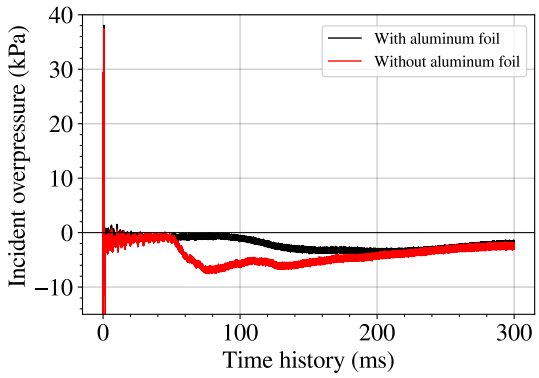


**(b)** Thermal transients in the incident overpressure measurements for long duration.

**Figure D.1:** Thermal transients in the incident overpressure measurements for short duration (a) and long duration (b), for wire diameter = 0.6 mm, wire length = 3.6 cm and energy $E_C$ = 10.0 kJ.

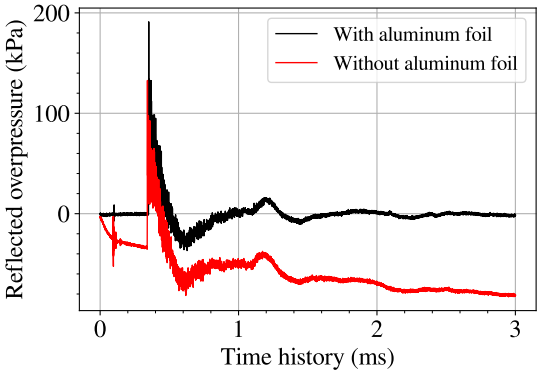


**(a)** Thermal transients in the reflected overpressure measurements for short duration.

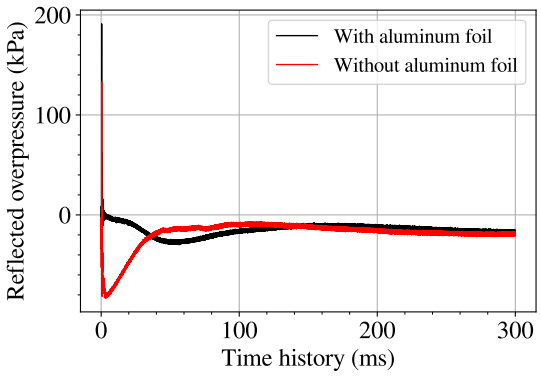


**(b)** Thermal transients in the reflected overpressure measurements for long duration.

**Figure D.2:** Thermal transients in the reflected overpressure measurements for short duration (a) and long duration (b), for wire diameter = 0.6 mm, wire length = 3.6 cm and energy $E_C$ = 5.0 kJ.

# Appendix E

# Sound meter

A SEFRAM 9836 portable sound level meter is used to measure the sound produced during our experiments. The SEFRAM 9835 model has a time weighting (fast/slow). The Min/Max mode allows to display the values over a defined period. Moreover, we can record data and sounds in real time, up to 128,000 samples. The specifications of the portable sound level meter are summarized in Table E.1.

**Table E.1:** Specifications of the SEFRAM 9836 portable sound level meter

| | |
|---|---|
| Data logger | 1 ÷ 128000 points |
| Frequency range | 20Hz ÷ 8KHz |
| Range of measurement | 30 ÷ 130dB |
| Resolution | 2db (4 digits) |
| Refresh rate | 0.5 sec |
| Precision | 1dB |
| Memory | 128 000 points |
| Operating temperature | 0 ÷ 4°C (32 ÷ 104°F) |
| Operating humidity | 10 ÷ 90% RH |
| Mass | 305 g |

# Appendix F

# Dependency of the incident impulse and pressure on the explosive type and shape

Different explosive sources yield to a different incident peak pressures and reduced impulses, see for example Departments of the Army, the Navy, and the Air Force (1990). We study hereafter the dependency of the incident impulse and pressure on the explosion type and shape. In order to compare the data we need to normalize them, this is why we introduce hereafter the reduced impulse $i_{sow}$, defined as:

$$i_{sow} = \frac{i_{so}}{m_{\mathrm{TNT}}^{1/3}}, \tag{F.1}$$

We define $m_{\mathrm{TNT}}$ as the equivalent TNT mass (see Section 3.1). We aim here, to determine whether the values of $P_{so}$ and $i_{sow}$ varies quantitatively and qualitatively the same across different explosive types and shapes for a given values of $Z$.

For this purpose, we present in Figures F.1, F.2, F.3, the influence of the explosive type and shape in terms of incident peak overpressure $P_{so}$ and reduced peak impulse $i_{sow}$, as function of $Z$, (the plots are digitized from Departments of the Army, the Navy, and the Air Force (1990)). It can be observed that the same explosive types but with different explosive shapes yield different values for the $P_{so}$ and $i_{sow}$. Furthermore, different explosives have qualitatively but not quantitatively the same behavior in terms of pressure and impulse variation.

By using different explosive type and shape it is not necessary to have the same qualitative and quantitative behavior of $P_{so}$ and $i_{sow}$. Then, in terms of our explosive source (exploding wire), may not necessarily correspond with other high explosives in terms of pressure and impulse for the same $Z$. Then, explosive sources has a distinct behavior in terms of blast parameters (pressure, impulse, time, etc.) for the same valuem of $Z$.

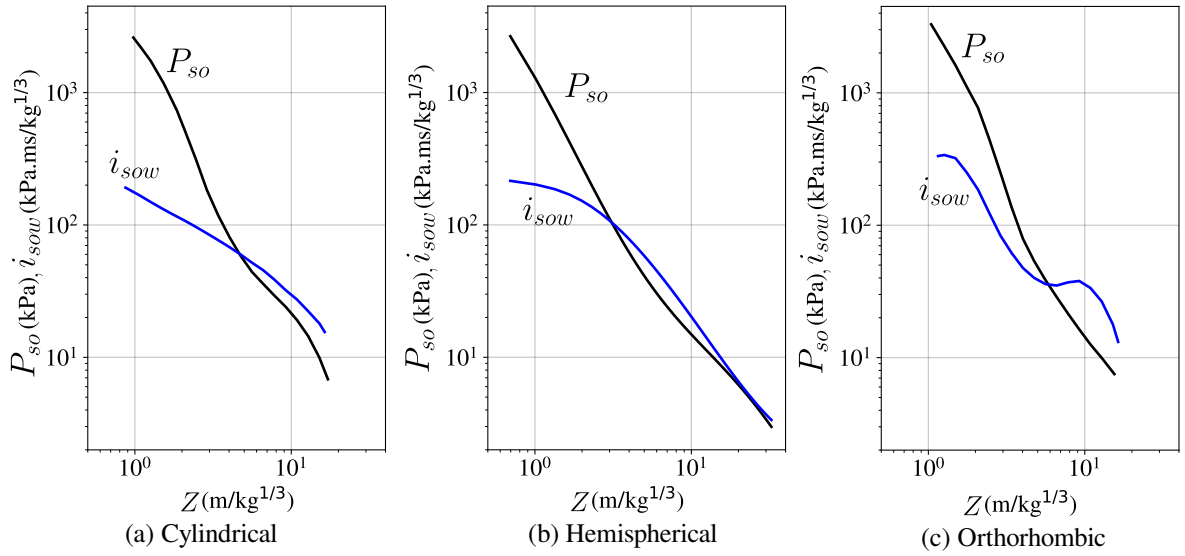


**Figure F.1:** Incident peak overpressure $P_{so}$ and reduced incident peak impulse $i_{sow}$ as function of $Z$ for TNT.

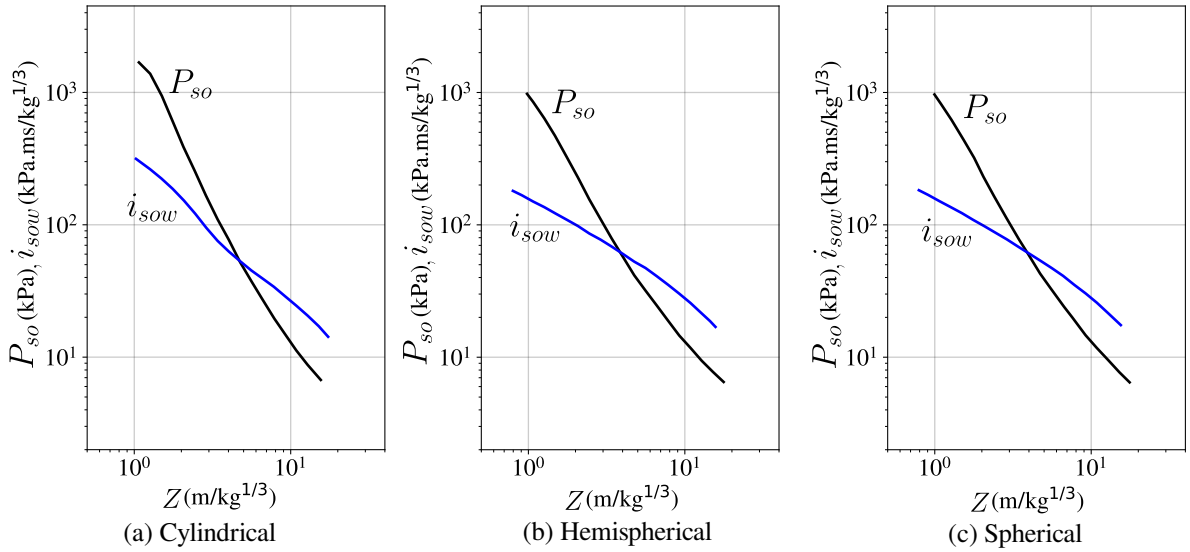


**Figure F.2:** Incident peak overpressure $P_{so}$ and reduced incident peak impulse $i_{sow}$ as function of $Z$ for composition B.

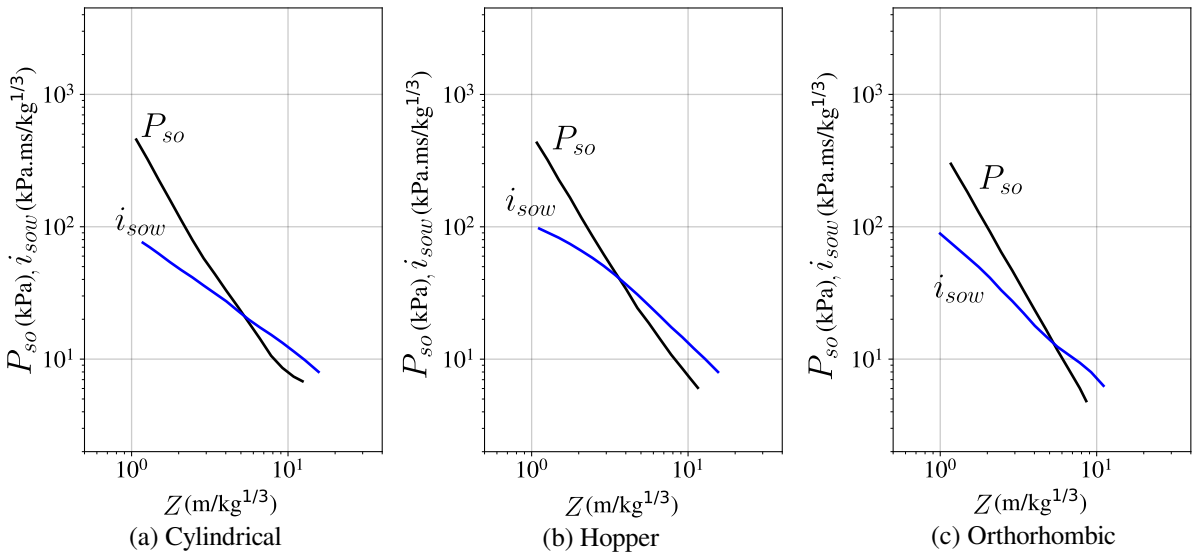


**Figure F.3:** Incident peak overpressure $P_{so}$ and reduced incident peak impulse $i_{sow}$ as function of $Z$ for NACO.

**Titre :** Essais expérimentaux de structures en maçonnerie soumises à des charges extrêmes

**Mots clés :** Maçonnerie, Charges explosives, Dynamique rapide, Expériences de conception, Lois d'échelle, Fils explosifs, Réponse des structures

**Résumé :** Au cours des dernières décennies, le nombre de structures historiques et anciennes soumises à des charges explosives a régulièrement augmenté, en raison d'explosions accidentelles ou délibérées, comme celles survenues sur le site archéologique de Palmyre en 2015 et à Beyrouth en 2020. La protection de ces biens contre les charges explosives est essentielle. Cependant, l'étude de la réponse des structures aux explosions ne peut se faire uniquement en se basant sur des outils numériques et analytiques. Des tests expérimentaux sont nécessaires pour améliorer la compréhension actuelle et valider les modèles existants.

Les expériences à grande échelle ne peuvent être menées que dans des zones d'essais spéciales avec un accès restreint, des problèmes de sécurité et une répétabilité réduite.

Une solution alternative pour étudier les effets des charges explosives sur les structures est de s'appuyer sur des expériences à échelle réduite dans des conditions de laboratoire. Les expériences à échelle réduite assurent un haut degré de reproductibilité, des coûts modérés et des risques réduits liés à l'environnement. Nous présentons ici une nouvelle plateforme (miniBLAST) pour étudier les structures en maçonnerie en se basant sur les lois d'échelle pour la réponse des structures à corps rigide. En particulier, l'utilisation de fils explosifs permet de recréer des conditions de charge analogues à celles d'une explosion, avec des coûts minimes et une grande reproductibilité. La configuration et la méthodologie proposées peuvent être utilisées, pour la première fois, pour étudier la réponse des structures en maçonnerie aux charges explosives dans un environnement de laboratoire sécurisé.

**Title :** Experimental testing of masonry structures subjected to extreme loads

**Keywords :** Masonry, Blast loads, Fast-dynamics, Design experiments, Scaling laws, Exploding wires, Structures response

**Abstract :** In the last decades, the number of historical and ancient structures subjected to blast loads has steadily increased, due to either accidental or deliberate explosions, e.g. the archaeological site of Palmyra in 2015 and Beirut in 2020. The protection of such assets against blast loadings is essential. However, the response of structures to explosions cannot be investigated relying solely on numerical and analytical tools. Experimental tests are necessary to improve current understanding and validate existing models.

Large-scale experiments can be conducted only in special testing areas with restricted access, safety issues, and reduced repeatability.

An alternative solution to investigate the effects of a blast loads on structures is to rely on reduced scale experiments in laboratory conditions. Reduced-scale experiments ensure a high degree of repeatability, moderate cost, and reduced hazards associated with environmental.

We present herein a novel platform (miniBLAST), to study masonry assets based on scaling laws for the rigid-body response of structures. In particular, exploding wires allow to recreate loading conditions analogue to those in an explosion, with minimum costs and high reproducibility. The proposed setup and methodology can be used to investigate, for the first time, the response of masonry structures under blast loads in a safe laboratory environment.